



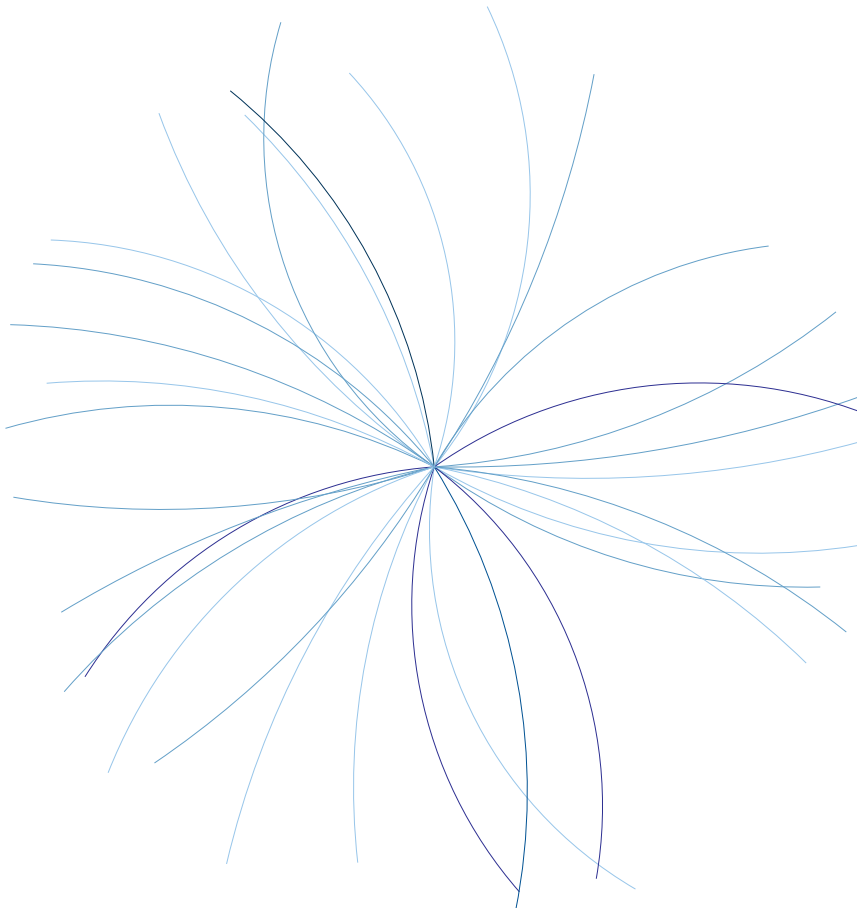
Technische Universität München  
Fakultät für Physik  
Dense and Strange Hadronic Matter



Masterthesis

# First Experimental Evidence of an Attractive Proton- $\phi$ Interaction

Emma Chizzali



Aufgabensteller: Prof. Dr. Laura Fabbietti

Betreuer: Dr. Andreas Mathis

Abgabetermin: 21.09.2021

# Abstract

In this work the first measurement of the  $p$ - $\phi$  correlation function, aiming to extract information on the strong  $p$ - $\phi$  interaction, is presented. This study has implications in various sectors of physics, ranging from the domain of astrophysics to the more fundamental nuclear- and particle physics.

In order to constrain the equation of state of dense objects like neutron stars and subsequently solve the puzzle about their content, it is crucial to understand the interaction between their hypothetical constituents. Hyperons ( $Y$ ) might be contained in the core of neutron stars, which also renders the hyperon-hyperon ( $Y$ - $Y$ ) interaction relevant at large densities. In this context, the  $\phi$  meson could serve as an effective exchange particle, mediating a repulsive interaction among the hyperons. This would lead to a stiffening of the equation of state of dense hyperonic matter, which might even support heavy  $\sim 2M_{\odot}$  neutron stars, discovered in the last decades.

Additionally, the  $\phi$  meson is an interesting probe to investigate the partial restoration of chiral symmetry within the hot and/or dense nuclear medium, predicted by theory. This would lead to modifications of hadronic properties like mass and width, which can be accessed through the spectral function of the meson. In order to properly interpret such measurements, the vacuum properties of the interaction between the  $\phi$  meson and nucleons have to be constrained.

This can be studied experimentally by measuring the  $p$ - $\phi$  correlation function in small colliding systems employing the femtoscopy technique. The small source size in  $pp$  collisions at  $\sqrt{s} = 13$  TeV at the Large Hadron Collider makes it possible to study the short-ranged strong interaction with unprecedented precision. The data used to derive the correlation function are measured by the ALICE experiment. The  $\phi$  candidates are reconstructed from their hadronic decay to charged kaons  $\phi \rightarrow K^+K^-$ , while the protons are detected directly. The resulting correlation function is corrected for non-genuine contributions. This includes the combinatorial  $p$ - $(K^+K^-)$  background arising from the finite purity of the reconstructed  $\phi$  candidates as well as minijet contributions, which consist of auto-correlated protons and  $\phi$  mesons, emitted in jet-like structures.

Both scattering length and effective range of the  $p$ - $\phi$  interaction are extracted from the fully corrected correlation function by means of the Lednický-Lyuboshits model. This results in a scattering length with a real and imaginary part of  $\Re(f_0) = 0.85 \pm 0.34$  (stat.)  $\pm 0.14$  (syst.) fm and  $\Im(f_0) = 0.16 \pm 0.10$  (stat.)  $\pm 0.09$  (syst.) fm, and an effective range of  $d_0 = 7.85 \pm 1.54$  (stat.)  $\pm 0.26$  (syst.) fm. The experimental data are found to reflect the pattern of a shallow attractive force between proton and  $\phi$  meson, characterized by the real part of the scattering length. The imaginary part of the scattering length vanishes within uncertainties and is significantly smaller than the real part, indicating that the  $p$ - $\phi$  interaction in vacuum is dominated by elastic contributions. Additionally, the effective range is large. These results contradict the possibility of the formation of a  $N$ - $\phi$  bound state.

Furthermore, the correlation functions obtained from phenomenological Gaussian- and Yukawa-type potentials are compared to the data, which yield similar results to the one from the Lednický-Lyuboshits approach. From the Yukawa-type potential, it is possible to derive the  $N$ - $\phi$  coupling constant  $g_{N-\phi} = 0.14 \pm 0.03$  (stat.)  $\pm 0.02$  (syst.), which can be linked to the  $Y$ - $Y$  interaction in neutron stars.



# Zusammenfassung

In dieser Arbeit wird die erste Messung der  $p$ - $\phi$  Korrelationsfunktion vorgestellt, die darauf abzielt, Informationen über die starke  $p$ - $\phi$  Wechselwirkung zu gewinnen. Diese Studie hat Auswirkungen auf verschiedene Bereiche der Physik, angefangen bei Astrophysik bis hin zur grundlegenden Kern- und Teilchenphysik.

Um die Zustandsgleichung von dichten Objekten wie Neutronensternen einzugrenzen und anschließend das Rätsel um ihren Inhalt zu lösen, ist es entscheidend, die Wechselwirkung zwischen ihren hypothetischen Bestandteilen zu verstehen. Im Kern von Neutronensternen könnten Hyperonen ( $Y$ ) enthalten sein, wodurch die Hyperon-Hyperon-Wechselwirkung ( $Y$ - $Y$ ) bei großen Dichten relevant wird. In diesem Zusammenhang könnte das  $\phi$ -Meson als effektives Austauscheteilchen dienen, welches eine abstoßende Wechselwirkung zwischen Hyperonen vermittelt. Dies würde zu einer Versteifung der Zustandsgleichung dichter hyperonischer Materie führen, welche sogar die Existenz von  $\sim 2M_{\odot}$  Neutronensternen unterstützen kann, die in den letzten Jahrzehnten entdeckt wurden.

Darüber hinaus ist das  $\phi$ -Meson eine interessante experimentelle Sonde, um die partielle Wiederherstellung von chiraler Symmetrie im heißen und/oder dichten nuklearen Medium zu untersuchen, welche von Theoretikern vorhergesagt wird. Dies würde zu einer Veränderung hadronischer Eigenschaften wie Masse und Breite führen, welche über die Spektralfunktion des Mesons zugänglich sind. Um solche Messungen richtig interpretieren zu können, müssen die Vakuumeigenschaften der Wechselwirkung zwischen  $\phi$ -Mesonen und Nukleonen bestimmt werden.

Dies kann experimentell durch die Messung der  $p$ - $\phi$ -Korrelationsfunktion in kleinen Kollisionssystemen mittels der Femtoskopie-Methode untersucht werden. Die geringe Größe der Emissionsquelle in  $pp$  Kollisionen bei  $\sqrt{s} = 13$  TeV am Large Hadron Collider ermöglicht es, die kurzreichweitige starke Wechselwirkung mit bisher unerreichter Präzision zu untersuchen. Die Daten, die zur Ableitung der Korrelationsfunktion verwendet werden, wurden mit dem ALICE-Experiment gemessen. Die  $\phi$ -Kandidaten werden aus ihrem hadronischen Zerfall zu geladenen Kaonen  $\phi \rightarrow K^+K^-$  rekonstruiert, während die Protonen direkt nachgewiesen werden. Die resultierende Korrelationsfunktion wird um Beiträge korrigiert, welche nicht dem tatsächlichen  $p$ - $\phi$  Anteil entsprechen. Dazu gehören der kombinatorische  $p$ - $(K^+K^-)$ -Hintergrund, der sich aus der begrenzten Reinheit der rekonstruierten  $\phi$ -Kandidaten ergibt, sowie Minijet-Beiträge, die aus autokorrelierten Protonen und  $\phi$ -Mesonen bestehen, welche in jetartigen Strukturen emittiert werden.

Sowohl die Streulänge als auch die effektive Reichweite der  $p$ - $\phi$ -Wechselwirkung werden mit Hilfe des Lednický-Lyuboshits-Modells aus der vollständig korrigierten Korrelationsfunktion extrahiert. Daraus ergibt sich eine Streulänge mit einem Real- und Imaginärteil von  $\Re(f_0) = 0.85 \pm 0.34$  (stat.)  $\pm 0.14$  (syst.) fm und  $\Im(f_0) = 0.16 \pm 0.10$  (stat.)  $\pm 0.09$  (syst.) fm und eine effektive Reichweite von  $d_0 = 7.85 \pm 1.54$  (stat.)  $\pm 0.26$  (syst.) fm. Die experimentellen Daten spiegeln das Muster einer schwachen Anziehungskraft zwischen Proton und  $\phi$ -Meson wider, die durch den Realteil der Streulänge gekennzeichnet ist. Der Imaginärteil der Streulänge verschwindet innerhalb der Unsicherheiten und ist deutlich kleiner als der Realteil, was darauf hinweist, dass die  $p$ - $\phi$ -Wechselwirkung im Vakuum von elastischen Beiträgen dominiert wird.

Außerdem ist die effektive Reichweite groß. Diese Ergebnisse widersprechen der Möglichkeit eines  $N$ - $\phi$  gebundenen Zustands.

Zusätzlich werden die Korrelationsfunktionen, welche aus phänomenologischen Gauß- und Yukawa-Potentialen gewonnen werden, mit den Daten verglichen. Dies liefert ähnliche Ergebnisse wie der Lednický–Lyuboshits Ansatz. Aus dem Yukawa-Potential lässt sich die  $N$ - $\phi$ -Kopplungskonstante  $g_{N-\phi} = 0.14 \pm 0.03$  (stat.)  $\pm 0.02$  (syst.) ableiten, die mit der  $Y$ - $Y$ -Wechselwirkung in Neutronensternen verknüpft werden kann.

# Contents

<b>1</b>	<b>Introduction</b>	<b>1</b>
1.1	QCD and Chiral Symmetry . . . . .	1
1.2	Properties of the Phi Meson . . . . .	4
1.3	Meson Exchange . . . . .	10
1.4	Implications for Neutron Stars . . . . .	12
<b>2</b>	<b>Femtосcopy</b>	<b>17</b>
2.1	Femtoscopic Framework . . . . .	18
2.2	The Scattering Problem . . . . .	22
2.2.1	Lednický–Lyuboshits Approach . . . . .	25
2.2.2	Potentials . . . . .	28
2.3	Coupled-channel dynamics . . . . .	30
<b>3</b>	<b>Experimental Setup</b>	<b>33</b>
3.1	The LHC . . . . .	33
3.2	ALICE . . . . .	34
3.2.1	Inner Tracking System (ITS) . . . . .	35
3.2.2	Time Projection Chamber (TPC) . . . . .	36
3.2.3	Time Of Flight Detector (TOF) . . . . .	38
3.3	Data Reconstruction . . . . .	39
<b>4</b>	<b>Data Analysis</b>	<b>43</b>
4.1	Data Set and Event Selection . . . . .	43
4.2	Particle Selection . . . . .	46
4.2.1	Proton Candidates . . . . .	46
4.2.2	Phi Candidates . . . . .	49
4.2.2.1	Kaon Selection . . . . .	49
4.2.2.2	Phi Resonance . . . . .	50
4.3	Particle pairing . . . . .	55
<b>5</b>	<b>The Correlation Function</b>	<b>57</b>
5.1	Detector Effects . . . . .	58
5.1.1	Unfolding of the correlation function . . . . .	61
5.2	Lambda Parameters . . . . .	63
5.3	Modeling of the measured Correlation Function . . . . .	66
5.3.1	Residual Correlations . . . . .	66
5.3.2	Non-femtoscopic Background . . . . .	72
5.3.3	Genuine Correlation Function . . . . .	73
5.4	Extracting the Genuine Correlation Function . . . . .	76
5.5	The Source . . . . .	77
5.6	Femtoscopic Fit . . . . .	82
5.7	Systematic uncertainties . . . . .	82
5.7.1	Data . . . . .	82
5.7.2	Genuine Correlation Function . . . . .	84

5.7.3	Femtoscopic Fit . . . . .	86
<b>6</b>	<b>Results and Discussion</b>	<b>87</b>
6.1	Accessing the strong FSI . . . . .	87
6.2	Discussion . . . . .	91
<b>7</b>	<b>Summary</b>	<b>95</b>
<b>A</b>	<b>Sideband kinematics and momentum transformation</b>	<b>97</b>
<b>B</b>	<b>Projector Method</b>	<b>103</b>
<b>C</b>	<b>Scattering parameters of the potential approach</b>	<b>107</b>
<b>D</b>	<b>Figures to the <math>p</math>-<math>\phi</math> femtoscopic fits</b>	<b>109</b>
D.1	Lednický-Lyuboshits approach with complex scattering length . . . . .	110
D.1.1	Full model . . . . .	110
D.1.2	Zero effective range approximation . . . . .	112
D.2	Lednický-Lyuboshits approach with real scattering length . . . . .	113
D.3	Potentials . . . . .	114
D.3.1	Yukawa-type . . . . .	114
D.3.2	Gaussian-type . . . . .	115
	<b>List of Figures</b>	<b>117</b>
	<b>List of Tables</b>	<b>125</b>
	<b>Bibliography</b>	<b>127</b>

# 1 Introduction

The strong interaction is one of the four fundamental interactions known by today. Together with the electroweak force, which unifies the electromagnetic and weak interaction, it is described by the Standard Model of particle physics. The color interaction confines quarks into hadrons and is also responsible for the nuclear force. However, despite many extensive studies over the last few decades, it is not yet fully understood how the latter emerges in detail. Therefore, it is of major interest for particle physics and an important topic of ongoing research to study the interaction among hadrons in order to increase the empirical knowledge on the underlying strong force.

## 1.1 QCD and Chiral Symmetry

The strong interaction between quarks is mediated by gluons and the underlying gauge theory is Quantum Chromodynamics (QCD). Its structure and interactions are governed by the principles of relativistic Quantum Field Theory (QFT) with a non-abelian gauge symmetry  $SU(3)_{\text{color}}$ , related to the color charges, which are internal degrees of freedom. Each quark comes in one of three possible colors, to which the gluons couple, themselves arising in eight states of color anti-color combinations.

At small distances and high energies, quarks behave as quasi-free particles. This is related to the self-coupling of the gluons, which leads to an anti-screening of the color charge causing the interaction to weaken at shorter distances. This phenomenon is also referred to as *asymptotic freedom*, which allows for a perturbative treatment of QCD. At large distances, on the other hand, corresponding to low energies and momenta, quarks and gluons are confined within color-neutral hadrons. They can therefore never be observed in isolation. When separating a quark-antiquark pair, the energy stored in the gluon fields increases until it is energetically favorable to produce another quark-antiquark pair. This initiates the process of hadronization, which ultimately results in the formation of hadrons. In the low-energy region of *color confinement*, QCD cannot be treated perturbatively anymore and effective field theories [1, 2] or numerical methods [3, 4] must be employed. Therefore, many features of low-energy QCD are not precisely known and rely on experimental input from studies of basic hadron properties or hadron-hadron interactions. The mentioned behaviour of the strong color interaction translates into a running of the coupling constant, which is depicted in Fig. 1.1. In the low-energy region of *color confinement* it is very large and decreases with increasing energy to the regime of *asymptotic freedom* at high energies.

The QCD Lagrangian is given by [6]

$$\mathcal{L}_{\text{QCD}} = \sum_f \bar{q}_f (i\mathcal{D}_\mu - m_f) q_f - \frac{1}{4} G_{\mu\nu}^a G_a^{\mu\nu}, \quad (1.1)$$

where the first term is summed over the six flavours  $f$  of quarks with current masses  $m_f$ , which are described by the quark fields  $q_f(x)$ . This first term gives the coupling between quarks and gluons via the gauge covariant derivative  $D_\mu = \partial_\mu + ig A_\mu^a \frac{\lambda_a}{2}$ , where  $A_\mu^a(x)$  are the gluon fields and  $\lambda_a$  the Gell-Mann matrices. The last term incorporates the gluon self-couplings involving the squared gluonic field-strength tensor  $G_{\mu\nu}^a(x) = \partial_\mu A_\nu^a - \partial_\nu A_\mu^a - g f^{abd} A_\mu^b A_\nu^c$ .

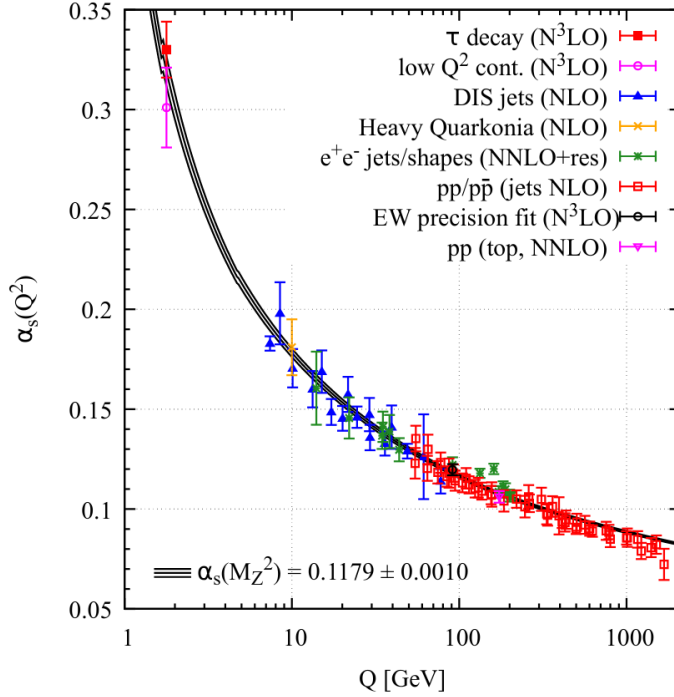


**Figure 1.1:** The strong coupling constant as a function of the energy scale  $Q$ , which is inversely proportional to distance  $Q \propto 1/R$ . Figure taken from [5].

The six quark flavors can be separated into two categories, the light quarks  $u, d$  and  $s$  with masses  $< 100 \text{ MeV}/c^2$  and the heavy ones  $c, b$  and  $t$ , which can be treated effectively as static in low-energy processes. This leaves the light quarks as the only active degrees of freedom. In the chiral limit, they are treated as massless particles which travel at the speed of light. Therefore, their helicity is independent of the Lorentz frame from which they are observed and the quark fields can be decomposed into left- and right-handed chiral components  $q_{fL}$  and  $q_{fR}$ , which are projected out by  $(1 \pm \gamma_5)/2$ .

The corresponding Lagrangian  $\mathcal{L}_{\text{QCD}}^0$  is obtained by setting  $m_{u,d,s} = 0$  in Eq. 1.1 and is invariant under independent rotations of  $q_{fL}$  and  $q_{fR}$  in the left and right flavour spaces, given by the unitary global transformations  $q_I \rightarrow V_I q_I$ , where  $I = L, R$  and  $V_I \in \text{U}(3)$ . The massless Lagrangian respects chiral symmetry  $\text{U}(3)_L \times \text{U}(3)_R = \text{SU}(3)_L \times \text{SU}(3)_R \times \text{U}(1)_V \times \text{U}(1)_A$ . The vector part  $\text{U}(1)_V$ , where both left- and right-handed quarks pick up a common phase, is connected to baryon number conservation [7] and the axial  $\text{U}(1)_A$  is explicitly broken through an anomaly [8, 9] (symmetry breaking by quantization).

The remaining  $\text{SU}(3)_L \times \text{SU}(3)_R$  is a symmetry of the massless Lagrangian but not of the ground state of the system, the QCD vacuum. Chiral symmetry is in fact spontaneously broken. This is characterized by a non-zero vacuum expectation value  $\langle 0 | \bar{q}q | 0 \rangle \neq 0$ , also referred to as chiral condensate. The QCD vacuum is populated by scalar quark-antiquark pairs that mix left- and right-handed quarks in the form  $\bar{q}q = \bar{q}_L q_R + \bar{q}_R q_L$  [10].

Any spontaneously broken global symmetry requires the existence of spinless Nambu-Goldstone bosons [11–13], which are identified as the eight pseudo-scalar mesons  $\pi^\pm, \pi^0, K^0, \bar{K}^0$  and  $\eta$ . Notably, they are significantly smaller in mass compared to the rest of the hadrons. The lightest

Nambu-Goldstone boson is the pion. Its mass  $m_\pi$  and decay constant  $f_\pi$  are related via the Gell-Mann-Oakes-Renner (GOR) relation [14]

$$m_\pi^2 f_\pi^2 = -m_q \langle 0 | \bar{q}q | 0 \rangle, \quad (1.2)$$

with an average current quark mass of  $m_q = \frac{1}{2}(m_u + m_d) = (3.45_{-0.15}^{+0.55})$  MeV [5]. A manifestation of spontaneous chiral symmetry breaking is for example the large mass-gap of  $\Delta M \approx 500$  MeV/ $c^2$  between chiral multiplets sharing all quantum numbers besides parity, e.g.  $\rho(770)$  and  $a_1(1260)$ . In case of a chirally symmetric ground state, their masses would be degenerate [15]. The effects of the spontaneous breaking are most apparent in the generation of hadron masses, which are much larger than the sum of the masses of their constituents. For example, it accounts for more than  $\sim 90\%$  of the mass of nucleons, which consist only of light  $u$  and  $d$  quarks. By introducing non-vanishing quark masses, chiral symmetry is explicitly broken, as left- and right-handed quark fields get mixed by the mass term in Eq. 1.1. Therefore, it is only an approximate symmetry of the QCD Lagrangian.

Chiral symmetry is expected to be partially restored in the medium and a drop of the chiral condensate  $\langle 0 | \bar{q}q | 0 \rangle \rightarrow 0$  is found for increasing temperature and/or density [10].

When considering only the two lightest quark flavours, the low-temperature dependence in the chiral limit is governed by massless pions and can be calculated model-independently from chiral perturbation theory as [16, 17]

$$\frac{\langle \bar{q}q \rangle_T}{\langle \bar{q}q \rangle_0} = 1 - \frac{T^2}{8f_\pi^2} - \frac{T^4}{384f_\pi^4} + \dots, \quad (1.3)$$

where the  $T^4$  term is connected to the interaction among pions and the quadratic term is related to the ideal bose gas by differentiating the pressure with respect to the quark mass. A density dependence can be obtained from substituting the GOR relation, Eq. 1.2, into the expression of the chiral condensate at finite density, which reads as [10]

$$\langle \bar{q}q \rangle_\rho = \langle \bar{q}q \rangle_0 + \langle N | \bar{q}q | N \rangle + \dots \Rightarrow \frac{\langle \bar{q}q \rangle_\rho}{\langle \bar{q}q \rangle_0} = 1 - \frac{\sigma_N}{m_\pi^2 f_\pi^2} \rho + \dots, \quad (1.4)$$

where  $\sigma_N$  is the nucleon sigma term, defined by the nucleon matrix element as  $\sigma_N = m_q \langle N | \bar{q}q | N \rangle$ . The behaviour of the chiral condensate for changing temperature and baryon density is shown in Fig. 1.2, which is based on calculations within the Nambu-Jona-Lasinio model [18].

Hadrons can be interpreted as excitations of the QCD vacuum. Therefore, changes of the chiral condensate within the medium translate into modifications of hadron properties. By studying them experimentally, it is possible to obtain (indirect) information on  $\langle \bar{q}q \rangle$  and learn about non-perturbative low energy QCD in the medium. However, it is essential, that the experimental probe decays inside the medium while the decay products leave the system without further strongly interacting with it since this would distort the information they carry on the in-medium hadron properties.

Vector mesons ( $J^P = 1^-$ ), specifically  $\rho$ ,  $\omega$  and  $\phi$ , are good candidates for studies of in-medium modifications (related to the partial restoration of chiral symmetry), accessible via their spectral functions. The dilepton decay channel fulfills the requirements perfectly, as the decay particles do not interact via the strong force, and hence are not disturbed by the environment. Accordingly, the  $\rho$  in-medium behavior was studied by the NA60 experiment at the CERN SPS by measuring

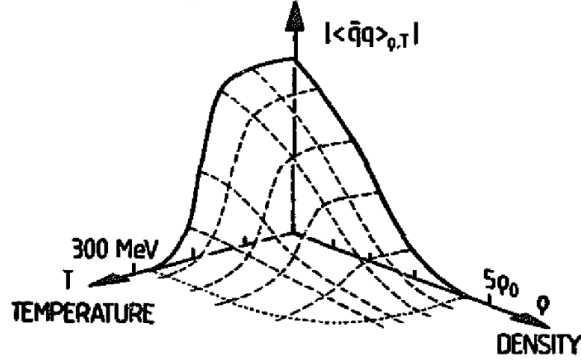


**Figure 1.2:** The chiral condensate  $|\langle\bar{q}q\rangle|$  as function of the temperature and baryon density, given in units of nuclear matter density  $\rho_0 = 0.17 \text{ fm}^{-3}$ . Figure taken from [10].

low-mass muon pairs [19]. The decay to  $e^+e^-$  was exploited to measure both the  $\rho$  and  $\omega$  spectral function with the KEK Proton Synchrotron [20]. However, the small branching ratio of decays of vector mesons into dielptons hampers precise measurements in this channel. Therefore, hadronic channels with much larger branching ratios might be investigated instead. However, they require sufficient knowledge and understanding of the corresponding final-state interactions [21].

The spectral shape can be obtained from theory by employing hadronic models, which rely on the current knowledge of meson-baryon interactions to correctly calculate the self-energy of the hadron within the strongly interacting medium. For vector mesons, both modifications of mass and width are predicted [21, 22]. The latter is related to absorption processes inside the medium, hence a modification of the lifetime of the particle. Constrains on the hadron properties are also provided by QCD sum rules [22–24] as they connect current-current correlation functions, which treat the particles on the quark-gluon level, to the QCD condensates [21–25] by means of the operator product expansion and dispersion relations.

## 1.2 Properties of the $\phi$ meson

The  $\phi$  vector meson is identified as a mixture of the SU(3) octet and singlet states  $\psi_8 = 1/\sqrt{6} \cdot (\bar{u}u + \bar{d}d - 2\bar{s}s)$  and  $\psi_1 = 1/\sqrt{3} \cdot (\bar{u}u + \bar{d}d + 2\bar{s}s)$  [5]

$$\phi(1020) = \psi_8 \cos \theta_V - \psi_1 \sin \theta_V. \quad (1.5)$$

This results in nearly a pure  $\bar{s}s$  state with small contributions from  $u$  and  $d$  quarks as the mixing angle between  $\omega$  and  $\phi$  meson is not the ideal  $\theta_{V,ideal} = 35.3^\circ$  but slightly larger  $\theta_V = 36.4^\circ$  [5].

As mentioned in Sec. 1.1, the  $\phi$  meson is a promising experimental probe to test the partial restoration of chiral symmetry within the nuclear medium, hence providing access to the non-perturbative low-energy sector of QCD. Its narrow width of  $\Gamma \approx 4.25 \text{ MeV}/c^2$  [5] in vacuum makes it clearly distinguishable from other resonances. The lifetime of  $c\tau_\phi \approx 46 \text{ fm}$ , on the other hand, is much larger than the typical radii of atomic nuclei or the size of the fireball created in heavy-ion collisions. This means that most of the  $\phi$  mesons produced in fixed target or collider experiments will decay outside the strongly interacting medium. Hence, their spectral shape is

governed by the  $\phi$  vacuum properties. However, as the decay length of a particle is defined as  $\beta\gamma c\tau$ , a reduction of the lifetime  $\tau = \hbar c/\Gamma$  results in an increased probability of decays within the nuclear environment. Indeed, some theoretical calculations predict an in-medium broadening of up to 10 times the natural width of the  $\phi$  meson, resulting in  $c\tau \sim 5$  fm, see for example [26–28]. Alternatively, as the decay length also depends on the particle velocity, a sizable fraction of slow  $\phi$  mesons might decay within the nuclear medium.

This was exploited by the KEK-PS E325 collaboration. Both mass-shift and width modification inside the nuclear medium were investigated by measuring the  $\phi$  spectral function in p–C and p–Cu reactions at 12 GeV for different velocity selections of the  $\phi$  candidates [29]. The mesons are reconstructed via their dilepton decay channel  $\phi \rightarrow e^+e^-$  (BR  $\approx 3 \times 10^{-4}$  % [5]). The resulting invariant mass distributions for both targets are shown in Fig. 1.3. They are fitted with a quadratic baseline, which accounts for the background, and a resonance shape consisting of a Breit-Wigner convoluted with the detector response. Notably, data from slow  $\phi$  candidates satisfying  $\beta\gamma < 1.25$  within the heavier copper target are not described well by the fit. An excess on the low-mass side of the  $\phi$  resonance is visible, which is interpreted as evidence for an in-medium modification of the  $\phi$  properties. The discrepancy is explained by a 3.4% decrease of the  $\phi$  mass and a broadening of the partial width of  $\phi \rightarrow e^+e^-$  by a factor of 3.6. The resulting lowering in the mass by  $\sim 35$  MeV/ $c^2$  is in the range of some theoretical predictions [22, 30], while others obtain smaller modifications [28, 31, 32].

An increase of the width was also obtained at the ANKE-COSY facility [35] when detecting the  $\phi$  in proton-induced reaction through the hadronic decay to  $K^+K^-$  (BR  $\approx 50$  % [5]). From the measured inclusive  $\phi$  production cross sections for different target nuclei (C, Cu, Au and Ag) of atomic mass number  $A$ , the transparency ratio  $T_A = \sigma_A/(A \cdot \sigma_N)$ , defined in terms of the nuclear ( $\sigma_A$ ) and nucleon cross section ( $\sigma_N$ ), is derived as

$$R = \frac{T_A}{T_C} = \frac{12\sigma_A}{A\sigma_C}. \quad (1.6)$$

Carbon (C) is chosen as reference, as it is a well-studied nucleus. In general, such normalization to a light nucleus reduces the sensitivity to secondary production processes as well as differences in the initial state interactions of hadron-induced reactions [36]. A decrease of  $R$  is observed with increasing  $A$ , see Fig. 1.4, indicating that more  $\phi$  mesons are absorbed in heavier nuclei. By comparing the results to theoretical predictions, a substantial increase in the total  $\phi$  width within the nuclear environment is found. From a parameterization using a local Fermi sea approach [33], an in-medium width of  $45_{-9}^{+17}$  MeV/ $c^2$  is found. This is displayed in Fig. 1.4(a). A fit with the Paryev model [34] yields a width of  $50_{-6}^{+10}$  MeV/ $c^2$ <sup>1</sup>. Similar model-dependent conclusions were reached by other experiments, e.g. [29, 37], all observing an in-medium width of 40 – 60 MeV/ $c^2$  [38], which is compatible with theoretical calculations [28, 31, 32, 39, 40].

However, in order to interpret the modification of the  $\phi$  meson properties within the nuclear medium, it is essential to have sufficient knowledge on the interaction among the involved particles. The meson-nucleus interaction can be described by the Klein-Gordon equation [38, 41]

$$E^2 - \vec{p}^2 - m^2 - \Pi(E, \vec{p}, \rho_N(r)) = 0, \quad (1.7)$$

---

<sup>1</sup> The value quoted in the original paper [35] of  $73_{-10}^{+14}$  MeV/ $c^2$  corresponds to the  $\phi$  meson Eigensystem.

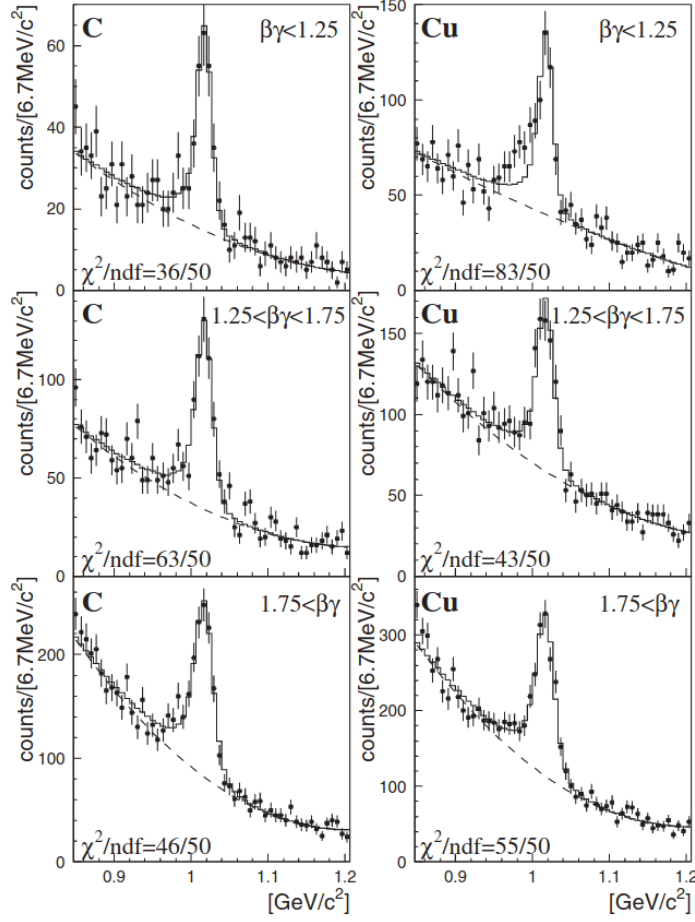


**Figure 1.3:** Invariant mass spectra of  $e^+e^-$ , measured in p-C and p-Cu reactions and categorized by  $\beta\gamma$  of the reconstructed  $\phi$  meson. The data are fitted with a resonance shape consisting of a Breit-Wigner function convoluted with the detector response simulated for the different  $\beta\gamma$  regions and a quadratic baseline. Figure taken from [29].

where  $\Pi(E, \vec{p}, \rho_N(r))$  is the self-energy of the meson with rest mass  $m$ , 3-momentum  $\vec{p}$  and energy  $E$  in the nuclear medium of local density  $\rho_N(r)$ .

The self-energy arises from to all the interactions of the meson within the nuclear medium and can be related to the complex-valued meson-nucleus optical potential  $U(E, \vec{p}, \rho_N(r))$  as [38]

$$\Pi(E, \vec{p}, \rho_N(r)) = 2\sqrt{\vec{p}^2 + m^2} U(E, \vec{p}, \rho_N(r)). \quad (1.8)$$

While the real part of the optical potential gives information on the attractiveness or repulsiveness of the interaction and is connected to the mass modification, the imaginary part is related to the inelastic (absorption) processes and can therefore be used to model the results of transparency ratio measurements.

The  $\phi$  meson couples strongly to the  $K\bar{K}$  system ( $K^+K^-$ ,  $K^0\bar{K}^0$ ), which is its dominant decay channel in vacuum with a branching ratio of about 83% [5]. Therefore, the  $K\bar{K}$  cloud contributes significantly to its self-energy [28, 42, 43]. The different interactions are depicted in Fig. 1.6.

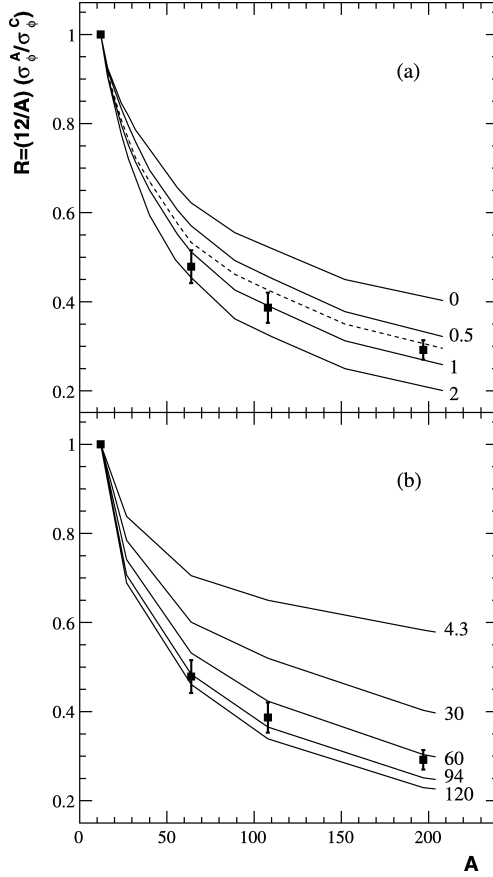


**Figure 1.4:** Transparency ratios for different nuclei of mass number  $A$ , normalized to  $C$ . The data are compared to Valencia calculations [33] in panel (a) and to the Paryev model [34] in panel (b). Figure taken from [35].

The relation between the vector meson and kaons was investigated by HADES in pion induced fixed-target collisions at beam energies of 1.65 GeV. Within uncertainties, a constant ratio  $\phi/K^-$  was observed for the different targets  $C$  and  $W$ , as shown in Fig. 1.5, in addition to a sizable absorption of the  $K^-$  particle in the heavy tungsten nuclei ( $W$ ) with respect to the lighter ones ( $C$ ) [44]. Therefore, also a strong  $\phi$  absorption is assumed. Besides to the  $K\bar{K}$  cloud, vector-meson baryon interactions contribute to the  $\phi$  self-energy, especially the  $N-\phi$  channel [43].

The left plot of Fig. 1.7 shows both the real and imaginary part of the optical potential when including only the contribution from the  $K\bar{K}$  cloud in the calculations as well as both  $K\bar{K}$  and  $N-\phi$  effects. The interaction mechanism between  $\phi$  meson and nucleons is incorporated by employing two different theoretical approaches, where one is based on SU(6) spin-flavor symmetry and the other on hidden local symmetry (HSL) [30]. In the right plot of Fig. 1.7 the corresponding spectral functions at nuclear saturation density  $\rho_0 \approx 0.17 \text{ fm}^{-3}$  are depicted. The vacuum result is plotted as a reference. It can be seen that a visible broadening is obtained for both approaches, while only the SU(6) treatment of the  $N-\phi$  contribution leads to a significant mass shift. This highlights the relevance of correctly implementing the  $N-\phi$  interaction in the model and the contributions from coupled vector-meson baryon pairs.

However, the  $N-\phi$  interaction is not well understood due to the lack of data. In general, the coupling of the  $\phi$  meson to nucleons is expected to be suppressed due to the OZI rule [45–47],

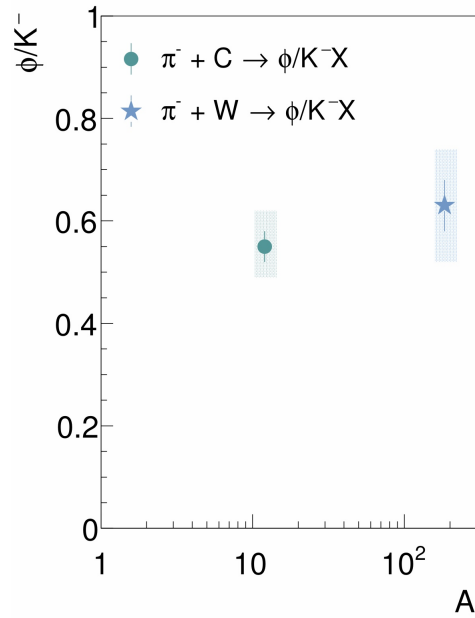


**Figure 1.5:**  $\phi/K^-$  ratio as function of the mass number  $A$ , measured by HADES in  $\pi^-$  induced reactions with two different target nuclei. Figure taken from [36].

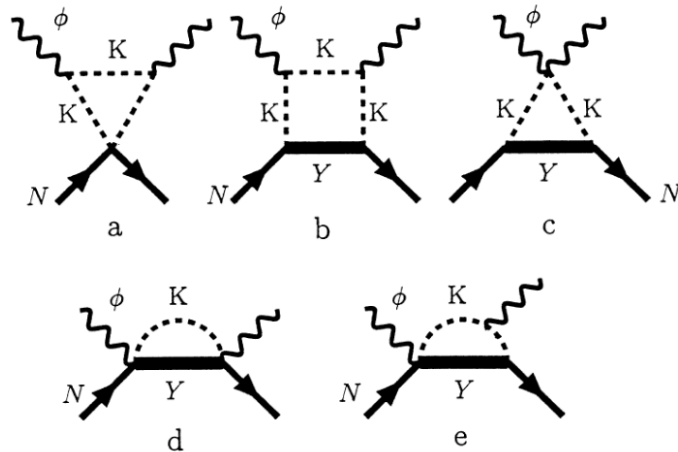


**Figure 1.6:** Diagrams which contribute to the leading s- and p-wave interactions of kaons within the nuclear medium [28]. The hyperon intermediate states  $Y$  include the ones of the baryon octet and baryon decuplet. Figure taken from [28].

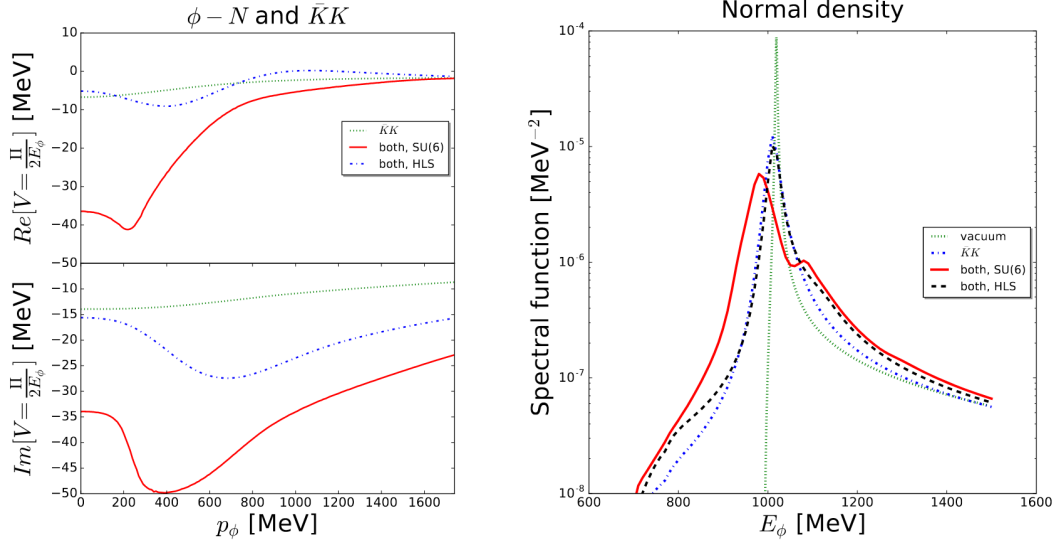


**Figure 1.7:** The left panel shows the real and imaginary part of the optical potential of the  $\phi$ , obtained from theoretical calculations of the self-energy [30], including contributions from the  $K\bar{K}$  cloud and the  $N$ - $\phi$  interaction within both SU(6) and HLS approaches. The right plot shows the corresponding spectral function. The plots are taken from [30].

which hinders processes with disconnected quark lines. A possible violation of the OZI rule was reported by the HADES collaboration [48]. As the  $\phi$  meson mainly consists of strange quarks, with only a small amount on the lighter  $u$  and  $d$  quarks, it might couple directly to the strange sea-quark content of the nucleon [49]. Alternatively, an attractive QCD van der Waals force might dominate the  $N$ - $\phi$  interaction, which is mediated by multi-gluon instead of quark exchange [50]. Even the formation of a  $N$ - $\phi$  bound state is suggested [51]. Following the approach described in [52], where a phenomenological model of high-energy Pomeron interactions was employed as well as a variational wave function, the QCD van der Waals force is found to be attractive enough to support a  $N$ - $\phi$  bound state with binding energy of  $E_B = 1.8$  MeV. This is also proposed within the framework of chiral quark models [53], where it is assumed that the constituent quarks interact with each other not only via the one-gluon exchange but also through the exchange of Nambu-Goldstone bosons and the octet scalar-mesons. The results, however, vary strongly between the different models. Direct  $N$ - $\phi$  processes can also proceed via the coupling to meson-baryon pairs, such as  $K^*-\Lambda$  and  $K^*-\Sigma$ , where the hidden strangeness of the  $\phi$  meson is exchanged with the nucleons without violating the OZI rule [28, 30, 43].

In summary, the present theoretical and experimental situation regarding the in-medium modification of the  $\phi$  meson properties is far from being resolved [54] and a consistent description of the available photon- and proton-induced data [35, 37, 55] is still out of reach [30]. Therefore, a direct measurement of the two-body  $N$ - $\phi$  interaction in vacuum is needed, in order to better constrain the different theoretical models, which are employed to interpret existing experimental data.

### 1.3 Meson Exchange

At low energies, quarks and gluons are confined within hadrons, as already mentioned in Sec. 1.1. In this non-perturbative regime of QCD, where the relevant degrees of freedom are hadrons [56], the baryon-baryon interaction can be modeled by one-boson exchange.

This phenomenological approach has its origin in the pioneering work of Yukawa [57], who suggested a massive boson to be the carrier of the interaction between nucleons. In 1947, after initially mistaking it for the muon, the meson was finally found and identified as pion [58]. The natural scale of the nuclear force is therefore given by the Compton wavelength of the pion as

$$\lambda_\pi = \frac{1}{m_\pi} \approx 1.5 \text{ fm} \quad (1.9)$$

In detail, the interaction Lagrangians, which couple the meson fields  $\Phi^{(i)}$  to the baryonic fields  $\psi_B$ , are given as as [56, 59]

$$\begin{aligned} \mathcal{L}_s &= g_s \bar{\psi}_B \psi_B \Phi^{(s)} \\ \mathcal{L}_{ps} &= g_{ps} \bar{\psi}_B i \gamma_5 \psi_B \Phi^{(ps)} \\ \mathcal{L}_v &= g_v \bar{\psi}_B \gamma_\mu \psi_B \Phi^{(v)} \\ \mathcal{L}_{pv} &= g_{pv} \bar{\psi}_B \gamma_5 \gamma^\mu \psi_B \partial_\mu \Phi^{(ps)}, \end{aligned} \quad (1.10)$$

where  $g_i$  is the corresponding coupling constant and  $i$  runs over the different types of interactions: scalar ( $s$ ), pseudo-scalar ( $ps$ ), vector ( $v$ ) and pseudo-vector ( $pv$ ). The interaction potentials are derived from one-meson exchange diagrams. A strong attractive central force arises in the case of scalar mesons. This force is repulsive for vector mesons [59], due to the additional  $\gamma_\mu$  term in  $\mathcal{L}_v$ .

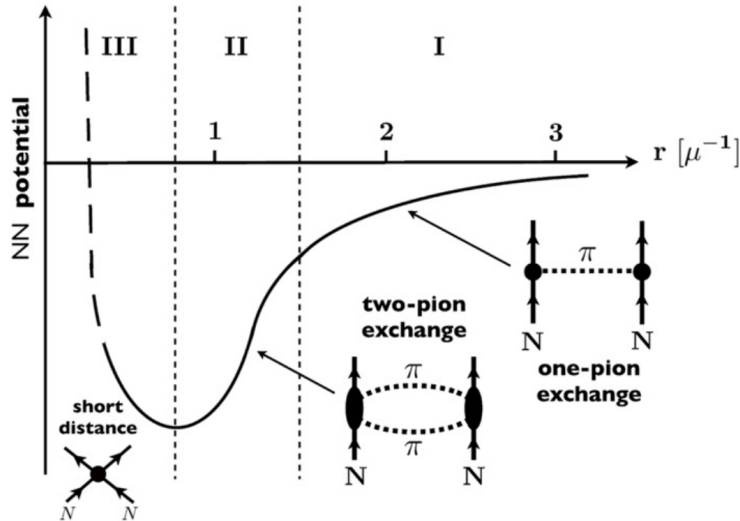


**Figure 1.8:** Nucleon-nucleon potential as function of the distance  $r$  given in units of the pion Compton wavelength  $m_\pi^{-1} \approx 1.5 \text{ fm}$  (denoted by  $\mu^{-1}$  in the plot) with the different regions depending on the interaction range. Figure taken from [60].

The classical one-pion exchange introduced by Yukawa, which describes the longest-range part of the N–N interaction, can be extended to shorter distances by including an intermediate-range attractive interaction governed by  $2\pi$  exchange. The short-range repulsive behavior from Pauli-blocking at the quark level however remains unresolved at the low-energy scales of nuclear physics. It might be governed by multi-pion or heavy vector-meson exchange. The hierarchy of scales is shown schematically for a typical central nucleon-nucleon potential in Fig. 1.8. The concept was first introduced by Taketani *et al.* in 1951 [61].

Later on, more precise potentials for the nucleon-nucleon interaction have been developed. The most known are the CD-Bonn potential [62], the Nijmegen I and II [63, 64] as well as the Argonne  $v_{18}$  (AV18) [65]. Especially, the latter was successfully used to access the p–p interaction from correlation measurements, as shown in Fig. 1.9. Such meson-exchange potentials are also available for the complete baryon octet, e.g. [66–68], including more exotic baryon-baryon interactions like Y–N [69–72].

Figure 1.10 shows exemplarily the exchange of a pion between a neutron and a proton and the underlying quark-gluon structure. Such a picture underlines the limitation of meson-exchange models to regions, where modifications due to the structure of the hadrons are not yet of concern. However, the high-energy, short-range part of the interaction, where quark degrees of freedom become relevant, is typically accounted for by introducing form factors, which effectively consider the spatial extension of hadrons [56, 60].

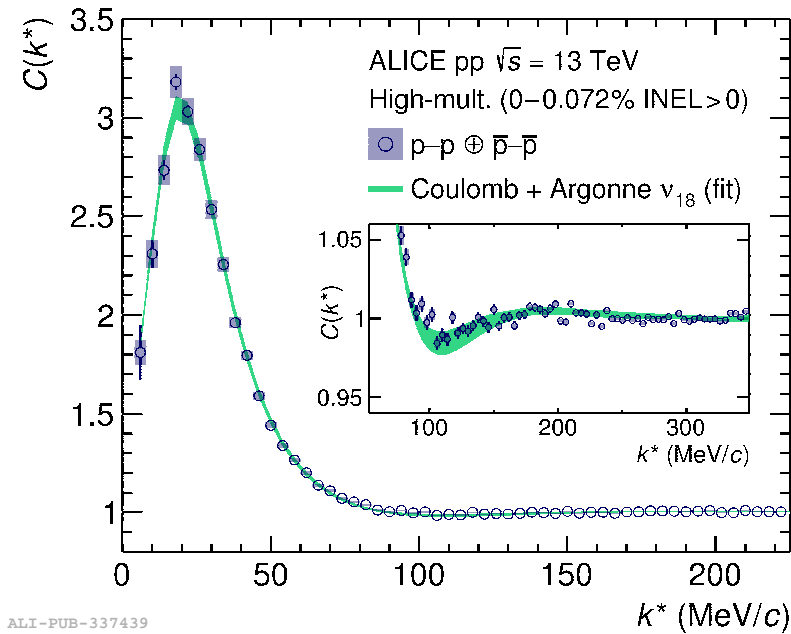


**Figure 1.9:** Proton-proton correlation function, measured in pp collisions. Figure taken from [73].

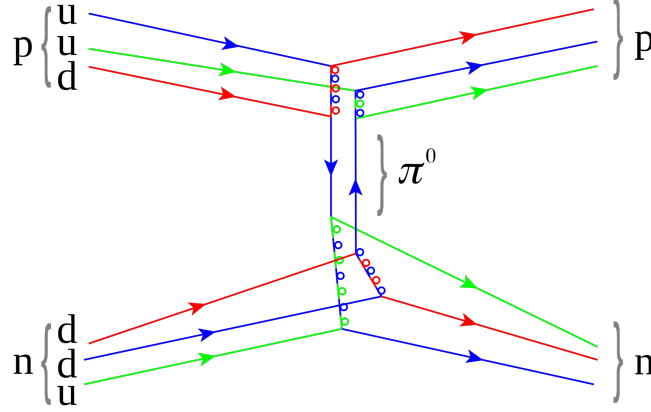


**Figure 1.10:** Diagram for the scattering between proton and neutron, mediated by a pion. The individual quarks are shown as well. Figure taken from [74].

## 1.4 Implications for Neutron Stars

Neutron stars (NS) are very dense and compact astrophysical objects, characterized by radii around 10 km and masses between 1.17 and 2.0 times the one of our sun  $M_\odot$  [75]. They are formed in the aftermath of the gravitational collapse of the core of a giant star with a mass larger than eight  $M_\odot$  [76]. The NS crust contains mainly electrons, ions and neutrons, but the composition of the core region, where densities more than 4 times the nuclear saturation density  $\rho_0$  are reached [77], is not yet known. Such dense hadronic matter is characterized by the equations of state (EoS), which relates pressure  $p$  to energy density  $\varepsilon$ . It depends on the specific constituents that are considered as well as the interaction among them. A given EoS provides a unique solution of the Tolman-Oppenheimer-Volkoff (TOV) equations [78, 79], which in general relativity describe the hydrostatic equilibrium of a spherically symmetric star

$$\frac{dp}{dr} = -\frac{G_N}{c^2} \frac{(p + \varepsilon)(m + 4\pi r^3 p/c^2)}{r^2[1 - 2G_N m/(rc^2)]}, \quad (1.11)$$

$$\frac{dm}{dr} = 4\pi r^2 \frac{\varepsilon}{c^2}, \quad (1.12)$$

where  $G_N$  Newton's gravitational constant,  $r$  the radial distance to the center of the star and  $m(r)$  the enclosed mass. Constraints are given by the boundary conditions  $m(r = 0) = 0$  and  $p(r = R) = 0$ , where  $R$  is the radius of the neutron star. From these equations, a mass-radius relation can be deduced, which gives an upper limit to the mass supported by a specific EoS and hence, puts constraints on the potential constituents of the core.

As the density increases towards the center of the NS, the Fermi energy  $\varepsilon_F \sim \rho^{2/3}$  of the NS constituents gets larger. Hyperons<sup>1</sup> ( $Y$ ) become energetically favorable once the chemical potential of neutrons,  $\mu_n = \varepsilon_{F,n} + m_n$ , exceeds their rest mass  $m_Y$ . Neutrons on the Fermi surface

<sup>1</sup> A hyperon is a baryon containing one or more strange quarks in addition to the light  $u$  and  $d$  quarks.

start to decay weakly into the most favored hyperons, e.g. the light  $\Lambda$ s ( $uds$ ), at sufficiently high densities, thereby forming strange hadronic matter at chemical equilibrium  $\mu_n = \mu_\Lambda$ .

Neutron star cores might therefore be populated by hyperons like  $\Lambda$  ( $uds$ ) and to smaller amounts by  $\Sigma$  ( $uus$ ,  $dds$  and  $uds$ ) and  $\Xi$  ( $uss$  and  $dss$ ) in addition to electrons and nucleons. However, the appearance of hyperons softens the EoS as the neutron degeneracy pressure decreases. This results in a reduction of the maximum reachable NS mass, which is not obviously compatible with the experimental observation of the  $1.97 \pm 0.04 M_\odot$  NS PSR J1614-2230 [80] or the more recent measurement of PSR J0740+6620, where a mass of  $2.14_{-0.09}^{+0.10} M_\odot$  was found [81]. This issue is known as the *hyperon puzzle* [82–84].

However, a stiffening of the EoS can be obtained by introducing a repulsive interaction, which shifts the onset of hyperons to higher densities, thereby decreasing the neutron stars strangeness fraction and increasing its maximally supported mass. It is therefore essential to understand not only the hyperon-nucleon (Y–N) interaction [85, 86] but also the interaction between hyperons themselves (Y–Y), especially at large densities, where hyperons become abundant. Several attempts have been made to solve the puzzle by employing meson-exchange models, e.g. [87–89], already introduced in Sec. 1.3. In particular, within the framework of relativistic mean field (RMF) models a repulsive Y–Y interaction might be introduced by  $\phi$  meson-exchange [82].

In the following, results from [88, 90, 91] are discussed in detail. Regarding the baryon-baryon interaction (B–B) the scalar  $\sigma$ ,  $\rho$  and  $\omega$  mesons are considered, while the interaction among hyperons themselves (Y–Y) is included via strange meson exchange with an attractive part mediated by a scalar meson  $\sigma^*$  as well as a repulsive contribution from  $\phi$  vector meson-exchange. This leads to the following Lagrangian density [88]

$$\mathcal{L}_{YY} = \sum_B \bar{\psi}_B (g_{\sigma^* B} \sigma^* - g_{\phi B} \gamma_\mu \phi^\mu) \psi_B + \frac{1}{2} (\partial_\mu \sigma^* \partial^\mu \sigma^* - m_{\sigma^*}^2 \sigma^{*2}) - \left( \frac{1}{4} \phi_{\mu\nu} \phi^{\mu\nu} - \frac{1}{2} m_\phi^2 \phi_\mu \phi^\mu \right). \quad (1.13)$$

The first term describes the meson-baryon interaction between the particles of the full baryon octet ( $J^P = \frac{1}{2}^+$ ) and the respective exchange mesons ( $\sigma^*$  or  $\phi$ ). A general formulation was already introduced in Eq. 1.10. The second term of Eq. 1.13 describes the scalar meson with the corresponding kinetic and mass term, and the last term the same for the vector meson.

The meson-nucleon coupling constants of this RMF model are fitted to the saturation properties of nuclear matter. While non-strange scalar meson-hyperon couplings are determined by the depth of the single-particle potential felt by a specific hyperon in nuclear matter at saturation density, the vector coupling constants follow from SU(6) relations.

Figure 1.11 shows the resulting mass-radius relation of neutron stars for different  $\Xi$  single-particle potentials  $U_\Xi$ . The lower set of lines is obtained by only considering the B–B interaction mediated by  $\sigma$ ,  $\omega$  and  $\rho$  (model  $\sigma\omega\rho$ ), while in the upper set of mass-radius relations also the repulsive Y–Y interaction is considered by including the  $\phi$ -meson exchange in the calculations (model  $\sigma\omega\rho\phi$ ). Recent studies by HAL QCD collaboration predict a slightly repulsive  $\Xi$  single-particle potential with  $U_{\Xi^-} \approx 6 \text{ MeV } c^{-1}$  in pure neutron matter [95]. These calculations are validated by ALICE correlation measurements in vacuum [96]. By comparing the results from lattice QCD to Fig. 1.11, it can be seen that by including a repulsive Y–Y mediated by the  $\phi$  meson, even  $2 M_\odot$  neutron stars are supported.

However, these model calculations rely on couplings between the  $\phi$  meson and baryons, which needs to be constrained by experimental data. By relating the coupling constants to the cor-

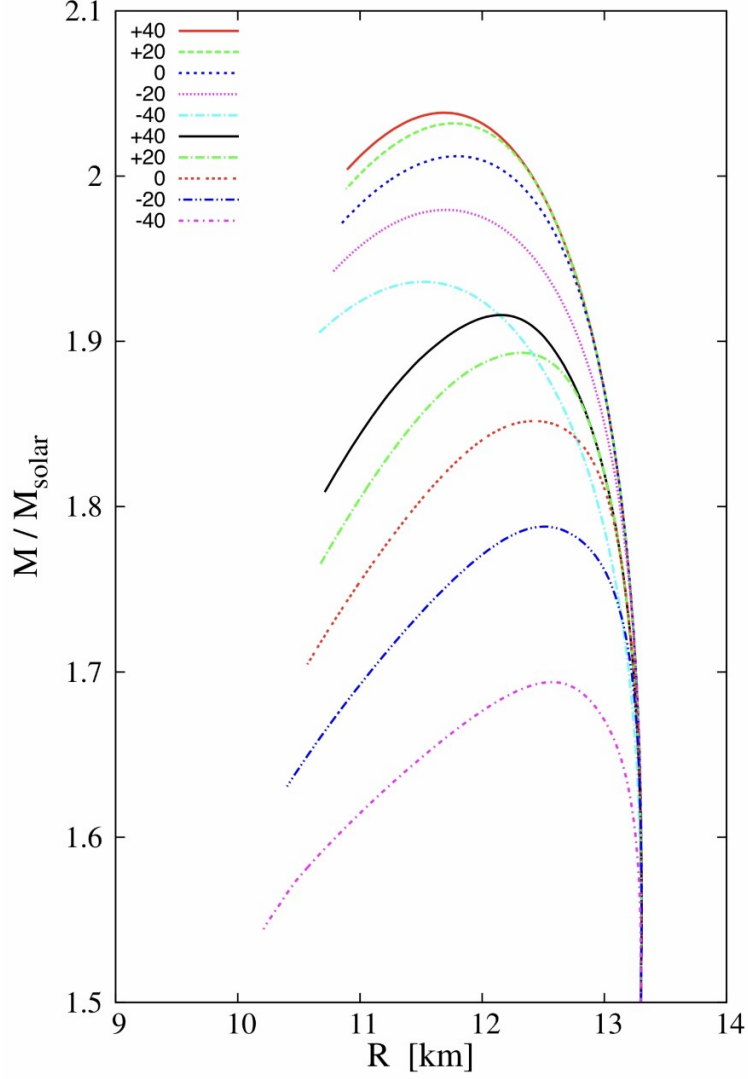


**Figure 1.11:** The mass-radius relation of neutron stars for different  $\Xi$  single-particle potentials  $U_{\Xi}$  in MeV, when fixing  $U_{\Lambda} = -30$  MeV [92–94] and  $U_{\Sigma} = 30$  MeV. Upper set of lines: model  $\sigma\omega\rho\phi$ , lower set of lines: model  $\sigma\omega\rho$ . Figure taken from [88].

responding nucleon couplings and employing SU(3) symmetry, one finds the following relations [91]

$$\begin{aligned}
 \frac{g_{N\phi}}{g_{N\omega}} &= -\frac{\sqrt{3} - \sqrt{2}(4\alpha_V - 1)z}{\sqrt{6} + (4\alpha_V - 1)z}, \\
 \frac{g_{\Lambda\phi}}{g_{N\omega}} &= -\frac{\sqrt{3} + 2\sqrt{2}(1 - \alpha_V)z}{\sqrt{6} + (4\alpha_V - 1)z}, \\
 \frac{g_{\Sigma\phi}}{g_{N\omega}} &= -\frac{\sqrt{3} - 2\sqrt{2}(1 - \alpha_V)z}{\sqrt{6} + (4\alpha_V - 1)z}, \\
 \frac{g_{\Xi\phi}}{g_{N\omega}} &= -\frac{\sqrt{3} + \sqrt{2}(1 + 2\alpha_V)z}{\sqrt{6} + (4\alpha_V - 1)z},
 \end{aligned} \tag{1.14}$$

where the parameter  $\alpha_V = F/(F + D)$  weighs the symmetric (D) and the anti-symmetric (F) part of the octet-octet interaction and  $z = g_8/g_1$  is the ratio of the meson singlet and octet coupling constants  $g_1$  and  $g_8$ .

Figure 1.12 shows the resulting parameter space for constant NS masses and strangeness fractions  $f_s = |S|/B$ , when both parameters are varied. Equations 1.14 can easily be extended to the SU(6) quark model, which is employed in the calculation of the mass-radius relations in Fig. 1.11, as it is a special case of the flavor SU(3) combined with spin SU(2). This is done by fixing the parameters to  $z = 1/\sqrt{6}$  and  $\alpha_V = 1$ . Notably, it results in a vanishing  $g_{N\phi}$ . The SU(6) case is favored by experimental measurements, where the strangeness content of the nucleon was found to be small and a small spin-orbit splitting was observed for  $\Lambda$  hypernuclei [91]. Therefore, deviations from the SU(6) quark model are expected to be small. However, a direct correlation measurement of the N- $\phi$  interaction could bring more clearance to the situation and put constraints on the parameter space.

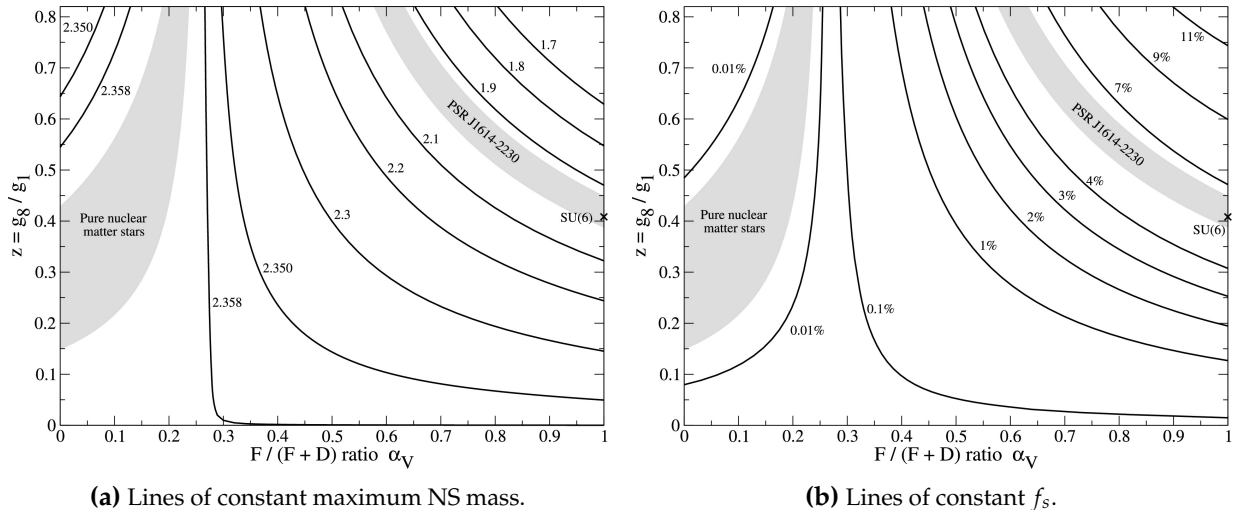


**Figure 1.12:** Planes spanned by the parameters  $\alpha_V$  and  $z$  in model  $\sigma\omega\rho\phi$ . The gray shaded area on the right corresponds to the constraints from the NS PSR J1614-2230 [80] while the one on the left contains configurations yielding purely nucleonic stars. The spin-flavour SU(6) symmetry with  $z = 1/\sqrt{6}$  and  $\alpha_V = 1$  is also marked. Figures taken from [91]



## 2 Femtoscscopy

The method of femtoscopy originates from *intensity interferometry*. It is based on the construction of a correlation function, which is proportional to the intensity of particles, emitted by two point sources  $a$  and  $b$ , with relative distance  $\vec{R}$ , see Fig. 2.1 (a). After traveling a certain path of length  $\vec{L}$ , they are measured by two detectors 1 and 2, which are separated by a baseline  $\vec{d}$ . For identical particles with momenta  $p$ , the correlation function is then given by [97]

$$C(\vec{R}, \vec{d}) = \frac{\langle I_1 I_2 \rangle}{\langle I_1 \rangle \langle I_2 \rangle} = 1 + \frac{2|\alpha|^2 |\beta|^2}{(|\alpha|^2 + |\beta|^2)^2} \cos(p(r_{1a} - r_{2a} - r_{1b} + r_{2b})), \quad (2.1)$$

where  $\langle I_i \rangle$  are the averaged intensities measured at detector  $i$ ,  $\langle I_1 I_2 \rangle$  the time averaged coincidence rate,  $r_{ij}$  the distance between detector  $i$  and emission point  $j$  and  $\alpha$  and  $\beta$  are the emission amplitudes at  $a$  and  $b$ .

Developed in the 1950s by Hanbury-Brown and Twiss, therefore also referred to as *HBT interferometry* [99–101], it was first used in astrophysics to study radio-wave sources in the galaxies Cygnus and Cassiopea [102]. The method was later employed to determine the angular size of Sirius [103] by measuring the number of photons emitted from different points on the surface of the star. A schematic illustration can be seen in Fig. 2.1 (b). As  $\vec{R} \gg \vec{d}$ , the cosine in Eq. 2.1 reduces to  $\cos(\vec{d}(\vec{p}_a - \vec{p}_b))$ , where  $\vec{p}_i = p\vec{e}_i$  depends on the unit vector  $\vec{e}_i$ , which gives the direction from the detectors to emission point  $i$ . Therefore, varying the distance  $\vec{d}$  induces an oscillation to the signal from which it is ultimately possible to extract the angular separation of the emission points,

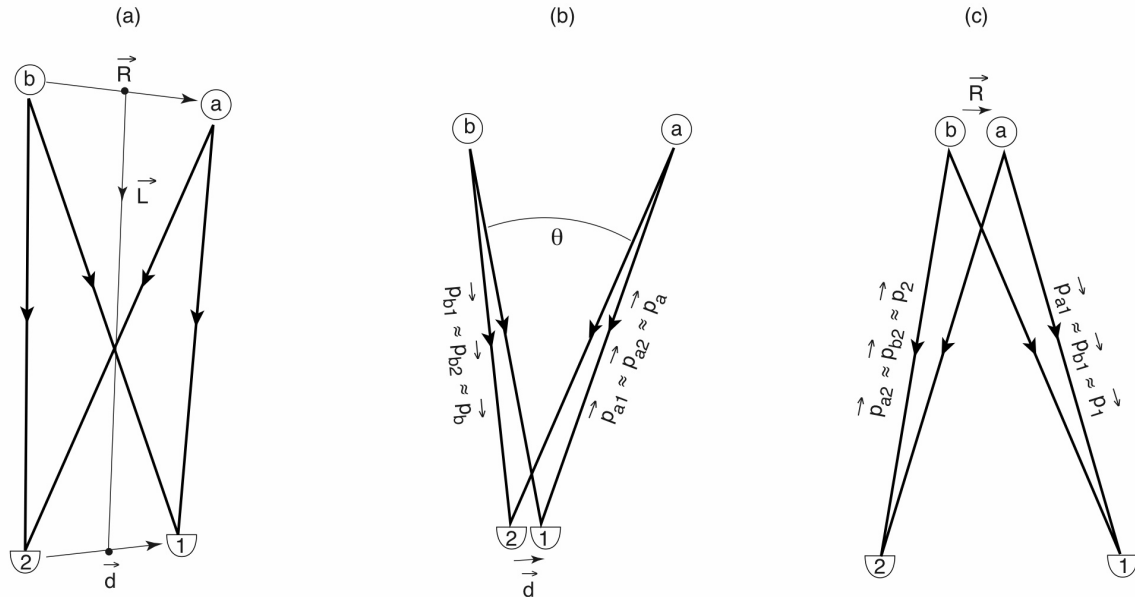


**Figure 2.1:** (a) General scheme of the derivation of the distance  $\vec{R}$  between two sources  $a$  and  $b$  by measuring and correlating the intensities in detectors 1 and 2. (b) Illustration of the *HBT interferometry* in astronomy, where the angular diameter  $\theta$  is measured. (c) Situation in particle physics. Figure taken from [98].

as  $|\vec{p}_a - \vec{p}_b| \sim \theta/\lambda$  [97].

In particle physics, a similar method was developed in the late 1950s to extract the angular distribution of pions in  $p\bar{p}$  annihilation [104]. This was done by investigating momentum correlations, which are the result of the interference of the production amplitudes due to the symmetrization requirement of quantum statistics (QS) for identical mesons [105]. Unlike the situation in astrophysics, discussed previously,  $\vec{R} \ll \vec{d}$ , hence the cosine in Eq. 2.1 becomes  $\cos(\vec{R}(\vec{p}_1 - \vec{p}_2))$ . By controlling the momentum difference  $\vec{p}_1 - \vec{p}_2$ , the source size  $\vec{R}$  can be extracted from the oscillation period [97]. This is illustrated in Fig. 2.1 (c).

In the early 1970s the basics of modern femtoscopy were developed by Kopylov and Podgoretsky [106, 107], providing a practical approach to study correlations as a function of the separation of particles in momentum space. They also suggested deriving such a correlation function from the ratio of correlated and uncorrelated particle yields, where the latter are constructed by employing mixing techniques. More details can be found in Sec. 2.1.

Femtoscopy is used in particle physics to study momentum correlations induced by both final-state interactions (FSI) and QS in connection with the spatio-temporal aspect of the emission function, when two or more particles are produced at small relative momenta. Such correlations can therefore be employed to study the characteristics of their production process at the femtoscopic level of  $10^{-15}$  fm [105] for known FSI. Vice versa it is possible to obtain information on the underlying interaction between specific particles, given that the emission process is well understood. Hence, the framework of femtoscopy provides a valuable tool to extract information on the strong FSI of exotic particle pairs for which classical approaches like scattering experiments are unfeasible, due to the lack of stable particle beams and/or targets. Especially in the case of  $p\text{-}\phi$ , a beam of  $\phi$  mesons can neither be produced easily, due to the short lifetime of the particles, nor handled well as its constituents are charge neutral. Also using a proton beam instead is no reasonable approach as it is impossible to create a  $\phi$  target for the same reasons.

## 2.1 Femtoscopic Framework

The final-state interaction between two particles emitted at small relative momenta  $\vec{q} = \vec{p}_1 - \vec{p}_2 = 2\vec{k}$ , the QS effects in case of identical particles, and the characteristics of their emission region lead to modifications of the momentum space configuration. Such effects can be studied via the two-particle correlation function defined as the ratio between the conditional probability  $P(\vec{p}_1, \vec{p}_2)$  of observing simultaneously particles with momenta  $\vec{p}_1$  and  $\vec{p}_2$  to the probability of finding each particle independently [108]. The probabilities can also be expressed in the form of Lorentz-invariant spectra [97] and the correlation function can be written as

$$C(\vec{p}_1, \vec{p}_2) = \frac{P(\vec{p}_1, \vec{p}_2)}{P(\vec{p}_1)P(\vec{p}_2)} = \frac{E_1 E_2 dN / (d^3 p_1 d^3 p_2)}{(E_1 dN / d^3 p_1)(E_2 dN / d^3 p_2)}. \quad (2.2)$$

In absence of any correlation, it is equal to unity, as the particles are independent and  $P(\vec{p}_1, \vec{p}_2) = P(\vec{p}_1) \cdot P(\vec{p}_2)$ .

Following [97] and [98] the correlation function in momentum space can be related to the particle-emitting source in coordinate space via a convolution with the wave-function. This results in

$$C(p_1, x_1, p_2, x_2) = \frac{\int d^4x_1 d^4x_2 S_1(p_1, x_1) S_2(p_2, x_2) |\psi(p_1, x_1, p_2, x_2)|^2}{\int d^4x_1 S_1(p_1, x_1) \int d^4x_2 S_2(p_2, x_2)}, \quad (2.3)$$

where  $S_i(p_i, x_i)$  describes the emission of a single particle with four-momentum  $p_i = (E_i, \vec{p}_i)$  at a space-time point  $x_i = (t_i, \vec{x}_i)$ . The squared Bethe-Salpeter amplitude  $|\psi(p_1, x_1, p_2, x_2)|^2$  serves as a weight and accounts for the interaction between two particles emitted at  $x_i$  and detected with  $p_i$ . Equation 2.3 can be simplified by several assumptions [105]:

1. The *two-particle approximation* assumes that the mean freeze-out phase space density is sufficiently small that the correlation of particles with a small relative momentum is only influenced by their mutual FSI and QS effects.
2. The *smoothness assumption* renders the momentum dependence of the single-particle emission probabilities  $S_i(p_i, x_i)$  inessential, when varying the particle four-momenta by characteristic amount regarding correlations due to QS and FSI.
3. An *independent and incoherent particle emission* is assumed.
4. *Equal time approximation* is used to simplify the Bethe-Salpeter amplitude  $\psi(p_1, x_1, p_2, x_2)$  of two particles, where it is assumed that both particles are emitted at equal times in the pair rest frame. This leads to  $\psi(p_1, x_1, p_2, x_2) \rightarrow \psi(\vec{k}^*, \vec{r}^*)$ , where  $\vec{r}^* = \vec{r}_1^* - \vec{r}_2^*$  the relative distance between the production points of the two particles and  $k^* = \frac{1}{2}(\vec{p}_1^* - \vec{p}_2^*)$  their relative momentum evaluated in the pair rest frame,  $\vec{p}_1^* - \vec{p}_2^* = 0$ , denoted by the  $*$ .

From this, the the *Koonin–Pratt equation* is obtained [109, 110]

$$C(k^*) = \int d^3r^* S(r^*) |\psi(\vec{k}^*, \vec{r}^*)|^2, \quad (2.4)$$

where  $S(r^*)$  is the relative source distribution, which, together with the relative two-particle wave-function  $\psi(\vec{k}^*, \vec{r}^*)$ , is the main ingredient that leads to a measurable correlation signal. In general, the correlation function is sensitive to the short-ranged strong FSI at small relative momenta  $k^* = \frac{1}{2}|\vec{p}_1^* - \vec{p}_2^*|$ . At larger  $k^*$  the particles separate too fast for an interaction to take place, leading to  $\lim_{k^* \rightarrow \infty} C(k^*) = 1$ .

In femtoscopy, it is often assumed that the spatial probability density  $S(\vec{r}^*)$  has the shape of a Gaussian of width  $r_0$  and neither explicit time nor momentum dependencies. Therefore, the source function can be written as

$$S_G(r^*) = (4\pi r_0^2)^{-3/2} \cdot \exp\left(-\frac{r^{*2}}{4r_0^2}\right). \quad (2.5)$$

Typical values of the Gaussian source size  $r_0$  in pp and p–Pb collisions at the LHC are between 1 – 1.5 fm [85, 96], while for Pb–Pb larger values of 3 – 6 fm are found [111]. A small source gives rise to pronounced correlation signals, as more particles are emitted within the reach of the short-ranged strong interaction potential. The influence of the source size on the correlation function is depicted on the right plot of Fig. 2.2.

Experimentally, the correlation function is obtained by replacing the probabilities in Eq. 2.2 by the corresponding correlated and uncorrelated particle pair yields. The former is extracted by pairing

particles from the same event<sup>1</sup>, whereas the latter has to be extracted by combining particles from different events, called event-mixing, which renders them uncorrelated [112]

$$C_{\text{exp}}(k^*) = \mathcal{N} \frac{N_{\text{same}}(k^*)}{N_{\text{mixed}}(k^*)}, \quad (2.6)$$

where  $N_{\text{same}}$  and  $N_{\text{mixed}}$  are the distributions of the relative momentum  $k^*$  between both particles. The normalization factor  $\mathcal{N}$  ensures  $C_{\text{exp}} = 1$  in the region of  $k^* > 200$  MeV/ $c$ , where the femtoscopic signal is expected to be absent. The femtoscopic principle of relating the experimentally measured correlation function to the theoretical Eq. 2.4 is illustrated qualitatively in Fig. 2.3.

In general, for non-identical particles, a genuine correlation function above unity is interpreted as attractive interaction as it leads to an increased amount of pairs with low  $k^*$ , while a signal smaller than 1 corresponds to repulsion.

There are different contributions to the FSI, depending on the specific particle pair, which is studied. In the case of two charged particles the Coulomb interaction  $\propto r^{-1}$  has to be considered. If the pair has the same charge, repulsion arises and leads to  $C(k^*) < 1$ , while opposite charge leads to attraction. This effect is well understood. More interesting, however, is the contribution from the short-ranged strong interaction as its fundamental laws are still not well described. If the particles are identical, QS effects have to be considered as well. Although this picture is very

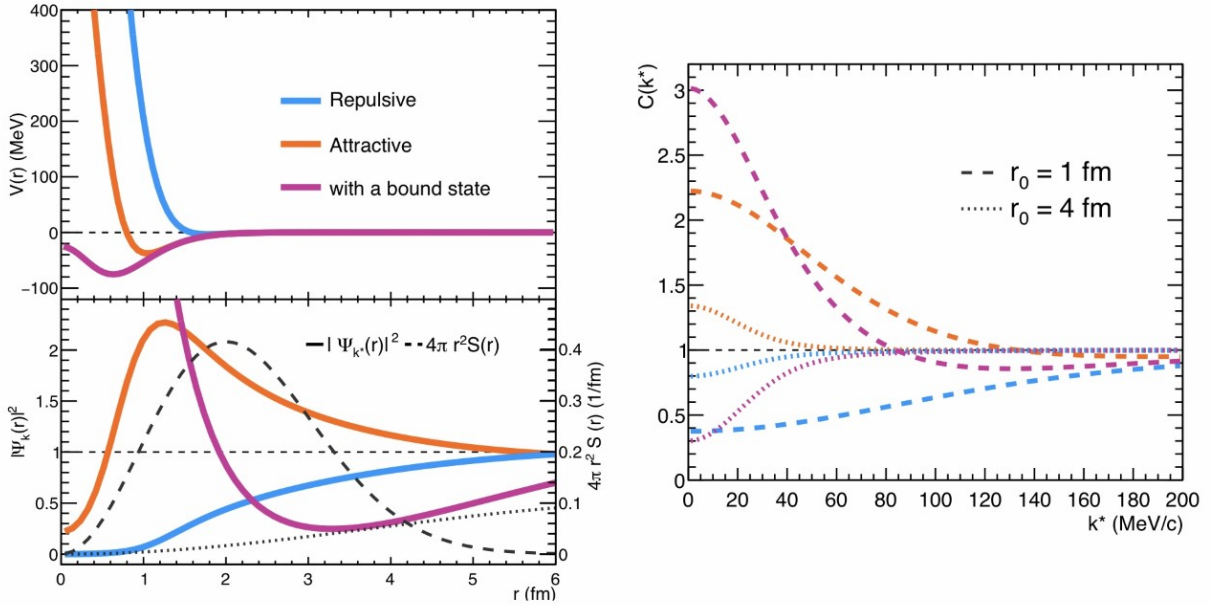


**Figure 2.2:** Illustration of the influence of the individual contributions of the correlation function on its shape. The upper left panel shows different types of potentials, also including a bound state (pink). The corresponding wave-functions are shown on the lower panel. On the same plot also a source of Gaussian profile is shown for a  $r_0$  of 1 fm (dashed line) and 4 fm (dotted). On the right panel, the resulting correlation functions for the two sources are depicted, illustrating the influence of the source size on the signal. Figures taken from [77].

<sup>1</sup> In this context events correspond to single-particle collisions.

intuitive, the presence of bound states or coupled channel dynamics can influence the signal as well and can complicate the physical interpretation of the measured correlation function.

The right panel of Fig. 2.2 shows exemplary correlation functions, which arise from different potentials and source sizes  $r_0$ . Blue lines correspond to a repulsive, orange ones to an attractive potential and pink lines are obtained from a potential including a shallow bound state. The potentials themselves are plotted on the upper left panel and the corresponding wave-function on the lower-left panel.

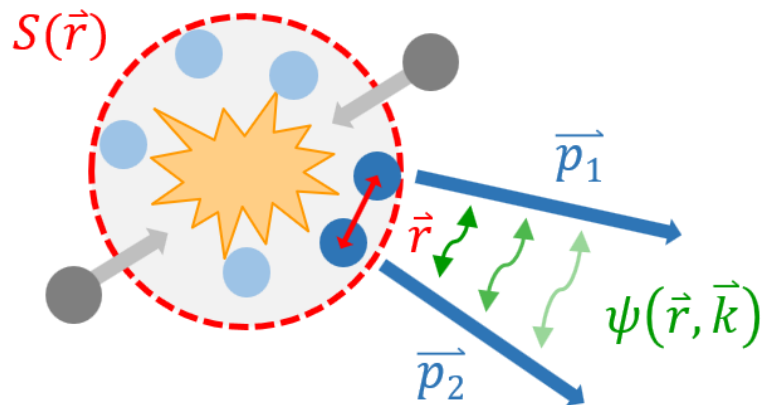


**Figure 2.3:** Illustration of the different parts of the correlation function. The two grey circles represent the colliding particles, the blue ones the particles produced in the collision and the red circle the emission source  $S(\vec{r})$ . If two particles 1 and 2 are emitted close to each other at distance  $\vec{r}$  and relative momentum  $\vec{k} = \vec{p}_1 - \vec{p}_2$ , they experience a correlation depicted by the green arrows that represent the interaction, encoded in the two-particle wave-function  $\psi(\vec{r}, \vec{k})$ .

## 2.2 The Scattering Problem

The interaction among two particles can be seen as a scattering problem, where the information is encoded within a short-ranged central potential  $V(r)$  which depends only on the distance  $r$  between particles and not on the direction. The two-body problem becomes an effective one-body problem of a fictitious particle with mass  $\mu = (m_1 m_2) / (m_1 + m_2)$ , corresponding to the reduced mass of the pair, and the coordinates  $\vec{k}^*$  and  $\vec{r}^*$  in the center of mass system.

It should be noted, that the problem can be treated non-relativistic, as only small relative momenta are studied. As the interaction time between the particles and the scattering potential is short, a steady-state is assumed. Consequently, the wave-function, which characterizes the system, is determined by the time-independent Schrödinger equation (SE)

$$E\psi(\vec{r}^*) = \mathcal{H}\psi(\vec{r}^*) := \left( -\frac{\hbar^2 \nabla^2}{2\mu} + V(r^*) \right) \psi(\vec{r}^*), \quad (2.7)$$

where the energy is given by  $E = \frac{\hbar^2 \vec{k}^{*2}}{2\mu}$ . Details on the mathematical and physical framework of scattering-problems can be found in [113–115], on which the following discussion is based.

As the interaction potential is short-ranged and falls fast with increasing  $r$ , the wave-function takes an asymptotic form ( $V(r^*) \rightarrow 0$  for  $r \rightarrow \infty$ ) at large distances, given by an incoming plane wave and an outgoing spherical wave, which radiates away from the center of the interaction region

$$\psi(\vec{r}^*) \xrightarrow{r^* \rightarrow \infty} (2\pi)^{-3/2} \left( e^{i\vec{k}^* \cdot \vec{r}^*} + f(\theta, \phi) \frac{e^{ik^* r^*}}{r^*} \right), \quad (2.8)$$

where  $f(\theta, \phi)$  is the scattering amplitude that contains information on the interaction potential. This is depicted schematically in Fig. 2.4 where  $\vec{k}^* = k^* \hat{z}$ . It has to be noted that both  $f(\theta, \phi)$  and  $\psi(\vec{r}^*)$  also depend on the relative momentum  $\vec{k}^*$ , but to simplify the notation. This will not be indicated unless required in the discussion. Further, if spin observables are neglected because either all involved particles have spin  $J = 0$  or their spins are unpolarized and the spin of the final-state particles are not detected [114], the system is independent of  $\phi$  and the scattering amplitude is a function of the polar angle  $\theta$  only. This assumption will be adopted in the following.

For a central potential which is invariant under any rotation around the origin, angular momentum is conserved. In this case, it is convenient to employ the *partial wave expansion*, where the wave-function is decomposed into components of the angular momentum specified by the quantum number  $l$ . Further, each partial wave is separated into a radial term  $R_l(r^*)$ , which depends on the potential  $V(r^*)$ , and an angular term  $Y_l(\theta)$ , expressed by the universal spherical harmonics. This leads to the following expression

$$\psi(\vec{r}^*) = \sum_{l=0}^{\infty} \psi_l(r^*) = \sum_{l=0}^{\infty} R_l(r^*) Y_l(\theta) = \sum_{l=0}^{\infty} \frac{u_l(r^*)}{r^*} \sqrt{\frac{2l+1}{4\pi}} P_l \cos(\theta), \quad (2.9)$$

where  $P_l \cos(\theta)$  is the Legendre polynomial and  $u_l(r^*) = r^* R_l(r^*)$  is the *reduced wave-function*

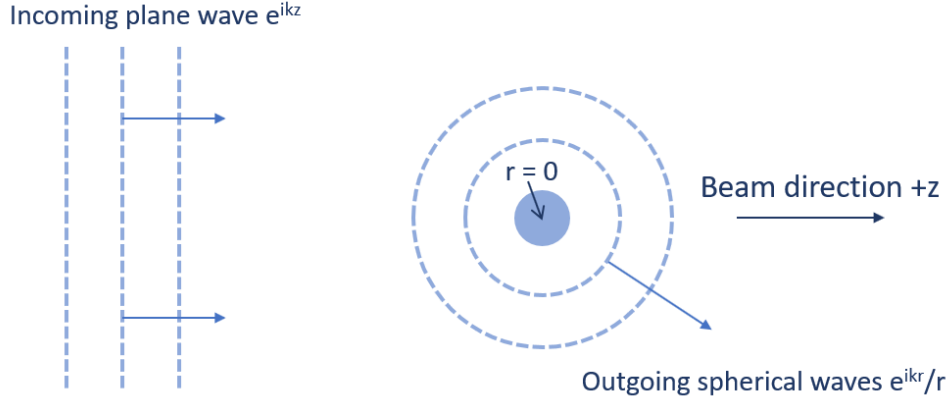


**Figure 2.4:** Schematic picture of the scattering problem of an incident plane wave in  $\hat{z}$  direction on a spherical target.

which satisfies the SE in spherical coordinates, called *radial equation*,

$$Eu_l(r^*) = \left( -\frac{\hbar}{2\mu} \frac{d^2}{dr^2} + \frac{l(l+1)\hbar^2}{2\mu r^{*2}} + V_l(r^*) \right) u_l(r^*). \quad (2.10)$$

For identical particles, QS effects have to be considered, which require an (anti-)symmetrization of the partial wave-functions for bosons(fermions), leading to

$$\psi_l(r^*) = \frac{1}{\sqrt{2}} \left[ \psi_l(r^*) + (-1)^{s+l} \psi_l(r^*) \right], \quad (2.11)$$

where  $s$  is the spin quantum number. Similarly to the wave-function also the scattering amplitude can be decoupled into partial waves

$$f(\theta) = \sum_{l=0}^{\infty} (2l+1) f_l(k^*) P_l(\cos\theta), \quad (2.12)$$

where  $f_l(k^*)$  denotes the partial-wave scattering amplitude that contains all the relevant physics of the interaction. Making use of the asymptotic behaviour,  $f_l(k^*)$  can be written as

$$f_l(k^*) = \frac{e^{i\delta_l(k^*)} \sin \delta_l(k^*)}{k} = \frac{1}{k^* \cot \delta_l(k^*) - ik^*}, \quad (2.13)$$

where  $\delta_l(k^*)$  denotes the phase-shift observed in the scattered partial waves of angular momentum  $l$  with respect to the incoming waves. The effect of the potential on the phase-shift is depicted in Fig. 2.5. An attractive potential manifests itself in a positive phase-shift, while for a repulsive potential the phase-shift is negative.

Also the incoming wave can be described by means of the partial-wave expansion

$$e^{i\vec{k}^* \cdot \vec{r}^*} = e^{ik^* r^* \cos\theta} = \sum_{l=0}^{\infty} (2l+1) i^l j_l(k^* r^*) P_l(\cos\theta) \xrightarrow{r^* \rightarrow \infty} \sum_{l=0}^{\infty} (2l+1) P_l(\cos\theta) \frac{(-1)^{l+1} e^{-ik^* r^*} + e^{ik^* r^*}}{2ik^* r^*}, \quad (2.14)$$

where in the last step the asymptotic form of the spherical Bessel function  $j_l$  is used. When expressing Eq. 2.8 in terms of Eq. 2.12 and 2.14 the scattering problem reduces to an effective one-dimensional interference problem of spherical waves

$$\psi(\vec{r}^*) \xrightarrow{r^* \rightarrow \infty} (2\pi)^{-3/2} \sum_{l=0}^{\infty} (2l+1) P_l(\cos \theta) i^l e^{i\delta_l} \frac{\sin(k^* r^* - l\frac{\pi}{2} + \delta_l)}{k^* r^*}. \quad (2.15)$$

By solving the *radial equation*, Eq. 2.10, it is possible to determine  $u_l(r^*)$ , and consequently  $\psi(\vec{r}^*)$  by using Eq. 2.9. The asymptotic solution can be expressed in terms of Eq. 2.15, permitting an evaluation of the phase-shifts.

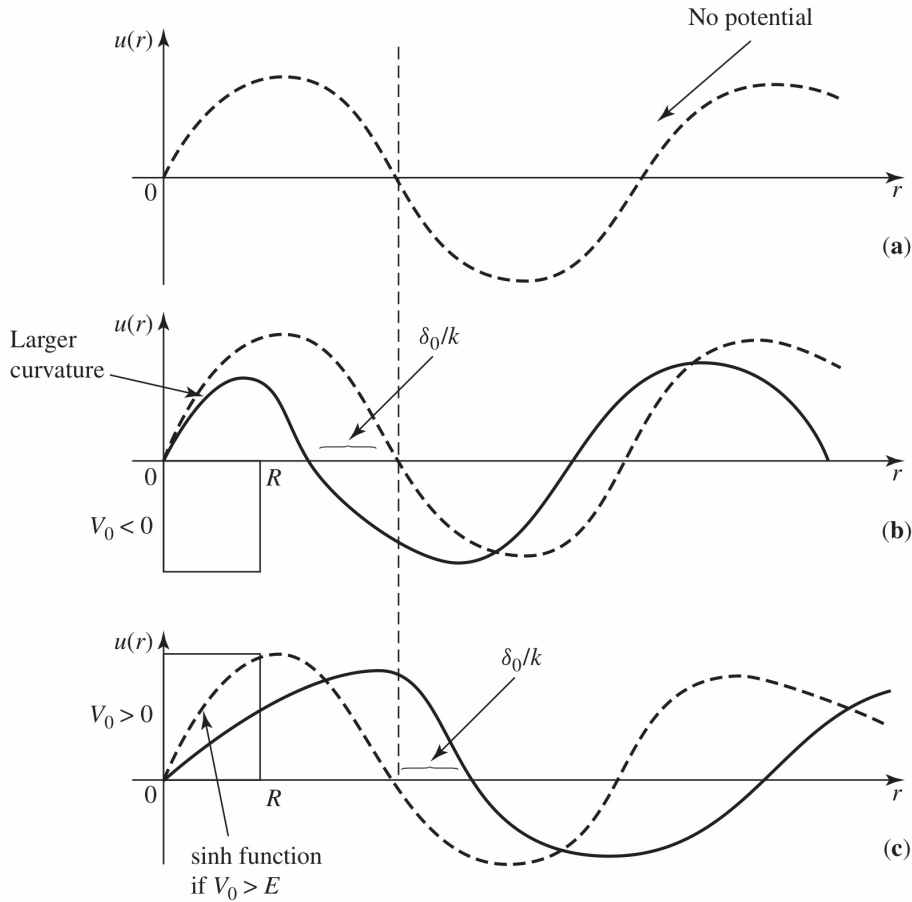


**Figure 2.5:** The *reduced wave-function* for s-wave scattering  $u_0$  as function of the relative distance  $r$  for different potentials [113]. (a)  $V=0$  wave-function (dashed line). (b) attractive potential  $V<0$ , which results in  $\delta_0 > 0$  with the wave-function (solid line) pushed in. (c) repulsive potential  $V>0$  resulting in the wave-function to be pulled out (solid line)  $\delta_0 < 0$ . Figure taken from [113]

At low energies that correspond to small relative momenta ( $k^* R \ll 1$ , where  $R$  is the typical range of potential), the s-wave channel, which is characterized by  $l = 0$ , dominates the scattering process as the particles do not have enough energy to overcome the centrifugal barrier. If the potential is short-ranged, the s-wave phase-shift converges for  $k^*$  approaching zero and the following parameterization based on the effective range theory, therefore also known as *effective*

range expansion, holds [116]

$$k^* \cot \delta_0(k^*) \xrightarrow{k^* \rightarrow 0} \frac{1}{f_0} + \frac{1}{2} d_0 k^{*2} + \mathcal{O}(k^{*4}), \quad (2.16)$$

where  $f_0$  is the scattering length and  $d_0$  the effective range.

The scattering length can also be seen as the effective size of the target. However, it has to be noted that there exist different sign conventions regarding the scattering length. In Eq. 2.16 a positive  $f_0$  denotes attraction. If  $f_0 < 0$  fm either a bound state is present or the interaction is repulsive. Even though, this might seem controversial at first, as a bound state requires an attractive interaction, Figure 2.6 might bring more clarity. It shows the reduced wave-function as a function of the distance  $r$  for different types of potentials of range  $R$  at extremely low energies ( $k^* \approx 0$ ), as well as the scattering length  $a$ , which corresponds to the intercept of the wave-function outside of the potential with the  $r$  axis. Here the opposite sign convention for  $a$  is used, hence  $a < 0$  fm indicates an attractive potential. Equation 2.16 therefore becomes  $\lim_{k^* \rightarrow 0} k^* \cot \delta_0(k^*) \xrightarrow{k^* \rightarrow 0} -\frac{1}{a}$ . As expected,  $a > 0$  fm for a repulsive (sub-figure 2.6(a)) and  $a < 0$  fm for an attractive potential (sub-figure 2.6(b)). However, if the attraction is increased as in sub-figure (c), the outside wave-function again crosses the  $r$ -axis of the positive half axis. If bound states are present, their binding energy  $E_B$  can be expressed in terms of the scattering parameters [117]

$$E_B = \frac{1}{\mu d_0^2} \left( 1 - \sqrt{1 + 2 \frac{d_0}{f_0}} \right)^2. \quad (2.17)$$

The scattering length can also be a complex number, where the real part  $\Re(f_0)$  gives information about the attractiveness or repulsiveness of the interaction and possible bound states, while the imaginary part is connected to inelastic scattering processes.  $\Im(f_0) = 0$  fm corresponds to totally elastic scattering between the particles and  $\Im(f_0) > 0$  fm hints at the existence of inelastic channels, which can wash out any bound state if they are the dominant contribution to the interaction. The coupled channel dynamics are treated in more detail in Sec. 2.3.

The other scattering parameter  $d_0$ , again of the dimension of a length, gives the energy dependence of scattering at low energies [114].

In general, scattering parameters provide valuable information on the underlying interaction. Therefore, it is reasonable to link them to the correlation function. This can be either achieved by means of potentials or via model predictions. Both approaches will be discussed in the following.

## 2.2.1 Lednický–Lyuboshits Approach

An established method to derive the scattering parameters is to employ the Lednický–Lyuboshits approach [118], which provides an analytical treatment of the asymptotic wave-function (Eq. 2.8) in Eq. 2.4. The FSI is modeled for isotropic sources of finite lifetime and Gaussian profile within the *effective range expansion* (Eq. 2.16) and s-wave approximation ( $l = 0$ ), as the relative momentum between the particles is small and therefore, the contribution of s-wave interaction is dominant.

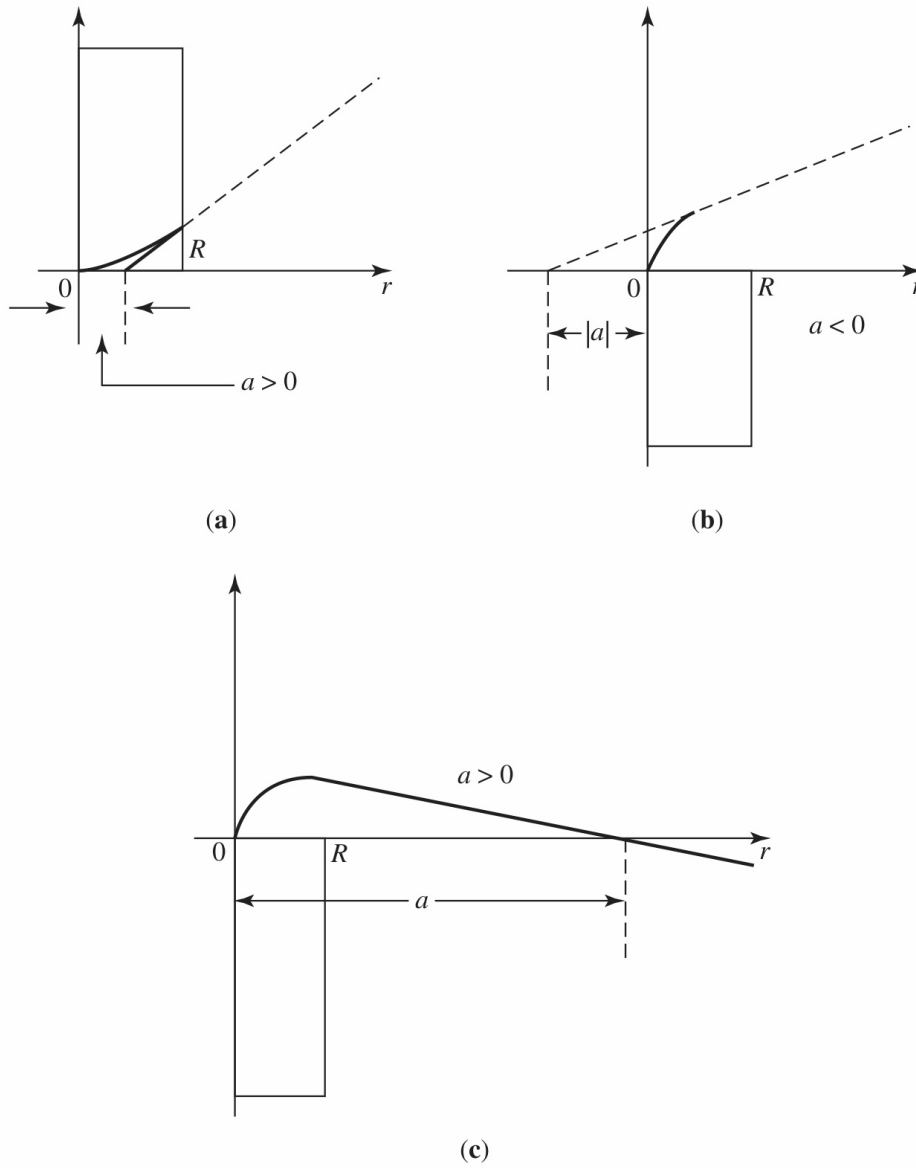


**Figure 2.6:** Reduced wave-function  $u(r)$  for zero-energy ( $k^* \approx 0$ ) as function of  $r$  for a repulsive potential (a), an attractive potential (b) and increased attractive potential (c). The intercept of the outside  $u(r)$  with the  $r$ -axis gives the scattering length  $a$ . Figures taken from [113].

From Eq. 2.16 and 2.13 the s-wave scattering amplitude can be written as [118]

$$f(k^*) = \frac{e^{2i\delta_0(k^*)} - 1}{2ik^*} \approx \left( \frac{1}{f_0} + \frac{1}{2}d_0k^{*2} - ik^* \right)^{-1}. \quad (2.18)$$

By substituting this expression in the asymptotic wave-function (Eq. 2.8), the Koonin-Pratt Eq. 2.4 can be solved analytically for a Gaussian source (Eq. 2.5). For uncharged non-identical particles

this results in

$$C_{LL}(k^*) = 1 + \frac{1}{2} \left| \frac{f(k^*)}{r_0} \right|^2 \left( 1 - \frac{d_0}{2\sqrt{\pi}r_0} \right) + \frac{2\Re(f(k^*))}{\sqrt{\pi}r_0} F_1(2k^*r_0) - \frac{\Im(f(k^*))}{r_0} F_2(2k^*r_0), \quad (2.19)$$

where  $F_1(2k^*r_0)$  and  $F_2(2k^*r_0)$  denote analytical functions from the approximation of the source with a Gaussian profile defined as

$$F_1(z) = \frac{1}{z} e^{-z^2} \int_0^z e^{x^2} dx \quad (2.20)$$

and

$$F_2(z) = \frac{1}{z} (1 - e^{-z^2}). \quad (2.21)$$

The term  $\left( 1 - \frac{d_0}{2\sqrt{\pi}r_0} \right)$  is a correction factor, that was introduced by Lednický in order to account for small sources, where a sizable amount of particles pairs is emitted within the range of the potential of the strong interaction. This factor is called *small source correction term* and serves the purpose of approximately model the deviation between the asymptotic form of the wave-function and the true solution.

**Identical particles** For identical particles a symmetrization of the wave-function for each spin state is required due to the Pauli principle. This is given by Eq. 2.11, where the partial waves  $\Psi_l(r)$  cancel depending on  $s + l$ . In absence of any FSI, hence  $\Psi_l(r)$  corresponds to a free wave, the correlation function is given as [119]

$$C_s(k^*) = 1 + (-1)^s e^{-4k^{*2}r_0^2}. \quad (2.22)$$

This is purely attributed to QS. Within the Lednický–Lyuboshits model, the following expression is derived [119]

$$C_{LL,s}(k^*) = 2 \cdot C_{LL}(k^*) - 1 - (1)^{(s+1)} e^{-4k^{*2}r_0^2}, \quad (2.23)$$

where the last term is given by Eq. 2.19. In the specific case of identical particles with total spin  $s = 1$ , Eq. 2.23 can be written as

$$C_{LL,1}(k^*) = \frac{1}{2} \left[ C_{LL}(k^*) + 1 - e^{-4k^{*2}r_0^2} \right]. \quad (2.24)$$

**Coulomb force** In case of charged particles, the correlation signal is modified by the Coulomb interaction, which can be treated analytically via the Gamow approximation [119]. The corresponding Coulomb penetration factor is given as [119]

$$A_C(\eta) = \frac{2\pi\eta}{e^{2\pi\eta} - 1}, \quad (2.25)$$

where  $\eta = \alpha\mu q_1 q_2 / k^*$  and  $\alpha$  is the fine structure constant. The Coulomb penetration factor, also referred to as Gamow factor, is then simply multiplied to the correlation function  $C(k^*)$ . Another

possibility is an exact treatment of the coulomb interaction by employing scattering theory and the asymptotic solution of a Coulomb wave-function [119].

**Zero-effective range approximation** This is an approach used for low-energy scattering problems where higher terms in the *effective range approximation* Eq. 2.16 are neglected. It builds on the fact, that the de Broglie wavelength  $\lambda = h/p$  of the incidence particle is much larger than the range of the potential, leading to the approximation  $d_0 = 0$  fm [120]. Historically it was derived prior to the *effective range expansion*. The latter was then introduced as finite-range correction to the zero-range theory [116].

For a particularly small source size  $r_0$  combined with a relatively large effective range  $d_0$ , the small source correction term within the Lednický–Lyuboshits approach, given by  $(1 - d_0/(2\sqrt{\pi}r_0))$ , might become dominant and even take negative values that result in an unphysical shape of the correlation function. This represents a limitation of the Lednický–Lyuboshits approach. Therefore, it is suggested to first validate the use of this model for small systems and/or large effective ranges. This can be done by utilizing the *zero effective range approximation*, where  $d_0 = 0$  fm, to evaluate the influence of the correction term on the scattering parameters.

## 2.2.2 Potentials

The correlation function can be computed by the convolution of the two-particle wave-function with a given emission source distribution  $S(\vec{r}^*)$  as in Eq. 2.4. Instead of employing the asymptotic solution of the wave-function as discussed in the previous Sec. 2.2.1, which only holds at distances far away from the scattering region, the exact wave-function might be used instead. It is computed numerically for a given local potential  $V(r)$  by employing the *Correlation Analysis Tool using the Schrödinger Equation* (CATS) [121], where Eq. 2.10 is solved for the relevant partial waves with the corresponding boundary conditions until convergence is reached, and allows the investigation of small emission regions. From the total wave-function it is then possible to determine the scattering parameters (Eq. 2.9).

The interaction potential  $V(r)$  is either provided by theory or phenomenological potentials have to be used, as for example the Yukawa-type potential [122]

$$V_{\text{Yukawa}}(r) = -A \cdot \frac{e^{-\alpha \cdot r}}{r}, \quad (2.26)$$

where  $A$  is dimensionless and proportional to the coupling strength  $g = \sqrt{A}$ . Also the Gaussian-type potential can be employed

$$V_{\text{Gaussian}}(r) = V_{\text{eff}} \cdot e^{-\mu \cdot r^2}, \quad (2.27)$$

where  $V_{\text{eff}}$  characterizes the potential strength and  $\frac{1}{\sqrt{\mu}}$  its range.

**Testing the accuracy of the Lednický–Lyuboshits model** The accuracy of the analytical Lednický–Lyuboshits model, especially for small sources and large effective ranges, can be tested by comparing it to the numerical approach employing a Gaussian type of potential, which is expected to hold well at small emission regions.

This is done by scanning the parameter space of the potential within  $V_{\text{eff}} \in [0.1, 56]$  MeV and  $\mu \in [0.1, 100]$  fm<sup>-2</sup> and calculating the corresponding correlation function. By employing Eq. 2.16, the *effective range expansion*, the scattering parameters can be deduced. The correlation function of the Gaussian-potential approach is then parameterized with the one from the Lednický–Lyuboshits approach. Figure 2.7 shows the resulting scattering parameter space. The color bar represents the relative deviation between the parameter values obtained from both approaches with respect to the Gaussian-type potential results. Notably, the deviation increases for both scattering parameters for increasing  $d_0$ . However, for small  $f_0 < 0.2$  fm the Lednický–Lyuboshits approach leads to accurate results also for large  $d_0$ .

This comparison can be used as an estimate only because it relies on the assumption of a simple Gaussian-type potential. The results might change when employing a different kind of potential.

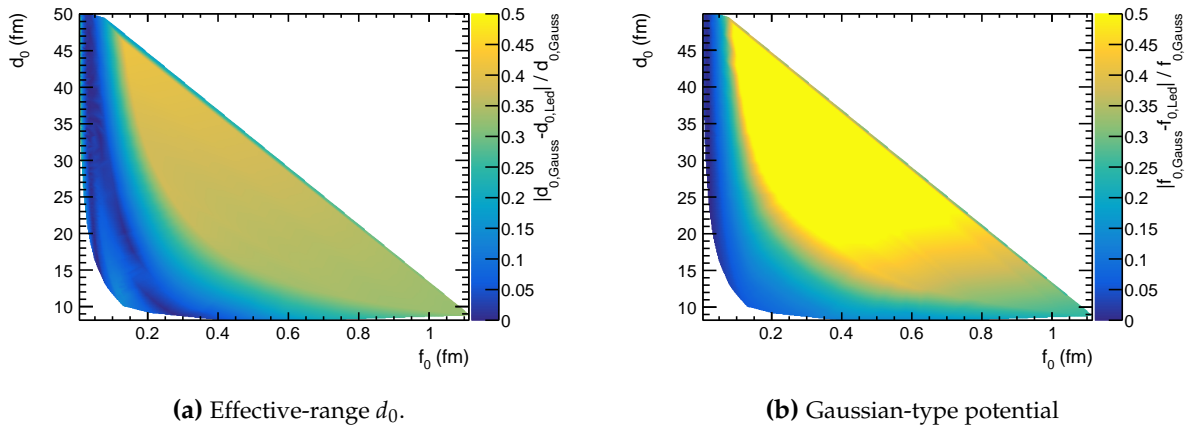


**Figure 2.7:** Scattering parameter phase-space of the Gaussian-type potential approach. The color bar shows the relative deviation between the parameters obtained from the potential and the Lednický–Lyuboshits approach, normalized to the potential approach values. While blue denotes good agreement between the two, yellow corresponds to a relative deviation of 50%. The left figure depicts the results for the effective range  $d_0$ , while the right figure shows the same for the scattering length  $f_0$ .

## 2.3 Coupled-channel dynamics

Whenever pairs of particles share the same quantum numbers, coupled-channel processes emerge. Phenomena such as bound states or resonances depend on the coupling between these inelastic channels, which when dominant can wash them out. Therefore, they have to be considered when studying hadron-hadron interactions. As the final-state particles are fixed in femtosopic measurements, the correlation function is sensitive to all the available inelastic channels produced in the initial collision. Hence, if a specific two-particle final-state is fed by coupled-channels [109, 123, 124] the correlation function in Eq. 2.4 has to be modified to [125]

$$C(k^*) = \int d^3r^* \sum_j \omega_j S_j(\vec{r}^*) |\Psi_j(\vec{k}^*, \vec{r}^*)|^2, \quad (2.28)$$

where the sum runs over all contributions which couple to the final-state.  $\Psi_j$  is the wave-function in the  $j$ th channel,  $S_j(\vec{r}^*)$  is the corresponding normalized source function and  $\omega_j$  the weight of the coupled-channel which is determined by the population of the initial state.

The wave-functions can be derived by solving the coupled-channel Schrödinger equation

$$\begin{pmatrix} \mathcal{H}_{1 \rightarrow 1} & \mathcal{H}_{1 \rightarrow 2} & \dots & \mathcal{H}_{1 \rightarrow M} \\ \mathcal{H}_{2 \rightarrow 1} & \mathcal{H}_{2 \rightarrow 2} & \dots & \mathcal{H}_{2 \rightarrow M} \\ \vdots & \vdots & \ddots & \vdots \\ \mathcal{H}_{M \rightarrow 1} & \mathcal{H}_{M \rightarrow 2} & \dots & \mathcal{H}_{M \rightarrow M} \end{pmatrix} \cdot \begin{pmatrix} \Psi_1(\vec{k}_1^*, \vec{r}^*) \\ \Psi_2(\vec{k}_2^*, \vec{r}^*) \\ \vdots \\ \Psi_M(\vec{k}_M^*, \vec{r}^*) \end{pmatrix} = E \cdot \begin{pmatrix} \Psi_1(\vec{k}_1^*, \vec{r}^*) \\ \Psi_2(\vec{k}_2^*, \vec{r}^*) \\ \vdots \\ \Psi_M(\vec{k}_M^*, \vec{r}^*) \end{pmatrix}, \quad (2.29)$$

where the diagonal elements of the Hamiltonian matrix correspond to the potentials of elastic processes  $i \rightarrow i$ , while the off-diagonal elements describe the potentials of inelastic transitions  $i \rightarrow j$  given by the strong interaction only. From energy and momentum conservation it is possible to estimate the  $k^*$  at which the individual channels open in the particle rest frame as

$$k^* = \sqrt{\frac{\Delta_i^2 - (m_1 \cdot m_2)^2}{(\tilde{m}_1 + \tilde{m}_2)^2}}, \quad (2.30)$$

where  $\Delta_i = \frac{1}{2} \cdot ((\tilde{m}_1 + \tilde{m}_2)^2 - (m_1^2 + m_2^2))$ ,  $m_j$  are the masses of the individual particles of a pair in MeV/c<sup>2</sup> and tilde denotes the heavier pair. This momentum corresponds to the minimum energy at which the individual coupled-channel particle pair can be produced.

Inelastic interactions influence the correlation function depending on their coupling strength. Above threshold channels alter the shape of the correlation function in form of a cusp, which appears close to their opening momentum  $k_i^*$ . This can be visible in the experimental results provided that the momentum-binning is granular enough. Channels, which open below threshold, on the other hand, induce an effective attraction, which leads to an increase of the correlation signal without modifying its shape. This qualitative discussion is supported by Fig. 2.8, which depicts the  $K^-p$  correlation function for a varying number of coupled-channels. While the  $\pi\Sigma$  and  $\pi\Lambda$  channels are already open at threshold,  $\bar{K}^0n$  opens at  $k^* \approx 58$  MeV/c (denoted as  $q$  in the figure) in the  $K^-p$  c.m., where a cusp structure appears in the correlation function. Compared to the result from including only the  $K^-p$  component, the cusp gets more pronounced when coupled-channels are considered. Additionally, the whole correlation function gets shifted to

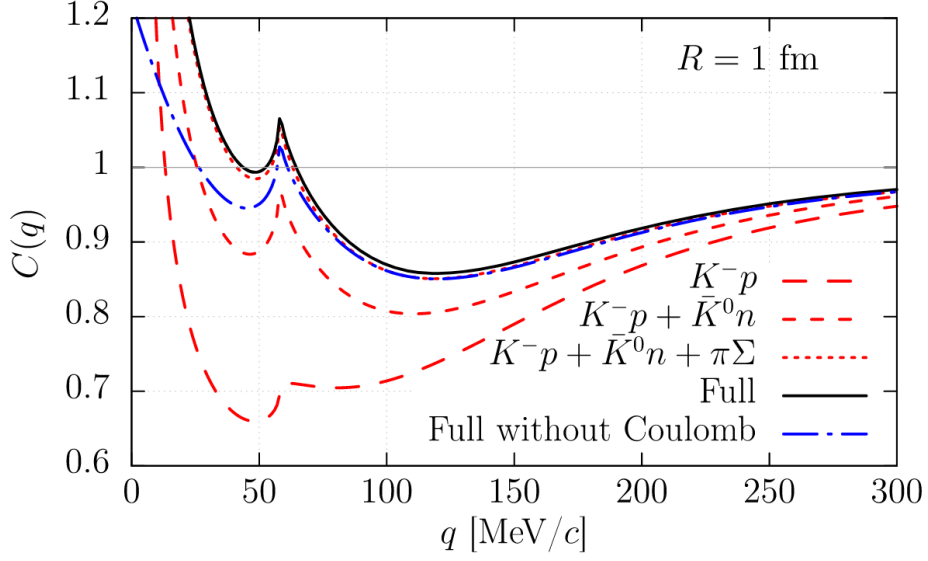


**Figure 2.8:** The  $K^-p$  correlation function evaluated in the  $\bar{K}N$ - $\pi\Sigma$ - $\pi\Lambda$  coupled-channel framework [125]. The long-dashed line corresponds to the result when only considering the  $K^-p$  component, while the others additionally include the  $\bar{K}^0n$ , both the  $\bar{K}^0n$  and  $\pi\Sigma$  and all coupled-channel components. All calculations are performed with realistic potentials based on chiral SU(3) dynamics, which fit the available scattering data. Figure taken from [125].

larger values, the more coupled-channels components are included. The enhancement due to the  $\bar{K}^0n$  channel is found to be the largest, followed by  $\pi\Sigma$ . More details can be found in [125, 126].

In case of  $p$ - $\phi$ , the system couples to channels with isospin  $I = 1/2$  and no net-strangeness  $S = 0$ . This includes  $\rho N$ ,  $\omega N$ ,  $K^*\Lambda$  and  $K^*\Sigma$ , where the latter two are believed to be most prominent [43]. Also  $K\Lambda$  and  $K\Sigma$  have to be considered for an angular momentum  $L \neq 0$ . The pair masses are shown in Fig. 2.9, in order to visualize their relative position to one another. Channels, which lie closer in mass to the  $p$ - $\phi$  pair, might induce a stronger effect on the correlation function.

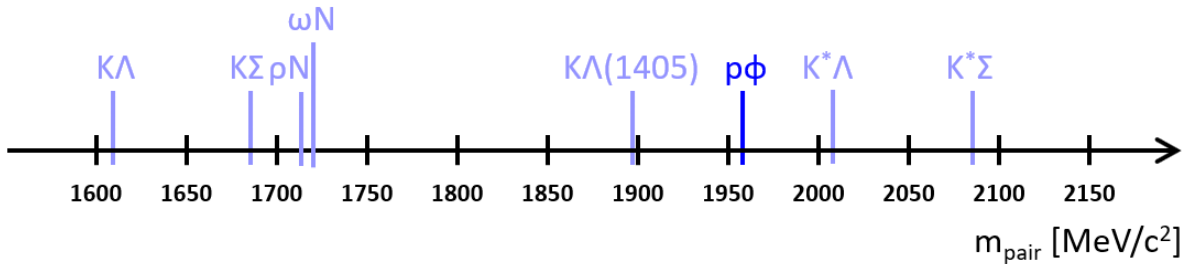


**Figure 2.9:** Pair mass of the different coupled-channels and  $p$ - $\phi$  respectively.



# 3 Experimental Setup

## 3.1 The LHC

The Large Hadron Collider (LHC) [127] is a two-ring accelerator and collider which aims to probe the high-energy frontier of physics and reveal physics beyond the standard model. In the Run 2 data-taking period from 2015 to 2018 it reached a maximum centre-of-mass energy of  $\sqrt{s} = 13$  TeV at a peak luminosity of  $\mathcal{L} = 10^{34} \text{ cm}^{-2}\text{s}^{-1}$  for pp collisions and in Run 3, starting in 2021, the LHC is planned to reach its designated energy of  $\sqrt{s} = 14$  TeV and double its luminosity to  $\mathcal{L} = 2 \times 10^{34} \text{ cm}^{-2}\text{s}^{-1}$  [128].

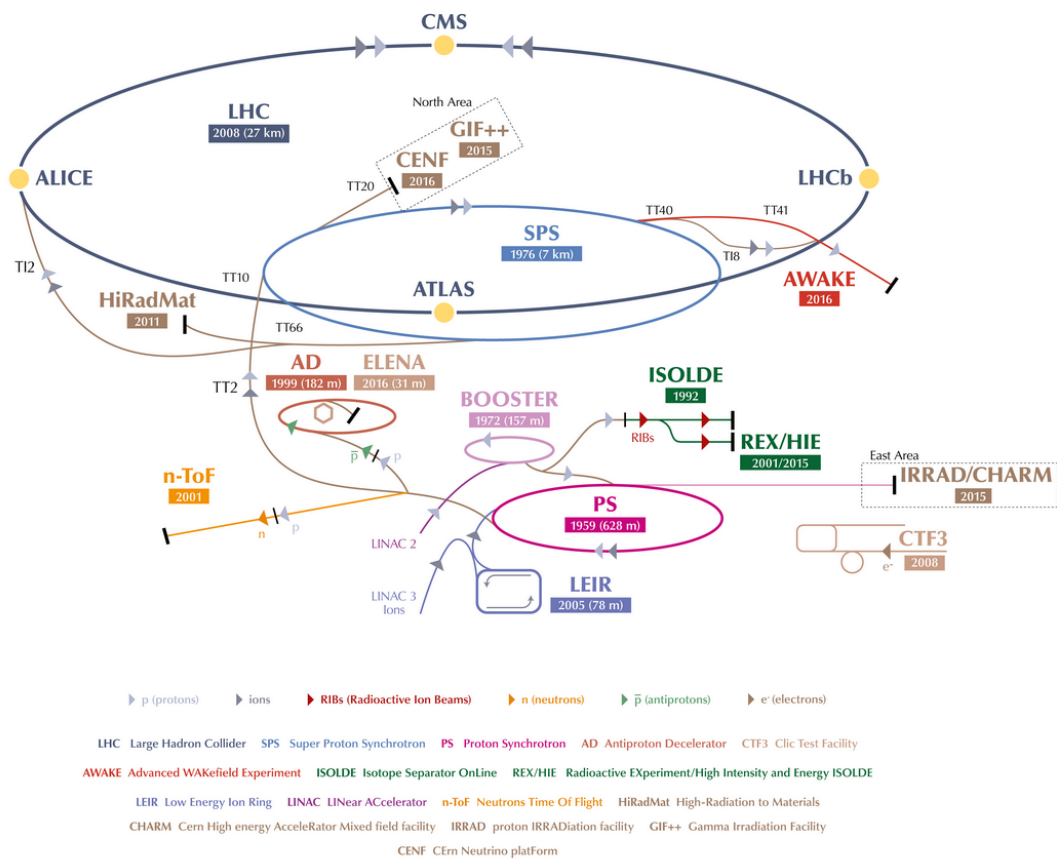


**Figure 3.1:** The CERN accelerator complex. The LHC is the last building block after a complex hadron injection chain, where the particles are accelerated to energies up to  $\sqrt{s} = 13$  TeV for pp collisions. Figure taken from [129].

It was build between 1998 and 2000 in the already existing tunnel of the Large Electron-Positron collider (LEP) at CERN, the European Organization for Nuclear Research, and consists of two rings with a circumference of 26.7 km in which beams of particles with the same charge rotate in opposite directions by means of superconducting twin-bore magnets, which are cooled to a temperature of 2 K [127]. The LHC operates with different colliding systems, i.e. pp, p–Pb and Pb–Pb. In 2017 there was a short run with Xe–Xe collisions [130] to demonstrate the colliders

flexibility with new species. The proton beams themselves consist of 2808 particle packages, so-called bunches, with a nominal spacing of 25 ns and a maximum proton-density of  $\sim 1.15 \times 10^{11}$ , which is limited by nonlinear beam-beam interaction between the particles in the collision [127].

Figure 3.1 shows the CERN accelerator complex, consisting of multiple building blocks which aim to accelerate the hadrons to the injection energies of the LHC. The proton injection chain starts with the linear accelerator Linac2, which contains the proton source. From there the particles move through the Proton Synchrotron Booster (PSB), where they are further accelerated, into the Proton Synchrotron (PS). Lead ions on the other hand are produced in long pulses by the Linac3 and are then transformed into short, dense bunches by the Low Energy Ion Ring (LEIR) before they move into the PS as well. From there the bunches are injected into the Super Proton Synchrotron (SPS), which accelerates them further to provide beams for the LHC, where a total of four experiments, ALICE, ATLAS, CMS and LHCb are located at different beam interaction points.

### 3.2 ALICE

ALICE (A Large Ion Collider Experiment) [131–135] is one of the LHC’s four major experiments with the main task to investigate the properties of QCD matter generated in heavy-ion collisions. The detector design is optimised for an instantaneous luminosity of the collider of  $\mathcal{L} = 10^{27} \text{ cm}^{-2}\text{s}^{-1}$  for Pb–Pb and to track and identify particles at high multiplicity densities up to  $dN_{ch}/d\eta \approx 8000$  at mid-rapidity [134]. It is required to provide an excellent performance of these tasks even for low  $p_T$ .

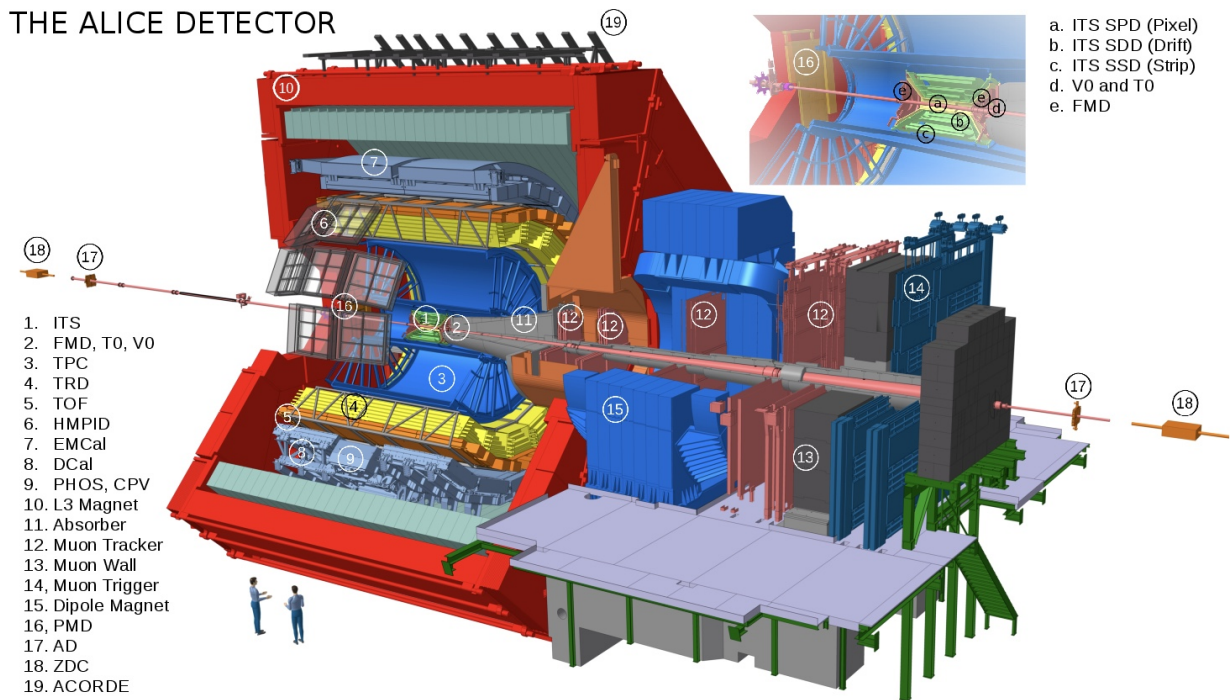


Figure 3.2: The schematic layout of the ALICE spectrometer. Figure taken from [136].

The schematic setup is shown in Fig. 3.2. ALICE consists of a forward arm of muon detectors, which cover a pseudorapidity region of  $-4.0 < \eta < -2.5$ , and the so-called central barrel, which is embedded in a large solenoid with a magnetic field of  $B = 0.5$  T and covers pseudorapidities of  $|\eta| < 0.9$  and the full azimuthal angle.

The central barrel has an onion-like structure. The Inner Tracking System (ITS), which is a silicon tracker, is located around the beam pipe. Progressing outwards there is the cylindrical, gas-filled Time Projection Chamber (TPC) followed by the Transition Radiation (TRD), the Time of Flight (TOF) and the Ring Imaging Cherenkov (HMPID) detector. Last, there are the photon spectrometer (PHOS) and the electromagnetic calorimeter (EMCaL), which are used to measure jets, photons and electrons. On top of the big magnet, the ACORDE scintillators are installed in order to trigger cosmic radiation. The main detectors i.e. ITS, TPC and TOF are explained in more detail in the following sections.

### 3.2.1 Inner Tracking System (ITS)

The ITS is the innermost part of the detector and surrounds the beam pipe at radii ranging from 3.9 cm to 43 cm with respect to the interaction point [132]. It consists of six layers of cylindrical silicon detectors and is designed for primary and secondary vertex reconstruction with a resolution of 10  $\mu\text{m}$  and 100  $\mu\text{m}$  respectively [137]. Additionally, the ITS is used for particle tracking and identification in the non-relativistic region.

The two innermost layers are made of Silicon Pixel Detectors (SPD). Their main purpose is to determine the primary vertex position and to measure the tracks of secondary particles from decays of heavy-flavored hadrons. The four outer layers are made of two Silicon Drift Detectors (SDD) followed by two Silicon Strip Detectors (SSD), which measure the ionization energy loss  $dE/dx$  of the particles [132]. In the case of low- $p_T$  particles the ITS represents the only PID information source [135].

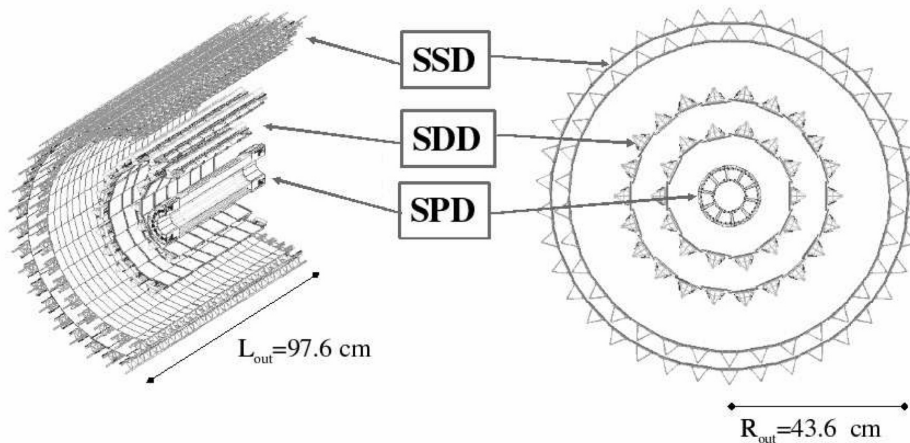
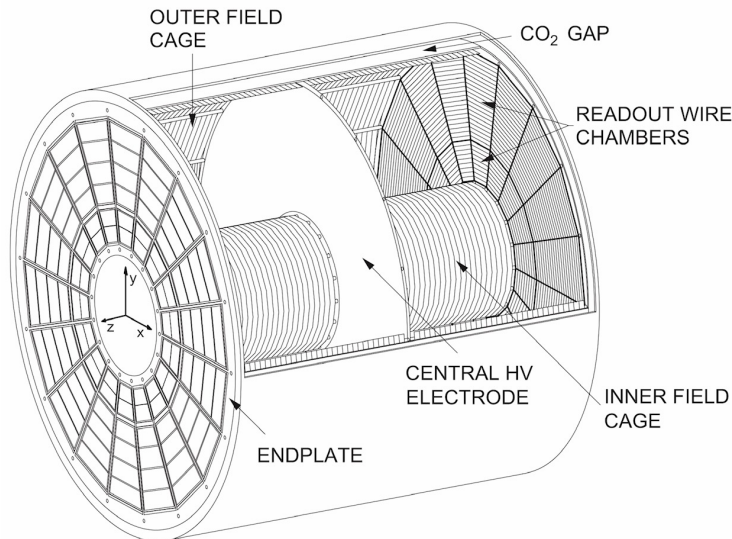


Figure 3.3: The ALICE ITS [131]

### 3.2.2 Time Projection Chamber (TPC)

The key objective of the TPC [132, 138] is to measure charged-particle momenta as well as particle identification. It is the main tracking device of ALICE and is positioned within 0.84 m and 2.47 m from the interaction point in radial direction. The TPC covers a large  $p_T$  range from 0.1 to 100 GeV  $c^{-1}$  at mid-rapidity  $|\eta| < 0.9$  [131].

The TPC consists of a cylindrical field cage enclosing a 90 m<sup>2</sup> drift volume, which is filled with a mixture of Ne, N<sub>2</sub> and CO<sub>2</sub> [138]. The end-plates of the TPC cylinder are divided into 18 sectors, each of which is radially separated into an inner and outer readout chamber, giving a total of 36 chambers, see Fig. 3.4. Their design is based on multi-wire proportional chambers (MWPCs) with pad readout. The chambers consist of a grid of anode wires running in azimuthal direction above the pad plane, followed by a cathode-wire grid and a gating grid [138]. Each inner readout chamber consists of 63 pad rows and the outer one of 96. The corresponding  $\sim 560,000$  readout channels keep a low occupancy and have a high resolution [138]. The TPC covers the full azimuth beside dead zones between neighboring readout chambers.



**Figure 3.4:** The ALICE TPC [138]

The field cage assures a uniform electrostatic field in the gas volume, which transports electrons, stemming from ionization processes caused by charged particles passing through the detector gas, to the readout chambers without significant perturbations. In the vicinity of the anode wire, after passing the open gating grid, the field strength increases and the electrons become energetic enough to ionize the gas, thereby creating an avalanche of electrons and positive ions. While the electrons are absorbed immediately by the anode wire, the ions, which have lower mobility and therefore, a slower drift-velocity, move towards the cathode grid where they are absorbed. The instantaneous current induced by charge carriers on an electrode depends on their velocity, both related via the Shockley-Ramo-theorem [139, 140]. Therefore, the signal is dominated by ions, which induce mirror charges on the pad plane, and is read out and further processed by the front-end electronics. The remaining ions, which were not absorbed, are stopped by the closed gating grid, as they can cause severe perturbations of the drift field.

The induced charge, together with the arrival time of the avalanche electrons, makes it possible

to reconstruct the particle tracks from which the momenta and the energy loss from collisions with the drift gas molecules can be deduced.

The specific energy loss  $dE/dx$  of a particle is related to its velocity  $\beta = \frac{v}{c}$  via the Bethe Bloch formula [141]

$$-\frac{dE}{dx} = \frac{4\pi n z^2}{m_e c^2 \beta} \left( \frac{e^2}{4\pi\epsilon_0} \right)^2 \left[ \ln \left( \frac{2m_e c^2 \beta^2}{I \cdot (1 - \beta^2)} \right) - \beta^2 \right], \quad (3.1)$$

with,  $ze$  the charge,  $n$  the electron number density and  $I$  the mean excitation level. Figure 3.5 shows the specific energy loss of different particle species within the TPC together with a parameterization of the Bethe-Bloch formula [142]. The deviation between the experimental measurement and the signal hypothesis for particle species  $i$  is given by  $n_{\sigma,i}$ , and is expressed in terms of the detector resolution  $\sigma$  [132]

$$n_{\sigma,i} = \frac{dE/dx_{\text{measured}} - \langle dE/dx \rangle_{\text{expected},i}}{\sigma}. \quad (3.2)$$

From the bending radius of the track within the magnetic field, the momentum of a particle can be determined and together with the measured  $dE/dx$  it can be identified through its mass via

$$M = \frac{p}{\beta\gamma}. \quad (3.3)$$

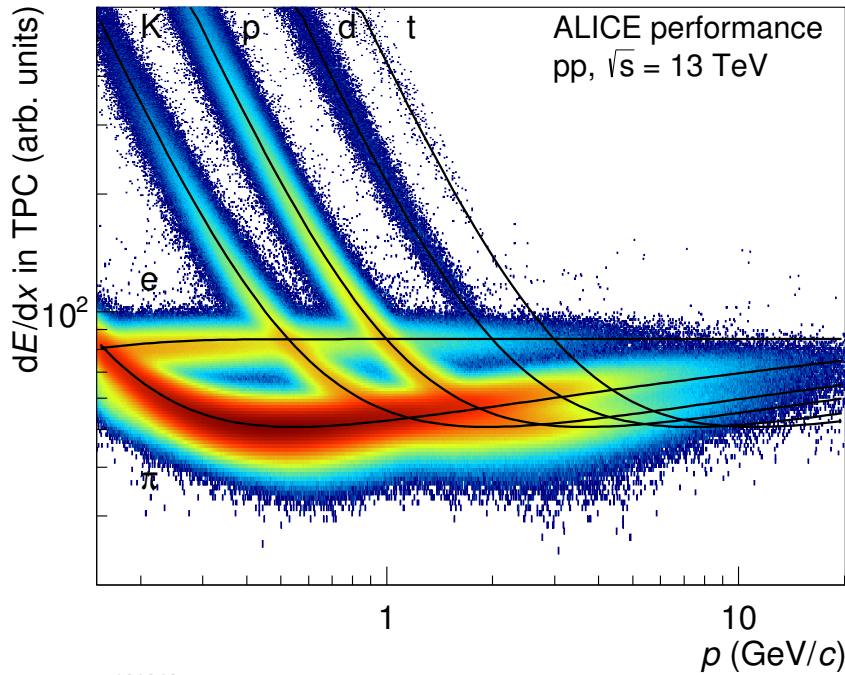


**Figure 3.5:** The TPC energy loss as a function of the momentum  $p$  [143].

For the LHC Run 3, an interaction rate of 50 kHz [144] is foreseen for lead ions, which requires an increased read-out rate. However, due to the gating grid of the MWPCs, which only opens for the duration of one drift-time interval of about 100  $\mu\text{s}$  upon a trigger signal [138] and is kept close for twice as long, the readout rate is limited to 3 kHz [144]. Therefore, the MWPCs will be

replaced with Gas Electron Multipliers (GEMs) which make a continuous read-out possible as they operate without the need of a gating grid [144, 145].

### 3.2.3 Time Of Flight Detector (TOF)

The TOF [132, 146] detector consist of 1593 glass Multigap Resistive Plate Chambers (MRPC) located between 3.70 m and 3.99 m from the beam axis and has a total active area of 141 m<sup>2</sup>. Like the TPC it covers the full azimuth and a pseudorapidity range of  $|\eta| < 0.9$ . It extends the track reconstruction and PID of ITS and TPC in the intermediate momentum range [132].

The MRPCs consist of two stacks of resistive glass plates, separated by equally thin gas-filled gaps. A total of three pickup electrodes positioned at both ends of the two-stack system as well as in-between the stacks are used for readout. The inner plates are not connected electrically and kept floating while on the outer surfaces of each stack a high voltage is applied. The latter results in a high and uniform electric field, which leads to an immediate electron avalanche from any ionization caused by a charged particle traversing the chamber. The avalanche is confined within the gaps but the resistive plates are transparent to the fast signal, which is induced on the pickup electrodes by the movement of the electrons. The total signal is then given by the sum from the signals from all gaps, which results in a high efficiency.

The narrow width of the gaps ensures a good time resolution of 80 ps [132]. Therefore, the exact arrival time  $t_{\text{TOF}}$  of the particles is measured with the TOF. Together with the time of the initial collision  $t_{\text{event}}$  it is possible to determine the time-of-flight  $t = t_{\text{TOF}} - t_{\text{event}}$ . The  $t_{\text{event}}$  is provided by the T0 detector, which consists of two rings of Cherenkov counters located close to the beam in the region of forward rapidity [147]. If no signal is provided by the T0, the start time is estimated from the arrival times at the TOF by an algorithm that minimizes the  $\chi^2$  between all the different mass hypotheses. Another possibility is to use an average start time for the run, which is only employed if none of the previous two methods are available. From the measured time-of-flight, a correlation between the mass  $M$  of the particle and its track momentum  $p$  can be calculated as [135]

$$M = \frac{p}{\beta\gamma} = p \sqrt{\frac{(ct)^2}{L^2} - 1}, \quad (3.4)$$

where  $L$  is the reconstructed length of the trajectory. Figure 3.6 shows the PID capabilities of the TOF. The estimator of the TOF PID for a specific particle hypothesis  $i$  is given by [146]

$$n_{\sigma,i} = \frac{t_{\text{TOF}} - t_{\text{event}} - t_{\text{expected},i}}{\sigma}, \quad (3.5)$$

where  $\sigma$  is the detector resolution, assuming a Gaussian description of the detector response function.

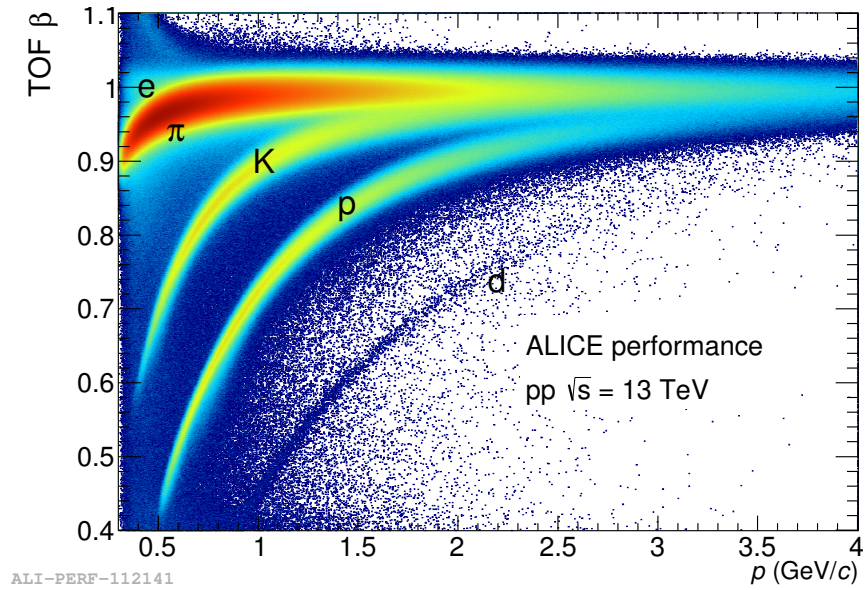


**Figure 3.6:** The velocity  $\beta$  measured with the TOF detector as a function of the momentum of the incident particle (measured by the TPC) [148].

### 3.3 Data Reconstruction

**Event reconstruction** The analysis process starts with the so-called event reconstruction, shown schematically in Fig. 3.7, which gives an overview of the steps explained in the following paragraphs. More details can be found in [131, 132, 135].

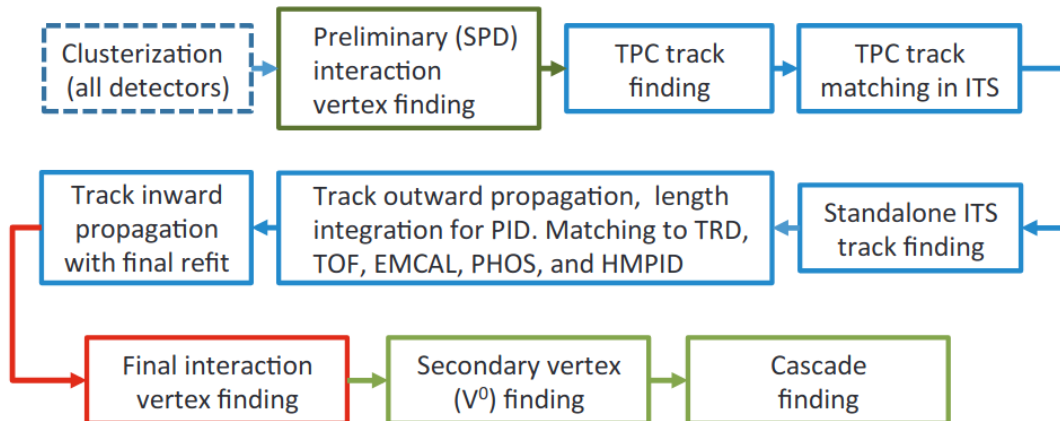


**Figure 3.7:** Event reconstruction in the central barrel [132].

The initial phase of finding tracks in the central barrel is the so-called clusterization, where raw signals are combined in each detector, depending on their position, amplitude and time. Next, the preliminary vertex of the primary interaction is determined as the point where the largest amount of tracklets converge by means of the two innermost ITS layers, the SPDs.

The actual track reconstruction (track finding and fitting) is performed with the Kalman filter technique [149], which relies on a realistic set of initial seed values for the track parameters

(position, inverse curvature, direction) and covariance matrix respectively. It starts at the outer radius of TPC with two clusters constrained by the point of the preliminary primary vertex and is then repeated with three clusters alone. From this, the initial seeds are obtained. The state vector of the track parameters and the covariance matrix are then propagated inwards and each time the filter finds a compatible space point in the new pad row the seeds are updated. At the inner radius of the TPC the track seeds are matched to clusters in the outermost layer of the ITS. If there is more than one possible matching space point, each is followed separately towards the innermost layer, producing a tree of possible tracks. Like in the TPC this procedure is done in two phases, first with vertex constraint and then without. After the ITS seeding is completed, the branch, which corresponds to the track with the highest quality from each hypothesis tree is used as prolongation of the TPC track and added to the reconstructed event. For low momenta, the reconstruction efficiency of the TPC drops due to energy loss and scattering with the detector material. Therefore, also a ITS-only track finding is performed with all the clusters that have not been used previously.

The tracks are then propagated outwards and refitted with the Kalman filter. Outliers are removed as the seeds are more precise than in the first step of the track reconstruction. This time also the TRD, TOF, HMPID and CPV, which is located in front of the PHOS, are included [131].

In the last step of the track reconstruction, the tracks are propagated inwards again. The previously found clusters are refitted on last time, determining the final values of the track parameters and the covariance matrix. The global tracks found with TPC and ITS are then used to find the primary vertex with more precision by extrapolating the tracks towards the nominal beamline. Outliers are removed and a vertex fit is performed.

The last step of the event reconstruction is the determination of vertices of secondary particles, which are produced either in direct decays of strange particles (neutral strange particles, eg.  $\Lambda \rightarrow p\pi^-$ ) or via cascades (charged strange particles, e.g.  $\Xi^- \rightarrow \Lambda\pi^- \rightarrow (p\pi^-)\pi^-$ ). The former are referred to as  $V_0$  candidates due to the characteristic decay pattern in form of a V, see Fig. 3.8. This is done by only using tracks with a relatively large impact parameter. Then the distance of closest approach (DCA) of such a pair of opposite-sign secondary tracks is calculated. In order to become a candidate for a secondary decay, the point of closest approach (PCA) has to be closer to the primary vertex than the first reconstructed points of both tracks. Furthermore, the DCA at the PCA of both tracks is required to be smaller than 1.5 cm [132]. The third requirement is  $\cos\theta < 0.9$ , where  $\theta$  is the angle between the connection line of primary and secondary vertex and the total momentum vector of the pair  $\vec{p}_{\text{pair}}$  [132]. This last requirement is relaxed if  $\vec{p}_{\text{pair}} < 1.5 \text{ GeV}/c$ , in order not to bias the candidate sample against cascades. In the analysis phase that follows, additional cuts are applied and more complex secondary vertices can be reconstructed.

**Data reconstruction and analysis** All information from the reconstruction process is stored in Event Summary Data (ESD) files and saved on the CERN computing grid. The ESDs are filtered into Analysis Object Data (AOD) files, by discarding information which is irrelevant for the majority of analyses. Finally, the data size is decreased again by adjusting it to the needs of the specific ALICE sub-groups and stored in NanoAODs. The analysis itself is then performed by means of the AliRoot framework [150].

For several parts of the analysis, full-scale Monte Carlo (MC) simulated collisions between elementary particles at high energies are needed. There are multiple sets of such general-purpose

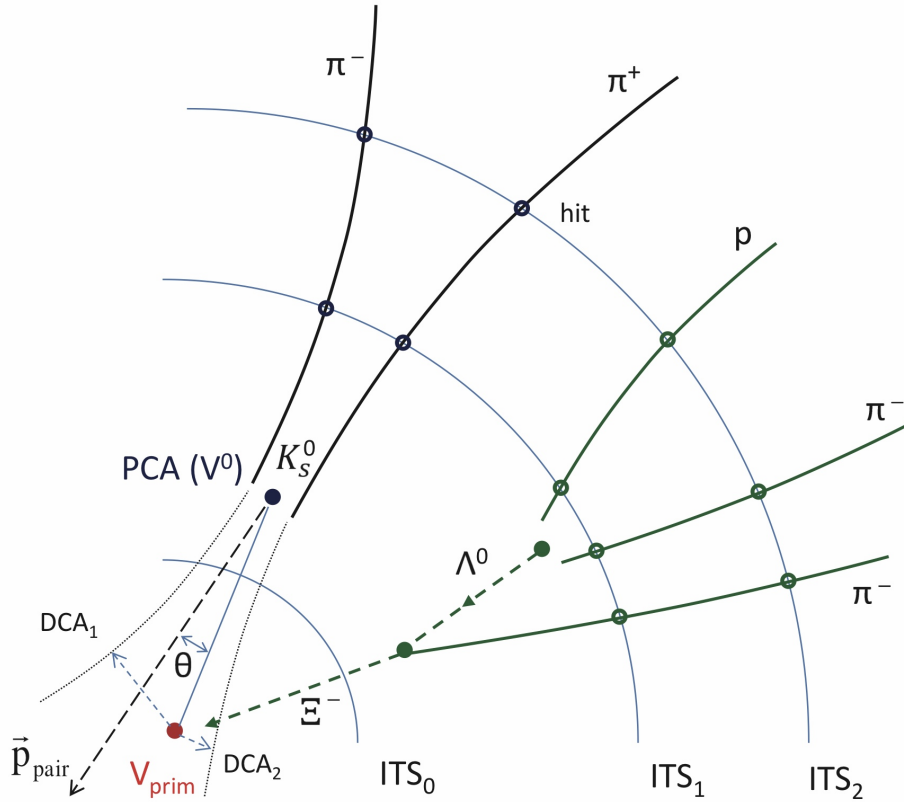


**Figure 3.8:** Reconstruction of the secondary vertex exemplary shown for  $K_S^0$  and  $\Sigma^0$  [132].

MC simulations provided by the ALICE collaboration, where each is anchored to specific data-taking periods as it is crucial that the exact experimental conditions are reproduced in the simulation.

In this analysis, the event generator PYTHIA 8 [151] is used and the subsequent transport of the particle through the detector material is obtained from GEANT 3 [152]. Finally, the resulting data is reconstructed by following the same algorithm as for raw data. MC data is for example needed to derive the purity of charged particles or the fraction of secondary particles from feed-down, which are both essential for the femtoscopic analysis.



## 4 Data Analysis

This chapter reviews the details concerning the analysis procedure from which the experimental correlation function is constructed. First, the data and event selection is discussed followed by the particle selection.

### 4.1 Data Set and Event Selection

Data from pp collisions at  $\sqrt{s} = 13$  TeV are analyzed, which have been recorded by the ALICE experiment during the LHC Run 2 from 2016 to 2018. The reconstruction follows Sec. 3.3 and the fully filtered NanoAODs are used as input. Events are selected by employing the common criteria of Run 2 analyses [85], summarized in Tab. 4.1.

In events with high multiplicities (HM) more particle pairs are produced. Additionally, an increased yield of particles with hidden and open strangeness is observed, see Fig. 4.1. While the proton yield remains rather constant, an enhanced  $\phi$  production can be noticed at higher multiplicities. Therefore, the `kHighMultV0` trigger is applied in order to select HM events, which consist of collisions with on average 30 produced charged particles in the pseudorapidity interval  $|\eta| < 0.5$  [154]. Figure 4.2 shows the relative amplitude measured by the V0 detector, which is used for triggering as it is proportional to the event multiplicity. The resulting data sample represents the upper 0.17% of the charged-particle distribution of all inelastic collisions with at least one charged particle in the range  $|\eta| < 1$  (referred to as `INEL > 0`) [73]. For the 2015 data sample of Run 2 no HM trigger is available. Additionally, the interaction rate is low. Therefore, as mentioned before, only the samples from 2016 to 2018 are employed in the analysis. To test various quantities relevant for this work, MC events are employed using the PYTHIA 8 [156] event generator with an additional selection on large charged-particle multiplicities, which mimic the effect of the HM trigger. Details on how the reconstructed MC is anchored to HM pp data can be found in the associated JIRA ticket<sup>1</sup>.

Provided, that there are enough tracks pointing to it, the distance between tracks and SPD vertex, whose resolution in  $z$  direction has to be below 0.25 cm, is restricted to values smaller than 0.5 cm. The primary vertex reconstructed from at least one global track, which requires both ITS and TPC clusters, has to be located within  $\pm 10$  cm to the nominal interaction point along the beam direction, to assure a uniform detector coverage.

Additionally, events with multiple reactions in one bunch crossing are rejected (in-bunch pile-up), if more than one interaction vertex is identified [132]. This leads to an estimated remainder of maximally 1.4% of all selected events from HM pp collisions at  $\sqrt{s} = 13$  TeV [73]. Inelastic reactions with other bunches, gases in the beam pipe or the LHC structures themselves (out-of-bunch pile-up) are rejected as well.

Meson-meson and meson-baryon correlation measurements in pp collisions are contaminated by a so-called minijet background. First observed in neutral and charged kaon pairs [157, 158] as well

---

<sup>1</sup> <https://alice.its.cern.ch/jira/browse/ALIROOT-8318>

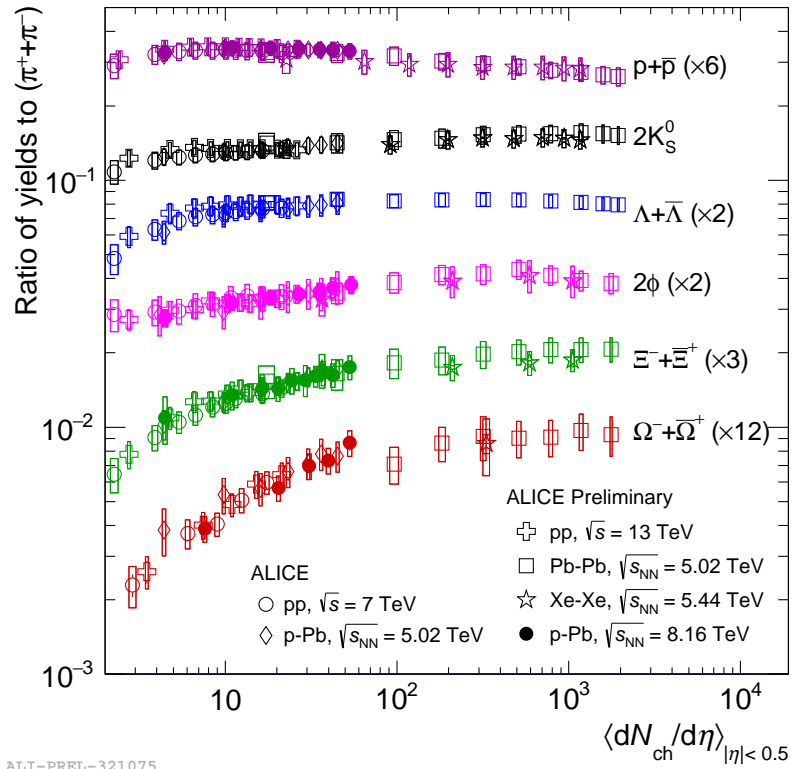


**Figure 4.1:** Particle-to-pion ratio as a function of multiplicity for different systems. The production of  $\phi$  mesons increases with multiplicity. For protons it slightly decreases but the overall yield remains significantly larger than the  $\phi$  yield. Figure taken from [153].

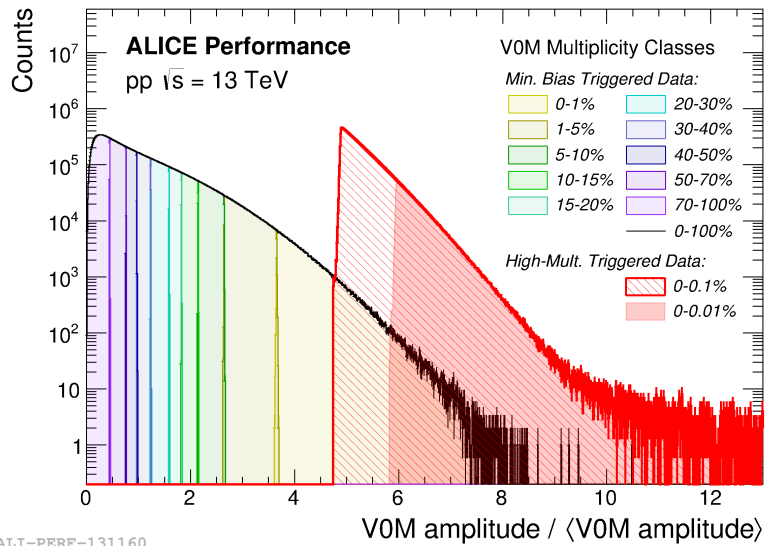


**Figure 4.2:** Distribution of the VOM amplitude scaled by its mean value, which is proportional to the event multiplicity [155].

as in charged pion pairs [159, 160], it was later shown to also affect meson-baryon femtoscopy in the case of proton-kaon [161]. Indeed it is also found to be present in the  $p$ - $\phi$  correlation function.

Minijets are believed to arise from the incoherent fragmentation of hard parton-parton scatterings [162]. Such processes produce jet-like structures containing auto-correlated particle pairs that induce long-range structures to the correlation function. They can be suppressed by employing a strict selection of the event shape, which itself is connected to the properties of the hadronic final-state after the particle collision.

The shape of an event can be classified mathematically by its transverse sphericity  $S_T$ , which is derived by diagonalizing the transverse momentum matrix [163]

$$\mathbf{S}_{xy} = \frac{1}{\sum_j p_{Tj}} \sum_i \frac{1}{p_{Ti}} \begin{bmatrix} p_{xi}^2 & p_{xi}p_{yi} \\ p_{yi}p_{xi} & p_{yi}^2 \end{bmatrix} \quad (4.1)$$

in order to obtain the corresponding eigenvalues  $\lambda_1$  and  $\lambda_2$ , with  $\lambda_1 > \lambda_2$ . The transverse sphericity is then calculated as

$$S_T = \frac{2\lambda_2}{\lambda_1 + \lambda_2}. \quad (4.2)$$

where  $S_T = 1.0$  corresponds to a spherical event and  $S_T = 0$  to a jet-like event. A schematic illustration is shown in Fig. 4.3.

Following [161], only events with a transverse sphericity of  $0.7 < S_T < 1.0$  are used in the analysis, to minimize the background associated to minijets, see Fig. 4.4. This selection is conjoined with using global tracks with  $|\eta| < 0.8$  and  $p_T > 0.5 \text{ GeV}/c$  and reduces the initial number of  $\sim 1 \times 10^9$  events to approximately its half. However, as it only reduces the contribution from minijets to the correlation function and not completely removes it, the topic is discussed again in Sec. 5.3.2.

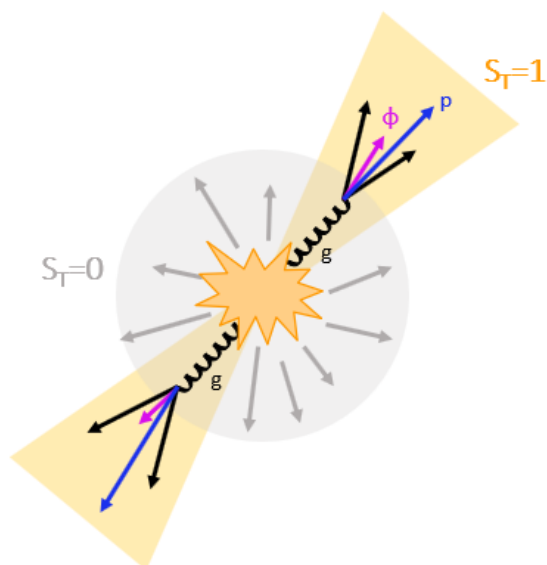


**Figure 4.3:** Visualization of the relation between minijets and transverse sphericity.

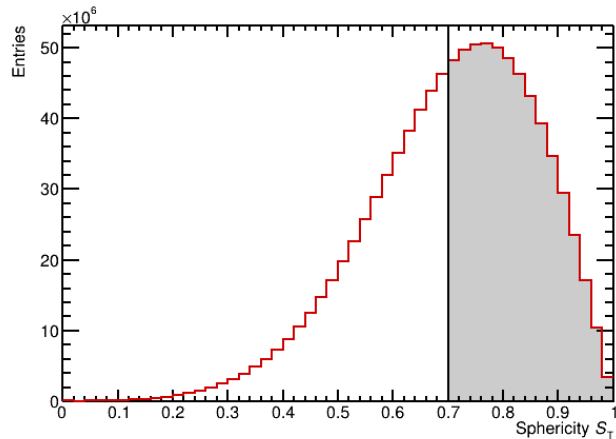


**Figure 4.4:** Sphericity distribution. The shaded area marks the remaining events after a cut of  $0.7 < S_T < 1.0$  is applied.

Selection criterion	Value
Trigger	kHighMultV0
Physics selection	default
Incomplete DAQ	check
z vertex	$ vtx_z  < 10$ cm
Contributors to track vertex	$N_{\text{contrib,track}} > 1$
Contributors to SPD vertex	$N_{\text{contrib,SPD}} > 0$
Distance between track and SPD vertex	$d_{\text{vtx,track-SPD}} < 0.5$ cm
SPD vertex z resolution	$\sigma_{\text{SPD},z} < 0.25$ cm
Pile-up rejection	AliEvent::IsPileUpFromSPD() AliEventUtils::IsSPDClusterVsTrackletBG()
Sphericity	$0.7 < S_T < 1.0$

**Table 4.1:** Event selection criteria.

## 4.2 Particle Selection

The identification of proton and  $\phi$  candidates, which are subsequently paired in order to obtain a correlation signal is conducted by applying several selection criteria on the reconstructed particle or particle-daughter tracks within a given event. The procedure for each species is explained in detail in the following.

### 4.2.1 Proton Candidates

The selection of protons and anti-protons follows [85, 164] and the criteria are summarized in Tab. 4.2. As the non-uniform acceptance in the ITS can cause biases, only particle tracks reconstructed within the TPC and constrained to the primary vertex are studied, without matching

them to ITS hits. The so obtained momentum resolution is comparable to the one of global tracks up to  $p_T \approx 10 \text{ GeV}/c$  [132].

Further, a limitation of the transverse momentum range of the proton candidates of  $0.5 < p_T < 4.05 \text{ GeV}/c$  is applied that results in the distribution shown in Fig. 4.5a. The low  $p_T$  cutoff is meant to reduce the number of protons originating from interactions of primary particles with the detector material, while the cutoff at high  $p_T$  is applied to increase the average purity of the reconstructed particle sample by eliminating the kinematic domain of moderate purity. In order to minimize unwanted effects related to the detector acceptance, the candidates are selected within  $|\eta| < 0.8$ .

Also, a selection regarding the TPC clusters is applied to ensure a good track quality and  $p_T$  resolution at large momenta, and to remove fake tracks from the sample. Therefore, tracks are required to be reconstructed from more than 80 clusters in the TPC and have crossed at least 70 out of the total 159 pad rows. The number of measured clusters depends on track reconstruction, threshold effects and noise in the electronics. Additionally, the ratio between the number of crossed rows and the number of clusters that can potentially be found has to be larger than 0.83. Candidates are rejected if the associated tracks share clusters with another one.

A strict selection of the distance of closest approach from the particle trajectory to the primary vertex in both the beam ( $DCA_z$ ) and transverse plane ( $DCA_{xy}$ ) is employed in order to increase the fraction of particles originating from the primary vertex of the collision.

The proton candidates are identified using the ALICE TPC and TOF detector. For momenta  $p_{\text{TPC}} < 0.75 \text{ GeV}/c$  only the PID selection provided by the TPC is used. As the separation power of the TPC decreases for larger momenta, see Fig. 3.5, the information of both detectors is combined for PID. This is characterized by  $n_{\sigma, \text{combined}} \equiv \sqrt{(n_{\sigma, \text{TPC}})^2 + (n_{\sigma, \text{TOF}})^2}$ , where  $n_{\sigma}$  is the number of standard deviations of the measured signal from the expected value at a given momentum, which depends on the detector resolution  $\sigma$ . In case of the TPC the expected signal is the specific energy loss of a particle derived from a parameterized Bethe-Bloch curve, whereas for the TOF it is the expected  $\beta$  of a particle with mass hypothesis  $M$  given by Eq. 3.4. The resulting distribution for the TPC  $n_{\sigma}$  is shown in Fig. 4.5b, which demonstrates the purity of the proton sample. Both  $p_T$  regions of the PID, where different detectors are involved, are clearly distinguishable from the plot.

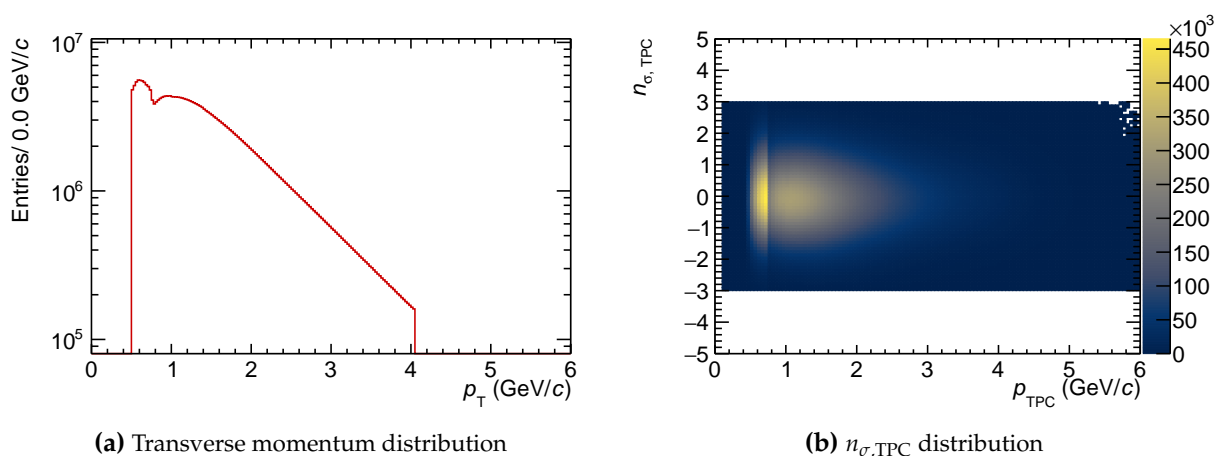


**Figure 4.5:** Transverse momentum and  $n_{\sigma, \text{TOF}}$  distribution of the proton candidates.

From this selection, a proton purity of 99.4% with a primary fraction of 82% is obtained [164] by analyzing events generated by PYTHIA 8 [156]. The purity is calculated by applying the same selection criteria as for data and checking if the identified particle really is a proton. The primary fraction of 82% is obtained by fitting MC templates to the experimental DCA distribution between the particle track and the primary interaction vertex. The remaining 18% of proton candidates are associated to interactions with the detector material and weakly decaying resonances that feed into protons. Using cross sections from PYTHIA 8 the feed-down fraction is found to consist of a 70% contribution from  $\Lambda$  and a 30% contribution from  $\Sigma^+$  hyperons.

**Table 4.2:** Proton selection criteria.

Selection criterion	Value
Filterbit	128 (TPC only tracks)
Pseudorapidity	$ \eta  < 0.8$
Transverse momentum	$0.5 < p_T < 4.05 \text{ GeV}/c$
TPC cluster	$n_{\text{TPC}} > 80$
Crossed TPC pad rows	$n_{\text{crossed}} > 70$ (out of 159)
Findable TPC clusters	$n_{\text{crossed}}/n_{\text{findable}} > 0.83$
Tracks with shared TPC clusters	rejected
Distance of closest approach $xy$	$ \text{DCA}_{xy}  < 0.1 \text{ cm}$
Distance of closest approach $z$	$ \text{DCA}_z  < 0.2 \text{ cm}$
Particle identification	$ n_{\sigma, \text{TPC}}  < 3$ for $p < 0.75 \text{ GeV}/c$
	$n_{\sigma, \text{combined}} < 3$ for $p > 0.75 \text{ GeV}/c$

## 4.2.2 $\phi$ Candidates

The charge-neutral  $\phi$  vector meson cannot be detected directly by ALICE. It is rather reconstructed from its decay products by employing the method of invariant mass [141]

$$M_\phi^2 c^4 = p_\phi^2 c^2 = \left( \sum_i \mathbf{p}_i c \right)^2 = \left( \sum_i E_i \right)^2 - \left( \sum_i \vec{p}_i c \right)^2, \quad (4.3)$$

where the sum runs over the products of one specific decay mode assuming a certain mass hypothesis.

The dominant channel, which is favoured by the OZI rule, is the strong decay to charged kaons  $\phi \rightarrow K^+ K^-$  with a branching ratio of  $\text{BR}_{\phi \rightarrow K^+ K^-} = (49.2 \pm 0.5)\%$  [5]. In this specific case of a two-body decay Eq. 4.3 can be written as

$$M_\phi^2 c^4 = m_{K^+}^2 c^4 + m_{K^-}^2 c^4 + 2(E_{K^+} E_{K^-} - |\vec{p}_{K^+}| |\vec{p}_{K^-}| c^2 \cos \theta), \quad (4.4)$$

where  $\theta$  denotes the angle between  $\vec{p}_{K^+}$  and  $\vec{p}_{K^-}$  and  $m_{K^\pm, \text{PDG}} = 493.68 \pm 0.02$  MeV [5] corresponds to the nominal kaon mass.

### 4.2.2.1 Kaon Selection

In the first step of the  $\phi$  meson reconstruction, kaon candidates are identified by employing the criteria summarized in Tab. 4.3. The  $p_T$ , TPC-cluster and  $\eta$  selection follows [165, 166].

As the lifetime of the  $\phi$  meson is very short and the detector resolution not good enough to resolve such small  $c\tau_\phi \sim 46$  fm, the kaon candidates are treated as primary particles in order to maximize the fraction originating from a  $\phi$  decay. Therefore, the selection is also oriented towards the proton selection 4.2.1. However, the DCA in both  $xy$  and  $z$  direction is increased with respect to the proton selection, as the values are optimized to enhance the  $\phi$  yield while retaining a reasonable purity of the sample.

For particle identification below  $p_{\text{TPC}} = 0.4 \text{ GeV } c^{-1}$  only the TPC is used, while at larger momenta its separation power to distinguish between kaons and other particles is not sufficient anymore. Here the PID information from TPC and TOF is combined. A relatively large PID interval of  $|n_\sigma| < 5$  is chosen, see Fig. 4.6b, in order to reconstruct as many  $\phi$  mesons as possible while their purity changes only slightly. This was studied by employing MB data, resulting in an increase of the  $\phi$  yield of  $\sim 13\%$  with respect to a more strict selection of  $|n_\sigma| < 3$ , also used for proton reconstruction, and a decrease of the purity of less than 1%. The separation between the two PID regions at  $p_{\text{TPC}} \approx 0.4 \text{ GeV } c^{-1}$  is visible in both the  $p_T$  (Fig. 4.6a) and the  $n_{\sigma, \text{TPC}}$  distributions (Fig. 4.6b). When further investigating the lower part of Fig. 4.6b at  $n_{\sigma, \text{TPC}} \sim -5$ , a contamination from electrons is visible around  $p_{\text{TPC}} \approx 0.4 \text{ GeV } c^{-1}$  in the left interval, where the kaon PID relies on the TPC only.

Following Sec. 4.2.1, the purity of the kaon sample is extracted from MC simulations, which are filtered through the ALICE detector and the reconstruction algorithm. Figure 4.7 shows the resulting  $K^+$  and  $K^-$  purities as a function of the transverse momentum  $p_T$ . Both are consistent with each other. For small transverse momenta, there is almost no contamination due to particle misidentification, while for large  $p_T$  the kaon purity decreases to  $\sim 75\%$ . The dip at  $p_T \approx 0.4 \text{ GeV } c$

is related to a contamination of the particle sample with electrons, as already mentioned in the previous paragraph.

#### 4.2.2.2 $\phi$ Resonance

The  $\phi$  candidates are reconstructed using the method of invariant mass (Eq. 4.4), by combining all selected  $K^+$  and  $K^-$  candidates in one single event. The resonance peak in the invariant mass distribution of the kaon pairs is then fitted with a Voigt function [166], which is a convolution of a Gaussian that accounts for the detector resolution and a relativistic Breit-Wigner peak that describes the natural line width

$$\frac{dN}{dm_{K^+K^-}} = \frac{A\Gamma}{(2\pi)^{3/2}\sigma} \int_{-\infty}^{+\infty} \exp\left[-\frac{(m_{K^+K^-} - m')^2}{2\sigma^2}\right] \frac{1}{(m' - M_\phi)^2 + \Gamma^2/4} dm', \quad (4.5)$$

where  $A$  is a scaling factor,  $\sigma$  the detector resolution,  $\Gamma$  the decay width of the resonance, fixed from the PDG value  $\Gamma = 4.25$  MeV [5], and  $M_\phi$  the mass of the  $\phi$  resonance. The background is described by a quadratic polynomial. The  $p_T$ -integrated spectrum is shown in Fig. 4.8 and the mass extracted from the fit  $M_\phi = 1019.550 \pm 0.002$  MeV/ $c^2$  is consistent with the PDG mass of  $M_{\phi,PDG} = (1019.461 \pm 0.016)$  MeV [5] within the detector resolution  $\sigma = 1.44$  MeV/ $c^2$ .

A cut on the invariant mass spectra of  $M_{\phi,PDG} \pm 8$  MeV/ $c^2$  is applied, which determines the intervals where the particle candidates are identified. There are a total of  $5.84 \times 10^6$   $\phi$  mesons reconstructed for HM data with an integrated purity of 66 %, which hints at the presence of a non-negligible contribution to the measured correlation signal arising from the combinatorial  $K^+K^-$  background.

Figure 4.9 displays the invariant mass spectra for eight different  $p_T$  intervals of width  $\Delta p_T = 0.5$  GeV  $c^{-1}$ . From the fit results it is possible to derive the purity as function of the transverse momentum, shown in Fig. 4.10a. A strong  $p_T$  dependence is observed and the purity decreases to almost its half at the minimum  $p_T$  with respect to the maximum.

**Table 4.3:** Kaon selection criteria.

Selection criterion	Value
Filterbit	128 (TPC only tracks)
Pseudorapidity	$ \eta  < 0.8$
Transverse momentum	$p_T > 0.15$ GeV/ $c$
TPC cluster	$n_{TPC} > 80$
Crossed TPC pad rows	$n_{crossed} > 70$ (out of 159)
Findable TPC clusters	$n_{crossed}/n_{findable} > 0.80$
Tracks with shared TPC clusters	rejected
Distance of closest approach $xy$	$ DCA_{xy}  < 0.8$ cm
Distance of closest approach $z$	$ DCA_z  < 0.4$ cm
Particle identification	$ n_{\sigma,TPC}  < 5$ for $p < 0.4$ GeV/ $c$
	$n_{\sigma,combined} < 5$ for $p > 0.4$ GeV/ $c$

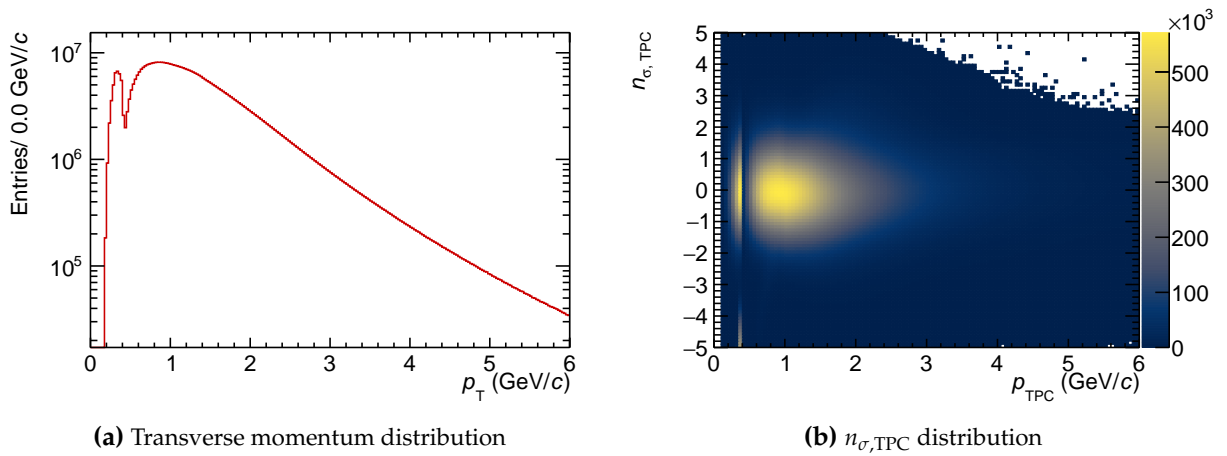


**Figure 4.6:** Transverse momentum and  $n_{\sigma,TPC}$  distribution of  $K^+$  candidates.

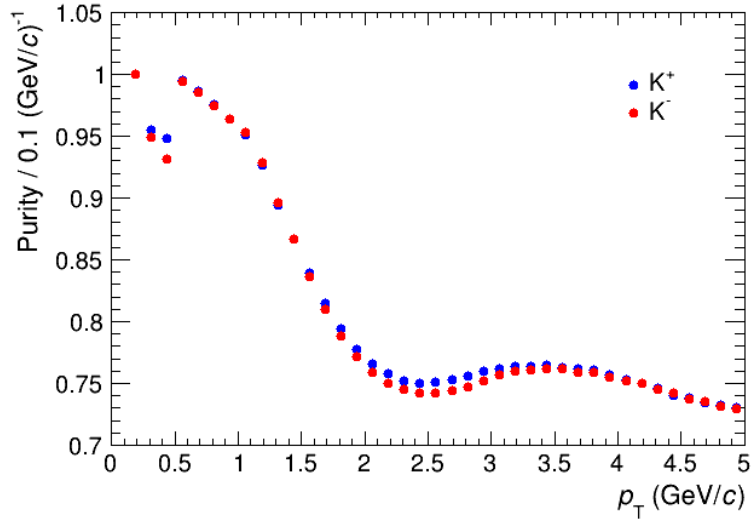


**Figure 4.7:** Purity of both  $K^+$  and  $K^-$  as function of the transverse momentum.

In order to check for varying pile-up conditions of the pp Run 2 data-taking period, the purity of the reconstructed  $\phi$  mesons is investigated for each period separately, see Fig. 4.10b. The ones with a low number of events and entries in the invariant mass spectra are left empty, as it is not possible to properly fit the corresponding distribution and extract a confident value. As can be seen, the purity does not vary significantly, which shows that the background is not modified by out-of-bunch pile-up. This implication can be explained in the following. The out-of-bunch pile-up contribution is sensitive to the interaction rate. Therefore, LHC periods with a larger interaction rate, hence more particles and more possible contaminations, would suffer from a larger background, resulting in a lower purity.

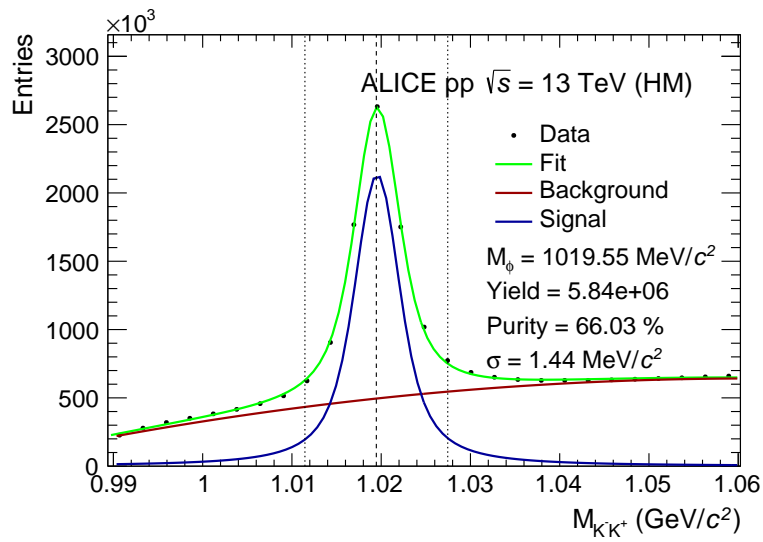


**Figure 4.8:**  $K^+K^-$  invariant mass distribution for high multiplicity events with sphericity cuts  $0.7 < S_T < 1.0$ . The dashed lines represent the  $M_\phi \pm 8 \text{ MeV}/c^2$  selection for the femtoscopic analysis.

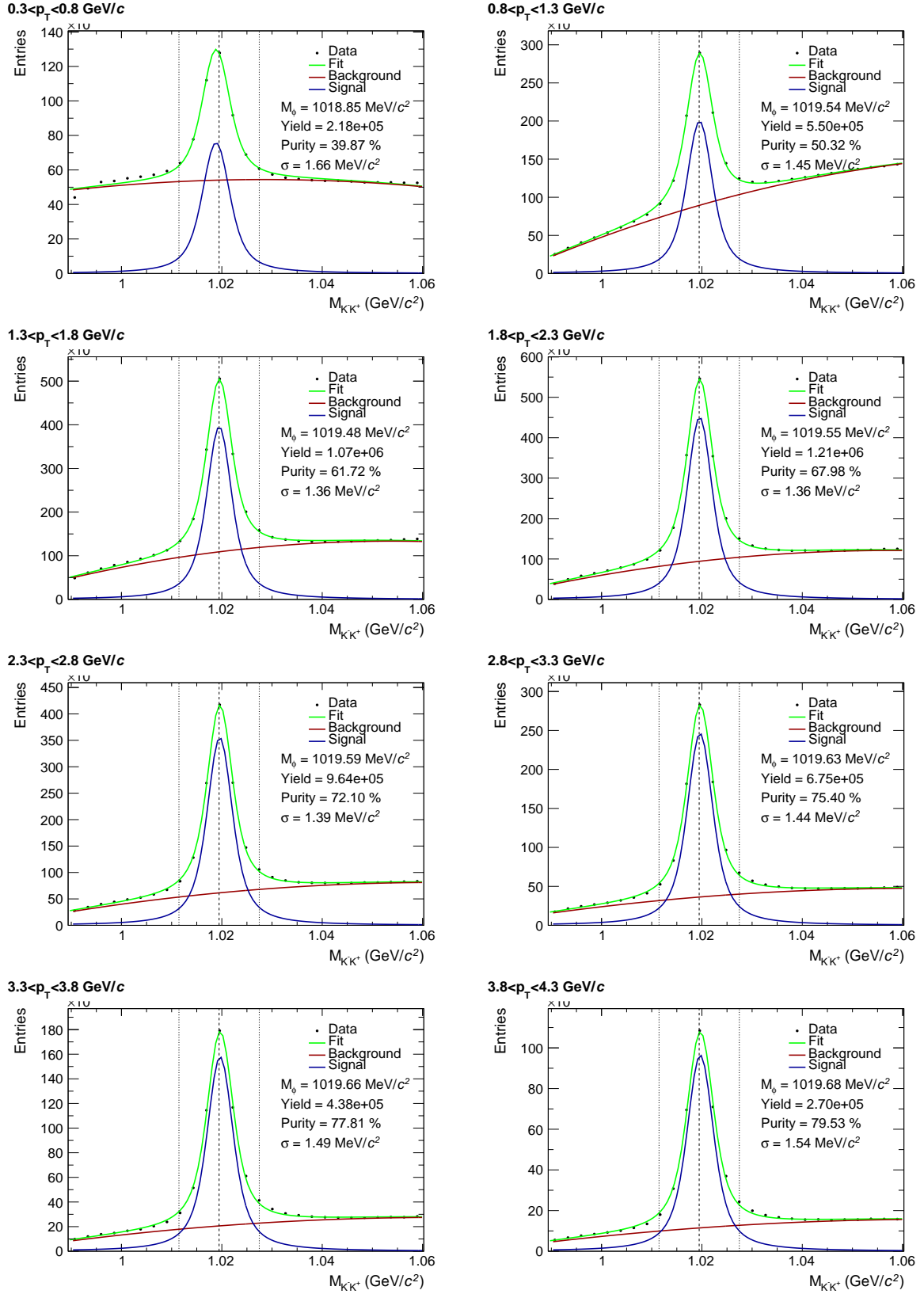
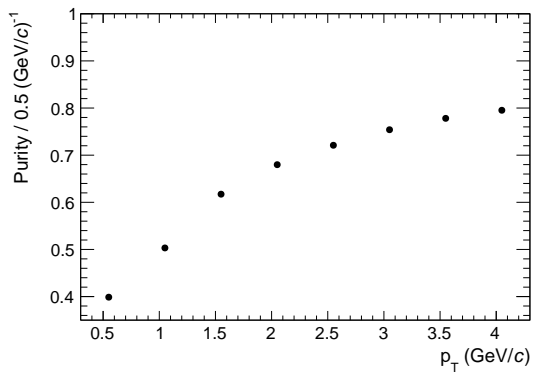
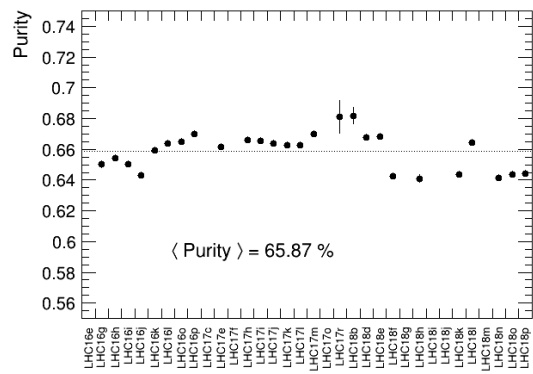


Figure 4.9:  $K^+K^-$  invariant mass spectra in  $p_T$  slices of width  $0.5 \text{ GeV}/c$ .



(a)  $\phi$  purity as function of  $p_T$ .



(b) Purity of the  $\phi$  candidates per LHC period.

**Figure 4.10:** Purity of the  $\phi$  candidates as function of  $p_T$ , which is integrated over all LHC periods on the left and on the right the  $p_T$  integrated purity as function of the different LHC periods.

### 4.3 Particle pairing

As particles within the same event are paired in order to obtain  $N_{\text{same}}$ , a  $\phi$  candidate is rejected, if one of its daughters uses the same track as a reconstructed primary proton in order to avoid auto-correlations, which arise from pairing particles that are related kinematically.

Table 4.4 summarizes the number of particle pairs, reconstructed in the analysis as well as the  $\phi$  yield. In comparison, the total number of available events is listed. Of special interest is the number of pairs within  $k^* < 200 \text{ MeV}/c$ , as it corresponds to the relative momentum region where the correlation function is sensitive to the strong FSI.

**Table 4.4:** Particle and pair count

total events without sphericity cuts	$971 \times 10^6$
total events $0.7 < S_T < 1.0$	$541 \times 10^6$
reconstructed $\phi$ yield	$5.84 \times 10^6$
Total $\phi$ -p pairs	$5.31 \times 10^6$
Total $\phi$ - $\bar{p}$ pairs	$4.63 \times 10^6$
$\phi$ -p with $k^* < 200 \text{ MeV}/c$	$4.17 \times 10^4$
$\phi$ - $\bar{p}$ with $k^* < 200 \text{ MeV}/c$	$3.61 \times 10^4$



## 5 The Correlation Function

The experimental  $p$ - $\phi$  correlation function is obtained from Eq. 2.6, where the normalization constant  $\mathcal{N}$  assures  $C_{\text{exp}}(k^*) = 1$  in the relative momentum interval  $0.8 < k^* < 1.0 \text{ GeV}/c$ . The selected window is rather wide to account for a large bin width of  $40 \text{ MeV}/c$ . As the  $p$ - $\phi$  correlation function is subject to various background contributions, which lead to the formation of structures in the intermediate  $k^*$  range, the normalization interval is positioned at large  $k^*$ , where all contributions are expected to be flat. To avoid acceptance effects of the detector system, the mixed event sample  $N_{\text{mixed}}$  is constructed only from particle pairs stemming from events with similar multiplicity and  $z$  position of the primary vertex [98].

Figure 5.1 shows the experimental correlation function of  $\bar{p}$ - $\phi$  and  $p$ - $\phi$  respectively. As the ratio between them is consistent with unity, both are combined as  $p$ - $\phi \oplus \bar{p}$ - $\phi$  to yield a higher pair yield. Therefore,  $p$ - $\phi$  will refer to  $p$ - $\phi \oplus \bar{p}$ - $\phi$  in the following. The resulting correlation function is shown in Fig. 5.2. For small relative momenta  $k^*$ , where the strong FSI influences the shape of the correlation function, it takes values larger than one, indicating an attractive interaction between the two particles. However, in the intermediate  $k^*$  region an enhancement is visible, suggesting the presence of background contributions to the measured signal. Therefore, any conclusion on the genuine  $p$ - $\phi$  interaction demands a treatment of all additional contributions. The rise at large  $k^*$  is attributed to energy-momentum conservation effects and is known from previous femtoscopic analyses [164].

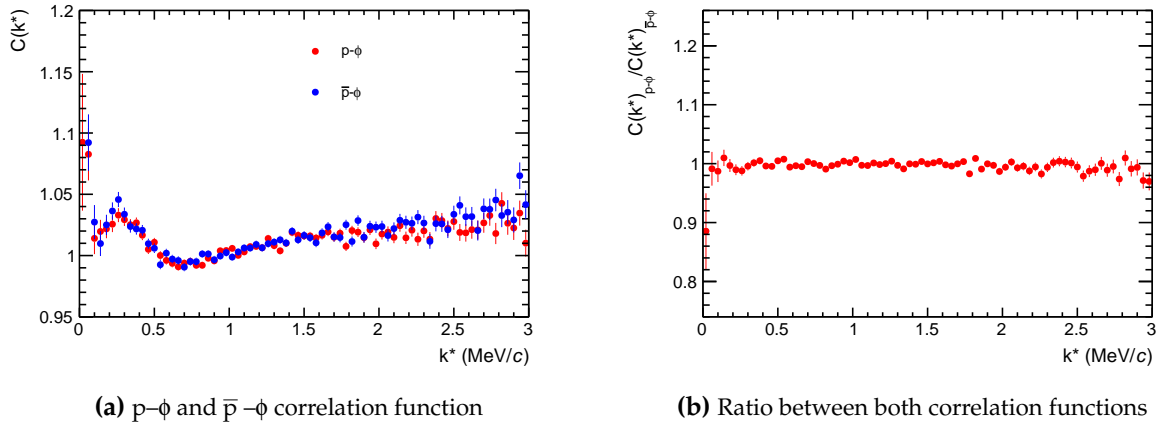


**Figure 5.1:** Comparison of the  $p$ - $\phi$  and  $\bar{p}$ - $\phi$  correlation functions.

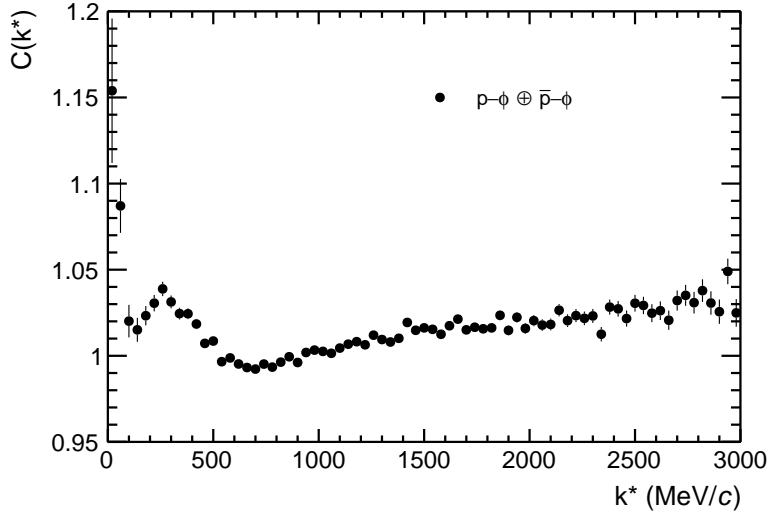
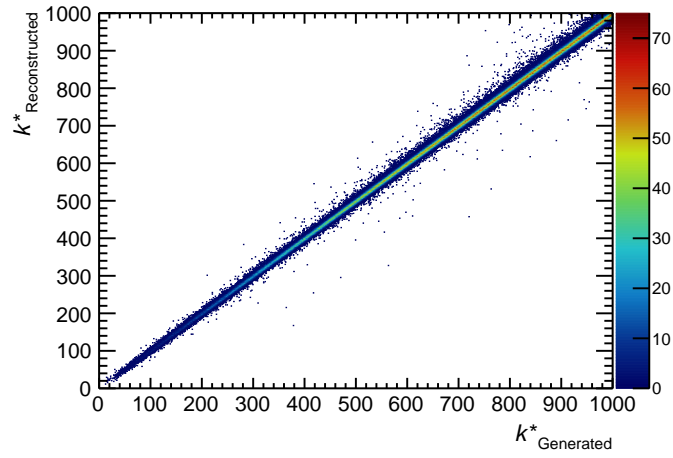


**Figure 5.2:** The combined  $p\text{-}\phi \oplus \bar{p}\text{-}\phi$  correlation function, normalized within  $0.8 < k^* < 1.0 \text{ GeV}/c$ .

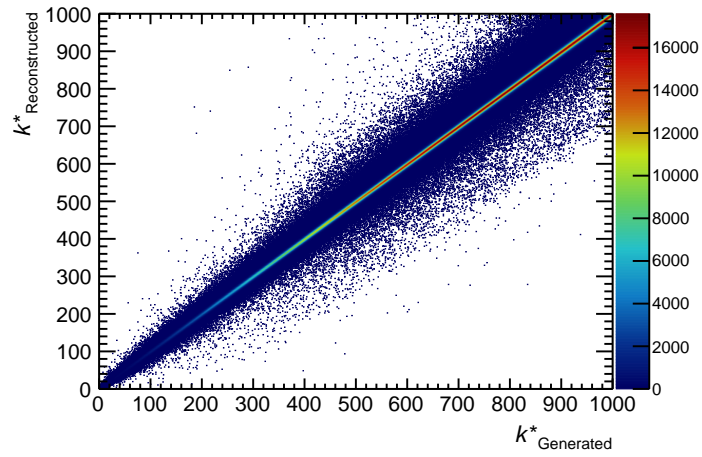
## 5.1 Detector Effects

The reconstructed particle tracks have a finite momentum resolution, which affects the measurement of the relative momentum  $k^*$ , hence, ultimately the correlation function. This can be studied by means of a MC-generated momentum resolution matrix, shown in Fig. 5.3b and discussed in more detail in Sec. 5.1.1. The matrix relates the generated relative momentum of the  $p\text{-}\phi$  pair ( $k_{\text{Generated}}^*$ ), which corresponds to the one obtained from the true single-particle momenta at the collision vertex, to the reconstructed relative momentum ( $k_{\text{Reconstructed}}^*$ ). Due to the scarce amount of entries in the matrix obtained from particles in the same event (SE), the one from mixed events (ME) is used instead. This is valid as the ratio between the two is  $\sim 1$  when normalizing the ME matrix to the number of entries in the one from SE to ensure an adequate comparison, shown in Fig. 5.3c.

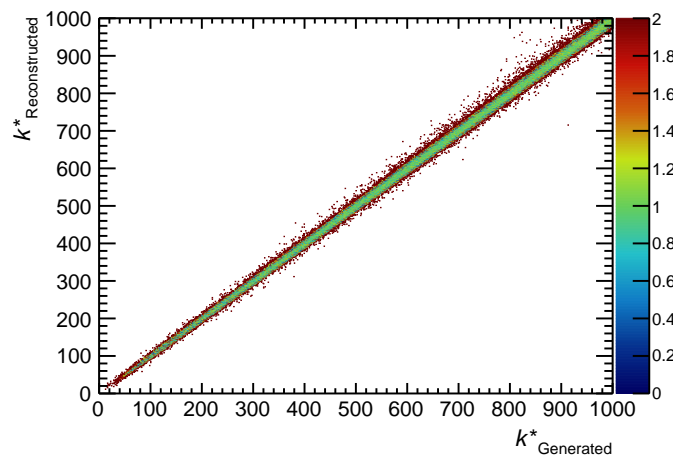
Other effects that can influence the correlation function are track merging (two tracks are reconstructed as one) and track splitting (one track is reconstructed as two), which can generate artificial correlations by modifying the particle pair yield at a given  $k^*$ . To examine whether or not they play a role in the  $p\text{-}\phi$  correlation, the two-dimensional  $\Delta\eta\Delta\phi^*$  distributions of SE and ME are investigated at different radii of the TPC, where the azimuthal angle  $\phi^*$  is corrected for the trivial modification of  $\phi$  in the magnetic field. Especially at low relative angles, either track merging or splitting should induce a visible signal. The distributions are obtained from MC simulated data, where no strong FSI between particles is expected. Figure 5.4 shows the ratios between the SE and ME distributions at different TPC-radii, in order to account for phase-space effects. It can be seen that the experimental data is indeed not affected by track splitting and merging, as the plots are flat and no bias is visible. Therefore, no further rejection on close particle tracks is applied. However, even if such effects are present, they would be smeared over the whole  $k^*$  and  $\phi^*$  range.



(a) Momentum resolution matrix obtained from SE particles



(b) Momentum resolution matrix obtained from ME particles.



(c) Ratio between the SE and normalized ME smearing matrices

**Figure 5.3:** Momentum resolution matrices, relating the MC generated relative momentum to the reconstructed one for both SE and ME particle pairs as well as the ratio between them.

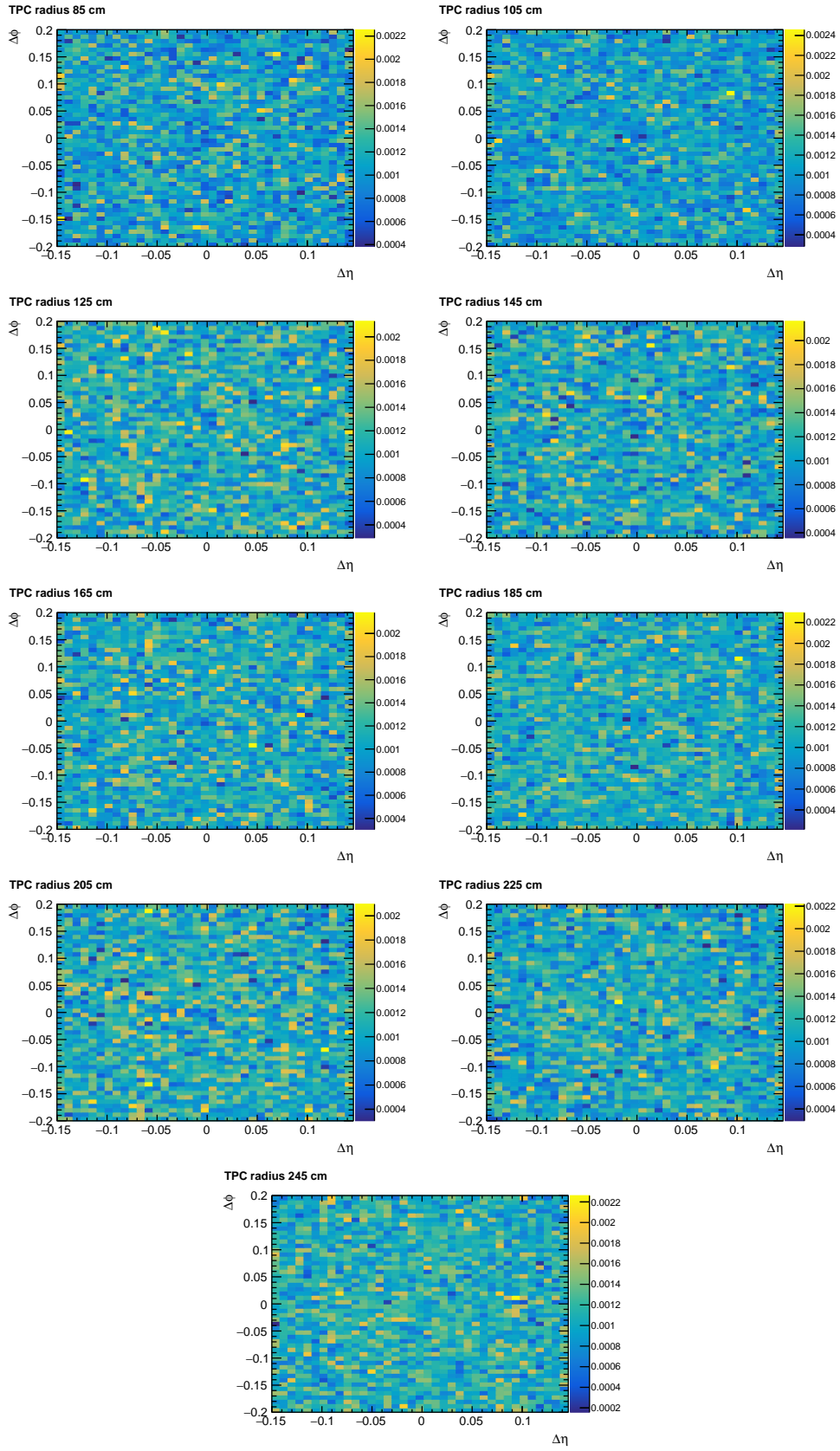


**Figure 5.4:**  $\Delta\eta\Delta\phi^*$  distribution for  $p\text{-}K^+$  pairs from the same event, normalized to mixed event pairs, for different TPC-radii. At low angles, where track splitting and merging would be visible, no signs for an angular dependence can be seen.

### 5.1.1 Unfolding of the correlation function

As already mentioned before, the limited momentum resolution of the reconstructed tracks induces modifications to the measured relative momentum, hence, to the SE and ME distributions from which the correlation function is obtained.

The measured distribution  $D(k_{\text{Reconstructed},i}^*)$  of either SE or ME, is given as

$$D(k_{\text{Reconstructed},i}^*) = \sum_j M(k_{\text{Reconstructed},i}^*, k_{\text{Generated},j}^*) \cdot D(k_{\text{Generated},j}^*), \quad (5.1)$$

where  $M(k_{\text{Reconstructed},i}^*, k_{\text{Generated},j}^*)$  is the discrete momentum resolution matrix, in this context also called response matrix, shown in Fig. 5.3b. To correct for momentum resolution effects the SE and ME distributions have to be transformed to the generated distributions by inverting Eq. 5.1. However, this is not straight forward, as the matrix inversion process is ill-posed and typically lacks an analytic solution. Therefore, the so-called Bayesian unfolding method [167] is used within the RooUnfold framework [168, 169]. It starts with a guess of the true distribution and is regulated by choosing a specific number of iterations until a stable result is obtained. In this analysis 5 iterations are chosen as default. For a smaller number, the relative uncertainties of the bins fluctuate a lot, while for a much larger amount of iterations the uncertainties themselves increase drastically and become unphysical. Furthermore, the developers of RooUnfold suggest a small integer of iterations and claim that reasonable results are obtained even without fine-tuning the parameters [169].

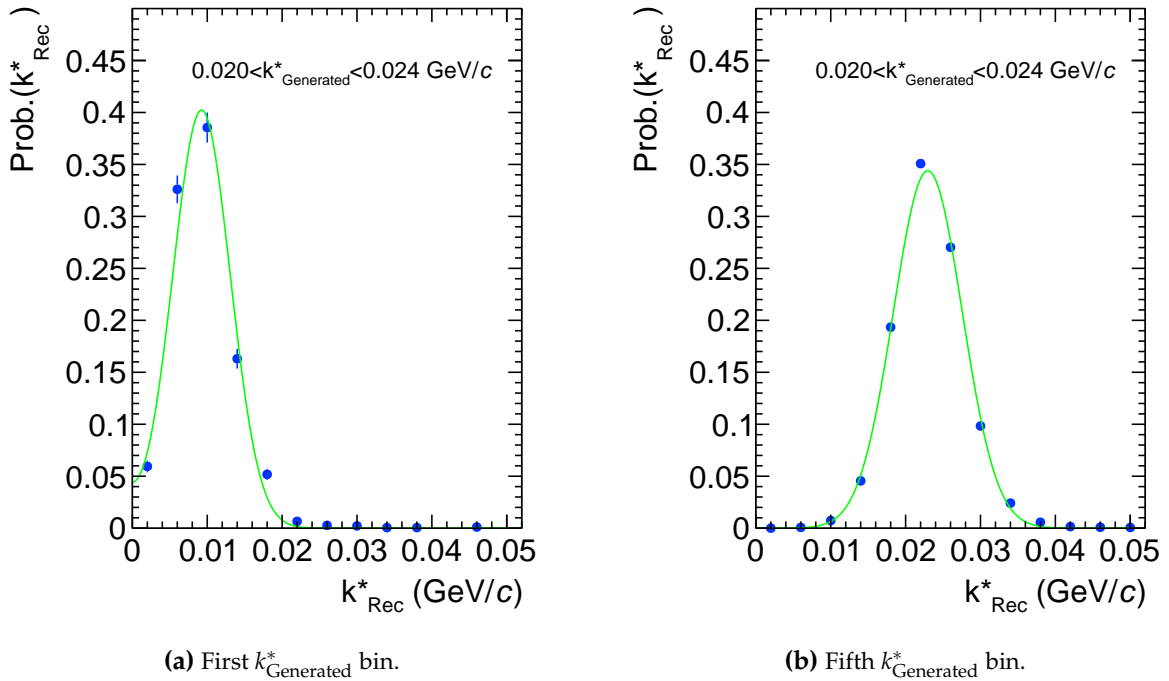
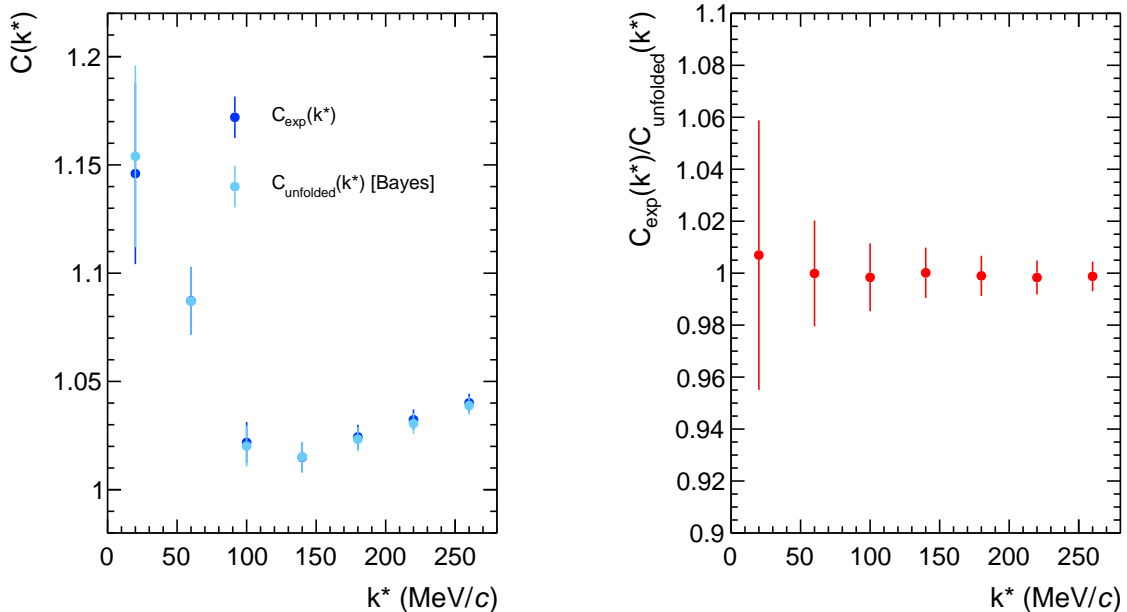


**Figure 5.5:** Projections of the momentum resolution matrix to the  $k_{\text{Reconstructed}}^*$  axis for different low momentum intervals in  $k_{\text{Generated}}^*$ . The fit with a folded normal distribution is plotted as well.

In order to account for systematic variations, which are relevant for the calculation of the uncertainties in Sec. 5.7, the response matrix is not used directly. It is rather projected to the  $k_{\text{Reconstructed}}^*$  axis in  $0.004 \text{ GeV}/c$ -wide intervals of  $k_{\text{Generated}}^*$ . Each of those slices is then normalized by the number of entries and fitted with a folded normal distribution, which is the sum of two Gaussian functions of equal width  $\sigma$  and equal but opposite signed mean  $\mu$ . The choice of the fit function is motivated by the fact that the relative momentum  $k^*$  is defined as the absolute value of the difference between both particle momentum vectors. Hence, negative differences are projected to the positive axis, as can be seen in Fig. 5.5a, where the first  $k_{\text{Generated}}^*$  interval of  $k_{\text{Generated}}^* < 0.004 \text{ GeV}/c$  is depicted. The resulting distribution, especially at low  $k^*$ , cannot be described by a simple Gaussian. Figure 5.5b shows the interval  $0.020 \text{ GeV}/c < k_{\text{Generated}}^* < 0.024 \text{ GeV}/c$  as comparison. The uncertainties decrease for increasing  $k_{\text{Generated}}^*$  as the number of entries in the momentum resolution matrix increases. This procedure results in a new matrix from which it is possible to obtain systematic variations, by altering the folded normal distribution in each  $k_{\text{Generated}}^*$  interval within the maximum uncertainties of the parameters. Regarding the mean of the folded normal distribution, the relative error with respect to the parameter value is  $\sim 3\%$  at max. For the width, a maximum of  $6\%$  is found.

From the unfolded SE and ME distributions, which are both obtained from the Bayesian method with 5 iterations and the default matrix, a corrected version of the correlation function can be deduced, which accounts for the finite momentum resolution of the ALICE detector. For  $p$ - $\phi$  it is shown in Fig. 5.6, together with the uncorrected version. Notably, the effect is most pronounced at low  $k^*$  and results in a maximum variation of  $0.7\%$  with respect to the measured signal. In the following, only unfolded correlation functions will be used.



(a)  $p$ - $\phi$  correlation function after unfolding with the Bayesian method (light blue) and before (dark blue). (b) The ratio between both is consistent with unity, hinting a small modification due to the detector response.

**Figure 5.6:** Influence of the detector response on the measured correlation function.

## 5.2 Lambda Parameters

There are two mechanisms, which can modify the experimentally measured correlation function. The misidentification of one or both particles of interest leads to a completely different particle pair that contributes to the correlation signal, whereas feed-down particles conserve the particle species of the reconstructed pair itself but induce correlations from the strong interaction among the primary particles before they decay into the particles of interest. Both are considered when decomposing the total measured correlation function as

$$C(k^*) = \lambda_{p-\phi} \cdot C_{p-\phi}(k^*) + \sum_{ij} \lambda_{ij} \cdot C_{ij}(k^*), \quad (5.2)$$

where the indices  $i$  and  $j$  denote all possible particle combinations contributing to the  $p-\phi$  correlation function, including impurities and feed-down. Each contribution is scaled by a so-called  $\lambda$ -parameter, calculated from the purity  $P_i$  of the specific particles and the fraction  $f_i$  of primaries or secondaries from feed-down of a specific long-lived decay channel as

$$\lambda_{ij} = \lambda_i \cdot \lambda_j = P_i f_i \cdot P_j f_j. \quad (5.3)$$

Details on the mathematical formalism can be found in [170]. In the case of  $p-\phi$  the following contributions have to be taken into account:

$$\{p-\phi\} = p-\phi + p_{\Lambda}-\phi + p_{\Sigma^+}-\phi + \tilde{p}-\phi + p-\tilde{\phi} + p_{\Lambda}-\tilde{\phi} + p_{\Sigma^+}-\tilde{\phi} + \tilde{p}-\tilde{\phi}, \quad (5.4)$$

where  $\tilde{X}$  refers to misidentified particles of species  $X$ . In particular,  $\tilde{\phi}$  refers to combinatorial combinations of uncorrelated  $K^+K^-$  pairs.

The  $\phi$  candidates are assumed to be only primary particles, as no relevant resonances contributing to the feed-down fraction are found [5]. As the  $\phi$  purity exhibits a pronounced  $p_T$  dependency, it is not sufficient to use the  $p_T$  integrated value of 66%. The purity is rather evaluated for those candidates contributing to the signal from strong FSI, hence entering the correlation function at small  $k^*$  in form of  $p-\phi$  pairs with similar single-particle momenta. Considering that the

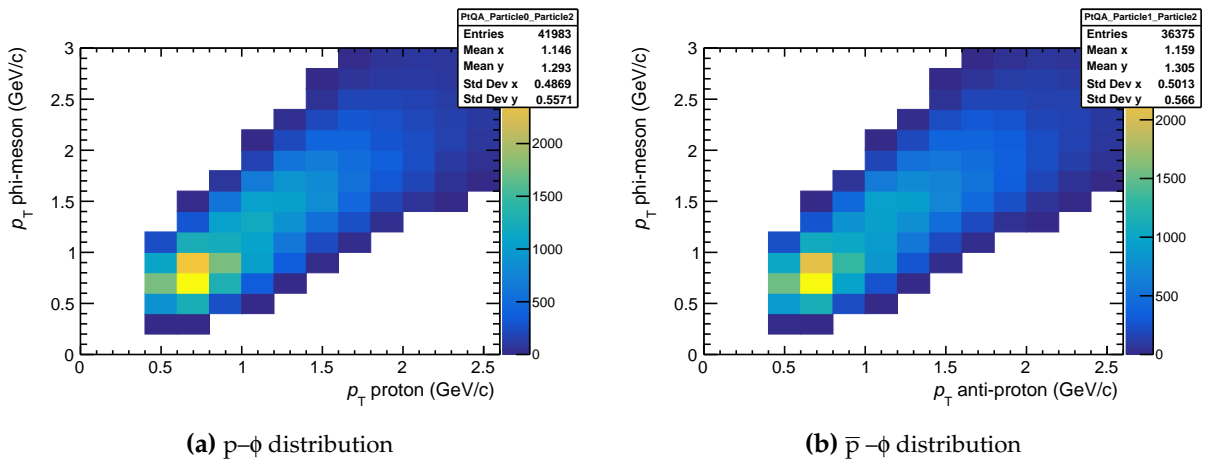


**Figure 5.7:** Transverse momentum distribution of the particle pairs of interest at small relative momenta  $k^* < 200$  MeV/c.

transverse momentum distributions of the reconstructed proton and  $\phi$  meson candidates tend to peak at very low values, particles forming pairs with small relative momentum, tend to have a small  $p_T$  as well. Indeed, as can be seen in Fig. 5.7, the average transverse momentum of the  $\phi$  candidates from  $p$ - $\phi$  pairs within the femtoscopic range of  $k^* < 200$  MeV/c is  $\langle p_{T,p-\phi} \rangle = 1.3$  GeV/c. When comparing it to the parameterization of the  $p_T$ -dependent purity shown in Fig. 5.8, a purity of only  $\sim 57\%$  can be derived, which is used in the following for the calculation of the  $\lambda$ -parameters.

As cross-check, whether or not it is adequate to take the value obtained from the average transverse momentum approach, the purity is also evaluated in terms of  $k^*$ , see Fig. 5.9. Indeed, the resulting weighted mean for small relative momenta of  $k^* < 200$  MeV/c, where the relative uncertainty of the data is considered, is found to be  $(56.6 \pm 2.7)\%$ . This is consistent with the previous result within the uncertainties.

For protons, on the other hand, the purity obtained from MC-generated data does not depend much on the transverse momentum and remains rather constant for  $p_T < 2$  GeV [85, 164]. Therefore, the  $p_T$  integrated value of 99.4% is used in the following. The primary fraction is 82% and the feed-down fraction arising from the decay of  $\Lambda$  hyperons is 12.6% [85, 164]. The remaining 5.4% is attributed to  $\Sigma^+$  decays.

The resulting  $\lambda$ -parameters obtained from Eq. 5.3, which are used to scale of the individual contributions, are summarized in Tab. 5.1.

**Table 5.1:** Weight parameters of the individual components of the  $p$ - $\phi$  correlation function.

Pair	$\lambda$ (%)	
$p$ - $\phi$	46.33	} $\lambda_{p-\phi}$
$p_\Lambda$ - $\phi$	7.10	
$p_{\Sigma^+}$ - $\phi$	2.93	} $\lambda_{\text{flat}}$
$\tilde{p}$ - $\phi$	0.32	
$p$ - $\tilde{\phi}$	35.40	} $\lambda_{p\text{KK}}$
$p_\Lambda$ - $\tilde{\phi}$	5.43	
$p_{\Sigma^+}$ - $\tilde{\phi}$	2.24	
$\tilde{p}$ - $\tilde{\phi}$	0.25	

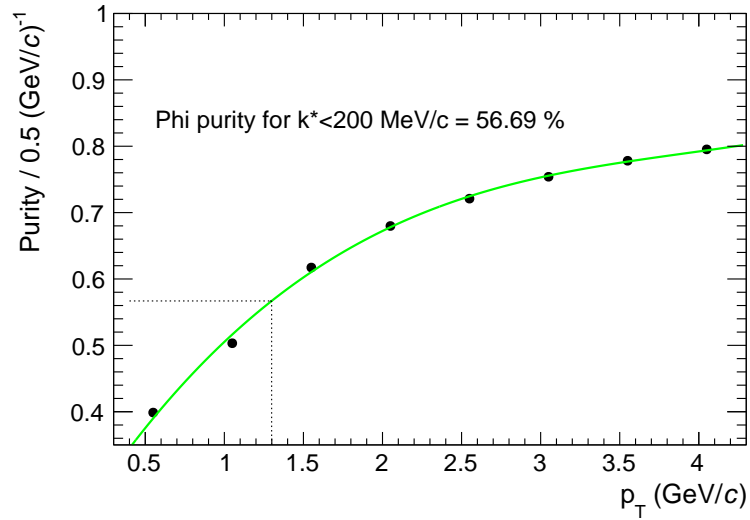


**Figure 5.8:**  $\phi$  meson purity as a function of the transverse momentum, obtained from the reconstruction procedure explained in Sec. 4.2.2.2. The data is fitted with a polynomial of 5<sup>th</sup> order, from which a purity of 56.69% is obtained for  $p_T = 1.3$  GeV/c. The  $p_T$  value corresponds to the average transverse momentum of the  $\phi$  mesons in p- $\phi$  particle pairs in the femtoscopic region with low relative momenta  $k^* < 200$  MeV/c.

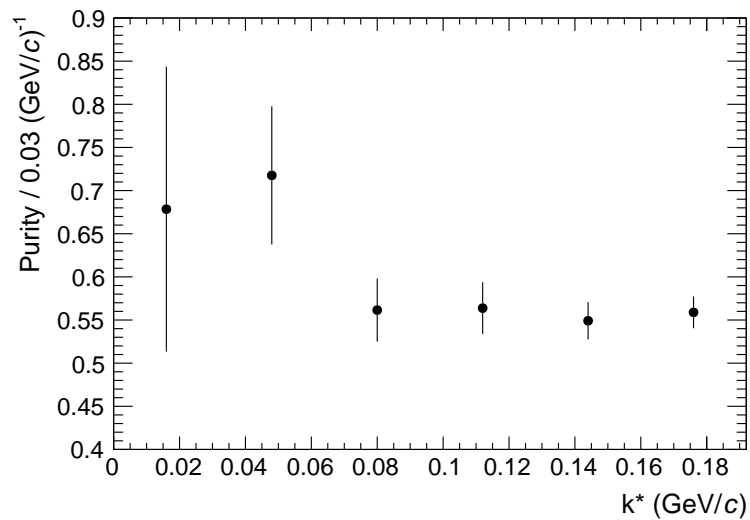


**Figure 5.9:** Purity of the  $\phi$  mesons as a function of the relative momentum. The weighted mean for  $k^* < 200$  MeV/c is  $(56.6 \pm 2.7)\%$ , which is consistent with the results from the  $p_T$  calculations.

## 5.3 Modeling of the measured Correlation Function

This section discusses the various contributions to the measured p- $\phi$  correlation function, which have been introduced in Sec. 5.2 and combined to three major ones in the following.

The measured correlation signal consists of 43.3% combinatorial  $K^+K^-$  background, which contains misidentified  $\phi$  mesons interacting with proton candidates.

Secondary and misidentified protons interacting with actual  $\phi$  mesons are combined to a 10.4% contribution to the correlation function. As the underlying interaction is not precisely known, the corresponding signal is assumed to be flat. This is supported by the fact, that the effect of the contribution related to secondary protons on the correlation function is small, as it is subject to a transformation  $k_{\text{Parent}}^* \rightarrow k_{\text{Measured}}^*$ , which smears it and results in a correlation signal close to unity. Additionally, as misidentified protons interacting with the  $\phi$  meson are scaled by a  $\lambda$ -parameter of only  $\sim 0.5\%$ . The resulting signal is also negligible.

Finally, the remaining 46.3%, which contribute to the correlation function, are attributed to the actual genuine p- $\phi$  interaction.

Accordingly, the measured correlation function is composed as

$$C_{\text{exp}}(k^*) = \mathcal{M} \cdot C_{\text{bkg}}(k^*) \cdot [\lambda_{\text{p-}\phi} \cdot C_{\text{p-}\phi}(k^*) + \lambda_{\text{flat}} \cdot C_{\text{flat}}(k^*)] + \lambda_{\text{pKK}} \cdot C_{\text{pKK}}(k^*), \quad (5.5)$$

where  $\mathcal{M}$  is a normalization constant and  $C_{\text{bkg}}(k^*)$  is the non-femtoscopic background.  $C_{\text{p-}\phi}(k^*)$  describes the genuine p- $\phi$  correlation function,  $C_{\text{flat}}(k^*)$  the flat contribution from feed-down as well as fake proton candidates and  $C_{\text{pKK}}(k^*)$  arises from combinatorial  $K^+K^-$  background, related to the finite purity of reconstructed  $\phi$  candidates. As the latter is directly obtained from experimental data, in contrast to the flat contribution  $C_{\text{flat}}(k^*)$  or  $C_{\text{p-}\phi}(k^*)$ , is already includes the non-femtoscopic background, which is assumed to consists of two contributions

$$C_{\text{bkg}}(k^*) = a + b \cdot (k^*)^2 + C_{\text{MJ,p-}\phi}(k^*), \quad (5.6)$$

where  $C_{\text{MJ,p-}\phi}(k^*)$  describes the minijet background of p- $\phi$  fixed from parameterizing results from PYTHIA 8 (MC truth) with a polynomial of fifth-order. More details can be found in Sec. 5.3.2. A quadratic polynomial is included as baseline to account for energy-momentum conservation effects, which result in a rise of the correlation function at large  $k^*$ . Such long-ranged structures are not properly reproduced by PYTHIA 8 [171]. The baseline is restricted to a vanishing derivative at  $k^* = 0$  MeV/c, which results in the coefficient of the linear term being zero.

### 5.3.1 Residual Correlations

The purity of the reconstructed  $\phi$  mesons is around 57% at low  $k^*$  where the correlation measurement is sensitive to the strong FSI interaction. The kaon purity on the other hand is very high in this region. Therefore, a significant amount of combinatorial background of  $K^+K^-$  is present, consisting of mainly two- but possibly to a certain amount also three-body interactions between proton,  $K^+$  and  $K^-$ . Figure 5.10 illustrates the genuine p- $\phi$  interaction in comparison to the one arising from the residual background of a proton interacting with a fake  $\phi$ .

The two-body interaction among p- $K^+$  and p- $K^-$  is measured by the ALICE Collaboration [161] with high precision. The corresponding measured correlation functions, depicted in Fig. 5.11, show a clear deviation from unity at small  $k^*$ , which arises from both Coulomb and strong FSI.

Therefore, a non-vanishing interaction among the triplet is expected, leading to a correlation signal scaled by  $\lambda_{pKK} = 43.3\%$  and referred to in the following as the combinatorial  $p\text{--}(K^+K^-)$  background.

This contribution can be studied by investigating sidebands, which correspond to intervals to the left and right of the  $\phi$  resonance in the  $K^+K^-$  invariant mass distribution. An interval-width of  $16 \text{ MeV}/c^2$  is selected, which is the same as the one used for  $\phi$  meson identification, in order to minimize kinematic deformations of the correlation function related to the width of the interval. The small mass difference between the  $\phi$  meson and its decay products, the two oppositely charged kaons, limits the possibilities to position the left sideband interval. Especially trying to avoid threshold effects from moving it too far away from the resonance, while also aiming to a similar pair count in both left and right sideband, results in even more restrictions. Therefore, the left sideband is defined within  $0.995 - 1.011 \text{ GeV}/c^2$  and the right within  $1.028 - 1.044 \text{ GeV}/c^2$ , see Fig. 5.12a. Both lie very close to the  $\phi$  resonance peak.

The correlation functions, which are used to obtain a description of the combinatorial  $p\text{--}(K^+K^-)$  background, are then obtained from pairing the candidates in the sideband intervals with protons and antiprotons. For both sidebands, the ratio between the  $p\text{--}(K^+K^-)$  and  $\bar{p}\text{--}(K^+K^-)$  correlation function is consistent with unity within the uncertainties, as shown in Fig. 5.13. Therefore, they are combined to increase the statistics. The resulting correlation functions are depicted in Fig. 5.12b. Notably, the left (green) and right (blue) sideband correlation functions deviate slightly from each other at relative momenta  $k^* \lesssim 500 \text{ GeV}/c$  due to different kinematics of the selected invariant mass window. To obtain a description of the combinatorial  $p\text{--}(K^+K^-)$  background, they are summed with a specific weight that corresponds to the relative amount of misidentified  $\phi$  particles on each half of the  $\phi$  resonance in the invariant mass spectra. This is done by integrating the background function used to describe the invariant mass distribution in Fig. 4.8, within an interval of  $[M_\phi - 8, M_\phi]$   $\text{MeV}/c^2$  for the left and  $[M_\phi, M_\phi + 8]$   $\text{MeV}/c^2$  for the right sideband, which results in  $w_{left} = 0.47$ .

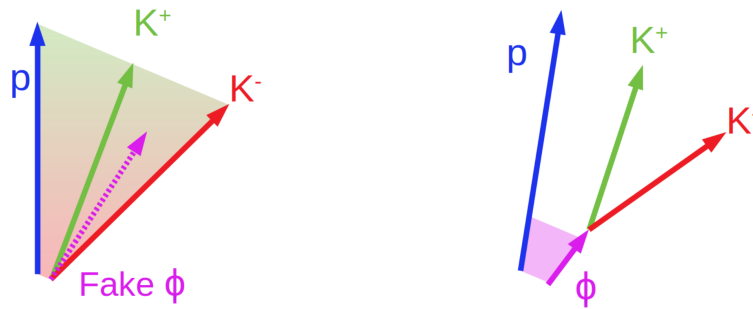
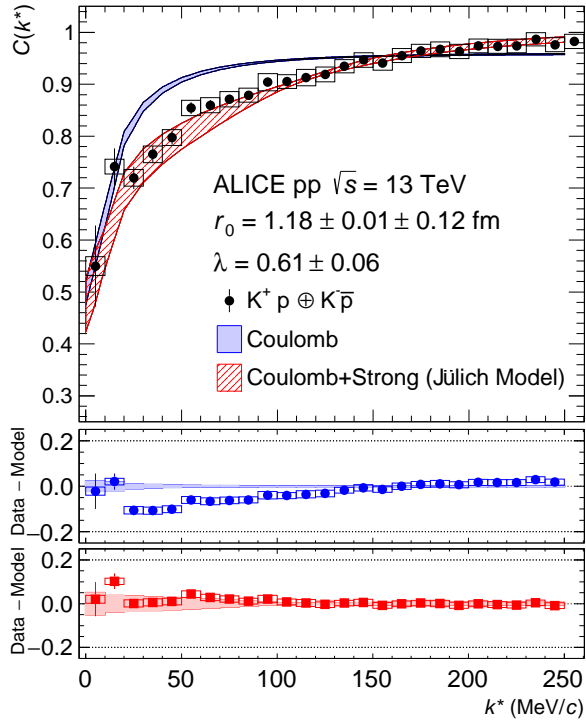
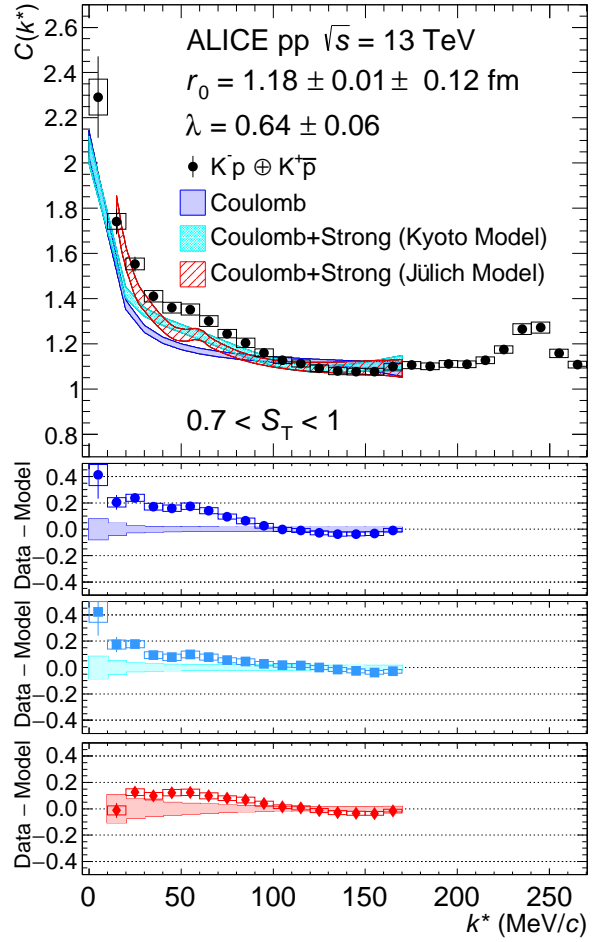


**Figure 5.10:** The left illustration shows the combinatorial background consisting of a mixture of two- and three-body interactions between proton,  $K^+$  and  $K^-$ , the right shows the genuine interaction between proton and  $\phi$ .



ALI-PUB-322719

(a) p-K<sup>+</sup> correlation function.

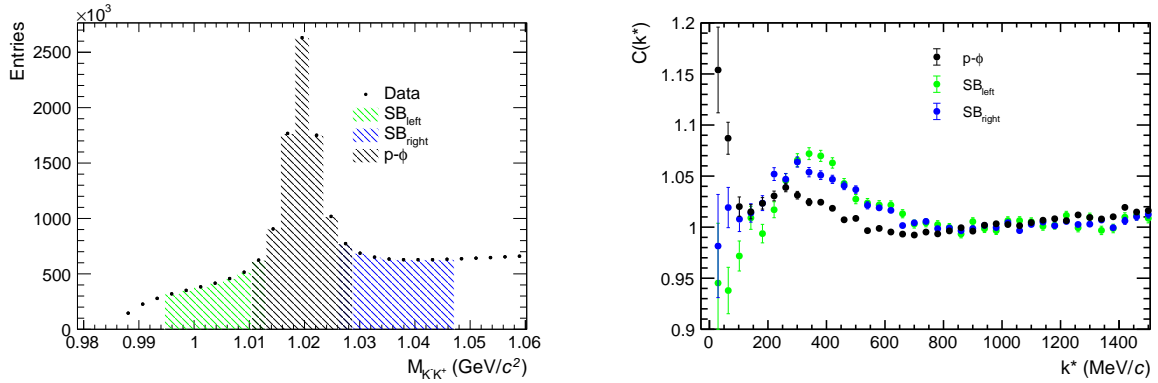


ALI-PUB-322458

(b) p-K<sup>+</sup> correlation function.

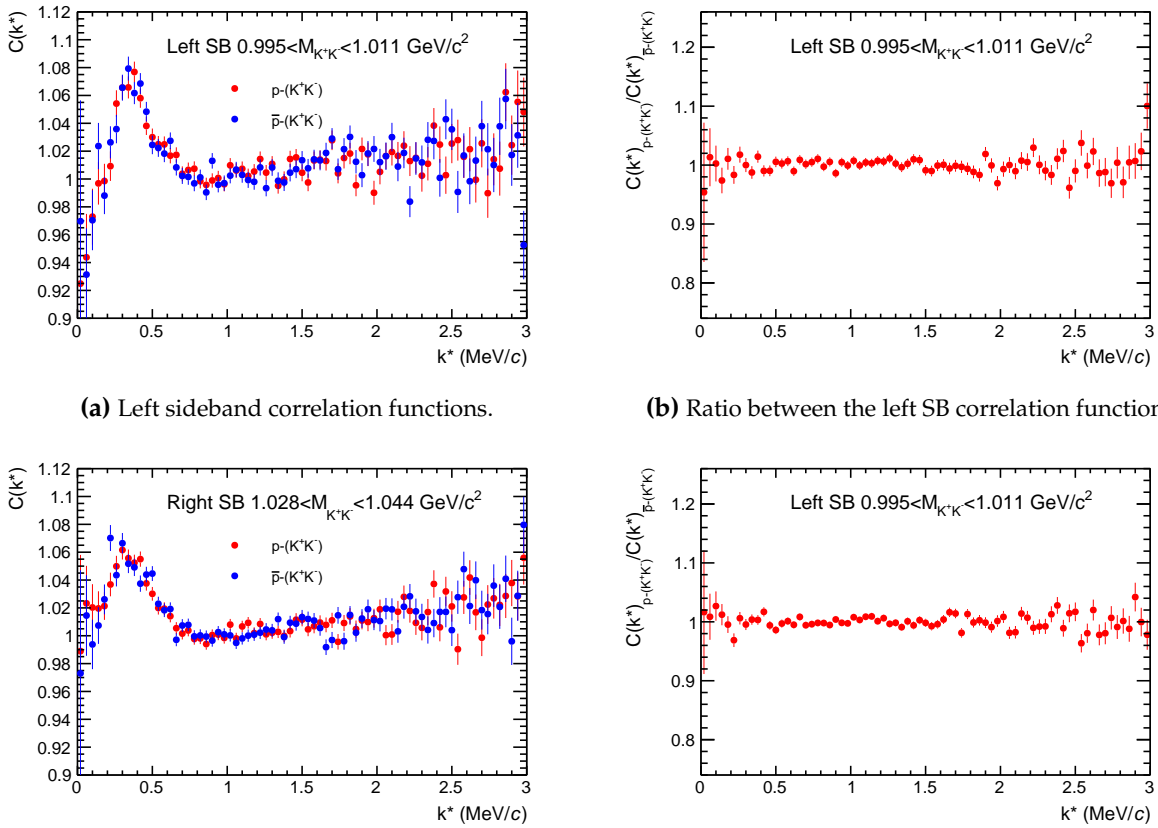
**Figure 5.11:** The experimental p-K<sup>+</sup> and p-K<sup>-</sup> correlation functions measured by ALICE in pp collisions at  $\sqrt{s} = 13$  TeV fitted with different model predictions (colored bands) [161]. A clear deviation between the data and the correlation function obtained from pure Coulomb interaction can be seen. The residual contribution to the experimental results is attributed to the strong interaction. Figures taken from [161].

By means of an alternative approach, where multiple sideband correlation functions distributed all over the  $k^*$  range, are combined, it is possible to derive a model for the combinatorial background, which matches the weighted sum of the experimental left and right sideband. Details can be found in Appendix A. Another approach, where the combinatorial background is built from the experimental two-body correlation functions among the p-(K<sup>+</sup>K<sup>-</sup>) triplet, projected into the relative momentum  $k^*$  of the p- $\phi$  pair, is described in Appendix B. Again a consistency with the data-driven sideband result is observed and it is found that p-(K<sup>+</sup>K<sup>-</sup>) is mainly driven by the two-body interaction among p-K<sup>+</sup> and p-K<sup>-</sup>. This affirms the use of  $w_{left} \cdot SB_{left} + (1 - w_{left}) \cdot SB_{right}$  to describe the combinatorial background  $C_{pKK,exp}(k^*)$  from experimental data, which is displayed in Fig. 5.14 together with the individual sideband correlation functions. Compared to the p-K<sup>+</sup> and p-K<sup>-</sup> correlation functions, depicted in Fig. 5.11,  $C_{pKK,exp}(k^*)$  extends also to larger  $k^*$ , which comes from kinematic reshuffling of the two-body correlation functions.



(a) Invariant mass distribution of  $K^+K^-$  displayed together with the two intervals that define the sidebands. (b)  $p$ - $\phi$  and sideband correlation functions depicted as comparison.

**Figure 5.12:** Invariant mass intervals and corresponding correlation function of  $p$ - $\phi$ , left and right SB.



(a) Left sideband correlation functions.

(b) Ratio between the left SB correlation functions

(c) Right sideband correlation functions.

(d) Ratio between the right SB correlation functions

**Figure 5.13:** Comparison between  $p$ -( $K^+K^-$ ) and  $\bar{p}$ -( $K^+K^-$ ) for both the left and right sideband interval.

There is a sizable amount of  $\phi$  mesons present in the sidebands, which arises from the tail of the  $\phi$  resonance extending into the sideband intervals, which lie very close to the  $\phi$  reconstruction interval, see Fig. 5.12a. Therefore, a correction is applied as it is not possible to shift the sideband intervals much further from the  $\phi$  meson peak as discussed before. The left sideband is already near threshold and when only slightly shifting the intervals, the contamination remains large while introducing additional kinematic effects that lead to even bigger deviations with respect to the properties underneath the  $\phi$  peak. The precise correction procedure is explained in the following paragraph.

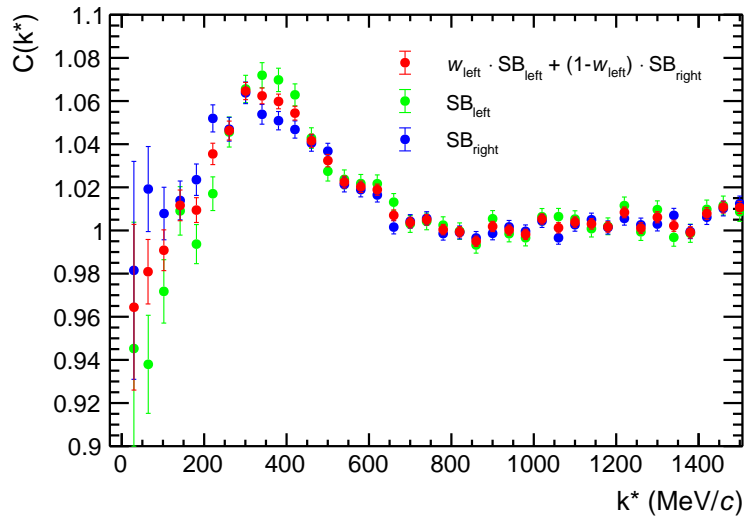


**Figure 5.14:** Left and right sideband and the weighted sum of them, which is used as  $C_{pKK,exp}(k^*)$ . The weights are obtained from the relative amount of particles in the background to the left and right of the  $\phi$  meson peak in the invariant mass spectra.

**Correction for  $\phi$  meson contamination in sidebands** Following the determination of the  $\phi$  purity in the femtoscopic region, where the average transverse momentum of the  $\phi$  candidates forming the  $p$ - $\phi$  pair is found to be  $\langle p_{T,p-\phi} \rangle = 1.3 \text{ GeV}/c$ , a  $\phi$  meson contamination of 10.73 % and 6.66% is obtained in the left and right sideband respectively, as shown in Fig. 5.15. The sum of the two values, weighted with the same  $w_{left} = 0.47$  as used for the derivation of  $C_{pKK,exp}(k^*)$ , is found to be 8.6 %. When additionally considering the proton purity and primary fraction, the genuine  $p$ - $\phi$  interaction contributes with 7% to the combinatorial background obtained from the sideband analysis ( $a = 0.07$ ). Due to the low amount of entries in the sidebands, the measured  $C_{pKK,exp}(k^*)$  is parameterized by a double Gaussian to account for fluctuations of the data points. Both data (black dots) and parameterization (red band) are shown in Fig. 5.16.

The correction is then performed by assuming

$$C_{pKK,exp} = (1 - a) \cdot C_{pKK} + \mathcal{M} \cdot C_{bkg}(k^*) \cdot a \cdot C_{p-\phi}(k^*), \quad (5.7)$$

The corrected  $C_{pKK}(k^*)$  (orange band), which describes the pure background signal without  $\phi$  contamination, is also included in Fig. 5.16. When substituting Eq. 5.7 into 5.5 the following expression is obtained

$$C_{exp}(k^*) = \mathcal{M} \cdot C_{bkg}(k^*) \cdot (\tilde{\lambda}_{p-\phi} \cdot C_{p-\phi}(k^*) + \lambda_{flat} \cdot C_{flat}(k^*)) + \tilde{\lambda}_{pKK} \cdot C_{pKK,exp}(k^*), \quad (5.8)$$

where  $\tilde{\lambda}_{p-\phi} = \left( \lambda_{p-\phi} - \frac{\lambda_{pKK} \cdot a}{1-a} \right)$  and  $\tilde{\lambda}_{pKK} = \frac{\lambda_{pKK}}{1-a}$  are the renormalized  $\lambda$ -parameters, which absorb the  $\phi$  contamination. Equation 5.8 will be used in the following to model the experimental correlation function.

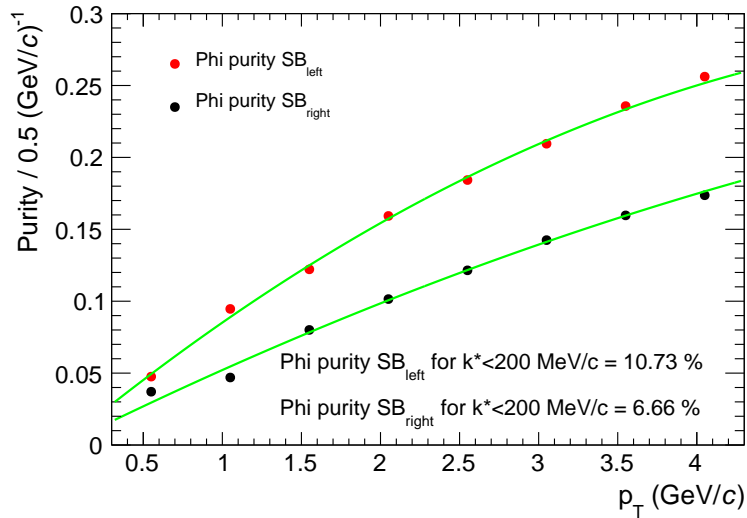


**Figure 5.15:**  $\phi$  purity within the sideband intervals in the invariant mass spectra.

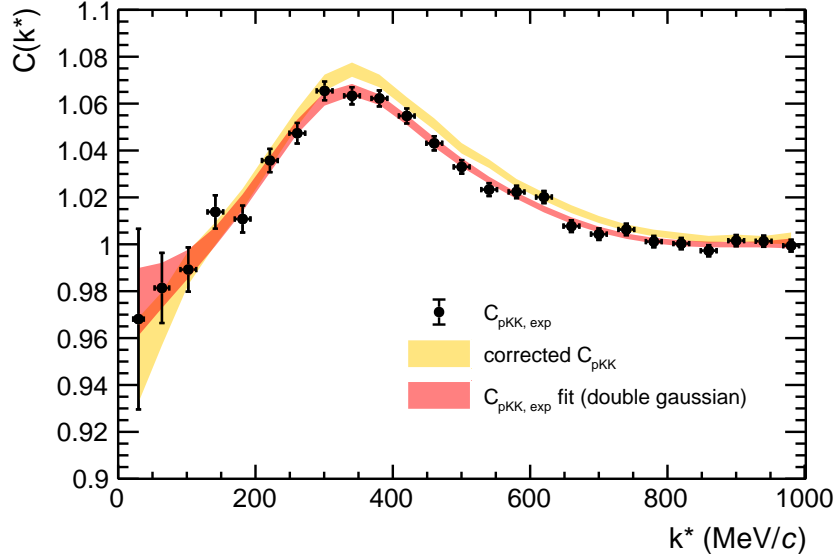


**Figure 5.16:** The combinatorial background obtained from the weighted sum of the left and right sideband correlation function, parameterized with a double Gaussian (red band), which is used in the correlation function modeling. The orange band corresponds to the actual combinatorial background, when corrected for  $\phi$  meson contamination of the sideband.

### 5.3.2 Non-femtoscopic Background

As already discussed in Sec. 4.1 the  $p$ - $\phi$  correlation function is affected by the emergence of minijets, which contain auto-correlated protons and  $\phi$  mesons emitted in jet-like structure. Minijets cause the appearance of long-range structures in the correlation function, which overshadow the genuine  $p$ - $\phi$  signal. By applying cuts on the event sphericity ( $0.7 < S_T < 1.0$  [161]), thereby selecting only spherical events, the non-femtoscopic minijet background is reduced significantly, even though not removed completely. Figure 5.17 shows the impact of such strict  $S_T$  selection on the correlation function.

The residual background is described by PYTHIA 8 [156] generated events following [159, 160], where it is shown that correlation structures related to minijet are well reproduced by MC simulated data. However, the  $\phi$  purity obtained from reconstructed MC data is reduced by  $\sim 10\%$  compared to the one from actual measurements. Additionally, the  $\phi$  yield is only half as large. In order to increase the number of pairs going into the correlation function, the particles of interest are selected from the generated MC stack via their PDG code, without including the ALICE detector response. This is referred to as MC truth in the following. After identifying kaons and protons, cuts on the transverse momentum and the pseudorapidity are applied, which are in agreement with the particle selection in Sec. 4.2.1 and 4.2.2. In a next step, the invariant mass of the kaons is calculated and a mass window of  $M_\phi \pm 8 \text{ MeV}/c^2$  is chosen, following the  $\phi$  meson selection. Next, the identity of the mother of the kaons is determined in order to establish whether or not the kaon pair originates from a  $\phi$ . Accordingly, the minijet contribution to the residual background of  $p$ -( $K^+K^-$ ) as well as the actual  $p$ - $\phi$  interaction can be studied. In both cases, a clear non-flat correlation is obtained from the MC truth sample, as depicted in Fig. 5.19a.

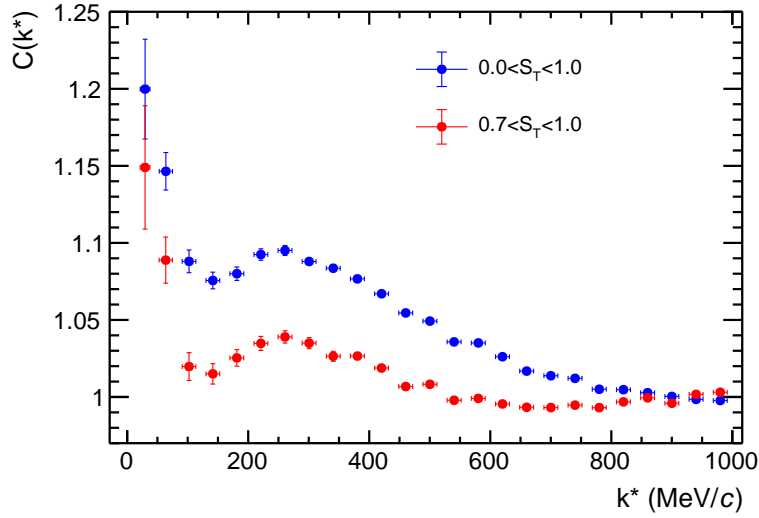


**Figure 5.17:** Due to strict cuts on the event sphericity, selecting only spherical events, the long-range enhancement caused by minijets is reduced.

When choosing the default normalization range, both functions deviate from each other, in particular at larger  $k^*$ . In order to highlight the similar slope of the minijet contribution at low  $k^*$ , correlation functions normalized within  $[600 - 800]$  MeV/c are shown in Fig. 5.19b. Indeed, they are in agreement. Additionally, a cross-check is performed, to probe whether or not detector response and tracking influence the shape of the correlation function. This is done by a comparison of the MC truth correlation function to the one obtained by employing reconstructed MC data, shown in Fig. 5.18. Both are found to be compatible within uncertainties with mild deviations arising at large  $k^*$ . When compared to the correlation functions from data, see Fig. 5.20, one can see that the MC truth data describes the enhancement at moderate  $k^*$  very well, especially in case of  $p-\phi$ .

In the final modeling of the correlation function by employing Eq. 5.8, the  $p-\phi$  minijet background is parameterized with a polynomial of fifth-order to obtain a smooth correlation signal. As the contribution is obtained from PYTHIA 8 generated data, which is not reconstructed through the ALICE detector, it is not subject to the unfolding process discussed in Sec. 5.1.1.

### 5.3.3 Genuine Correlation Function

In case of the genuine  $p-\phi$  correlation function, only the strong interaction is considered. The experimental data is used to constrain the scattering parameters of the interaction by comparing it to model predictions. As the  $\phi$  has no isospin and it is a vector meson of spin 1, the  $p-\phi$  pair can only have one isospin configuration with two possible spin states. However, the latter cannot be disentangled experimentally. Therefore, the model for singlets is used when modeling the correlation function with both the Lednický-Lyuboshits [118] and a potential approach, which results in spin-averaged scattering parameters.

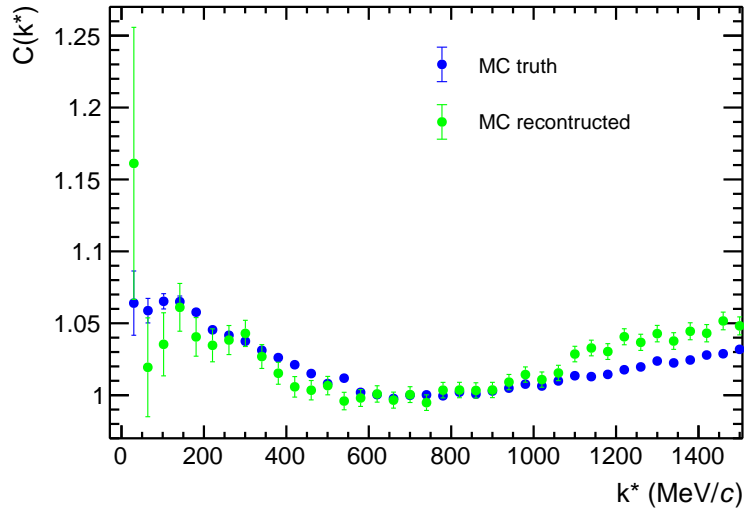
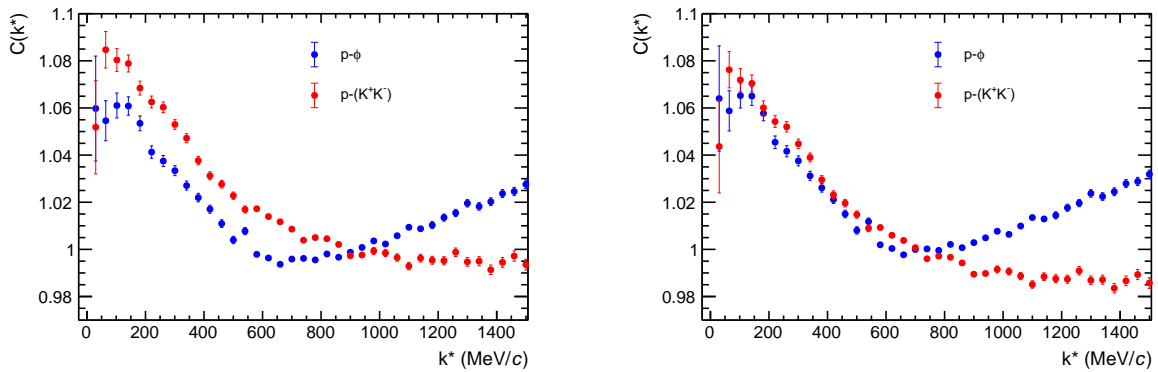


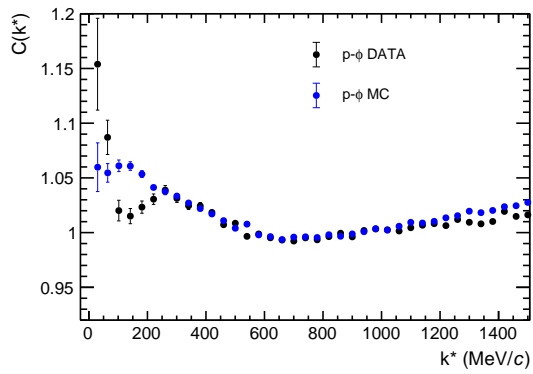
**Figure 5.18:** The  $p$ - $\phi$  correlation function from reconstructed MC and MC truth data, both normalized within  $k^* \in [600, 800]$  MeV/c. They are in agreement within the uncertainties up to  $k^* \sim 1000$  MeV/c.



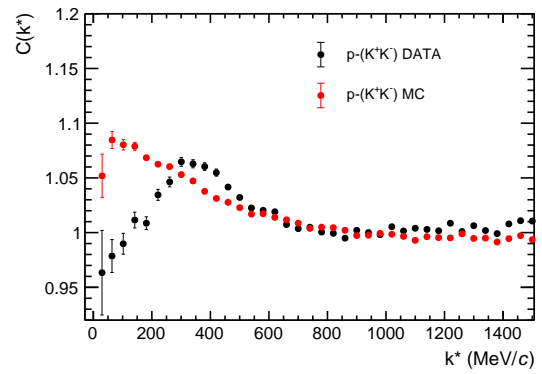
**(a)**  $k^* \in [800, 1000]$  MeV/c

**(b)**  $k^* \in [600, 800]$  MeV/c

**Figure 5.19:** Comparison between the MC truth results for  $p$ - $\phi$  and  $p$ - $(K^+K^-)$  for different normalization ranges. The discrepancy between the two correlation functions at low  $k^*$  visible in Fig. (a), where the default normalization window is used, is not present in Fig. (b). This implies that the difference seen on the left plot can be attributed to the normalization.



(a)  $p\text{-}\phi$



(b)  $p\text{-(K}^+\text{K}^-)$

**Figure 5.20:** Comparison between the correlation functions obtained from actual data and MC truth. All correlation functions are normalized within  $k^* \in [800, 1000]$  MeV/c.

## 5.4 Extracting the Genuine Correlation Function

All non-genuine contributions to the correlation function are removed from the measured signal in order to finally extract  $C_{p-\phi}(k^*)$ , which is then compared to the modeled correlation functions to obtain the scattering parameters of the interaction.

In order to account for the uncertainties of the input data, the bootstrap method is employed, where iteratively a random correlation function is generated for  $C_{MJ,p-\phi}(k^*)$ , left and right sideband correlation function, from which eventually  $C_{pKK,exp}(k^*)$  is deduced, and of course  $C_{exp}(k^*)$ . This is achieved by sampling each data point from a Gaussian distribution with the default value of the unfolded experimental data as mean and the statistical uncertainty as standard deviation. The whole procedure to derive a description of the total background, which is then removed from the total correlation function to extract the genuine  $p-\phi$  correlation function  $C_{p-\phi}$ , is repeated  $\sim 1000$  times in total to obtain reasonable results from bootstrap.

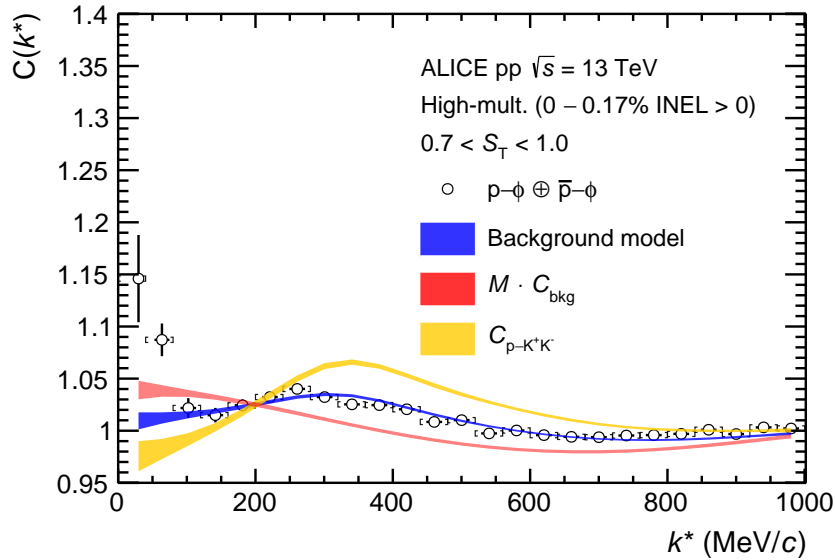


**Figure 5.21:** The experimental  $p-\phi$  correlation function and various contributions as described in Eq. 5.8, however, not yet scaled by the respective parameters. The blue band depicts the background model used to derive the genuine  $p-\phi$  correlation function.

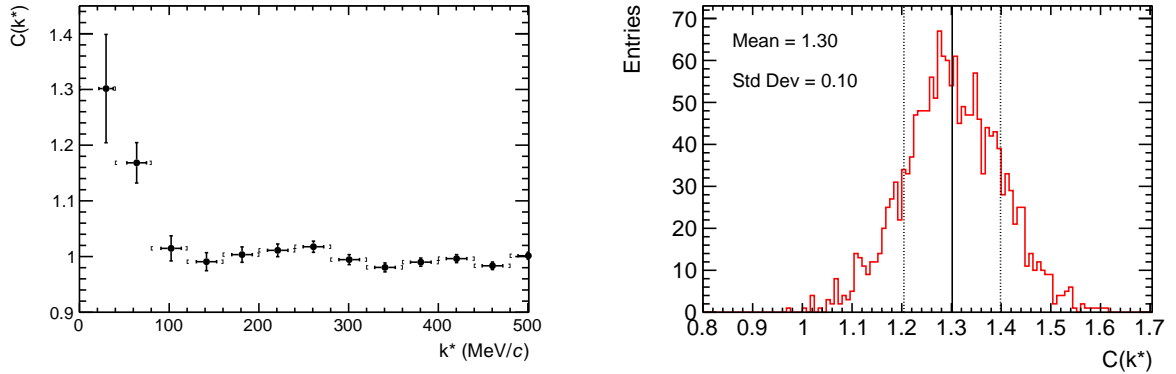
In a first step, the randomized total correlation function is fitted with a polynomial of second-order within  $k^* \in [600, 1500]$  MeV/c to get constraints for the baseline in Eq. 5.6. Aiming to get a description of the total background, also referred to as background model, it is assumed that  $C_{p-\phi}(k^*) = 1$  and the data is fitted with Eq. 5.8 within a range of  $k^* \in [200, 800]$  MeV/c. The  $\lambda$ -parameters as well as the functions describing minijet and combinatorial  $p-(K^+K^-)$  background are fixed from data, which leaves only the normalization constant  $\mathcal{M}$  and the baseline parameters  $a$  and  $b$  free. The latter are restricted to lie within  $3\sigma$  of the prefit results, as  $b_{prefit} - 3 \cdot e_{prefit} < b < b_{prefit} + 3 \cdot e_{prefit}$  and  $1 - a_{prefit} - 3 \cdot e_{prefit} < a < 1 - a_{prefit} + 3 \cdot e_{prefit}$  respectively. In particular  $1 - a_{prefit}$  is chosen to prevent the background model without normalization constant  $\mathcal{M}$  from reaching values much larger or smaller than  $\sim 1$ . The resulting background model is shown in Fig. 5.21 together with the different contributions. The overall trend of the experimental data

is well described and it accurately reproduces the enhancement in the intermediate  $k^*$  range of  $[300, 500]$  MeV/c and the behavior for large relative momenta. The mild discrepancies between data and fit within  $[200, 300]$  MeV/c are compatible within the uncertainties.

In a last step, the total background model is removed from  $C_{\text{exp}}(k^*)$  by rearranging Eq. 5.8, now with the normalization constant and baseline parameters fixed from the fitting procedure, in terms of the genuine correlation function.

Finally, the fully corrected genuine  $p$ - $\phi$  correlation function is shown in Fig. 5.22a. The value of each data point corresponds to the mean of the results from all bootstrap iterations combined and the statistical uncertainty to the respective standard deviation. As an example the bootstrap distribution of the first data point of  $C_{p-\phi}(k^*)$  is shown in Fig. 5.22b. Notably, the mean coincides with the value of the first data point in Fig. 5.22a and the standard deviation of the distribution with the statistical uncertainty of that point.

At low  $k^*$  there is a noticeable increase of the correlation signal, which suggests an attractive nature of the genuine interaction between proton and  $\phi$  meson. This enhancement is large compared to the experimental  $C_{\text{exp}}(k^*)$  in the same relative momentum range where the genuine  $p$ - $\phi$  correlation function is dampened by  $\lambda_{p-\phi}$  and overshadowed by the various background contributions, including minijets and combinatorial background. Furthermore, the correlation function is flat at large  $k^*$  as expected. A detailed discussion of the final results will follow in chapter 6.



**(a)** The genuine  $p$ - $\phi$  correlation function obtained after removing all contributions from the measured signal.

**(b)** Distribution of the first data point of the genuine  $p$ - $\phi$  correlation function, obtained from bootstrap. The mean corresponds to the value of the data point, whereas the standard deviation is the corresponding statistical uncertainty.

**Figure 5.22:** The genuine  $p$ - $\phi$  correlation function derived by employing the bootstrap method. Each data point is obtained by randomly sampling the input correlation functions, resulting in a distribution of possible correlation function values.

## 5.5 The Source

In order to interpret the data, the genuine  $C_{p-\phi}(k^*)$  is compared to a theoretical correlation function, defined by Eq. 2.16. It depends on both the particle-emission, characterized by the source function  $S(r^*)$ , and the two-particle wave-function. Therefore, following Chapter 2, the

source has to be constrained in order to obtain information on the interaction between proton and  $\phi$  meson.

As discussed in [85] and [164], the emission source, which is typically parameterized by a Gaussian source function (Eq. 2.5), is deformed by short-lived resonances with  $c\tau \lesssim 10$  fm, feeding into the particles of interest. This leads to an effective enhancement of the source radius as illustrated in Fig.5.23, which can be determined by considering the different origins of the final-state particles. The source function is given accordingly as [164]

$$S(r^*) = P_1 P_2 \times S_{P_1 P_2}(r^*) + \tilde{P}_1 P_2 \times S_{\tilde{P}_1 P_2}(r^*) + P_1 \tilde{P}_2 \times S_{P_1 \tilde{P}_2}(r^*) + \tilde{P}_1 \tilde{P}_2 \times S_{\tilde{P}_1 \tilde{P}_2}(r^*), \quad (5.9)$$

where  $\tilde{P}_{1(2)} = 1 - P_{1(2)}$  denotes the fraction of secondary particles originating from short-lived resonances,  $P_{1(2)}$  the primordial<sup>1</sup> fraction and  $S_{ij}(r^*)$  the corresponding source. In order to evaluate  $S(r^*)$ , the resonance yields are taken from the statistical hadronization model [172] and the propagation of the resonances as well as their relative orientation is modeled with EPOS [173].

Using the procedure described in [164], the source is parameterized in terms of a core Gaussian emission source of width  $r_{\text{core}}$ , which is assumed common for all hadrons. The additional effect of resonances is evaluated using the same model. Even though the final source function deviates slightly from a Gaussian function due to the exponential tail induced by the resonances, an effective Gaussian profile can still be employed to a good approximation. The corresponding effective source size  $r_{\text{eff}}$  can be obtained by fitting the true source distribution and will be slightly larger compared to  $r_{\text{core}}$ .

The core radius is extracted from correlation measurements of particle pairs, which undergo well-understood final-state interactions. By fitting the experimental correlation function with a given potential, it is possible to extract the source, which is then corrected for the effects from resonances. Figure 5.24 shows the resulting  $r_{\text{core}}$  for p-p and p- $\Lambda$ , both measured in pp collisions

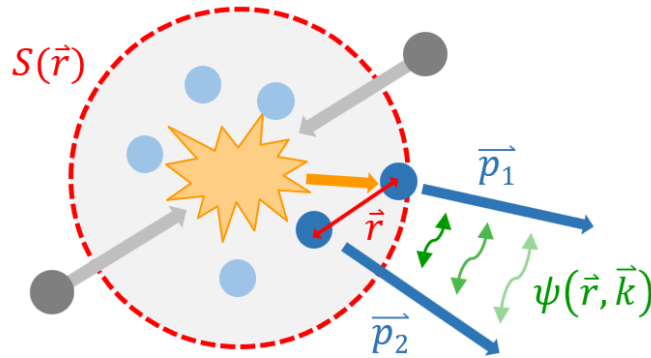


**Figure 5.23:** Illustration of the modification source size due to resonances feeding one of the particles of interest as for p- $\phi$ .

<sup>1</sup> Primordial particles are those created directly during the hadronization process, and do not stem from an intermediate decay.

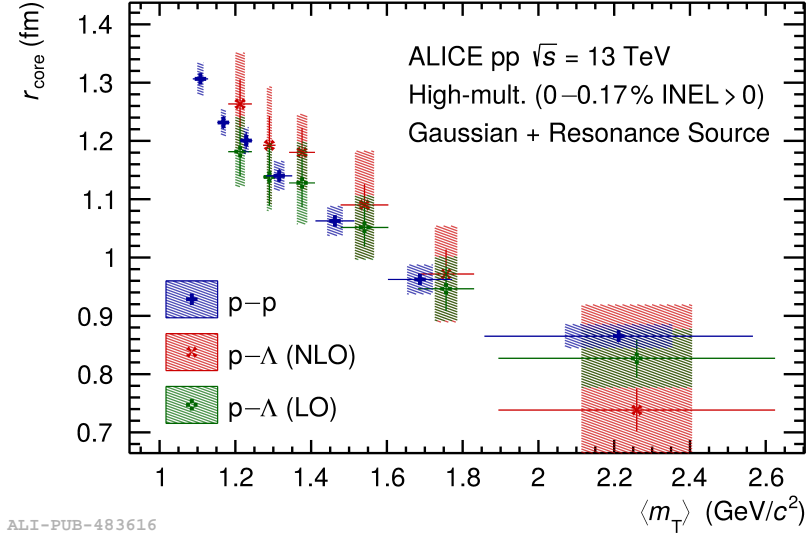


**Figure 5.24:** Gaussian core radius as a function of  $\langle m_T \rangle$  for different particle pairs. The blue data points are obtained by fitting the p-p correlation function with the strong Argonne  $\nu 18$  [65] potential. The green (red) data results from a fit of the p- $\Lambda$  correlation function with the strong  $\chi$ EFT LO [174] (NLO [175]) potential. Statistical uncertainties are shown as lines while the systematic uncertainties correspond to the boxes. Figure taken from [164].

at  $\sqrt{s} = 13$  TeV, as a function of the transverse mass, defined by

$$m_T = \sqrt{k_T^2 + m^2}, \quad (5.10)$$

where  $k_T$  the transverse momentum in the laboratory frame and  $m$  is the mean pair mass. The core radius scales with  $\langle m_T \rangle$ , which is mostly related to the collective expansion of the collision system. More remarkable is the fact that the data is in agreement within the uncertainties for both pairs, indicating the existence of a universal emission source altered only by short-lived resonances feeding into the specific particles. Hence, by interpolating these data, it is possible to calculate the core radius for any given particle pair by measuring its transverse mass.

Figure 5.26 depicts the p-p results, where the core radius is obtained from modeling the correlation function between the two particles with the strong Argonne  $\nu 18$  potential [65]. With an average of  $\langle m_T \rangle = 1.656$  GeV/c<sup>2</sup> for p- $\phi$  and  $\bar{p}$ - $\phi$  pairs with small relative momentum  $k^* < 200$  MeV/c, see Fig. 5.25, a Gaussian core radius of  $r_{\text{core}} = 0.98 \pm 0.04$  fm is extracted from the interpolation.

An effective description of the p- $\phi$  source is then obtained by including effects from short-lived resonances. While the primordial fraction of protons is only  $\sim 35.8\%$  [176], with the main feed-down contribution arising from  $\Delta$  resonances, there is no relevant contribution from strongly decaying resonances feeding to the  $\phi$  meson.

Figure 5.27 shows the resulting effective distribution of the p- $\phi$  source. With the known core radius of  $r_{\text{core}} = 0.98 \pm 0.04$  fm, an effective Gaussian size of  $r_{\text{eff}} = 1.08 \pm 0.05$  fm is derived by fitting the distribution with the Gaussian source function. In the interval of  $4.5 < r^* < 6.5$  fm a slight deviation between the fit function and the data points is visible, which is associated with modifications induced by resonances. Nevertheless, the Gaussian parameterization holds well in the relevant region where most of the pairs are found.

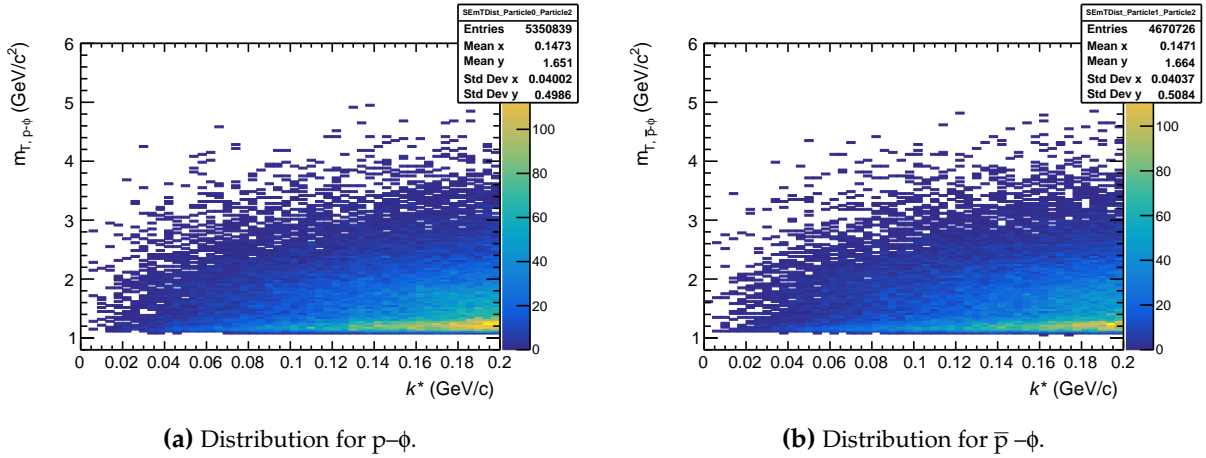


Figure 5.25: Distribution of the transverse mass at low relative momenta of  $p-\phi$  and  $\bar{p}-\phi$  respectively.

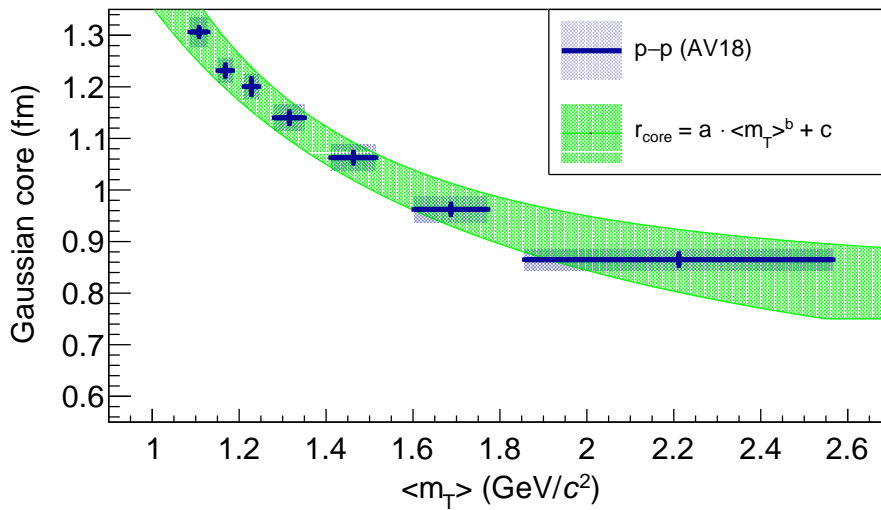


Figure 5.26: Gaussian core radius of a  $p-p$  source as function of  $\langle m_T \rangle$  and fit to the data (green). Solid bars depict the statistical uncertainties and shaded areas the systematic errors due to variations of the fit [164].

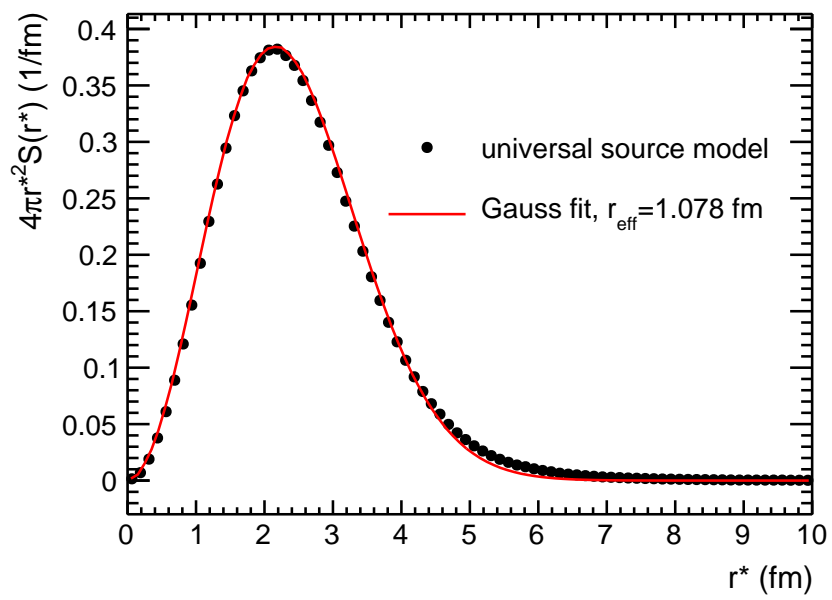


Figure 5.27: Universal source model for p- $\phi$  and fit with a Gaussian source function.

## 5.6 Femtoscopic Fit

Information on the interaction between two particles is typically obtained by comparing the data to model predictions, which in the case of p- $\phi$  include an analytical correlation function from the Lednický-Lyuboshits model [118] as well as an approach with phenomenological potentials, where the correlation function is evaluated numerically by employing the *The Correlation Analysis Tool using the Schrödinger Equation* (CATS) [121].

Therefore, each individual genuine correlation function, directly obtain from data by employing the total background model and bootstrap method discussed in Sec. 5.4, is fitted with the one derived from the various approaches within  $k^* < 200$  MeV/c. In order to ensure physical results, variations yielding  $\chi^2/\text{ndf} > 100$  within the fit range of  $k^* \in [0, 200]$  MeV/c are excluded. An even stricter selection is used for the Lednický-Lyuboshits approach by additionally refusing results with  $d_0 < 0$  fm and  $d_0 > 1000$  fm as well as  $\Im(f_0) < 0$  fm.

This results in a distribution of the fit parameters, which in the case of the Lednický-Lyuboshits approach are the scattering length  $f_0$  and effective range  $d_0$ , or else, the potential parameters from which the scattering parameters can be derived via Eq. 2.16. From these distributions, the values and statistical uncertainties of the individual parameters can be obtained as their mean and standard deviation, respectively. However, to account for the asymmetric shape of the parameter distributions, they are evaluated within the central interval enclosing 90% of the entries in case of the Lednický-Lyuboshits model with complex scattering length. Regarding all other approaches, the parameters and uncertainties are obtained by taking the truncated mean and the corresponding standard deviation when discharging the upper 10% of the entries. All parameter distributions are included in Appendix D.

## 5.7 Systematic uncertainties

### 5.7.1 Data

The systematic uncertainties of the measured data are extracted by randomly varying the selection criteria for protons and kaons as well as altering the lower value of the sphericity cut. A summary can be found in Tab. 5.2. Thus, the analysis is performed on a total of 25 sets of random combinations of these selection criteria, each leading to a slightly different shape of the correlation function.

As there are only a moderate number of pairs, which contribute to the correlation function at low  $k^*$ , even a moderate modification of the pair yield results in large statistical fluctuations of the results, ultimately biasing the derivation of systematic uncertainties. Therefore, in order to retain the statistical significance, the combinations are chosen not to exceed an upper limit of  $\pm 20\%$  of the pair yield  $N_{\text{same}}$  within  $k^* < 200$  MeV/c. The resulting relative pair variation of each of the 25 sets is shown in Fig. 5.28 and the corresponding maximum variation of the  $\phi$  purity is  $\sim 1.5\%$ .

For the sideband correlation function the same cut-variations and combinations are employed, whereas for the minijet contribution from MC truth only a variation of the transverse momentum and pseudorapidity of the proton and kaon candidates as well as the transverse sphericity is possible. The systematics of each default correlation function  $C_{\text{MJ},\text{p}-\phi}(k^*)$ ,  $\text{SB}_{\text{left/right}}(k^*)$  and

$C_{\text{exp}}(k^*)$  are derived by means of the bootstrap method including the 25 variations of the correlation functions. From this, a distribution for each data point in  $k^*$  is obtained, where the standard deviation corresponds to the total uncertainty of the points. Assuming that statistical errors and systematic uncertainties are uncorrelated, the following equation holds

$$\sigma_{\text{tot}}^2 = \sigma_{\text{stat}}^2 + \sigma_{\text{syst}}^2, \quad (5.11)$$

which can be rearranged as  $\sigma_{\text{syst}} = \sqrt{\sigma_{\text{tot}}^2 - \sigma_{\text{stat}}^2}$  in order to extract the systematic uncertainties, as the statistical uncertainty of the experimental correlation functions is known and obtained from the yield recorded by the ALICE detector.

The total experimental correlation function  $C_{\text{exp}}(k^*)$  is depicted in Fig. 5.29 together with the systematic and statistical uncertainties of the data. The relative systematic uncertainty is 2.8% at low  $k^*$ .

**Table 5.2:** Variations of the selection criteria.

Variable	Default	Variation
$p_{\text{T}}$ proton (GeV/c)	0.5	0.425, 0.575
$ \eta $ proton	0.8	0.75, 0.85
$n_{\sigma}$ proton	3	2.5, 3.5
$n_{\text{Cluster}}$ proton	80	70, 90
$p_{\text{T}}$ kaon (GeV/c)	0.15	0.075, 0.225
$ \eta $ kaon	0.8	0.75, 0.85
$n_{\sigma}$ kaon	5	4.25, 5.75
$n_{\text{Cluster}}$ kaon	80	70, 90
$S_{\text{T}}$ sphericity	0.7	0.665, 0.735

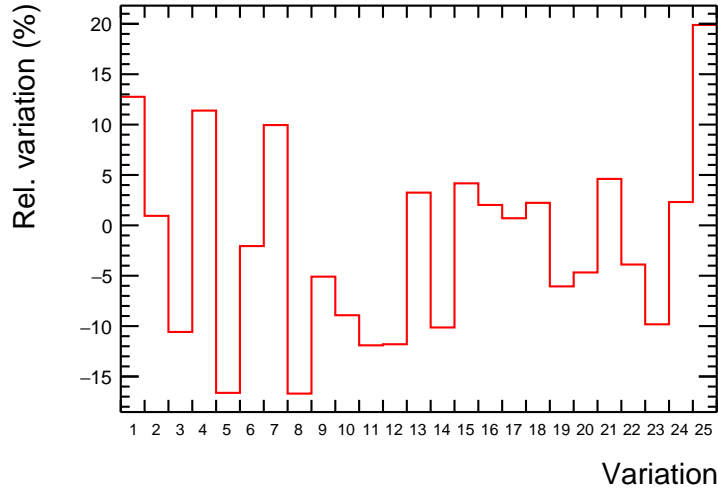


**Figure 5.28:** Effect of the systematic variations on the number of  $p$ - $\phi$  pairs for  $k^* < 200$  MeV/c.

## 5.7.2 Genuine Correlation Function

The systematic uncertainties of the data, discussed in Sec. 5.7.1, are only relevant for the visualization of the plotted functions. However, in order to derive the final genuine correlation function by employing the total background model to the data,  $C_{MJ,p-\phi}(k^*)$ ,  $SB_{\text{left/right}}(k^*)$  and  $C_{\text{exp}}(k^*)$  are used simultaneously. Therefore, the associated systematic uncertainties are evaluated by combining the bootstrap sampling of all the input correlation functions with systematic variations of the fitting procedure explained in Sec. 5.4.

In particular, the 25 systematic combinations of the input correlation functions  $C_{MJ,p-\phi}(k^*)$ ,  $SB_{\text{left/right}}(k^*)$  and  $C_{\text{exp}}(k^*)$  are combined randomly in each iteration. Each of them is corrected for the momentum resolution by randomly choosing the unfolding method, number of iterations and response matrix variation. Also, the fit ranges are varied in order to account for the possibility of systematic uncertainties related to the fitting procedure itself. Additionally, a linear baseline is included, as its shape affects the genuine correlation function, especially at low relative momentum  $k^*$ . A summary of all systematic variations can be found in Tab. 5.3.

After a total of  $\sim 1000$  repetitions of the fitting procedure a new distribution for each data point of  $C_{p-\phi}(k^*)$  is obtained, which has a standard deviation of  $\sigma_{\text{tot}}(k^*)$ . Together with the statistical uncertainties derived in Sec. 5.3.3 the systematic error of the genuine  $p-\phi$  correlation function is calculated from Eq. 5.11.

Figure 5.29 shows the total background model and various components with statistical and total uncertainties, from which the systematics of genuine  $p-\phi$  correlation function are obtained. The final results are shown in Fig. 5.30.

**Table 5.3:** Variations of the fitting procedure to derive the genuine  $p-\phi$  correlation function from the experimental data.

Variable	Default	Variation
Baseline	linear	quadratic
lower fit range of BG model	200 MeV/c	170 MeV/c, 230 MeV/c
upper fit range of BG model	800 MeV/c	770 MeV/c, 830 MeV/c
Variations of the prefit ranges of the pol1 baseline		
lower limit	600 MeV/c	550 MeV/c, 650 MeV/c
upper limit	1000 MeV/c	950 MeV/c, 1050 MeV/c
Variations of the prefit ranges of the pol2 baseline (flat at $k^* = 0$ MeV/c)		
lower limit	600 MeV/c	550 MeV/c, 650 MeV/c
upper limit	1500 MeV/c	1450 MeV/c, 1550 MeV/c
Variations of the unfolding process		
unfolding method	Bayesian	bin-by-bin
iterations	5	4, 6
response matrix	folded normal distribution (FND)	FND upper limit, FND lower limit

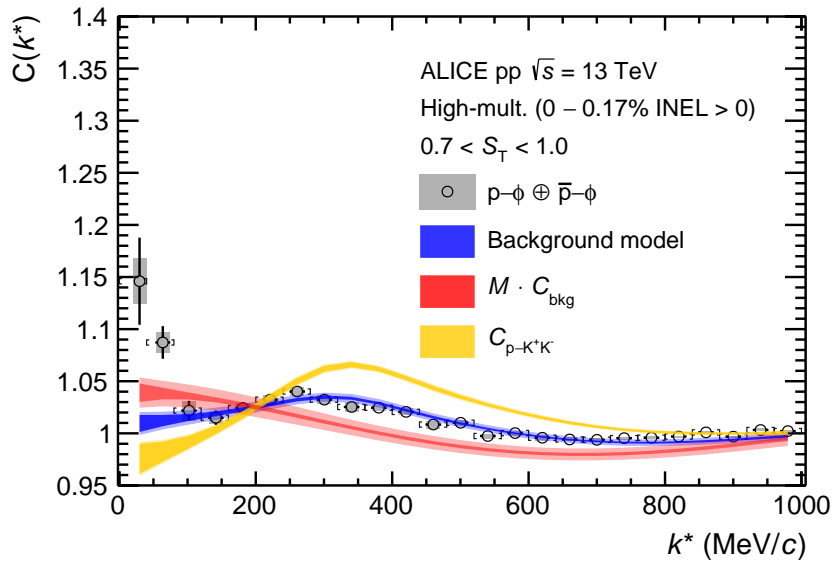


**Figure 5.29:** The experimental  $p\text{-}\phi$  correlation function and the various contributions as described in Eq. 5.5. It has to be considered that they are not scaled by the respective  $\lambda$ -parameters. Statistical (bars) and systematic uncertainties (boxes) are shown separately. The width of the dark (light) shaded bands corresponds to one standard deviation of the statistical (total) uncertainty. The figure published in [177].

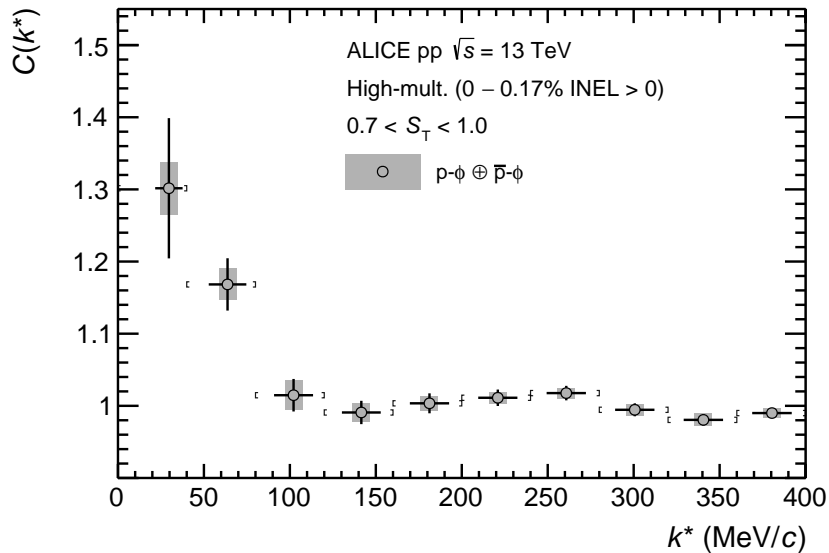


**Figure 5.30:** The genuine  $p\text{-}\phi$  correlation function with statistical (bars) and systematic (grey boxes) uncertainties [177]

### 5.7.3 Femtoscopic Fit

To incorporate possible systematic uncertainties related to the femtoscopic fit, the uncertainties of the effective Gaussian size from Sec. 5.5 are accounted for by including the respective extreme values in the random sampling. Additionally, the upper limit of the fit range is varied by changing the number of points that are included in the procedure by  $\pm 1$ . A summary can be found in Tab. 5.4. Following the procedure explained in Sec.5.6 and additionally including all of these systematic variations, the total uncertainties of the fit parameters can be derived, from which finally the systematic uncertainties are obtained by employing Eq. 5.11.

**Table 5.4:** Systematic variations of the femtoscopic fits.

Variable	Default	Variation
upper fit range (MeV/ $c$ )	200	170, 230
$r_{\text{eff}}$ (fm)	1.078	1.031, 1.126

## 6 Results and Discussion

In this section, the final results on the interaction between proton and  $\phi$  meson for HM data in pp collisions at  $\sqrt{s} = 13$  TeV are presented. Various models are employed to extract the interaction parameters from the genuine p- $\phi$  correlation function. The statistical significance of the measured deviation with respect to the null-hypothesis  $C(k^*) = 1$  is found to be  $5.7 \pm 0.8$  (stat.)  $\pm 0.5$  (syst.)  $\sigma$  in the region  $k^* < 200$  MeV/ $c$  (see Fig. D.1 in Appendix D). This evidences the strong FSI between the two particles.

### 6.1 Accessing the strong FSI

The genuine p- $\phi$  correlation function shows the characteristics of an attractive interaction, as it takes values above unity at low  $k^*$ , where the strong FSI becomes relevant. However, contributions from coupled-channels might be present, which influence the shape of the correlation function. They have to be considered when accessing the parameters of the p- $\phi$  interaction.

As discussed in Sec. 2.3, inelastic channels, which open below threshold lead to an effective increase of the correlation function, while the ones that appear above threshold lead to a cusp structure close to their threshold  $k^*$ . Due to the large uncertainties and bin width of the genuine p- $\phi$  correlation function, no structures related to the opening of above-threshold channels can be observed at the opening momenta of the  $\Lambda$ - $K^*$  ( $k^* = 221.6$  MeV/ $c$ ) and  $\Sigma$ - $K^*$  ( $k^* = 357.4$  MeV/ $c$ ) channels. However, sub-threshold channels might be present as well. In order to account for the possibility of such inelastic contributions, characterized by  $\Im(f_0) > 0$ , a fit with the Lednický-Lyuboshits approach with complex scattering length is performed. The resulting correlation function is shown in Fig. 6.1 and the corresponding scattering parameters are summarized in Tab. 6.1.

Notably,  $\Re(f_0) > 0$  indicates an attractive nature of the p- $\phi$  interaction in vacuum. This conclusion is supported by an imaginary part of the scattering length,  $\Im(f_0)$ , that vanishes within the uncertainties, suggesting that the elastic p- $\phi$  interaction, characterized by the real part of the scattering length, is dominant in vacuum. The effective range is found to be  $d_0 = 7.85 \pm 1.54$  (stat.)  $\pm 0.26$  (syst.) fm. Therefore, the existence of a N- $\phi$  bound state, which is characterized by  $\Re(f_0) < 0$  and a small  $d_0$ , is not supported by data.

The large effective range combined with the small p- $\phi$  source might be troublesome in case of the Lednický-Lyuboshits approach (Eq. 2.19), which includes a correction term  $\propto \frac{d_0}{r_{\text{eff}}}$  [118]. In order

**Table 6.1:** Scattering parameters with statistical and systematic uncertainties extracted from the bootstrap fit with the Lednický-Lyuboshits approach with complex scattering length.

Variable	Result	$\sigma_{\text{stat}}$	$\sigma_{\text{syst}}$
$d_0$ (fm)	7.85	1.54	0.26
$\Re(f_0)$ (fm)	0.85	0.34	0.14
$\Im(f_0)$ (fm)	0.16	0.10	0.09

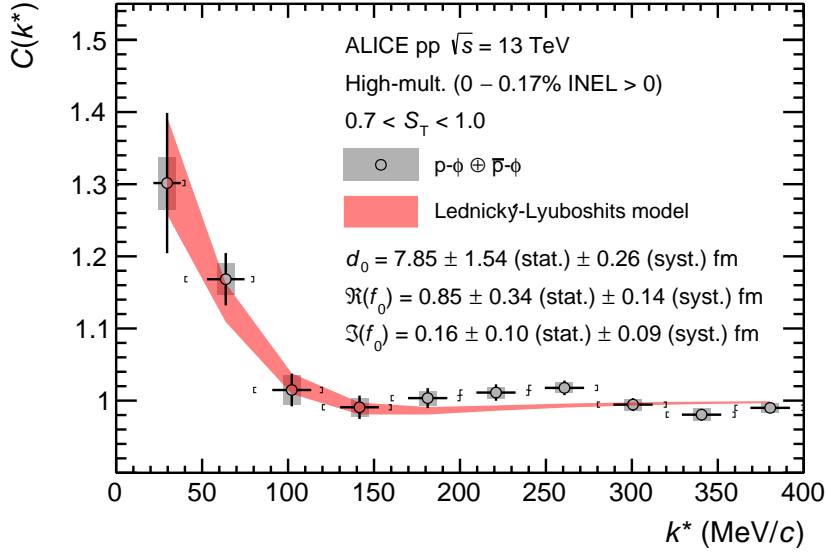


**Figure 6.1:** The genuine  $p$ - $\phi$  correlation function with statistical (bars) and systematic uncertainties (boxes). The red band depicts the results from the fit employing the Lednický–Lyuboshits [118]. The width corresponds to one standard deviation of the uncertainty of the fit. Figure published in [177].

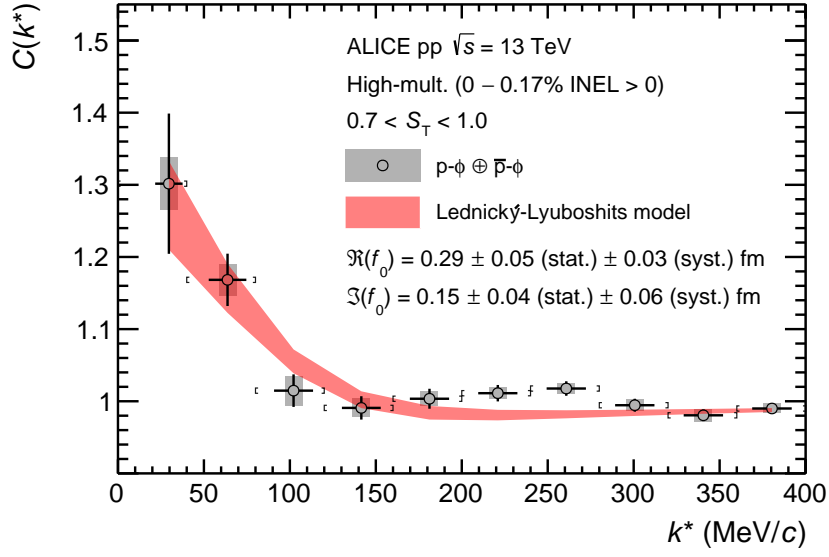
to test the stability of the previously obtained  $f_0$  values and the influence of the correction term, the  $p$ - $\phi$  correlation function is also evaluated within the *zero effective range approximation* by fixing  $d_0 = 0$  fm in the fit. The results are shown in Fig. 6.2. Even though the description of the data is slightly worse than with inclusion of the effective range parameter in the fitting procedure, the scattering length is in agreement within the uncertainties in both approaches.

Similar to the OZI suppressed  $N$ - $\phi$  case, also the  $N$ - $J/\psi$  interaction is expected to be driven by gluon exchange, as the  $J/\psi$  ( $c\bar{c}$ ) does not share common valence quarks with the nucleons. Therefore, in line with studies of charmonium states [52], phenomenological potentials are employed to evaluate the  $p$ - $\phi$  interaction [51].

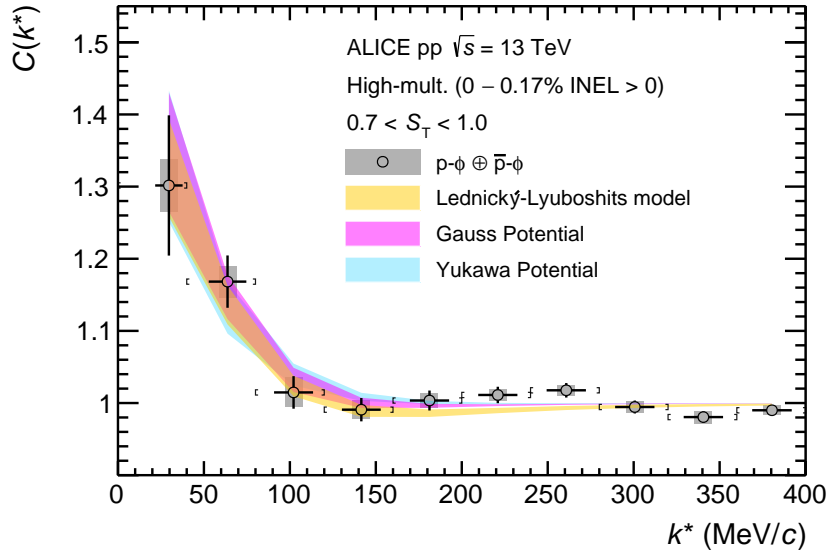
Such approaches include Yukawa- (Eq. 2.26) and Gaussian-type potentials (Eq. 2.27). The corresponding correlation functions are obtained by solving the Schrödinger Equation numerically with the *The Correlation Analysis Tool using the Schrödinger Equation* (CATS) [121]. However, the potentials can only be evaluated with real parameters  $\in \mathbb{R}$ . Nonetheless, reasonable results are obtained as inelastic contributions, characterized by the imaginary part of the scattering length, do not dominate the  $N$ - $\phi$  interaction in vacuum, as demonstrated. It is also possible to extract the scattering parameters of the potential approaches from the phase-shift of the corresponding wave-function via the relation Eq. 2.16. A detailed discussion can be found in Appendix C.

Figure 6.3 shows the correlation functions obtained for the different interaction potentials. As a comparison also the result from a fit with the Lednický–Lyuboshits approach with real scattering parameters  $f_0, d_0 \in \mathbb{R}$  is shown. The corresponding values can be found in Tab. 6.2. Both effective range and scattering length are slightly increased in comparison to the values from the approach with complex  $f_0$ , however compatible within uncertainties.

The values obtained for the parameters of the Gaussian-type potential, namely its strength  $V_{\text{eff}}$



**Figure 6.2:** The correlation function for  $p\text{-}\phi$  compared to the Lednický-Lyuboshits approach with complex scattering length and zero effective range approximation.



**Figure 6.3:** Correlation functions obtained from the potentials by employing CATS in comparison to the result from the Lednický-Lyuboshits approach with real scattering length.

**Table 6.2:** Scattering parameters with statistical and systematic uncertainties extracted from the bootstrap fit with the Lednický-Lyuboshits approach with real scattering length.

Variable	Result	$\sigma_{\text{stat}}$	$\sigma_{\text{syst}}$
effective range $d_0$ (fm)	8.90	1.25	0.71
scattering length $f_0$ (fm)	0.95	0.41	0.23

and range, accessible via  $\mu \approx 1/R^2$ , can be found in Tab. 6.3. Similar to the results obtained by the Lednický–Lyuboshits approach, the small  $V_{\text{eff}}$  indicates a shallowly attractive strong interaction, with a moderate range of  $\sim 3$  fm. In particular, this potential is much more shallow than results on the strong interaction among  $N\text{-}J/\psi$  obtained from lattice QCD calculations, performed by the HAL QCD collaboration [178]. A parameterization of these results with a Gaussian-type potential yields  $V_{\text{eff}} = 133.4$  MeV and  $\mu = 5.5$  fm $^{-2}$ .

The fit results from the Yukawa-type potential are summarized in Tab. 6.4. The parameter values are found to be significantly smaller than the ones from studies of possible  $N\text{-}\phi$  bound states, which use the same kind of potential with  $\alpha = 600$  MeV and  $A = 1.25$  [51]. Therefore, the data analysis performed in this work excludes a possible bound state.

Summarizing, the  $p\text{-}\phi$  interaction measured in  $pp$  collisions, hence vacuum, is found to be attractive and dominated by elastic contributions. A bound state is not supported. This conclusion is obtained by employing the Lednický–Lyuboshits approach, which yields consistent results for three different hypotheses, including (i)  $f_0 \in \mathbb{C}$ ,  $d_0 \in \mathbb{R}$ , (ii)  $f_0 \in \mathbb{C}$ ,  $d_0 = 0$  fm and (iii)  $f_0, d_0 \in \mathbb{R}$ . These results are compatible with the ones obtained numerically from phenomenological potentials, which also yield a shallowly attractive strong FSI between proton and  $\phi$  meson. A paper based on the results of this work [177], has been accepted for publication in *Physical Review Letters*.

**Table 6.3:** Parameters of the Gaussian-type of potential with statistical and systematic uncertainties extracted from the bootstrap fit.

Variable	Result	$\sigma_{\text{stat}}$	$\sigma_{\text{syst}}$
$V_{\text{eff}}$ (MeV)	2.52	0.85	1.40
$\mu$ (fm $^{-2}$ )	0.14	0.06	0.09

**Table 6.4:** Parameters of the Yukawa-type of potential with statistical and systematic uncertainties extracted from the bootstrap fit.

Variable	Result	$\sigma_{\text{stat}}$	$\sigma_{\text{syst}}$
$A$	0.021	0.009	0.006
$\alpha$ (MeV)	65.90	38.04	17.52

## 6.2 Discussion

There are several approaches and experiments which derive the scattering length of the  $p$ - $\phi$  interaction and can be used as a comparison to the results obtained in this work. Some are listed in the following:

- An analysis of differential cross section measurements near threshold from  $\phi$  photoproduction data recorded with the CLAS experiment reports  $|f_0| = (0.063 \pm 0.010)$  fm [179].
- From QCD sum rules a value of  $f_0 = (-0.15 \pm 0.02)$  fm [180] is obtained, which is in agreement with results of the  $\phi$  differential cross section near-threshold, measured by the LEPS collaboration [181, 182].
- By modeling the forward  $N$ - $\phi$  scattering amplitude based on an effective Lagrangian combining chiral SU(3) dynamics with vector meson dominance, an effective scattering length of  $f_0 = (-0.01 + i0.08)$  fm is found [183].
- By means of an attractive QCD van der Waals potential for  $N$ - $\phi$ , employed in a bound state analysis, a scattering length of 2.37 fm is found [51]. This approach assumes a Yukawa-type potential of strength  $A = 1.25$  and  $\alpha = 600$  MeV.

Notably, the values from literature are inconclusive as they deviate among the different approaches and contradict the results presented in Sec. 6.1. Besides some of the results being only theoretical calculations, the measured ones listed above, are derived in a model-dependent manner as the data refer to the properties of the  $\phi$  meson within the nucleus. Therefore, they are strongly dependent on the exact modeling of the surrounding medium. Accessing the interaction in a two-body system instead, provides a much cleaner approach. Therefore, the femtoscopy method utilized in this work to directly measure the two-body  $N$ - $\phi$  interaction in vacuum, provides constraints to theoretical models, hence, improves the interpretation of results from nuclear collisions, related to the search for chiral symmetry restoration.

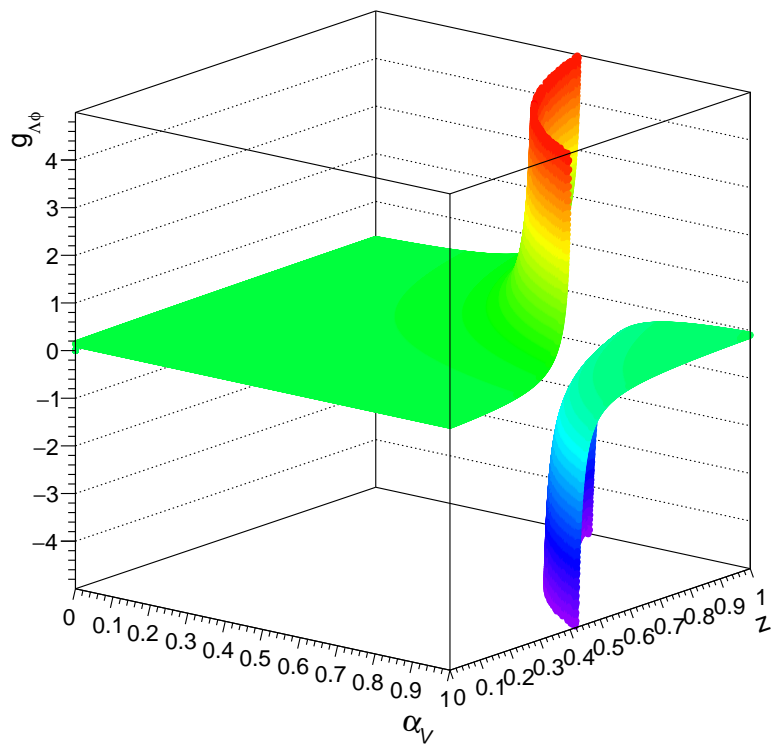
Additionally, the  $N$ - $\phi$  coupling constant can be directly extracted from the results obtained from the Yukawa-type potential as  $g_{N-\phi} = \sqrt{A}$ . It is found to be  $g_{N-\phi} = 0.14 \pm 0.03$  (stat.)  $\pm 0.02$  (syst.). This result contradicts calculations employing pure SU(6) symmetry, which lead to a vanishing  $g_{N-\phi} = 0$ . However, the small value found in this work is compatible with expectations of a weak  $N$ - $\phi$  coupling, as discussed in Sec. 1.4. The  $N$ - $\phi$  coupling constant also provides indirect access to the  $Y$ - $Y$  interaction in neutron stars via Eq. 1.14, where the measured  $g_{N-\phi}$  are related to  $g_{Y-\phi}$ , relevant for the  $\phi$  meson exchange between hyperons in NS.

Figure 6.4 shows the resulting coupling constant in the specific case of  $\Lambda$  hyperons as function of  $\alpha_V$  and  $z$ , assuming  $g_{N-\phi} = 0.14$ . As already discussed in Sec. 1.4, the variable  $\alpha_V = F/(F + D)$  weighs the symmetric (D) and the anti-symmetric (F) part of the octet-octet interaction, while  $z = g_8/g_1$  is the ratio of the meson singlet and octet coupling constants  $g_1$  and  $g_8$ . In the specific case of SU(6) symmetry, these variables take the values  $z = 1/\sqrt{6}$  and  $\alpha_V = 1$ . Notably, most combinations of  $z$  and  $\alpha_V$  lead to a vanishing  $g_{\Lambda-\phi}$ . This is in agreement with results obtained from femtosopic measurements of the  $\Lambda$ - $\Lambda$  interaction, which is found to be weakly attractive [184].

As discussed in Sec. 6.1, the parameter values of a Gaussian-type potential used to parameterize the results on the strong interaction among  $N$ - $J/\psi$  ( $N$ - $c\bar{c}$ ) obtained from lattice QCD calculations [178] deviate strongly from the ones obtained for  $p$ - $\phi$  ( $N$ - $s\bar{s}$ ). As the interaction mechanism

is expected to be similar for both pairs, it might be interesting to extend correlation measurements to the charm sector, in order to investigate and understand the origin of such difference.

However, as the uncertainties of the experimental results are still relatively large, more data are needed to extract precise parameter values, especially of the imaginary part of the scattering length, and the here reported results should serve as an input for more advanced modelings in medium. Data taken at the LHC during the upcoming Run 3 and Run 4 will significantly improve the precision of the extracted interaction parameters.



**Figure 6.4:** The coupling constant  $g_{\Lambda\phi}$  as function of  $\alpha_V$  and  $z$ , assuming  $g_{N-\phi} = 0.14$ .



## 7 Summary

This work presents the first femtoscopic measurement of the  $p$ - $\phi$  correlation function in high multiplicity pp collisions at  $\sqrt{s} = 13$  TeV. A paper based on the results of this work [177], has been accepted for publication in *Physical Review Letters*.

The analysis is conducted employing data measured by the ALICE experiment at the Large Hadron Collider (LHC) during the Run 2 data-taking period. The  $\phi$  candidates are reconstructed from the  $\phi \rightarrow K^+K^-$  decay channel with a branching ratio of  $\sim 50\%$ , while the protons are detected directly. In total, about  $4.17 \times 10^4$   $p$ - $\phi$  and  $3.61 \times 10^4$   $\bar{p}$ - $\phi$  pairs with small relative momenta of  $k^* < 200$  MeV/ $c$  are found. The corresponding measured correlation functions are compatible within uncertainties and consequently combined as  $p$ - $\phi \oplus \bar{p}$ - $\phi$ .

The resulting total correlation function  $C_{\text{tot}}(k^*)$  shows indicates an attractive interaction between the two particles at small  $k^*$ , where it is sensitive to the strong final-state interaction (FSI). However, an enhancement in the intermediate  $k^*$  region hints at the existence of additional contributions, which are studied and accounted for in the analysis in order to obtain a conclusion on the genuine  $p$ - $\phi$  interaction.

First of all,  $C_{\text{tot}}(k^*)$  is affected by so-called minijets, which are associated with hard parton-parton scatterings. The resulting long-ranged contribution to the measured correlation function consists of auto-correlated protons and  $\phi$  mesons emitted in jet-like structures and can be effectively suppressed by selecting spherical events. This is achieved by applying cuts on the transverse sphericity of the event ( $0.7 < S_T < 1.0$  [161]). The remaining mini-jet background  $C_{\text{MJ},p-\phi}$  is modelled using PYTHIA 8 simulated data. The rise of the correlation function at large  $k^*$  is associated to energy-momentum conservation effects and accounted for by a baseline. Both contributions do not arise from strong FSI and therefore contribute to the non-femtoscopic background.

As the reconstructed  $\phi$  candidates have a moderate purity of  $\sim 57\%$  in the transverse momentum region of interest, additional contributions from the combinatorial  $p$ -( $K^+K^-$ ) background are present in the measured signal. The observed correlation signal arises mainly from two-body interactions among the triplet. It can be measured by pairing protons with the candidates in the sidebands, which correspond to the intervals next to the  $\phi$  resonance in the invariant mass distribution. The so obtained left and right sideband correlation functions are combined as weighted sum in order to describe the combinatorial background  $C_{pKK}(k^*)$ . The weights correspond to the relative amount of background present underneath the  $\phi$  meson resonance in the left and right half of the invariant mass interval, which is also used to reconstruct the  $\phi$  candidates. All other femtoscopic contributions which can be associated with strong FSI are assumed to be flat.

Finally, the background contributions are combined with the respective weights, which are obtained from single-particle properties. By correcting the measured signal for these contributions, the genuine  $p$ - $\phi$  correlation function is extracted from the data.

In order to access information on the underlying strong interaction, the genuine  $p$ - $\phi$  correlation function is compared to the one obtained from different theoretical approaches and models. In addition to the two-particle wave-function, incorporating the FSI, the correlation function also depends on the particle-emission via the source function, which has to be well understood in

order to study the  $p\text{-}\phi$  interaction. It is parameterized by a Gaussian core, which depends on the transverse mass of the pair and is constrained from  $p\text{-}p$  correlation measurements [164]. Short-lived strongly decaying resonances feeding protons, which effectively increase the core radius, are taken into account.

Having constrained the particle-emitting source it is possible to extract the scattering parameters of the interaction. The fit of the genuine  $p\text{-}\phi$  correlation with the Lednický-Lyuboshits model determines  $\Re(f_0) = 0.85 \pm 0.34$  (stat.)  $\pm 0.14$  (syst.) fm,  $\Im(f_0) = 0.16 \pm 0.10$  (stat.)  $\pm 0.09$  (syst.) fm, and  $d_0 = 7.85 \pm 1.54$  (stat.)  $\pm 0.26$  (syst.) fm. Remarkably, the imaginary contribution to the scattering length vanishes within the uncertainties, indicating that inelastic processes do not play a prominent role and the  $p\text{-}\phi$  interaction in vacuum is dominated by elastic contributions. Also, a  $N\text{-}\phi$  bound state can be excluded due to the large effective range  $d_0$  and  $\Re(f_0) > 0$ .

Finally, phenomenological potentials are probed. The corresponding correlation function is derived by employing the Correlation Analysis Tool using the Schrödinger Equation (CATS) [121], which solves the Schrödinger Equation for a given potential.

The values of the parameters for a Gaussian-type potential (Eq.2.27) are found to be  $V_{\text{eff}} = 2.52 \pm 0.85$  (stat.)  $\pm 1.40$  (syst.) MeV and  $\mu = 0.14 \pm 0.06$  (stat.)  $\pm 0.09$  (syst.)  $\text{fm}^{-2}$ , again indicating a shallow strong interaction potential. The  $N\text{-}\phi$  ( $N\text{-}\bar{s}s$ ) system is expected to behave very similar to  $N\text{-}J/\psi$  ( $N\text{-}\bar{c}c$ ), as in both cases the interaction is expected to be suppressed by the OZI rule. However, the  $N\text{-}\phi$  potential is much more shallow than results from lattice QCD calculations of the strong interaction among  $N\text{-}J/\psi$  performed by the HAL QCD collaboration [178].

Employing a Yukawa-type potential (Eq. 2.26) yields  $A = 0.021 \pm 0.009$  (stat.)  $\pm 0.006$  (syst.) and  $\alpha = 65.90 \pm 38.04$  (stat.)  $\pm 17.52$  (syst.) MeV. The  $N\text{-}\phi$  coupling constant can be directly extracted from these results as  $g_{N\text{-}\phi} = \sqrt{A}$  and is found to be  $g_{N\text{-}\phi} = 0.14 \pm 0.03$  (stat.)  $\pm 0.02$  (syst.), which suggests a weak but non-vanishing coupling between the two particles. Additionally, the parameter values are significantly smaller than the ones from studies of possible  $N\text{-}\phi$  bound states, which use the same kind of potential with  $\alpha = 600$  MeV and  $A = 1.25$  [51].

Overall, this work provides valuable experimental input to improve the understanding of the  $N\text{-}\phi$  interaction, which is relevant for the more fundamental studies on the partial restoration of chiral symmetry in-medium. Additionally, in the context of the effective meson-exchange picture of the interaction, it is possible to link the extracted  $N\text{-}\phi$  coupling constant to the hyperon-hyperon interaction in neutron stars via SU(3) relations. Such results can contribute to pin down the equation of state of dense hadronic matter, which is still an important topic of ongoing research.

Data from the upcoming Run 3 of the LHC will significantly reduce the uncertainties, providing even more stringent constraints. Also extending correlation measurements to the charm sector will help to understand the unexpected deviation between the predicted  $N\text{-}J/\psi$  interaction potential and the one obtained experimentally for  $N\text{-}\phi$ . Therefore, this work paves the way for a detailed understanding of the gluon-exchange picture of the interaction.

# A Sideband kinematics and momentum transformation

In the following a data-driven approach is described to derive an effective proton-kaon correlation function  $p\text{-}K_{\text{eff}}$ , incorporating the two- and three-body interactions among  $p$ ,  $K^+$  and  $K^-$ , which can be used to extract the combinatorial background of the experimental  $p\text{-}\phi$  correlation function.

The main obstacle to obtaining a description of the combinatorial background is the fact that the measured left and right sideband differ from each other at low  $k^*$  and it is not obvious that they can be combined. The different choice of  $M_{K^+K^-}$  modifies the kinematics and accordingly different kinematic regimes of the correlation function are probed. The assumption of the approach, presented in the following, is that the actual interaction among the triplet  $p\text{-}(K^+K^-)$  is independent of the invariant mass of the system.

To correct for the different kinematics resulting from the different choice of invariant mass of the  $K^+K^-$  system, phase space simulations are conducted. Therefore, by using random values of  $\eta$ ,  $p_T$  and  $\varphi$  of the kaon and proton candidates according to the experimental distributions, the relative momenta of  $p\text{-}K^+$  and  $p\text{-}K^-$  and  $p\text{-}(K^+K^-)$  can be related to one another. Since the mass of  $K^+$  and  $K^-$  is the same, no differentiation among the two is necessary. Accordingly, the three-body variables of  $p\text{-}(K^+K^-)$  can be projected onto an effective two-body system. This way, different kinematic transformation matrices are computed for different invariant mass windows  $M_{K^+K^-}$ , where the relative momentum of the  $p\text{-}K$  system can be found on the  $x$ -axis. The  $y$ -axis displays the  $k^*$  of  $p\text{-}(K^+K^-)$  or  $p\text{-}\phi$ , depending on the selected invariant mass interval, which is also the relative momentum of the measured correlation functions.

With these momentum transformation matrices, it is possible to transform the  $k^*$  of one momentum system to another and study the kinematic effects in the sidebands. The goal is then to use different sidebands, distributed all over the  $k^*$  range, to derive a general  $p\text{-}K_{\text{eff}}$  correlation function describing the interaction among the triplet. In a final step, this correlation function is transformed to the kinematic regime of the  $p\text{-}\phi$  pair. The whole process can be written as

$$p\text{-}(K^+K^-) \rightarrow p\text{-}K_{\text{eff}} \rightarrow p\text{-}\phi. \quad (\text{A.1})$$

The second transformation,  $p\text{-}K \rightarrow p\text{-}\phi$ , is a simple matrix multiplication  $\text{BG}_{p\text{-}\phi} = M_{p\text{-}\phi} \cdot \text{BG}_{pK}$ , where the lower index describes the momentum system depending on the invariant mass window,  $M$  is the corresponding momentum transformation matrix and  $\text{bkg}_{p\text{-}\phi}$  is the combinatorial background of  $p\text{-}(K^+K^-)$  in the kinematic regime of the  $p\text{-}\phi$  correlation function.  $\text{BG}_{pK}$  will be denoted as effective proton-kaon correlation function  $p\text{-}K_{\text{eff}}$ , incorporating the two- and three-body interactions, which are not yet known.

The first transformation, namely  $p\text{-}(K^+K^-) \rightarrow p\text{-}K$ , is more complicated as the experimental sideband correlation functions are measured in the  $p\text{-}(K^+K^-)$  momentum system. Therefore, by matrix inversion an expression for the effective proton-kaon correlation function is obtained  $\text{BG}_{pK} = M_{p\text{-}(K^+K^-),i}^{-1} \cdot \text{BG}_{p\text{-}(K^+K^-),i}$ , where  $\text{BG}_{p\text{-}(K^+K^-),i}$  corresponds to the measured sideband correlation function in the invariant mass interval  $i$ .

As it is not trivial to invert the momentum transformation matrices in order to unfold the measured sideband correlation functions, an alternative approach is used to obtain  $p\text{-}K_{\text{eff}}$ , which uses

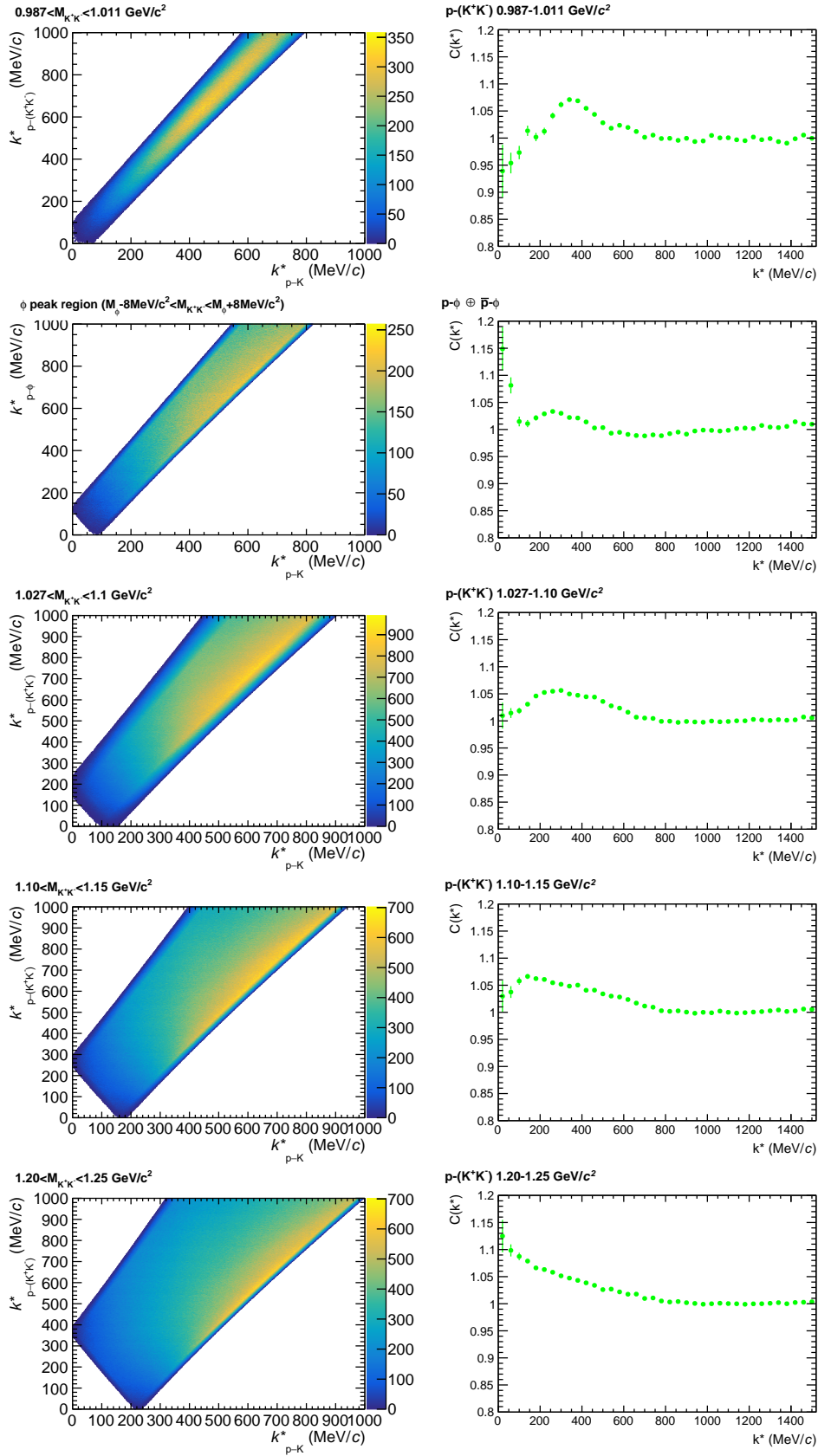
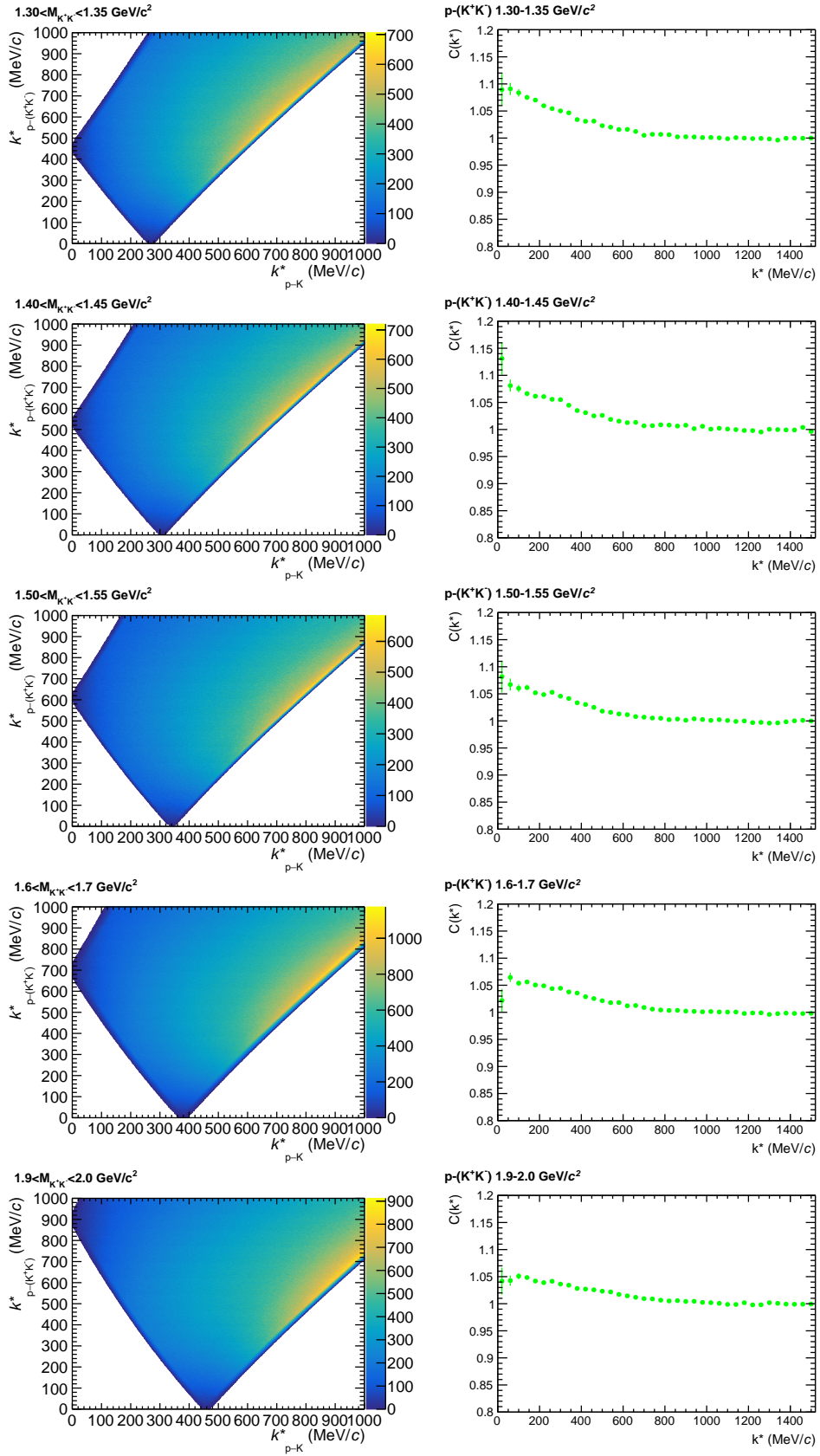


Figure A.1: Momentum transformation matrices and correlation function for different invariant mass windows.



**Figure A.2:** Momentum transformation matrices and correlation function for different invariant mass windows.

the fact that for low relative momentum of the sidebands ( $y$ -axis of the matrices) the momentum of the  $p - K$  system is tested within a relatively small range ( $x$ -axis), see Fig. A.1 and A.2. What is also noticeable, is the fact that with increasing invariant mass, this sector moves to larger  $k_{pK}^*$ . This can be ultimately used to derive  $p-K_{\text{eff}}$  by combining different sideband correlation functions. The method is illustrated in Fig. A.3. It takes a low  $k^*$ -bin of one sideband correlation function while considering the bin width. The corresponding slice in the momentum transformation matrix of the sideband is then projected to the  $x$ -axis to get a distribution of the relative momentum in the kinematic system of  $p - K$ . The mean value of this distribution is then taken as  $k_{pK}^*$  and the width of the distribution is the corresponding uncertainty in  $x$ , whereas the  $y$ -value and statistical uncertainty is taken from the bin in the sideband correlation function. This is then repeated for several invariant mass windows of the sidebands, where each time one data point of the effective proton-kaon function is obtained. The relative momentum of the specific function can then be transformed to the system of interest via the corresponding transformation matrix ( $BG_{p-i} = M_{p-i} \cdot BG_{pK}$ ), which gives the correlation function of the combinatorial background, considering the kinematics of the system. The results from using first, second and third bin of the sideband correlation functions are in agreement within the uncertainties, see Fig. A.4. Therefore, the second bin is used to extract  $p-K_{\text{eff}}$ , as it is the best choice concerning the uncertainties in  $x$  and the statistical ones. Due to the still large errors the data points will be only used as rough estimate of the shape of  $p-K_{\text{eff}}$ .

In a next step, the graph is pre-fitted with a Gaussian on top of a background described by polynomials. The latter consists of a polynomial of second-order up to 600 MeV/c matched with a first-order polynomial to describe the flat behavior at large  $k_{pK}^*$ . The uncertainties of the data points are reflected in relatively large errors of the fit result. Therefore, it is necessary to also include the measured sidebands next to the  $\phi$ -peak (notably not the same intervals as left and right sideband of Sec. 5.3.1) and the corresponding sideband functions in the fitting procedure, to constrain  $p-K_{\text{eff}}$  more efficiently. These sideband functions are obtained when transforming  $p-K_{\text{eff}}$  to the momentum system of the left and right sideband ( $BG_{\text{left/right}} = M_{\text{left/right}} \cdot BG_{pK}$ ). If the effective proton-kaon function is accurate, they should agree with the measured sideband correlation function.

In a next step, the Minuit minimization package is used [185] with the Migrad algorithm and start parameters obtained by the pre-fit, in order to parallel minimize the  $\chi^2$  of the  $p-K_{\text{eff}}$ -fit and the  $\chi^2$  obtained from the difference between the experimental left and right sideband and the corresponding sideband functions obtained by momentum transformation. The results of the pre-fit, as well as the parallel minimization fit, can be seen in Fig. A.5. From the Minuit result of  $p-K_{\text{eff}}$  a function for the combinatorial background can be derived via the transformation  $p-K \rightarrow p-\phi$  and a re-normalization, which is in agreement with the weighted sum of left and right sideband from Sec. 5.3.1, see Fig. A.5. As it is a more direct and data-driven approach, the latter is employed to model the contribution of the combinatorial background in the correlation function. However, the method introduced in this section can be used to cross-check and validate the experimental results.

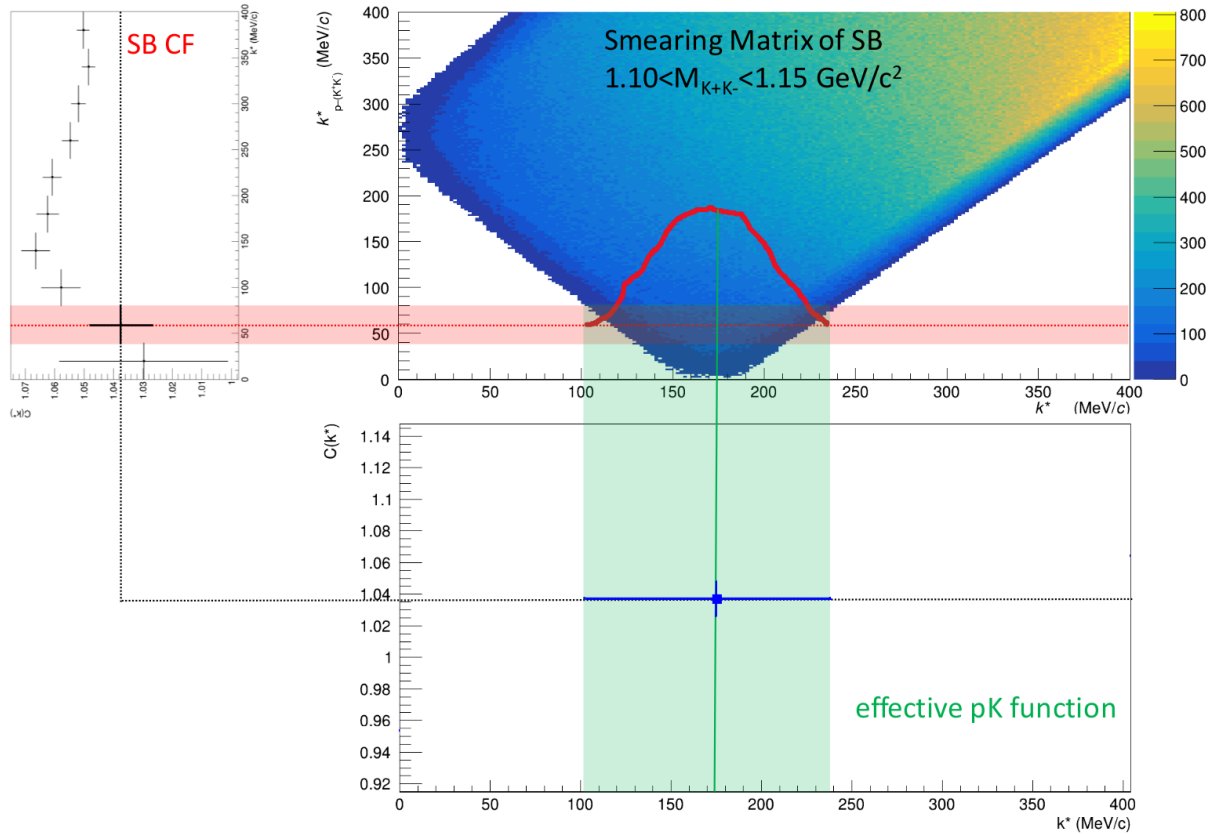


**Figure A.3:** Illustration of how a qualitative description of  $p\text{-}K_{\text{eff}}$  is derived. At the beginning, the second bin of a sideband correlation function (here the one within  $1.028 < M_{K^+K^-} < 1.044$  GeV) is taken, while also considering its bin-width. Then the corresponding slice of the momentum smearing matrix is projected to the x-axis to obtain a momentum distribution in  $k_{pK}^*$ . From this a point of  $p\text{-}K_{\text{eff}}$  is acquired, where  $k_{pK}^*$  the mean value of the distribution, with an uncertainty that corresponds to the width of the distribution and the y-value and corresponding statistical uncertainty is taken from the measured sideband bin.

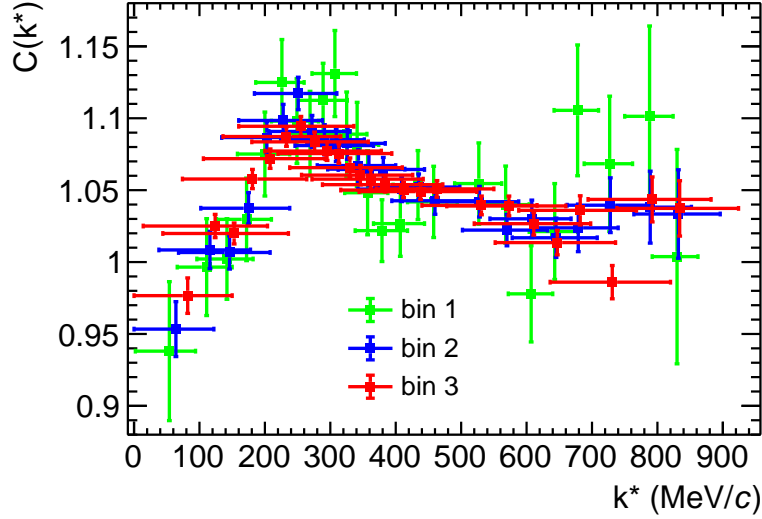


**Figure A.4:** The  $p$ - $K_{\text{eff}}$  obtained by using the first, second and third bin entry of the measured sideband correlation functions. Within the uncertainties they are in agreement with each other.

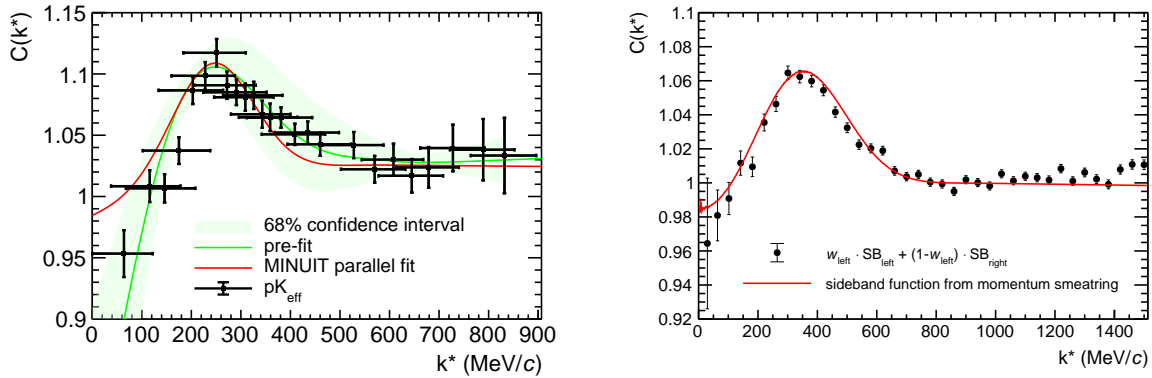


**Figure A.5:** On the left plot the effective proton-kaon correlation function  $p$ - $K_{\text{eff}}$  is shown as well as the pre-fit with confidence interval and the result of the parallel minimization using MINUIT. The right plot shows the combinatorial background obtained from experimental data together with the function that is derived from  $p$ - $K_{\text{eff}}$  using the transformation matrix that relates the relative momentum of  $p$ - $\phi$  to  $p$ - $K$ .

## B Projector Method

The combinatorial background of  $p\text{--}(K^+K^-)$ , which arises from the moderate purity of the  $\phi$  mesons reconstructed through the decay to charged kaons, can be studied by employing the projector method [186]. This formalism describes the three-body correlation function between the  $p\text{--}(K^+K^-)$  triplet in terms of the respective two-body correlation functions by projecting them into the  $p\text{--}\phi$  relative momentum  $k_{p\phi}^*$ . In the following the three-body interaction is assumed to be negligibly small.

According to the Kubo's cumulant expansion rule [187], the triplet sample denoted by  $(p, K^+, K^-)$  can be decomposed as

$$(p, K^+, K^-) = -2 \times (p)(K^+)(K^-) + ([p, K^+], K^-) + ([p, K^-], K^+) + ([K^+, K^-], p) + ([p, K^+, K^-]), \quad (\text{B.1})$$

where the particles in the squared brackets interact with each other, while the ones outside are not correlated and treated as spectators. Hence, in absence of a genuine three-body interaction the contribution from  $([p, K^+, K^-])$  drops out. In terms of correlation functions, this results in

$$C_3(\vec{p}_p, \vec{p}_{K^+}, \vec{p}_{K^-}) = C_3([\vec{p}_p, \vec{p}_{K^+}], \vec{p}_{K^-}) + C_3([\vec{p}_p, \vec{p}_{K^-}], \vec{p}_{K^+}) + C_3([\vec{p}_{K^+}, \vec{p}_{K^-}], \vec{p}_p) - 2, \quad (\text{B.2})$$

where  $\vec{p}_i$  are the momentum vectors of the individual particles in the laboratory reference frame. It is shown in Ref. [186] that, if one of the three particle is a spectator, the correlation function  $C_3([\vec{p}_i, \vec{p}_j], \vec{p}_k)$  is equivalent to the two-body correlation function of the interacting pair, i.e.  $C_3([\vec{p}_i, \vec{p}_j], \vec{p}_k) = C_{ij}(\vec{p}_i, \vec{p}_j)$ .

The relative momentum of the  $p\text{--}\phi$  pair is defined as

$$\vec{k}_{p\phi} = \frac{m_\phi}{m_p + m_\phi} \vec{p}_p - \frac{m_p}{m_p + m_\phi} (\vec{p}_{K^+} + \vec{p}_{K^-}). \quad (\text{B.3})$$

In the non-relativistic approximation the relative momentum is a Lorentz invariant and  $k_{p\phi} = k_{p\phi}^*$ , where the \* symbol denotes the center-of-mass frame of the  $p\text{--}\phi$  pair. The projection of each term in the right side of Eq. B.2 onto  $k_{p\phi}^*$  is performed as

$$C_{ij}(k_{p\phi}^*) = \iiint_{(\vec{p}_i, \vec{p}_j, \vec{p}_k) \in \mathcal{D}} C_{ij}(\vec{p}_i, \vec{p}_j) d^3\vec{p}_i d^3\vec{p}_j d^3\vec{p}_k, \quad (\text{B.4})$$

where the integration domain  $\mathcal{D}$  is defined by the equation  $k_{p\phi}^* = \text{constant}$ . Applying now Eq. B.4 to all the terms in Eq. B.2 the correlation function due to the combinatorial  $p\text{--}(K^+K^-)$  background is obtained as

$$C_{pK^+K^-}(k_{p\phi}^*) = C_{pK^+}(k_{p\phi}^*) + C_{pK^-}(k_{p\phi}^*) + C_{K^+K^-}(k_{p\phi}^*) - 2. \quad (\text{B.5})$$

More precisely, to account for the kinematic constraint imposed by the cut in the  $K^+K^-$  invariant mass (i.e.  $M_{K^+K^-} \in [M_\phi - \delta, M_\phi + \delta]$  with  $\delta = 8 \text{ MeV}/c^2$ ) used to select the  $\phi$  candidates (see Fig. 4.8), the projection is performed in two steps. First, the integral in Eq. B.4 is calculated by

fixing the invariant mass  $M_{K^+K^-}$ . The integration domain is then

$$\mathcal{D} = \{(\vec{p}_1, \vec{p}_2, \vec{p}_3) \in \mathcal{S} | k_{p\phi}^* = \text{constant} \wedge M_{K^+K^-} = \text{constant}\}. \quad (\text{B.6})$$

In the second step, the resulting projected correlation function  $C_{ij}(k_{p\phi}^*; M_{K^+K^-})$  at fixed  $M_{K^+K^-}$  is weighted as

$$C_{ij}(k_{p\phi}^*) = \int_{M_{\phi}-\delta}^{M_{\phi}+\delta} C_{ij}(k_{p\phi}^*; M_{K^+K^-}) w_{bkg}(M_{K^+K^-}) dM_{K^+K^-}. \quad (\text{B.7})$$

The weight  $w_{bkg}$  is given by

$$w_{bkg}(M_{K^+K^-}) = \frac{f_{bkg}(M_{K^+K^-})}{\int_{M_{\phi}-\delta}^{M_{\phi}+\delta} f_{bkg}(M_{K^+K^-}) dM_{K^+K^-}}, \quad (\text{B.8})$$

where  $f_{bkg}$  is the function used to describe the background, which is a quadratic polynomial in the specific case of  $p$ - $\phi$ .

The two-body correlation functions are obtained experimentally by employing the same kaon and proton candidate selection cuts as in Tab. 4.2 and 4.3 in chapter 4. Given the conditions in Eq. B.6, the contribution from  $K^+K^-$  is flat when projected onto  $k_{p\phi}^*$ . Therefore, the shape of the combinatorial background  $p$ -( $K^+K^-$ ) is driven by the interaction among  $p$ - $K^+$  and  $p$ - $K^-$ . The corresponding experimental correlation functions, not yet projected into the  $k_{p\phi}^*$ , are shown in Fig. B.1. Following [161], both are normalized within  $k^* \in [400, 600]$  MeV/c. No unfolding is performed, which accounts for the finite momentum resolution of ALICE, as the effect is found to be negligible [161].

Figure B.2 shows the combinatorial  $p$ -( $K^+K^-$ ) background obtained from the projector method

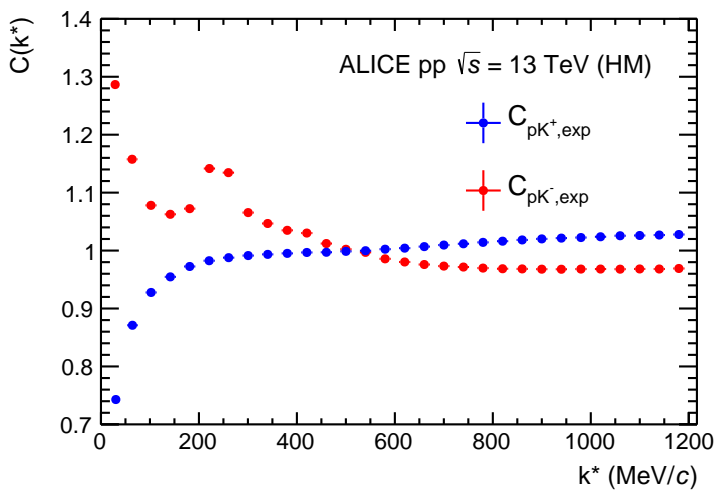


**Figure B.1:** Experimental correlation function of  $p$ - $K^+$  and  $p$ - $K^-$  obtained from the particle selection in Sec. 4.2.2.1. Both are normalized in the range  $[400, 600]$  MeV/c, following [161].

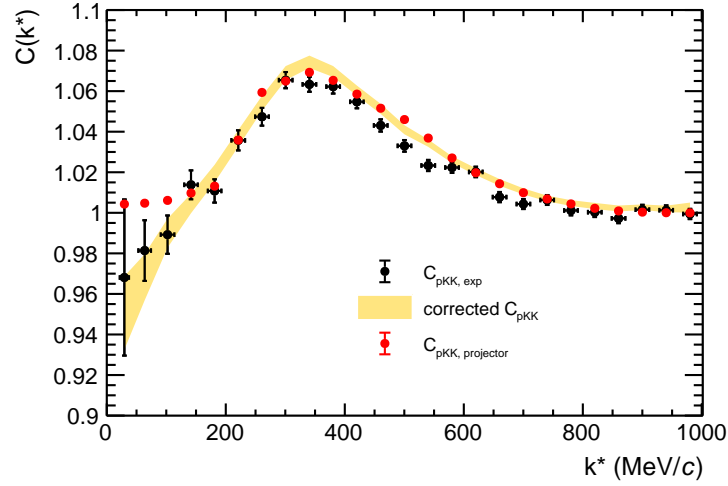


**Figure B.2:** Comparison of the combinatorial background obtained from the sideband analysis and projector method.

(red dots). Within the uncertainties, it is compatible with the results from the sideband approach (black dots). When compared to the corrected sideband correlation function (orange band), where the residual  $\phi$  mesons in the sideband intervals are considered (Sec. 5.3.1), a deviation at small  $k^*$  is found. This might suggest that the genuine three-body interaction among the triplet is non-negligible. Deeper studies are required in order to draw a final conclusion. For this reason, the data-driven sideband approach has been used to extract the final results of this analysis. Anyways, the study performed with the projector method confirms that the combinatorial  $p-(K^+K^-)$  background to the  $p-\phi$  correlation function is properly accounted for by the sideband approach.



## C Scattering parameters of the potential approach

It is possible to extract the scattering parameters of a potential from the phase-shift of the corresponding wave-function via Eq. 2.16. Figure C.1 shows exemplary the phase-shift as function of  $k^*$  for a Gaussian-type of potential with parameters from Sec. 6.1. The corresponding  $k^* \cot(\delta(k^*))$  and parameterization with the *effective range expansion* (Eq. 2.16) is depicted on the right.

When considering systematic and statistic uncertainties of both the Gaussian- and Yukawa-type potential obtained from the fit to data (Sec. 6.1), a phase-space of possible scattering parameters can be derived. For each parameter combination a correlation function is obtained by employing CATS and the degree of consistency between data and calculation is expressed by the  $\chi^2$  for  $k^* < 200$  MeV/c. Figure C.2 shows the resulting phase-space for both potential types and the corresponding  $n\sigma$  levels with respect to the minimum  $\chi^2$ . It can be seen that the Yukawa-type potential, Fig. C.2a, yields much larger effective ranges than the Gaussian one, shown in Fig. C.2b, and does not constrain the phase-space significantly, including also unphysically large values of the scattering length. The  $1\sigma$  contour constrains the scattering parameters to  $f_0 \in [0.33, 1.16]$  fm and  $d_0 \in [11.48, 16.73]$  fm for the Gaussian-type of potential. In case of the Yukawa-type  $f_0 \in [0.39, 9.03]$  fm and  $d_0 \in [17.19, 35.62]$  fm are obtained. While the scattering length  $f_0$  is found to be consistent with the results obtained from the Lednický–Lyuboshits approach, summarized in Tab. 6.2, the effective range  $d_0$  is much larger.

Additionally, this approach allows testing the results obtained from the Lednický–Lyuboshits model, which includes a correction term for small sources [118]. However, as already mentioned in Sec. 2.2.2, this might result in additional uncertainties on the resulting scattering parameters due to their limited accuracy for large effective ranges induced by the correction term  $\propto d_0/r_0$ .

Figure C.3 shows the correlation function of the Lednický–Lyuboshits approach with values from Tab. 6.2 and the best matching Gaussian potential, from which  $d_0 = 15.10 \pm 0.51$  fm and

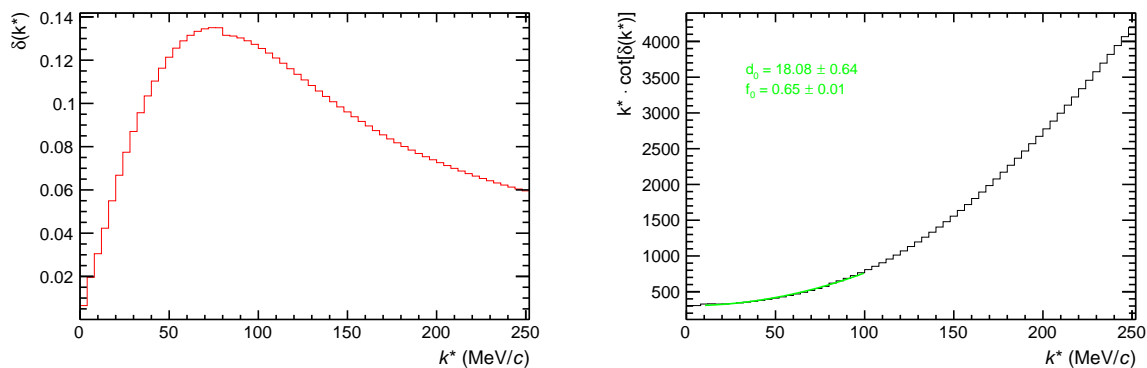


**Figure C.1:** *Left:* The phase-shift of the wave-function evaluated for a Gaussian potential ( $V_{\text{eff}} = 2.52$  MeV,  $\mu = 0.14$  fm $^{-2}$ ) as function of  $k^*$ . *Right:* Corresponding  $k^* \cot(\delta(k^*))$  fitted with Eq. 2.16 to extract the scattering parameters.

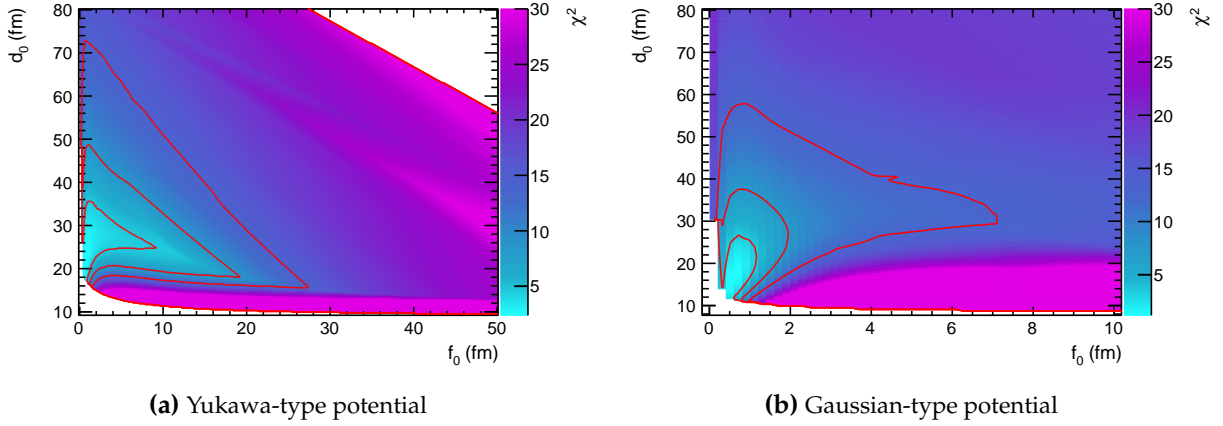


**Figure C.2:** Scattering parameter phase-space for both Yukawa (left) and Gaussian type of potential (right). The degree of consistency is expressed as the number of  $\sigma$  with regard to the  $\chi^2$  for  $k^* < 200$  MeV/c between data and correlation function of the respective potential, which is obtained by employing CATS.

$f_0 = 0.62 \pm 0.01$  fm can be derived. When compared to the Lednický-Lyuboshits values a deviation of 6.8 fm between the effective ranges  $d_0$  is observed and 0.33 fm between the scattering lengths  $f_0$ .

Due to a lack of alternative methods, those could be interpreted as the errors related to the small source correction term in the Lednický-Lyuboshits approach, which also hold when considering a complex scattering length. However, this conclusion assumes that the Gaussian-type of potential is the correct approach to the  $p$ - $\phi$  interaction. Generally, such inconsistency just highlights the importance of more advanced theoretical models.

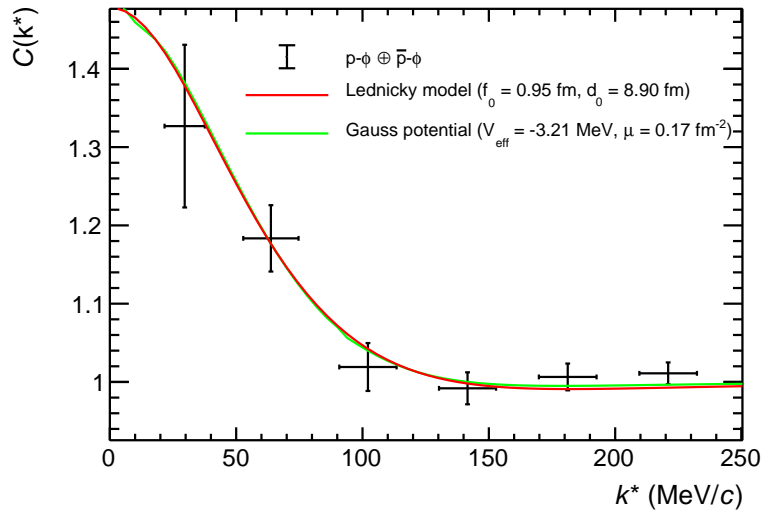


**Figure C.3:** Comparison between the Lednický-Lyuboshits approach and Gaussian potential approach. From the potential the scattering parameters  $d_0 = 15.10 \pm 0.51$  fm and  $f_0 = 0.62 \pm 0.01$  fm can be derived, which deviate from the Lednický-Lyuboshits result.

## D Figures to the $p\text{--}\phi$ femtoscopic fits

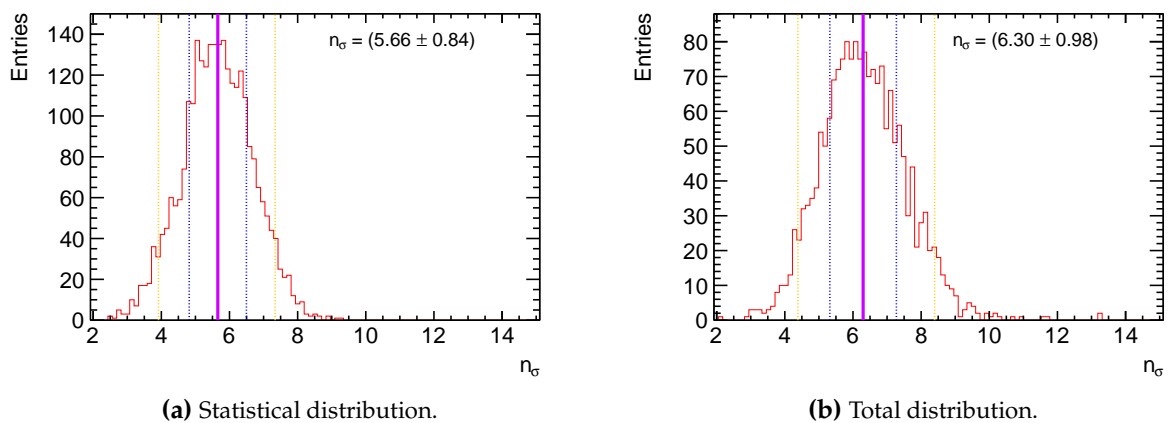


**Figure D.1:** Distribution of  $n_\sigma$  between data and  $C(k^*) = 1$  obtained from the bootstrap only method and combined with systematic variations. The mean of the central interval (including 90% of the entries) is displayed as solid pink line and the corresponding limits within the standard deviation as dashed blue lines. The interval limits are dashed yellow lines. From this, the value and statistical and total error of the parameters is obtained.

## D.1 Lednický-Lyuboshits approach with complex scattering length

### D.1.1 Full model

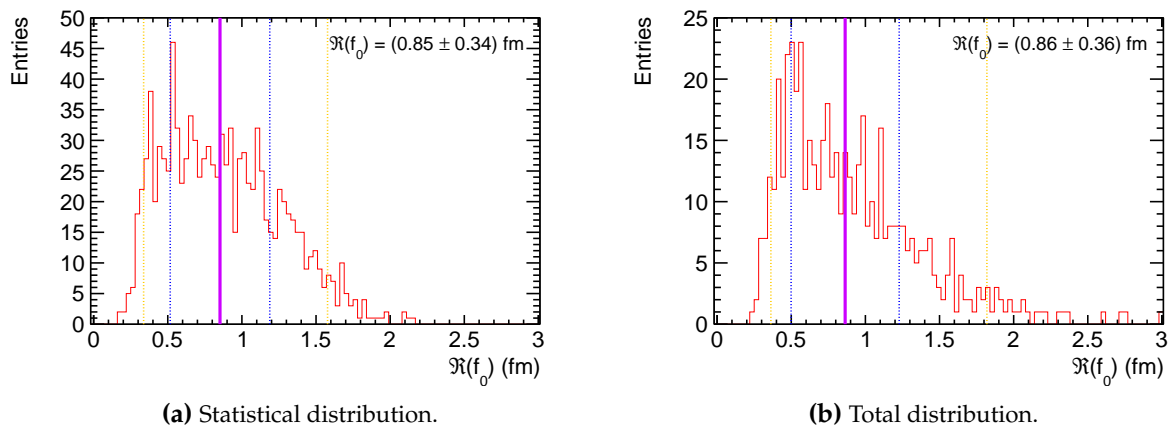
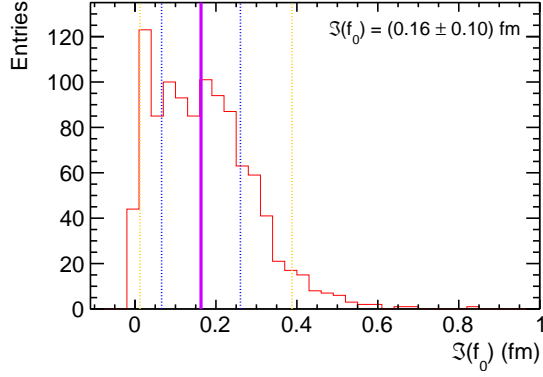
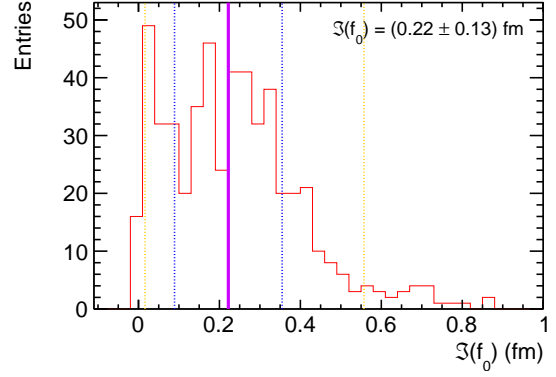


**Figure D.2:** Distribution of  $\Re(f_0)$  obtained from the bootstrap only method and combined with systematic variations. The mean of the central interval (including 90% of the entries) is displayed as solid pink line and the corresponding limits within the standard deviation as dashed blue lines. The interval limits are dashed yellow lines. From this, the value and statistical and total error of the parameters is obtained.

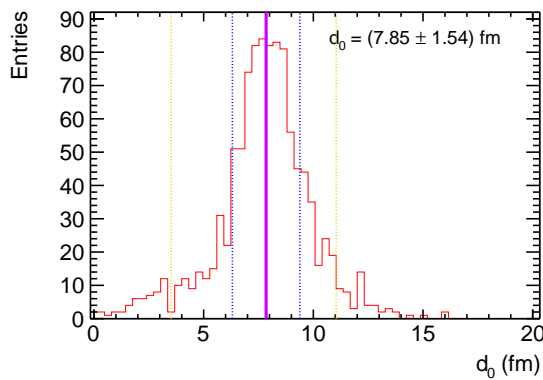


(a) Statistical distribution.

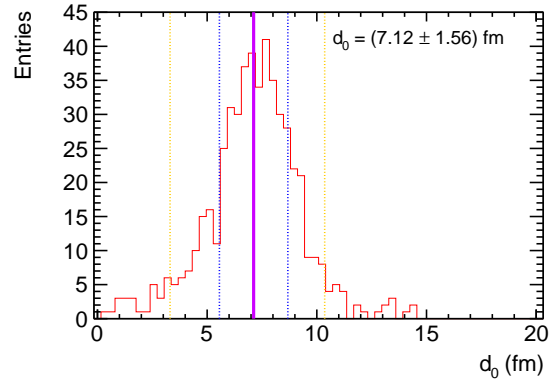


(b) Total distribution.

**Figure D.3:** Distribution of  $\mathfrak{S}(f_0)$  obtained from the bootstrap only method and combined with systematic variations. The mean of the central interval (including 90% of the entries) is displayed as solid pink line and the corresponding limits within the standard deviation as dashed blue lines. The interval limits are dashed yellow lines. From this, the value and statistical and total error of the parameters is obtained.



(a) Statistical distribution.



(b) Total distribution.

**Figure D.4:** Distribution of  $d_0$  obtained from the bootstrap only method and combined with systematic variations. The mean of the central interval (including 90% of the entries) is displayed as solid pink line and the corresponding limits within the standard deviation as dashed blue lines. The interval limits are dashed yellow lines. From this, the value and statistical and total error of the parameters is obtained.

## D.1.2 Zero effective range approximation

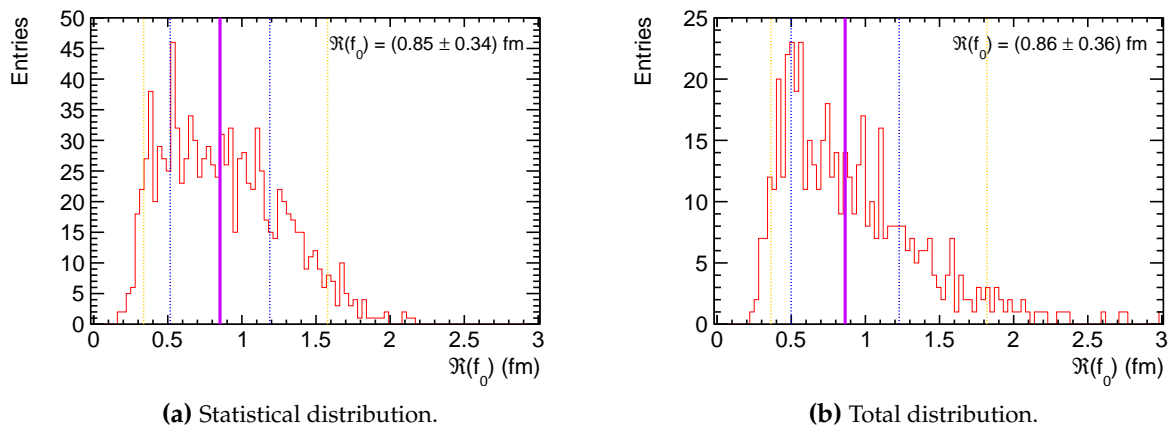
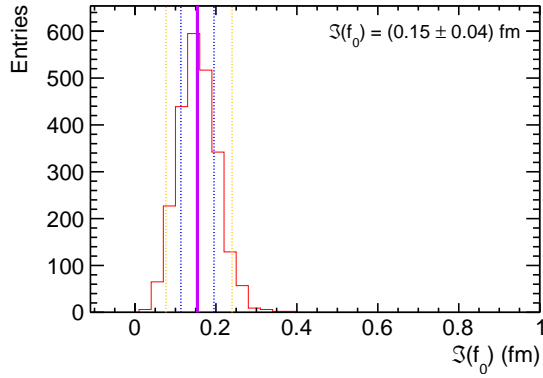
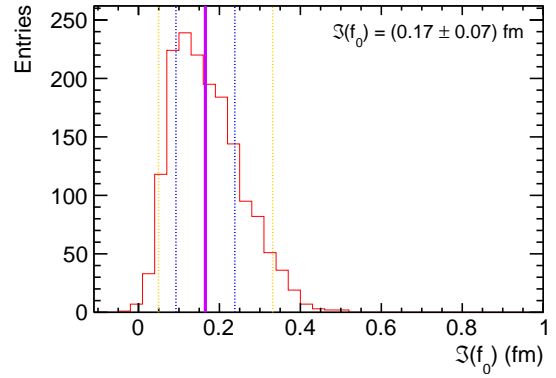


**Figure D.5:** Distribution of  $\Re(f_0)$  obtained from the bootstrap only method and combined with systematic variations. The mean of the central interval (including 90% of the entries) is displayed as solid blue line and the corresponding limits within the standard deviation as dashed blue lines. The interval limits are dashed yellow lines. From this, the value and statistical and total error of the parameters is obtained.



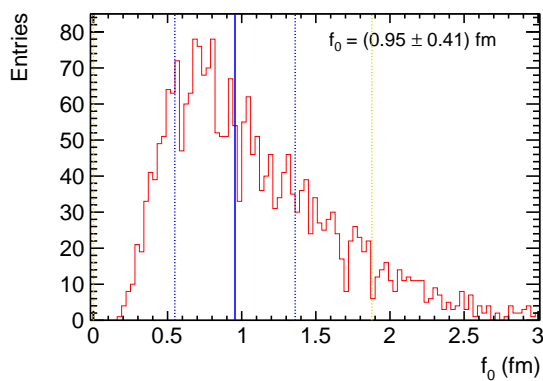
(a) Statistical distribution.



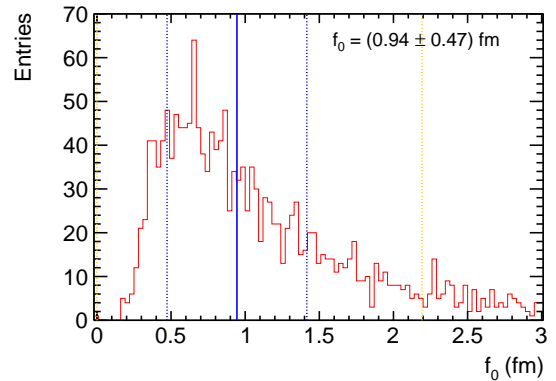
(b) Total distribution.

**Figure D.6:** Distribution of  $\Im(f_0)$  obtained from the bootstrap only method and combined with systematic variations. The mean of the central interval (including 90% of the entries) is displayed as solid pink line and the corresponding limits within the standard deviation as dashed blue lines. The interval limits are dashed yellow lines. From this, the value and statistical and total error of the parameters is obtained.

## D.2 Lednický-Lyuboshits approach with real scattering length

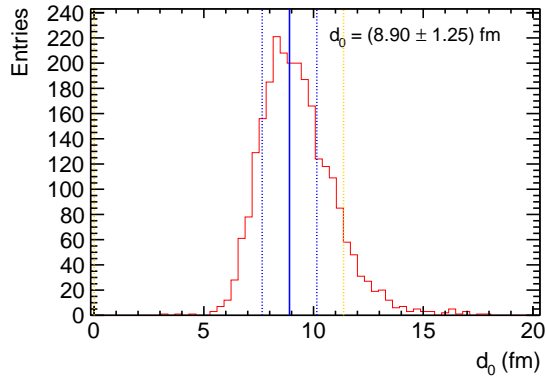


(a) Statistical distribution.

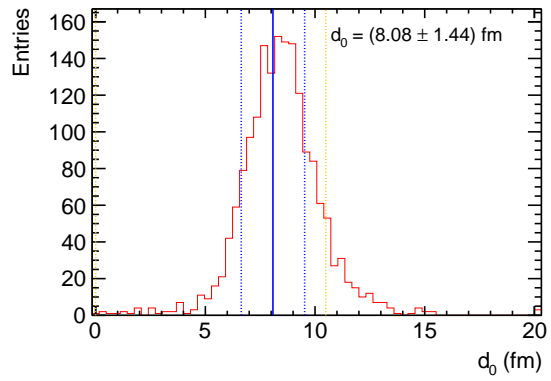


(b) Total distribution.

**Figure D.7:** Distribution of  $f_0$  obtained from the bootstrap only method and combined with systematic variations. The mean of the truncated interval (excluding the upper 10% of the entries) is displayed as solid blue line and the corresponding limits within the standard deviation as dashed blue lines. The interval limits are dashed yellow lines. From this, the value and statistical and total error of the parameters is obtained.



(a) Statistical distribution.

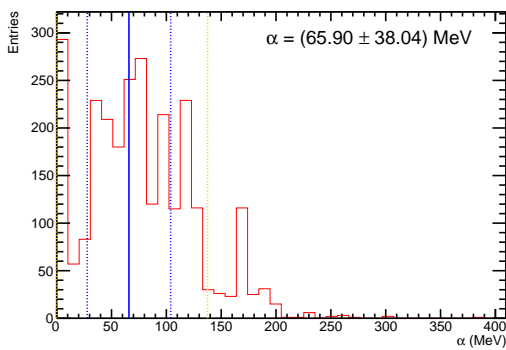


(b) Total distribution.

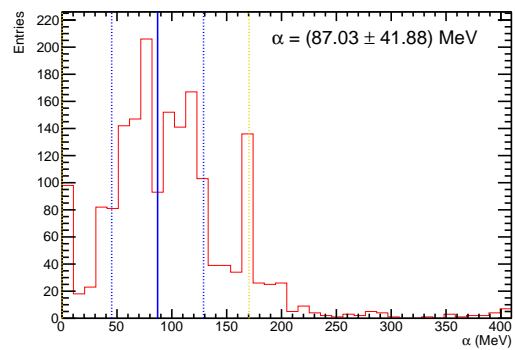
**Figure D.8:** Distribution of  $d_0$  obtained from the bootstrap only method and combined with systematic variations. The mean of the truncated interval (excluding the upper 10% of the entries) is displayed as solid pink line and the corresponding limits within the standard deviation as dashed blue lines. The interval limits are dashed yellow lines. From this the value and statistical and total error of the parameters is obtained.

## D.3 Potentials

### D.3.1 Yukawa-type

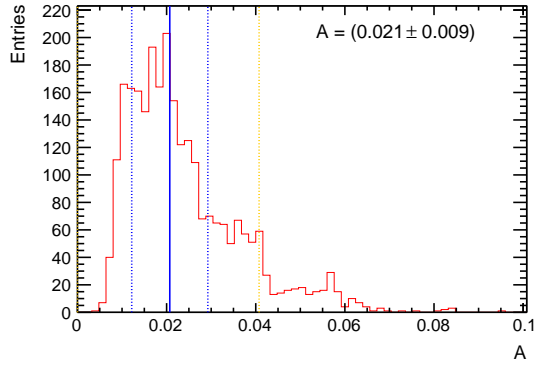


(a) Statistical distribution.

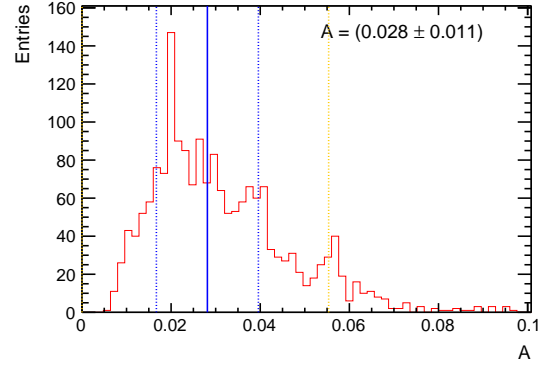


(b) Total distribution.

**Figure D.9:** Distribution of the Yukawa-type potential parameter  $\alpha$  obtained from the bootstrap only method and combined with systematic variations. The mean of the truncated interval (excluding the upper 10% of the entries) is displayed as solid blue line and the corresponding limits within the standard deviation as dashed blue lines. The interval limits are dashed yellow lines. From this the value and statistical and total error of the parameters is obtained.



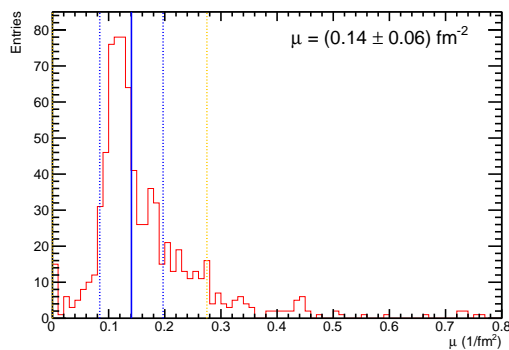
(a) Statistical distribution.



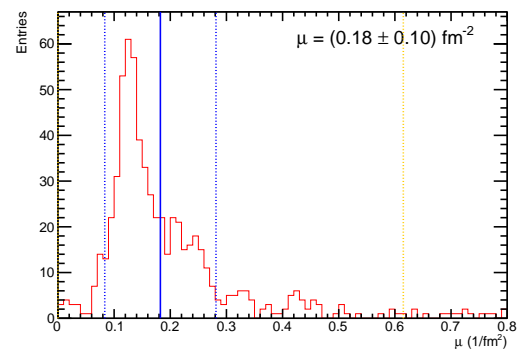
(b) Total distribution.

**Figure D.10:** Distribution of the Yukawa-type potential parameter  $A$  obtained from the bootstrap only method and combined with systematic variations. The mean of the truncated interval (excluding the upper 10% of the entries) is displayed as solid pink line and the corresponding limits within the standard deviation as dashed blue lines. The interval limits are dashed yellow lines. From this the value and statistical and total error of the parameters is obtained.

### D.3.2 Gaussian-type

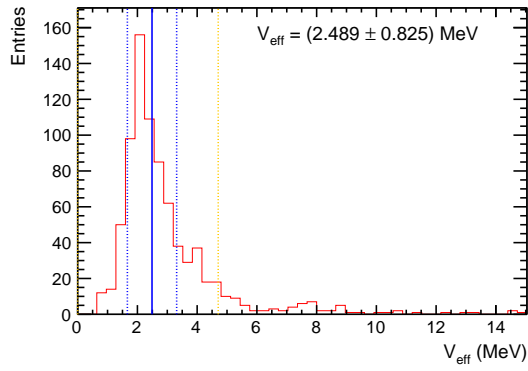


(a) Statistical distribution.

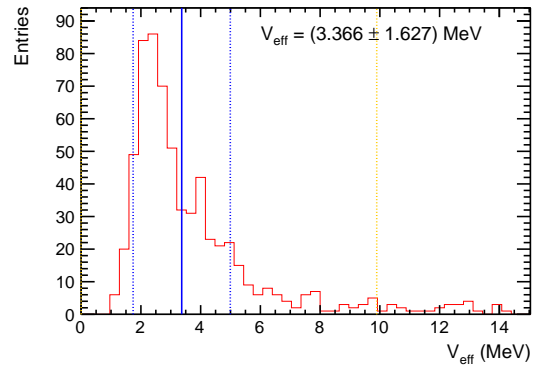


(b) Total distribution.

**Figure D.11:** Distribution of the Gaussian-type potential parameter  $\mu$  obtained from the bootstrap only method and combined with systematic variations. The mean of the truncated interval (excluding the upper 10% of the entries) is displayed as solid blue line and the corresponding limits within the standard deviation as dashed blue lines. The interval limits are dashed yellow lines. From this the value and statistical and total error of the parameters is obtained.



(a) Statistical distribution.



(b) Total distribution.

**Figure D.12:** Distribution of the Gaussian-type potential parameter  $V_{\text{eff}}$  obtained from the bootstrap only method and combined with systematic variations. The mean of the truncated interval (excluding the upper 10% of the entries) is displayed as solid pink line and the corresponding limits within the standard deviation as dashed blue lines. The interval limits are dashed yellow lines. From this the value and statistical and total error of the parameters is obtained.

# List of Figures

1.1	The strong coupling constant as a function of the energy scale $Q$ , which is inversely proportional to distance $Q \propto 1/R$ . Figure taken from [5]. . . . .	2
1.2	The chiral condensate $ \langle \bar{q}q \rangle $ as function of the temperature and baryon density, given in units of nuclear matter density $\rho_0 = 0.17 \text{ fm}^{-3}$ . Figure taken from [10]. .	4
1.3	Invariant mass spectra of $e^+e^-$ , measured in p-C and p-Cu reactions and categorized by $\beta\gamma$ of the reconstructed $\phi$ meson. The data are fitted with a resonance shape consisting of a Breit-Wigner function convoluted with the detector response simulated for the different $\beta\gamma$ regions and a quadratic baseline. Figure taken from [29]. . . . .	6
1.4	Transparency ratios for different nuclei of mass number $A$ , normalized to C. The data are compared to Valencia calculations [33] in panel (a) and to the Paryev model [34] in panel (b). Figure taken from [35]. . . . .	7
1.5	$\phi/K^-$ ratio as function of the mass number $A$ , measured by HADES in $\pi^-$ induced reactions with two different target nuclei. Figure taken from [36]. . . . .	8
1.6	Diagrams which contribute to the leading s- and p-wave interactions of kaons within the nuclear medium [28]. The hyperon intermediate states $Y$ include the ones of the baryon octet and baryon decuplet. Figure taken from [28]. . . . .	8
1.7	The left panel shows the real and imaginary part of the optical potential of the $\phi$ , obtained from theoretical calculations of the self-energy [30], including contributions from the $K\bar{K}$ cloud and the N- $\phi$ interaction within both SU(6) and HSL approaches. The right plot shows the corresponding spectral function. The plots are taken from [30]. . . . .	9
1.8	Nucleon-nucleon potential as function of the distance $r$ given in units of the pion Compton wavelength $m_\pi^{-1} \approx 1.5 \text{ fm}$ (denoted by $\mu^{-1}$ in the plot) with the different regions depending on the interaction range. Figure taken from [60]. . . . .	10
1.9	Proton-proton correlation function, measured in pp collisions. Figure taken from [73].	11
1.10	Diagram for the scattering between proton and neutron, mediated by a pion. The individual quarks are shown as well. Figure taken from [74]. . . . .	12
1.11	The mass-radius relation of neutron stars for different $\Xi$ single-particle potentials $U_\Xi$ in MeV, when fixing $U_\Lambda = -30 \text{ MeV}$ [92–94] and $U_\Sigma = 30 \text{ MeV}$ . Upper set of lines: model $\sigma\omega\rho\phi$ , lower set of lines: model $\sigma\omega\rho$ . Figure taken from [88]. . . . .	14
1.12	Planes spanned by the parameters $\alpha_V$ and $z$ in model $\sigma\omega\rho\phi$ . The gray shaded area on the right corresponds to the constraints from the NS PSR J1614-2230 [80] while the one on the left contains configurations yielding purely nucleonic stars. The spin-flavour SU(6) symmetry with $z = 1/\sqrt{6}$ and $\alpha_V = 1$ is also marked. Figures taken from [91]. . . . .	15
2.1	(a) General scheme of the derivation of the distance $\vec{R}$ between two sources $a$ and $b$ by measuring and correlating the intensities in detectors 1 and 2. (b) Illustration of the <i>HBT interferometry</i> in astronomy, where the angular diameter $\theta$ is measured. (c) Situation in particle physics. Figure taken from [98]. . . . .	17

2.2	Illustration of the influence of the individual contributions of the correlation function on its shape. The upper left panel shows different types of potentials, also including a bound state (pink). The corresponding wave-functions are shown on the lower panel. On the same plot also a source of Gaussian profile is shown for a $r_0$ of 1 fm (dashed line) and 4 fm (dotted). On the right panel, the resulting correlation functions for the two sources are depicted, illustrating the influence of the source size on the signal. Figures taken from [77]. . . . .	20
2.3	Illustration of the different parts of the correlation function. The two grey circles represent the colliding particles, the blue ones the particles produced in the collision and the red circle the emission source $S(\vec{r})$ . If two particles 1 and 2 are emitted close to each other at distance $\vec{r}$ and relative momentum $\vec{k} = \vec{p}_1 - \vec{p}_2$ , they experience a correlation depicted by the green arrows that represent the interaction, encoded in the two-particle wave-function $\psi(\vec{r}, \vec{k})$ . . . . .	21
2.4	Schematic picture of the scattering problem of an incident plane wave in $\hat{z}$ direction on a spherical target. . . . .	23
2.5	The <i>reduced wave-function</i> for s-wave scattering $u_0$ as function of the relative distance $r$ for different potentials [113]. (a) $V=0$ wave-function (dashed line). (b) attractive potential $V<0$ , which results in $\delta_0 > 0$ with the wave-function (solid line) pushed in. (c) repulsive potential $V>0$ resulting in the wave-function to be pulled out (solid line) $\delta_0 < 0$ . Figure taken from [113] . . . . .	24
2.6	Reduced wave-function $u(r)$ for zero-energy ( $k^* \approx 0$ ) as function of $r$ for a repulsive potential (a), an attractive potential (b) and increased attractive potential (c). The intercept of the outside $u(r)$ with the $r$ -axis gives the scattering length $a$ . Figures taken from [113]. . . . .	26
2.7	Scattering parameter phase-space of the Gaussian-type potential approach. The color bar shows the relative deviation between the parameters obtained from the potential and the Lednický–Lyuboshits approach, normalized to the potential approach values. While blue denotes good agreement between the two, yellow corresponds to a relative deviation of 50%. The left figure depicts the results for the effective range $d_0$ , while the right figure shows the same for the scattering length $f_0$ . 29	
2.8	The $K^-p$ correlation function evaluated in the $\bar{K}N-\pi\Sigma-\pi\Lambda$ coupled-channel framework [125]. The long-dashed line corresponds to the result when only considering the $K^-p$ component, while the others additionally include the $\bar{K}^0n$ , both the $\bar{K}^0n$ and $\pi\Sigma$ and all coupled-channel components. All calculations are performed with realistic potentials based on chiral SU(3) dynamics, which fit the available scattering data. Figure taken from [125]. . . . .	31
2.9	Pair mass of the different coupled-channels and $p-\phi$ respectively. . . . .	31
3.1	The CERN accelerator complex. The LHC is the last building block after a complex hadron injection chain, where the particles are accelerated to energies up to $\sqrt{s} = 13$ TeV for pp collisions. Figure taken from [129]. . . . .	33
3.2	The schematic layout of the ALICE spectrometer. Figure taken from [136]. . . . .	34
3.3	The ALICE ITS [131] . . . . .	35
3.4	The ALICE TPC [138] . . . . .	36
3.5	The TPC energy loss as a function of the momentum $p$ [143]. . . . .	37
3.6	The velocity $\beta$ measured with the TOF detector as a function of the momentum of the incident particle (measured by the TPC) [148]. . . . .	39

3.7	Event reconstruction in the central barrel [132]. . . . .	39
3.8	Reconstruction of the secondary vertex exemplary shown for $K_S^0$ and $\Sigma^0$ [132]. . . . .	41
4.1	Particle-to-pion ratio as a function of multiplicity for different systems. The production of $\phi$ mesons increases with multiplicity. For protons it slightly decreases but the overall yield remains significantly larger than the $\phi$ yield. Figure taken from [153]. . . . .	44
4.2	Distribution of the V0M amplitude scaled by its mean value, which is proportional to the event multiplicity [155]. . . . .	44
4.3	Visualization of the relation between minijets and transverse sphericity. . . . .	45
4.4	Sphericity distribution. The shaded area marks the remaining events after a cut of $0.7 < S_T < 1.0$ is applied. . . . .	46
4.5	Transverse momentum and $n\sigma_{\text{TOF}}$ distribution of the proton candidates. . . . .	47
4.6	Transverse momentum and $n_{\sigma,\text{TPC}}$ distribution of $K^+$ candidates. . . . .	51
4.7	Purity of both $K^+$ and $K^-$ as function of the transverse momentum. . . . .	51
4.8	$K^+K^-$ invariant mass distribution for high multiplicity events with sphericity cuts $0.7 < S_T < 1.0$ . The dashed lines represent the $M_\phi \pm 8 \text{ MeV}/c^2$ selection for the femtosopic analysis. . . . .	52
4.9	$K^+K^-$ invariant mass spectra in $p_T$ slices of width $0.5 \text{ GeV}/c$ . . . . .	53
4.10	Purity of the $\phi$ candidates as function of $p_T$ , which is integrated over all LHC periods on the left and on the right the $p_T$ integrated purity as function of the different LHC periods. . . . .	54
5.1	Comparison of the $p-\phi$ and $\bar{p}-\phi$ correlation functions. . . . .	57
5.2	The combined $p-\phi \oplus \bar{p}-\phi$ correlation function, normalized within $0.8 < k^* < 1.0 \text{ GeV}/c$ . . . . .	58
5.3	Momentum resolution matrices, relating the MC generated relative momentum to the reconstructed one for both SE and ME particle pairs as well as the ratio between them. . . . .	59
5.4	$\Delta\eta\Delta\phi^*$ distribution for $p-K^+$ pairs from the same event, normalized to mixed event pairs, for different TPC-radii. At low angles, where track splitting and merging would be visible, no signs for an angular dependence can be seen. . . . .	60
5.5	Projections of the momentum resolution matrix to the $k_{\text{Reconstructed}}^*$ axis for different low momentum intervals in $k_{\text{Generated}}^*$ . The fit with a folded normal distribution is plotted as well. . . . .	61
5.6	Influence of the detector response on the measured correlation function. . . . .	62
5.7	Transverse momentum distribution of the particle pairs of interest at small relative momenta $k^* < 200 \text{ MeV}/c$ . . . . .	63
5.8	$\phi$ meson purity as a function of the transverse momentum, obtained from the reconstruction procedure explained in Sec. 4.2.2.2. The data is fitted with a polynomial of 5 <sup>th</sup> order, from which a purity of 56.69% is obtained for $p_T = 1.3 \text{ GeV}/c$ . The $p_T$ value corresponds to the average transverse momentum of the $\phi$ mesons in $p-\phi$ particle pairs in the femtosopic region with low relative momenta $k^* < 200 \text{ MeV}/c$ . . . . .	65
5.9	Purity of the $\phi$ mesons as a function of the relative momentum. The weighted mean for $k^* < 200 \text{ MeV}/c$ is $(56.6 \pm 2.7)\%$ , which is consistent with the results from the $p_T$ calculations. . . . .	65

5.10	The left illustration shows the combinatorial background consisting of a mixture of two- and three-body interactions between proton, $K^+$ and $K^-$ , the right shows the genuine interaction between proton and $\phi$ . . . . .	67
5.11	The experimental $p$ - $K^+$ and $p$ - $K^-$ correlation functions measured by ALICE in $pp$ collisions at $\sqrt{s} = 13$ TeV fitted with different model predictions (colored bands) [161]. A clear deviation between the data and the correlation function obtained from pure Coulomb interaction can be seen. The residual contribution to the experimental results is attributed to the strong interaction. Figures taken from [161]. . . . .	68
5.12	Invariant mass intervals and corresponding correlation function of $p$ - $\phi$ , left and right SB. . . . .	69
5.13	Comparison between $p$ - $(K^+K^-)$ and $\bar{p}$ - $(K^+K^-)$ for both the left and right sideband interval. . . . .	69
5.14	Left and right sideband and the weighted sum of them, which is used as $C_{pKK,exp}(k^*)$ . The weights are obtained from the relative amount of particles in the background to the left and right of the $\phi$ meson peak in the invariant mass spectra. . . . .	70
5.15	$\phi$ purity within the sideband intervals in the invariant mass spectra. . . . .	71
5.16	The combinatorial background obtained from the weighted sum of the left and right sideband correlation function, parameterized with a double Gaussian (red band), which is used in the correlation function modeling. The orange band corresponds to the actual combinatorial background, when corrected for $\phi$ meson contamination of the sideband. . . . .	72
5.17	Due to strict cuts on the event sphericity, selecting only spherical events, the long-range enhancement caused by minijets is reduced. . . . .	73
5.18	The $p$ - $\phi$ correlation function from reconstructed MC and MC truth data, both normalized within $k^* \in [600, 800]$ MeV/c. They are in agreement within the uncertainties up to $k^* \sim 1000$ MeV/c. . . . .	74
5.19	Comparison between the MC truth results for $p$ - $\phi$ and $p$ - $(K^+K^-)$ for different normalization ranges. The discrepancy between the two correlation functions at low $k^*$ visible in Fig. (a), where the default normalization window is used, is not present in Fig. (b). This implies that the difference seen on the left plot can be attributed to the normalization. . . . .	74
5.20	Comparison between the correlation functions obtained from actual data and MC truth. All correlation functions are normalized within $k^* \in [800, 1000]$ MeV/c. . . . .	75
5.21	The experimental $p$ - $\phi$ correlation function and various contributions as described in Eq. 5.8, however, not yet scaled by the respective parameters. The blue band depicts the background model used to derive the genuine $p$ - $\phi$ correlation function. . . . .	76
5.22	The genuine $p$ - $\phi$ correlation function derived by employing the bootstrap method. Each data point is obtained by randomly sampling the input correlation functions, resulting in a distribution of possible correlation function values. . . . .	77
5.23	Illustration of the modification source size due to resonances feeding one of the particles of interest as for $p$ - $\phi$ . . . . .	78
5.24	Gaussian core radius as a function of $\langle m_T \rangle$ for different particle pairs. The blue data points are obtained by fitting the $p$ - $p$ correlation function with the strong Argonne $\nu 18$ [65] potential. The green (red) data results from a fit of the $p$ - $\Lambda$ correlation function with the strong $\chi$ EFT LO [174] (NLO [175]) potential. Statistical uncertainties are shown as lines while the systematic uncertainties correspond to the boxes. Figure taken from [164]. . . . .	79

5.25	Distribution of the transverse mass at low relative momenta of $p\text{-}\phi$ and $\bar{p}\text{-}\phi$ respectively. . . . .	80
5.26	Gaussian core radius of a $p\text{-}p$ source as function of $\langle m_T \rangle$ and fit to the data (green). Solid bars depict the statistical uncertainties and shaded areas the systematic errors due to variations of the fit [164]. . . . .	80
5.27	Universal source model for $p\text{-}\phi$ and fit with a Gaussian source function. . . . .	81
5.28	Effect of the systematic variations on the number of $p\text{-}\phi$ pairs for $k^* < 200$ MeV/c. . . . .	83
5.29	The experimental $p\text{-}\phi$ correlation function and the various contributions as described in Eq. 5.5. It has to be considered that they are not scaled by the respective $\lambda$ -parameters. Statistical (bars) and systematic uncertainties (boxes) are shown separately. The width of the dark (light) shaded bands corresponds to one standard deviation of the statistical (total) uncertainty. The figure published in [177]. . . . .	85
5.30	The genuine $p\text{-}\phi$ correlation function with statistical (bars) and systematic (grey boxes) uncertainties [177] . . . . .	85
6.1	The genuine $p\text{-}\phi$ correlation function with statistical (bars) and systematic uncertainties (boxes). The red band depicts the results from the fit employing the Lednický-Lyuboshits [118]. The width corresponds to one standard deviation of the uncertainty of the fit. Figure published in [177]. . . . .	88
6.2	The correlation function for $p\text{-}\phi$ compared to the Lednický-Lyuboshits approach with complex scattering length and <i>zero effective range approximation</i> . . . . .	89
6.3	Correlation functions obtained from the potentials by employing CATS in comparison to the result from the Lednický-Lyuboshits approach with real scattering length. . . . .	89
6.4	The coupling constant $g_{\Lambda\phi}$ as function of $\alpha_V$ and $z$ , assuming $g_{N\text{-}\phi} = 0.14$ . . . . .	93
A.1	Momentum transformation matrices and correlation function for different invariant mass windows. . . . .	98
A.2	Momentum transformation matrices and correlation function for different invariant mass windows. . . . .	99
A.3	Illustration of how a qualitative description of $p\text{-}K_{\text{eff}}$ is derived. At the beginning, the second bin of a sideband correlation function (here the one within $1.028 < M_{K^+K^-} < 1.044$ GeV) is taken, while also considering its bin-width. Then the corresponding slice of the momentum smearing matrix is projected to the x-axis to obtain a momentum distribution in $k_{pK}^*$ . From this a point of $p\text{-}K_{\text{eff}}$ is acquired, where $k_{pK}^*$ the mean value of the distribution, with an uncertainty that corresponds to the width of the distribution and the y-value and corresponding statistical uncertainty is taken from the measured sideband bin. . . . .	101
A.4	The $p\text{-}K_{\text{eff}}$ obtained by using the first, second and third bin entry of the measured sideband correlation functions. Within the uncertainties they are in agreement with each other. . . . .	102
A.5	On the left plot the effective proton-kaon correlation function $p\text{-}K_{\text{eff}}$ is shown as well as the pre-fit with confidence interval and the result of the parallel minimization using MINUIT. The right plot shows the combinatorial background obtained from experimental data together with the function that is derived from $p\text{-}K_{\text{eff}}$ using the transformation matrix that relates the relative momentum of $p\text{-}\phi$ to $p\text{-}K$ . . . . .	102

B.1	Experimental correlation function of p-K <sup>+</sup> and p-K <sup>-</sup> obtained from the particle selection in Sec. 4.2.2.1. Both are normalized in the range [400, 600] MeV/c, following [161]. . . . .	104
B.2	Comparison of the combinatorial background obtained from the sideband analysis and projector method. . . . .	105
C.1	<i>Left:</i> The phase-shift of the wave-function evaluated for a Gaussian potential ( $V_{\text{eff}} = 2.52$ MeV, $\mu = 0.14$ fm <sup>-2</sup> ) as function of $k^*$ . <i>Right:</i> Corresponding $k^* \cot(\delta(k^*))$ fitted with Eq. 2.16 to extract the scattering parameters. . . . .	107
C.2	Scattering parameter phase-space for both Yukawa (left) and Gaussian type of potential (right). The degree of consistency is expressed as the number of $\sigma$ with regard to the $\chi^2$ for $k^* < 200$ MeV/c between data and correlation function of the respective potential, which is obtained by employing CATS. . . . .	108
C.3	Comparison between the Lednický-Lyuboshits approach and Gaussian potential approach. From the potential the scattering parameters $d_0 = 15.10 \pm 0.51$ fm and $f_0 = 0.62 \pm 0.01$ fm can be derived, which deviate from the Lednický-Lyuboshits result. . . . .	108
D.1	Distribution of $n_\sigma$ between data and $C(k^*) = 1$ obtained from the bootstrap only method and combined with systematic variations. The mean of the central interval (including 90% of the entries) is displayed as solid pink line and the corresponding limits within the standard deviation as dashed blue lines. The interval limits are dashed yellow lines. From this, the value and statistical and total error of the parameters is obtained. . . . .	109
D.2	Distribution of $\Re(f_0)$ obtained from the bootstrap only method and combined with systematic variations. The mean of the central interval (including 90% of the entries) is displayed as solid pink line and the corresponding limits within the standard deviation as dashed blue lines. The interval limits are dashed yellow lines. From this, the value and statistical and total error of the parameters is obtained.110	
D.3	Distribution of $\Im(f_0)$ obtained from the bootstrap only method and combined with systematic variations. The mean of the central interval (including 90% of the entries) is displayed as solid pink line and the corresponding limits within the standard deviation as dashed blue lines. The interval limits are dashed yellow lines. From this, the value and statistical and total error of the parameters is obtained.111	
D.4	Distribution of $d_0$ obtained from the bootstrap only method and combined with systematic variations. The mean of the central interval (including 90% of the entries) is displayed as solid pink line and the corresponding limits within the standard deviation as dashed blue lines. The interval limits are dashed yellow lines. From this, the value and statistical and total error of the parameters is obtained.111	
D.5	Distribution of $\Re(f_0)$ obtained from the bootstrap only method and combined with systematic variations. The mean of the central interval (including 90% of the entries) is displayed as solid blue line and the corresponding limits within the standard deviation as dashed blue lines. The interval limits are dashed yellow lines. From this, the value and statistical and total error of the parameters is obtained.112	

D.6	Distribution of $\mathfrak{S}(f_0)$ obtained from the bootstrap only method and combined with systematic variations. The mean of the central interval (including 90% of the entries) is displayed as solid pink line and the corresponding limits within the standard deviation as dashed blue lines. The interval limits are dashed yellow lines. From this, the value and statistical and total error of the parameters is obtained.	113
D.7	Distribution of $f_0$ obtained from the bootstrap only method and combined with systematic variations. The mean of the truncated interval (excluding the upper 10% of the entries) is displayed as solid blue line and the corresponding limits within the standard deviation as dashed blue lines. The interval limits are dashed yellow lines. From this, the value and statistical and total error of the parameters is obtained.	113
D.8	Distribution of $d_0$ obtained from the bootstrap only method and combined with systematic variations. The mean of the truncated interval (excluding the upper 10% of the entries) is displayed as solid pink line and the corresponding limits within the standard deviation as dashed blue lines. The interval limits are dashed yellow lines. From this the value and statistical and total error of the parameters is obtained.	114
D.9	Distribution of the Yukawa-type potential parameter $\alpha$ obtained from the bootstrap only method and combined with systematic variations. The mean of the truncated interval (excluding the upper 10% of the entries) is displayed as solid blue line and the corresponding limits within the standard deviation as dashed blue lines. The interval limits are dashed yellow lines. From this the value and statistical and total error of the parameters is obtained.	114
D.10	Distribution of the Yukawa-type potential parameter $A$ obtained from the bootstrap only method and combined with systematic variations. The mean of the truncated interval (excluding the upper 10% of the entries) is displayed as solid pink line and the corresponding limits within the standard deviation as dashed blue lines. The interval limits are dashed yellow lines. From this the value and statistical and total error of the parameters is obtained.	115
D.11	Distribution of the Gaussian-type potential parameter $\mu$ obtained from the bootstrap only method and combined with systematic variations. The mean of the truncated interval (excluding the upper 10% of the entries) is displayed as solid blue line and the corresponding limits within the standard deviation as dashed blue lines. The interval limits are dashed yellow lines. From this the value and statistical and total error of the parameters is obtained.	115
D.12	Distribution of the Gaussian-type potential parameter $V_{\text{eff}}$ obtained from the bootstrap only method and combined with systematic variations. The mean of the truncated interval (excluding the upper 10% of the entries) is displayed as solid pink line and the corresponding limits within the standard deviation as dashed blue lines. The interval limits are dashed yellow lines. From this the value and statistical and total error of the parameters is obtained.	116



# List of Tables

4.1	Event cuts . . . . .	46
4.2	Proton cuts . . . . .	48
4.3	Kaon cuts . . . . .	50
4.4	Particle pairs . . . . .	55
5.1	Lambda parameters . . . . .	64
5.2	Systematic uncertainties . . . . .	83
5.3	Systematic Variations of the background model . . . . .	84
5.4	Systematic variations of the femtoscopic fits . . . . .	86
6.1	Fit results Complex Lednický-Lyuboshits . . . . .	87
6.2	Fit results real Lednický-Lyuboshits . . . . .	89
6.3	Fit results Gauss . . . . .	90
6.4	Fit results Yukawa . . . . .	90



# Bibliography

- [1] C. Burgess, “An introduction to effective field theory,” *Annual Review of Nuclear and Particle Science* **57** no. 1, (Nov, 2007) 329–362.  
<http://dx.doi.org/10.1146/annurev.nucl.56.080805.140508>.
- [2] S. Petschauer, J. Haidenbauer, N. Kaiser, U.-G. Meißner, and W. Weise, “Hyperon-nuclear interactions from  $su(3)$  chiral effective field theory,” *Frontiers in Physics* **8** (Feb, 2020) .  
<http://dx.doi.org/10.3389/fphy.2020.00012>.
- [3] F. Karsch, “Lattice QCD at high temperature and density,” *Lect. Notes Phys.* **583** (2002) 209–249, arXiv:hep-lat/0106019.
- [4] **HPQCD, UKQCD, MILC, Fermilab Lattice** Collaboration, C. T. H. Davies *et al.*, “High precision lattice QCD confronts experiment,” *Phys. Rev. Lett.* **92** (2004) 022001, arXiv:hep-lat/0304004.
- [5] **Particle Data Group** Collaboration, P. D. Group, P. A. Zyla, *et al.*, “Review of Particle Physics,” *Progress of Theoretical and Experimental Physics* **2020** no. 8, (08, 2020) ,  
<https://academic.oup.com/ptep/article-pdf/2020/8/083C01/34673722/ptaa104.pdf>.  
<https://doi.org/10.1093/ptep/ptaa104.083C01>.
- [6] F. Halzen and A. D. Martin, *QUARKS AND LEPTONS: AN INTRODUCTORY COURSE IN MODERN PARTICLE PHYSICS*. 1984.
- [7] S. Scherer, “Introduction to chiral perturbation theory,” *Adv. Nucl. Phys.* **27** (2003) 277, arXiv:hep-ph/0210398.
- [8] S. L. Adler, “Axial-vector vertex in spinor electrodynamics,” *Phys. Rev.* **177** (Jan, 1969) 2426–2438. <https://link.aps.org/doi/10.1103/PhysRev.177.2426>.
- [9] J. S. Bell and R. Jackiw, “A PCAC puzzle:  $\pi^0 \rightarrow \gamma\gamma$  in the  $\sigma$ -model,” *Nuovo Cimento A Serie* **60** no. 1, (Mar., 1969) 47–61.
- [10] W. Weise, “Nuclear aspects of chiral symmetry,” *Nuclear Physics A* **553** (1993) 59–72.  
<https://www.sciencedirect.com/science/article/pii/0375947493906155>.
- [11] Y. Nambu, “Quasi-particles and gauge invariance in the theory of superconductivity,” *Phys. Rev.* **117** (Feb, 1960) 648–663. <https://link.aps.org/doi/10.1103/PhysRev.117.648>.
- [12] J. Goldstone, “Field Theories with Superconductor Solutions,” *Nuovo Cim.* **19** (1961) 154–164.
- [13] J. Goldstone, A. Salam, and S. Weinberg, “Broken symmetries,” *Phys. Rev.* **127** (Aug, 1962) 965–970. <https://link.aps.org/doi/10.1103/PhysRev.127.965>.
- [14] M. Gell-Mann, R. J. Oakes, and B. Renner, “Behavior of current divergences under  $su_3 \times su_3$ ,” *Phys. Rev.* **175** (Nov, 1968) 2195–2199.  
<https://link.aps.org/doi/10.1103/PhysRev.175.2195>.

- [15] R. Rapp, J. Wambach, and H. van Hees, "The chiral restoration transition of qcd and low mass dileptons: Datasheet from landolt-börnstein - group i elementary particles, nuclei and atoms · volume 23: "relativistic heavy ion physics" in springermaterials ([https://doi.org/10.1007/978-3-642-01539-7\\_6](https://doi.org/10.1007/978-3-642-01539-7_6))."  
[https://materials.springer.com/lb/docs/sm\\_lbs\\_978-3-642-01539-7\\_6](https://materials.springer.com/lb/docs/sm_lbs_978-3-642-01539-7_6). accessed 2021-04-29.
- [16] J. Gasser and H. Leutwyler, "Light quarks at low temperatures," *Physics Letters B* **184** no. 1, (1987) 83–88.  
<https://www.sciencedirect.com/science/article/pii/0370269387904928>.
- [17] P. Gerber and H. Leutwyler, "Hadrons below the chiral phase transition," *Nuclear Physics B* **321** no. 2, (1989) 387–429.  
<https://www.sciencedirect.com/science/article/pii/0550321389903490>.
- [18] S. Klimt, M. Lutz, and W. Weise, "Chiral phase transition in the su(3) nambu and jona-lasinio model," *Physics Letters B* **249** no. 3, (1990) 386–390.  
<https://www.sciencedirect.com/science/article/pii/037026939091003T>.
- [19] NA60 Collaboration, R. Arnaldi *et al.*, "First measurement of the rho spectral function in high-energy nuclear collisions," *Phys. Rev. Lett.* **96** (2006) 162302, arXiv:nucl-ex/0605007.
- [20] M. Naruki *et al.*, "Experimental signature of the medium modification for rho and omega mesons in 12-GeV p + A reactions," *Phys. Rev. Lett.* **96** (2006) 092301, arXiv:nucl-ex/0504016.
- [21] S. Leupold, V. Metag, and U. Mosel, "Hadrons in strongly interacting matter," *Int. J. Mod. Phys. E* **19** (2010) 147.
- [22] T. Hatsuda and S. H. Lee, "Qcd sum rules for vector mesons in the nuclear medium," *Phys. Rev. C* **46** (Jul, 1992) R34–R38. <https://link.aps.org/doi/10.1103/PhysRevC.46.R34>.
- [23] S. Zschocke, O. P. Pavlenko, and B. Kampfer, "Evaluation of QCD sum rules for light vector mesons at finite density and temperature," *Eur. Phys. J. A* **15** (2002) 529.
- [24] F. Klingl, N. Kaiser, and W. Weise, "Current correlation functions, qcd sum rules and vector mesons in baryonic matter," *Nuclear Physics A* **624** no. 4, (Oct, 1997) 527–563.  
[http://dx.doi.org/10.1016/S0375-9474\(97\)88960-9](http://dx.doi.org/10.1016/S0375-9474(97)88960-9).
- [25] M. Shifman, "Snapshots of hadrons," *Progress of Theoretical Physics Supplement* **131** (1998) 1–71. <http://dx.doi.org/10.1143/PTPS.131.1>.
- [26] E. Oset and A. Ramos, " $\phi$  decay in nuclei," *Nuclear Physics A* **679** no. 3, (2001) 616–628.  
<https://www.sciencedirect.com/science/article/pii/S0375947400003638>.
- [27] D. Cabrera and M. J. Vicente Vacas, " $\phi$  meson mass and decay width in nuclear matter," *Phys. Rev. C* **67** (Apr, 2003) 045203.  
<https://link.aps.org/doi/10.1103/PhysRevC.67.045203>.
- [28] F. Klingl, T. Waas, and W. Weise, "Modification of the  $\phi$ -meson spectrum in nuclear matter1work supported in part by gsi and bmbf.1," *Physics Letters B* **431** no. 3, (1998) 254–262. <https://www.sciencedirect.com/science/article/pii/S0370269398004912>.
- [29] KEK-PS-E325 Collaboration, R. Muto *et al.*, "Evidence for in-medium modification of the phi meson at normal nuclear density," *Phys. Rev. Lett.* **98** (2007) 042501.

- [30] D. Cabrera, A. Hiller Blin, M. Vicente Vacas, and P. Fernández De Córdoba, “ $\phi$  meson transparency in nuclei from  $\phi N$  resonant interactions,” *Phys. Rev.* **C96** (2017) 034618.
- [31] P. Gubler and W. Weise, “Moments of  $\phi$  meson spectral functions in vacuum and nuclear matter,” *Physics Letters B* **751** (2015) 396–401.  
<https://www.sciencedirect.com/science/article/pii/S0370269315008278>.
- [32] P. Gubler and W. Weise, “Phi meson spectral moments and qcd condensates in nuclear matter,” *Nuclear Physics A* **954** (2016) 125–148.  
<https://www.sciencedirect.com/science/article/pii/S0375947416300677>. Recent Progress in Strangeness and Charm Hadronic and Nuclear Physics.
- [33] V. K. Magas, L. Roca, and E. Oset, “ $\phi$  meson width in the medium from proton induced  $\phi$  production in nuclei,” *Phys. Rev. C* **71** (Jun, 2005) 065202.  
<https://link.aps.org/doi/10.1103/PhysRevC.71.065202>.
- [34] E. Y. Paryev, “Near-threshold  $\phi$  meson production in proton–nucleus reactions and  $\phi$  width in finite nuclei,” *Journal of Physics G: Nuclear and Particle Physics* **36** no. 1, (Oct, 2008) 015103. <https://doi.org/10.1088/0954-3899/36/1/015103>.
- [35] A. Polyanskiy *et al.*, “Measurement of the in-medium phi-meson width in proton-nucleus collisions,” *Phys. Lett.* **B695** (2011) 74.
- [36] J. Wirth, (*Strange*) *Meson Production in Pion-Nucleus Collisions at 1.7 GeV/c*. PhD thesis, Technische Universität München, 2019.
- [37] CLAS Collaboration, M. Wood *et al.*, “Absorption of the  $\omega$  and  $\phi$  Mesons in Nuclei,” *Phys. Rev. Lett.* **105** (2010) 112301.
- [38] V. Metag, M. Nanova, and E. Paryev, “Meson–nucleus potentials and the search for meson–nucleus bound states,” *Progress in Particle and Nuclear Physics* **97** (Nov, 2017) 199–260. <http://dx.doi.org/10.1016/j.ppnp.2017.08.002>.
- [39] P. Mühlich and U. Mosel, “Attenuation of  $\phi$  mesons in  $\gamma a$  reactions,” *Nuclear Physics A* **765** no. 1, (2006) 188–196.  
<https://www.sciencedirect.com/science/article/pii/S0375947405011966>.
- [40] J. Cobos-Martínez, K. Tsushima, G. Krein, and A. Thomas, “ $\phi$  meson mass and decay width in nuclear matter and nuclei,” *Physics Letters B* **771** (2017) 113–118.  
<https://www.sciencedirect.com/science/article/pii/S0370269317303982>.
- [41] E. FRIEDMAN and A. GAL, “In-medium nuclear interactions of low-energy hadrons,” *Physics Reports* **452** no. 4-5, (Nov, 2007) 89–153.  
<http://dx.doi.org/10.1016/j.physrep.2007.08.002>.
- [42] P. Gubler and W. Weise, “Phi meson spectral moments and QCD condensates in nuclear matter,” *Nucl. Phys.* **A954** (2016) 125.
- [43] D. Cabrera, A. N. Hiller Blin, and M. J. Vicente Vacas, “ $\phi$  meson self-energy in nuclear matter from  $\phi n$  resonant interactions,” *Phys. Rev.* **C95** (2017) 015201.
- [44] HADES Collaboration, J. Adamczewski-Musch *et al.*, “Strong absorption of hadrons with hidden and open strangeness in nuclear matter,” *Phys. Rev. Lett.* **123** (2019) 022002.
- [45] S. Okubo, “Phi meson and unitary symmetry model,” *Phys. Lett.* **5** (1963) 165.

- [46] G. Zweig, "An  $SU_3$  model for strong interaction symmetry and its breaking; Version 2." CERN-TH-412, 1964.
- [47] J. Iizuka, "Systematics and phenomenology of meson family," *Prog. Theor. Phys. Suppl.* **37** (1966) 21.
- [48] **HADES** Collaboration, G. Agakishiev *et al.*, "Dielectron production in Ar+KCl collisions at 1.76A GeV," *Phys. Rev.* **C84** (2011) 014902.
- [49] R. Young, "Particle physics: Strangeness in the proton," *Nature* **544** (04, 2017) .
- [50] T. Appelquist and W. Fischler, "Some remarks on van der Waals forces in QCD," *Phys. Lett.* **B77** (1978) 405.
- [51] H. Gao, T. Lee, and V. Marinov, " $\phi$  - N bound state," *Phys. Rev.* **C63** (2001) 022201.
- [52] S. J. Brodsky, I. Schmidt, and G. F. de Téramond, "Nuclear-bound quarkonium," *Phys. Rev. Lett.* **64** (1990) 1011.
- [53] X. Liu, H. Huang, and J. Ping, "Hidden strange pentaquark states in constituent quark models," *Phys. Rev.* **C98** (2018) 055203.
- [54] L. Tolos and L. Fabbietti, "Strangeness in Nuclei and Neutron Stars," *Prog. Part. Nucl. Phys.* **112** (2020) 103770.
- [55] T. Ishikawa *et al.*, " $\phi$  photo-production from Li, C, Al, and Cu nuclei at  $E(\gamma) = 1.5$  GeV to 2.4 GeV," *Phys. Lett.* **B608** (2005) 215.
- [56] I. Vidaña, "Hyperons: the strange ingredients of the nuclear equation of state," *Proceedings of the Royal Society A: Mathematical, Physical and Engineering Sciences* **474** no. 2217, (2018) 20180145, <https://royalsocietypublishing.org/doi/pdf/10.1098/rspa.2018.0145>.  
<https://royalsocietypublishing.org/doi/abs/10.1098/rspa.2018.0145>.
- [57] H. Yukawa, "On the Interaction of Elementary Particles. I," *Progress of Theoretical Physics Supplement* **1** (01, 1955) 1–10,  
<https://academic.oup.com/ptps/article-pdf/doi/10.1143/PTPS.1.1/5310694/1-1.pdf>.  
<https://doi.org/10.1143/PTPS.1.1>.
- [58] C. M. G. Lattes, H. Muirhead, G. P. S. Occhialini, and C. F. Powell, "PROCESSES INVOLVING CHARGED MESONS," *Nature* **159** (1947) 694–697.
- [59] R. Machleidt, "THE MESON THEORY OF NUCLEAR FORCES AND NUCLEAR MATTER," 9, 1985.
- [60] J. W. Holt, N. Kaiser, and W. Weise, "Nuclear chiral dynamics and thermodynamics," *Progress in Particle and Nuclear Physics* **73** (2013) 35–83.  
<https://www.sciencedirect.com/science/article/pii/S0146641013000756>.
- [61] M. Taketani, S. Nakamura, and M. Sasaki, "On the Method of the Theory of Nuclear Forces," *Progress of Theoretical Physics* **6** no. 4, (08, 1951) 581–586,  
<https://academic.oup.com/ptp/article-pdf/6/4/581/5419152/6-4-581.pdf>.  
<https://doi.org/10.1143/ptp/6.4.581>.
- [62] R. Machleidt, "High-precision, charge-dependent bonn nucleon-nucleon potential," *Phys. Rev. C* **63** (Jan, 2001) 024001. <https://link.aps.org/doi/10.1103/PhysRevC.63.024001>.

- [63] T. A. Rijken, “Extended-soft-core baryon-baryon model. i. nucleon-nucleon scattering with the esc04 interaction,” *Phys. Rev. C* **73** (Apr, 2006) 044007.  
<https://link.aps.org/doi/10.1103/PhysRevC.73.044007>.
- [64] T. A. Rijken, M. M. Nagels, and Y. Yamamoto, “Extended-soft-core baryon-baryon model esc16,” *AIP Conference Proceedings* **2130** no. 1, (2019) 020003,  
<https://aip.scitation.org/doi/pdf/10.1063/1.5118371>.  
<https://aip.scitation.org/doi/abs/10.1063/1.5118371>.
- [65] R. B. Wiringa, V. G. J. Stoks, and R. Schiavilla, “Accurate nucleon-nucleon potential with charge-independence breaking,” *Phys. Rev. C* **51** (Jan, 1995) 38–51.  
<https://link.aps.org/doi/10.1103/PhysRevC.51.38>.
- [66] T. A. Rijken, V. G. J. Stoks, and Y. Yamamoto, “Soft-core hyperon-nucleon potentials,” *Phys. Rev. C* **59** (Jan, 1999) 21–40. <https://link.aps.org/doi/10.1103/PhysRevC.59.21>.
- [67] T. A. Rijken, M. M. Nagels, and Y. Yamamoto, “Baryon-Baryon Interactions: — Nijmegen Extended-Soft-Core Models —,” *Progress of Theoretical Physics Supplement* **185** (06, 2010) 14–71,  
<https://academic.oup.com/ptps/article-pdf/doi/10.1143/PTPS.185.14/5334308/185-14.pdf>.  
<https://doi.org/10.1143/PTPS.185.14>.
- [68] V. G. J. Stoks and T. A. Rijken, “Soft-core baryon-baryon potentials for the complete baryon octet,” *Phys. Rev. C* **59** (Jun, 1999) 3009–3020.  
<https://link.aps.org/doi/10.1103/PhysRevC.59.3009>.
- [69] T. A. Rijken and Y. Yamamoto, “Extended-soft-core baryon-baryon model. ii. hyperon-nucleon interaction,” *Phys. Rev. C* **73** (Apr, 2006) 044008.  
<https://link.aps.org/doi/10.1103/PhysRevC.73.044008>.
- [70] M. M. Nagels, T. A. Rijken, and Y. Yamamoto, “Extended-soft-core baryon-baryon model esc16. ii. hyperon-nucleon interactions,” *Phys. Rev. C* **99** (Apr, 2019) 044003.  
<https://link.aps.org/doi/10.1103/PhysRevC.99.044003>.
- [71] J. Haidenbauer and U.-G. Meißner, “Jülich hyperon-nucleon model revisited,” *Phys. Rev. C* **72** (Oct, 2005) 044005. <https://link.aps.org/doi/10.1103/PhysRevC.72.044005>.
- [72] B. Holzenkamp, K. Holinde, and J. Speth, “A meson exchange model for the hyperon-nucleon interaction,” *Nuclear Physics A* **500** no. 3, (1989) 485 – 528.  
<http://www.sciencedirect.com/science/article/pii/0375947489902236>.
- [73] ALICE Collaboration, S. Acharya *et al.*, “Investigation of the  $p$ - $\Sigma^0$  interaction via femtoscopy in pp collisions,” *Phys. Lett.* **B805** (2020) 135419.
- [74] F. Oyster, “Feynman diagram of proton–neutron scattering mediated by a pion, with individual quarks shown,” 2014.  
<https://commons.wikimedia.org/w/index.php?curid=35299139>. Accessed on 2021-09-01.
- [75] F. Özel and P. Freire, “Masses, Radii, and the Equation of State of Neutron Stars,” *Annual Review of Astronomy and Astrophysics* **54** no. 1, (2016) 401–440.  
<https://doi.org/10.1146/annurev-astro-081915-023322>.

- [76] J. M. Lattimer and M. Parakash, “The Physics of Neutron Stars,” *Science, New Series* **302** (2004) 536–542. <https://doi.org/10.1126/science.1090720>.
- [77] L. Fabbietti, V. M. Sarti, and O. V. Doce, “Hadron-hadron interactions measured by alice at the lhc,” 2020.
- [78] J. R. Oppenheimer and G. M. Volkoff, “On Massive Neutron Cores,” *Phys. Rev.* **55** (Feb, 1939) 374–381. <https://link.aps.org/doi/10.1103/PhysRev.55.374>.
- [79] R. C. Tolman, “Static Solutions of Einstein’s Field Equations for Spheres of Fluid,” *Phys. Rev.* **55** (Feb, 1939) 364–373. <https://link.aps.org/doi/10.1103/PhysRev.55.364>.
- [80] P. Demorest, T. Pennucci, S. Ransom, M. Roberts, and J. Hessels, “Shapiro Delay Measurement of A Two Solar Mass Neutron Star,” *Nature* **467** (2010) 1081–1083, [arXiv:1010.5788](https://arxiv.org/abs/1010.5788) [astro-ph.HE].
- [81] H. T. Cromartie, E. Fonseca, S. M. Ransom, P. B. Demorest, Z. Arzoumanian, H. Blumer, P. R. Brook, M. E. DeCesar, T. Dolch, J. A. Ellis, and et al., “Relativistic shapiro delay measurements of an extremely massive millisecond pulsar,” *Nature Astronomy* **4** no. 1, (Sep, 2019) 72–76. <http://dx.doi.org/10.1038/s41550-019-0880-2>.
- [82] I. Bombaci, “The hyperon puzzle in neutron stars,” *Proceedings of the 12th International Conference on Hypernuclear and Strange Particle Physics (HYP2015)* (Jul, 2017) . <http://dx.doi.org/10.7566/JPSCP.17.101002>.
- [83] H. Dapo, B.-J. Schaefer, and J. Wambach, “Appearance of hyperons in neutron stars,” *Phys. Rev. C* **81** (Mar, 2010) 035803. <https://link.aps.org/doi/10.1103/PhysRevC.81.035803>.
- [84] L. Tolos and L. Fabbietti, “Strangeness in nuclei and neutron stars,” *Progress in Particle and Nuclear Physics* **112** (2020) 103770. <https://www.sciencedirect.com/science/article/pii/S014664102030017X>.
- [85] ALICE Collaboration, S. Acharya *et al.*, “p-p, p- $\Lambda$  and  $\Lambda$ - $\Lambda$  correlations studied via femtoscopy in pp reactions at  $\sqrt{s} = 7$  TeV,” *Phys. Rev. C* **99** no. 2, (2019) 024001, [arXiv:1805.12455](https://arxiv.org/abs/1805.12455) [nucl-ex].
- [86] J. Haidenbauer, U. G. Meißner, N. Kaiser, and W. Weise, “Lambda-nuclear interactions and hyperon puzzle in neutron stars,” *Eur. Phys. J.* **A53** no. 6, (2017) 121, [arXiv:1612.03758](https://arxiv.org/abs/1612.03758) [nucl-th].
- [87] E. van Dalen, G. Colucci, and A. Sedrakian, “Constraining hypernuclear density functional with  $\lambda$ -hypernuclei and compact stars,” *Physics Letters B* **734** (2014) 383–387. <https://www.sciencedirect.com/science/article/pii/S0370269314003979>.
- [88] S. Weissenborn, D. Chatterjee, and J. Schaffner-Bielich, “Hyperons and massive neutron stars: the role of hyperon potentials,” *Nucl. Phys.* **A881** (2012) 62–77, [arXiv:1111.6049](https://arxiv.org/abs/1111.6049) [astro-ph.HE].
- [89] T. Miyatsu, T. Katayama, and K. Saito, “Effects of fock term, tensor coupling and baryon structure variation on a neutron star,” *Physics Letters B* **709** no. 3, (2012) 242–246. <https://www.sciencedirect.com/science/article/pii/S0370269312001281>.
- [90] S. Weissenborn, D. Chatterjee, and J. Schaffner-Bielich, “Hyperons and massive neutron stars: vector repulsion and SU(3) symmetry,” *Phys. Rev. C* **85** no. 6, (2012) 065802, [arXiv:1112.0234](https://arxiv.org/abs/1112.0234) [astro-ph.HE]. [Erratum: *Phys. Rev.C*90,no.1,019904(2014)].

- [91] S. Weissenborn, D. Chatterjee, and J. Schaffner-Bielich, "Hyperons and massive neutron stars: Vector repulsion and strangeness," *Nucl. Phys. A* **914** (2013) 421–426.
- [92] D. J. Millener, C. B. Dover, and A. Gal, " $\Lambda$ -nucleus single-particle potentials," *Phys. Rev. C* **38** (Dec, 1988) 2700–2708. <https://link.aps.org/doi/10.1103/PhysRevC.38.2700>.
- [93] J. Schaffner, C. Greiner, and H. Stöcker, "Metastable exotic multihypernuclear objects," *Phys. Rev. C* **46** (Jul, 1992) 322–329. <https://link.aps.org/doi/10.1103/PhysRevC.46.322>.
- [94] J. Mares, E. Friedman, A. Gal, and B. Jennings, "Constraints on  $\Sigma$ -nucleus dynamics from dirac phenomenology of  $\Sigma$ -atoms," *Nuclear Physics A* **594** no. 3, (1995) 311–324. <https://www.sciencedirect.com/science/article/pii/0375947495003588>.
- [95] T. Inoue, "Hyperon Single-particle Potentials from QCD On Lattice," *PoS INPC2016* (2017) 277.
- [96] **A Large Ion Collider Experiment Collaboration** Collaboration, S. e. a. Acharya, "First observation of an attractive interaction between a proton and a cascade baryon," *Phys. Rev. Lett.* **123** (Sep, 2019) 112002. <https://link.aps.org/doi/10.1103/PhysRevLett.123.112002>.
- [97] U. Heinz and B. V. Jacak, "Two-Particle Correlations in Relativistic Heavy-Ion Collisions," *Annual Review of Nuclear and Particle Science* **49** no. 1, (1999) 529–579. <https://doi.org/10.1146/annurev.nucl.49.1.529>.
- [98] M. A. Lisa, S. Pratt, R. Soltz, and U. Wiedemann, "Femtoscscopy in relativistic heavy ion collisions," *Ann. Rev. Nucl. Part. Sci.* **55** (2005) 357–402, arXiv:nucl-ex/0505014 [nucl-ex].
- [99] R. H. Brown and R. Twiss, "Lxxiv. a new type of interferometer for use in radio astronomy," *The London, Edinburgh, and Dublin Philosophical Magazine and Journal of Science* **45** no. 366, (1954) 663–682, <https://doi.org/10.1080/14786440708520475>. <https://doi.org/10.1080/14786440708520475>.
- [100] R. H. Brown, R. Q. Twiss, A. C. B. Lovell, and g. surName, "Interferometry of the intensity fluctuations in light - i. basic theory: the correlation between photons in coherent beams of radiation," *Proceedings of the Royal Society of London. Series A. Mathematical and Physical Sciences* **242** no. 1230, (1957) 300–324, <https://royalsocietypublishing.org/doi/pdf/10.1098/rspa.1957.0177>. <https://royalsocietypublishing.org/doi/abs/10.1098/rspa.1957.0177>.
- [101] R. H. Brown, R. Q. Twiss, and A. C. B. Lovell, "Interferometry of the intensity fluctuations in light. ii. an experimental test of the theory for partially coherent light," *Proceedings of the Royal Society of London. Series A. Mathematical and Physical Sciences* **243** no. 1234, (1958) 291–319, <https://royalsocietypublishing.org/doi/pdf/10.1098/rspa.1958.0001>. <https://royalsocietypublishing.org/doi/abs/10.1098/rspa.1958.0001>.
- [102] R. C. Jennison and M. K. Das Gupta, *Fine Structure of the Extra-terrestrial Radio Source Cygnus I*, pp. 291–295. Springer Netherlands, Dordrecht, 1982. [https://doi.org/10.1007/978-94-009-7752-5\\_33](https://doi.org/10.1007/978-94-009-7752-5_33).
- [103] R. Hanbury Brown and R. Q. Twiss, "A Test of a new type of stellar interferometer on Sirius," *Nature* **178** (1956) 1046–1048.

- [104] G. Goldhaber, S. Goldhaber, W. Lee, and A. Pais, "Influence of bose-einstein statistics on the antiproton-proton annihilation process," *Phys. Rev.* **120** (Oct, 1960) 300–312.  
<https://link.aps.org/doi/10.1103/PhysRev.120.300>.
- [105] R. Lednický, "Femtoscopy: Theory," *AIP Conference Proceedings* **828** no. 1, (2006) 423–429,  
<https://aip.scitation.org/doi/pdf/10.1063/1.2197450>.  
<https://aip.scitation.org/doi/abs/10.1063/1.2197450>.
- [106] G. I. Kopylov and M. I. Podgoretsky, "Correlations of identical particles emitted by highly excited nuclei," *Sov. J. Nucl. Phys.* **15** (1972) 219–223.
- [107] G. I. Kopylov, "Like particle correlations as a tool to study the multiple production mechanism," *Phys. Lett. B* **50** (1974) 472–474.
- [108] S. Pratt, "Pion Interferometry for Exploding Sources," *Phys. Rev. Lett.* **53** (Sep, 1984) 1219–1221. <https://link.aps.org/doi/10.1103/PhysRevLett.53.1219>.
- [109] S. E. Koonin, "Proton pictures of high-energy nuclear collisions," *Physics Letters B* **70** no. 1, (1977) 43 – 47.  
<http://www.sciencedirect.com/science/article/pii/0370269377903409>.
- [110] S. Pratt, T. Csörgő, and J. Zimányi, "Detailed predictions for two-pion correlations in ultrarelativistic heavy-ion collisions," *Phys. Rev. C* **42** (Dec, 1990) 2646–2652.  
<https://link.aps.org/doi/10.1103/PhysRevC.42.2646>.
- [111] **ALICE Collaboration** Collaboration, S. e. a. Acharya, "Kaon femtoscopy in pb-pb collisions at  $\sqrt{s_{NN}} = 2.76$  tev," *Phys. Rev. C* **96** (Dec, 2017) 064613.  
<https://link.aps.org/doi/10.1103/PhysRevC.96.064613>.
- [112] G. Kopylov, "Like particle correlations as a tool to study the multiple production mechanism," *Physics Letters B* **50** no. 4, (1974) 472 – 474.  
<http://www.sciencedirect.com/science/article/pii/0370269374902639>.
- [113] J. J. Sakurai and J. Napolitano, *Modern Quantum Mechanics*. Cambridge University Press, 2 ed., 2017.
- [114] S. Wong, *Introductory Nuclear Physics, Second Edition*. 12, 2007.
- [115] D. Furnstahl, "Lecture Notes TALENT/INT course on Nuclear Forces," 2013. [https://www.int.washington.edu/PROGRAMS/talent13/notes/M1b\\_Scattering\\_1\\_furnstahl.pdf](https://www.int.washington.edu/PROGRAMS/talent13/notes/M1b_Scattering_1_furnstahl.pdf).
- [116] H. A. Bethe, "Theory of the effective range in nuclear scattering," *Phys. Rev.* **76** (Jul, 1949) 38–50. <https://link.aps.org/doi/10.1103/PhysRev.76.38>.
- [117] P. Naidon and S. Endo, "Efimov physics: a review," *Reports on Progress in Physics* **80** no. 5, (Mar, 2017) 056001. <http://dx.doi.org/10.1088/1361-6633/aa50e8>.
- [118] R. Lednický and V. L. Lyuboshits, "Final State Interaction Effect on Pairing Correlations Between Particles with Small Relative Momenta," *Sov. J. Nucl. Phys.* **35** (1982) 770.
- [119] D. Mihaylov, *Analysis techniques for femtoscopy and correlation studies in small collision systems and their applications to the investigation of p- $\Lambda$  and  $\Lambda$ - $\Lambda$  interactions with ALICE*. PhD thesis, Technische Universität München, 2020.

- [120] E. Popovicz Seidel and F. Arretche, “Zero range potential approximation in quantum scattering problems,” *American Journal of Physics* **87** no. 10, (2019) 796–801, <https://doi.org/10.1119/1.5125110>. <https://doi.org/10.1119/1.5125110>.
- [121] D. L. Mihaylov, V. M. Sarti, O. W. Arnold, L. Fabbietti, B. Hohlweger, and A. M. Mathis, “A femtoscopic Correlation Analysis Tool using the Schrödinger equation (CATS),” arXiv:1802.08481 [hep-ph].
- [122] H. Yukawa, “On the Interaction of Elementary Particles I,” *Proc. Phys. Math. Soc. Jap.* **17** (1935) 48–57.
- [123] A. Badalyan, L. Kok, M. Polikarpov, and Y. Simonov, “Resonances in coupled channels in nuclear and particle physics,” *Physics Reports* **82** no. 2, (1982) 31–177. <https://www.sciencedirect.com/science/article/pii/037015738290014X>.
- [124] J. Oller, “Coupled-channel approach in hadron–hadron scattering,” *Progress in Particle and Nuclear Physics* **110** (2020) 103728. <https://www.sciencedirect.com/science/article/pii/S0146641019300638>.
- [125] Y. Kamiya, T. Hyodo, K. Morita, A. Ohnishi, and W. Weise, “ $K^-p$  correlation function from high-energy nuclear collisions and chiral  $su(3)$  dynamics,” *Phys. Rev. Lett.* **124** (Apr, 2020) 132501. <https://link.aps.org/doi/10.1103/PhysRevLett.124.132501>.
- [126] J. Haidenbauer, “Coupled-channel effects in hadron–hadron correlation functions,” *Nuclear Physics A* **981** (2019) 1–16. <https://www.sciencedirect.com/science/article/pii/S0375947418303774>.
- [127] L. Evans and P. Bryant, “LHC machine,” *Journal of Instrumentation* **3** no. 08, (Aug, 2008) S08001–S08001. <https://doi.org/10.1088/1748-0221/3/08/s08001>.
- [128] J. T. Boyd, “Lhc run-2 and future prospects,” 2020.
- [129] E. Mobs, “The CERN accelerator complex. Complexe des accélérateurs du CERN,” <http://cds.cern.ch/record/2197559>. General Photo.
- [130] M. Schaumann *et al.*, “First Xenon-Xenon Collisions in the LHC,” in *9th International Particle Accelerator Conference*, p. MOPMF039. 2018.
- [131] ALICE Collaboration, K. Aamodt *et al.*, “The ALICE experiment at the CERN LHC,” *J. Instrum.* **3** (2008) S08002.
- [132] ALICE Collaboration, B. B. Abelev *et al.*, “Performance of the ALICE Experiment at the CERN LHC,” *Int. J. Mod. Phys. A* **29** (2014) 1430044, arXiv:1402.4476 [nucl-ex].
- [133] F. N. and, “ALICE results from run-1 and run-2 and perspectives for run-3 and run-4,” *Journal of Physics: Conference Series* **1014** (May, 2018) 012010. <https://doi.org/10.1088/1742-6596/1014/1/012010>.
- [134] ALICE Collaboration, F. Carminati *et al.*, “ALICE: Physics Performance Report, Volume I,” *J. Phys. G* **30** (2004) 1517.
- [135] ALICE Collaboration, B. Alessandro *et al.*, “ALICE: Physics Performance Report, Volume II,” *J. Phys. G* **32** (2006) 1295.
- [136] ALICE Collaboration, “3D ALICE Schematic RUN2 - with Description,” 2017. <https://alice-figure.web.cern.ch/node/11218>. Accessed on 2021-04-15.

- [137] ALICE Collaboration, L. Barioglio, "Operational experience with ALICE ITS," *PoS VERTEX2018* (2019) 005.
- [138] J. Alme *et al.*, "The ALICE TPC, a large 3-dimensional tracking device with fast readout for ultra-high multiplicity events," *Nucl. Instrum. Meth.* **A622** (2010) 316.
- [139] S. Ramo, "Currents induced by electron motion," *Proceedings of the IRE* **27** no. 9, (1939) 584–585.
- [140] W. Shockley, "Currents to conductors induced by a moving point charge," *Journal of Applied Physics* **9** no. 10, (1938) 635–636. <https://doi.org/10.1063/1.1710367>.
- [141] B. Povh, K. Rith, C. Scholz, and F. Zetsche, *Teilchen und Kerne: Eine Einführung in die physikalischen Konzepte; 8th ed.* Springer-Lehrbuch. Springer, Heidelberg, 2009. <https://cds.cern.ch/record/1494496>. Also available in English version.
- [142] W. Blum, W. Riegler, and L. Rolandi, *Particle detection with drift chambers; 2nd ed.* Springer, Berlin, 2008. <https://cds.cern.ch/record/1105920>.
- [143] A. P. Kalweit, "ALICE TPC dE/dx performance in Run2 13 TeV (0.2T)," 2015. <https://alice-figure.web.cern.ch/node/8670>. Accessed on 2021-07-21.
- [144] A. Mathis, "From gated to continuous readout - the gem upgrade of the alice tpc," 2018.
- [145] ALICE TPC Collaboration, J. Adolfsson *et al.*, "The upgrade of the ALICE TPC with GEMs and continuous readout," *JINST* **16** no. 03, (2021) P03022, arXiv:2012.09518 [physics.ins-det].
- [146] A. Akindinov *et al.*, "Performance of the ALICE Time-of-Flight detector at the LHC," *Eur. Phys. J. Plus* **128** (2013) 44.
- [147] V. A. Grigoriev *et al.*, "ALICE T0 detector," in *2004 IEEE Nuclear Science Symposium and Medical Imaging Conference*. 2004.
- [148] T. Jimenez, "TOF beta vs momentum performance in pp at 13 TeV (LHC15f)," 2016. <https://alice-figure.web.cern.ch/node/9564>. Accessed on 2019-08-21.
- [149] R. Frühwirth, "Application of kalman filtering to track and vertex fitting," *Nuclear Instruments and Methods in Physics Research Section A: Accelerators, Spectrometers, Detectors and Associated Equipment* **262** no. 2, (1987) 444–450. <https://www.sciencedirect.com/science/article/pii/0168900287908874>.
- [150] A. Collaboration, "AliPhysics," 2020. <https://github.com/alice/alicePhysics>. Accessed on 2021-03-05.
- [151] T. Sjöstrand, S. Ask, J. R. Christiansen, R. Corke, N. Desai, P. Ilten, S. Mrenna, S. Prestel, C. O. Rasmussen, and P. Z. Skands, "An introduction to pythia 8.2," *Computer Physics Communications* **191** (Jun, 2015) 159–177. <http://dx.doi.org/10.1016/j.cpc.2015.01.024>.
- [152] GEANT4 Collaboration, S. Agostinelli *et al.*, "GEANT4—a simulation toolkit," *Nucl. Instrum. Meth. A* **506** (2003) 250–303.
- [153] L. Bianchi, "Particle-to-pion ratio as a function of multiplicity in pp7, pp13, p-Pb5, p-Pb8, Pb-Pb5 and Xe-Xe," 2019. <https://alice-figure.web.cern.ch/node/15504>. Accessed on 2019-08-21.

- [154] ALICE Collaboration, S. Acharya *et al.*, “Unveiling the strong interaction among hadrons at the LHC,” *Nature* **588** (2020) 232–238, arXiv:2005.11495 [nucl-ex].
- [155] R. Derradi De Souza, “V0M/⟨V0M⟩ distributions MB VHM triggers,” 2017. <https://alice-figure.web.cern.ch/node/11516>. Accessed on 2019-08-21.
- [156] T. Sjöstrand *et al.*, “An Introduction to PYTHIA 8.2,” *Comput. Phys. Commun.* **191** (2015) 159.
- [157] ALICE Collaboration, B. Abelev *et al.*, “ $K_s^0 K_s^0$  correlations in pp collisions at  $\sqrt{s} = 7$  TeV from the LHC ALICE experiment,” *Physics Letters B* **717** no. 1, (2012) 151 – 161. <http://www.sciencedirect.com/science/article/pii/S0370269312009574>.
- [158] B. Abelev, J. Adam, D. Adamová, A. M. Adare, M. M. Aggarwal, G. Aglieri Rinella, M. Agnello, A. G. Agocs, A. Agostinelli, Z. Ahammed, and *et al.*, “Charged kaon femtoscopic correlations in pp collisions at  $\sqrt{s} = 7$  tev,” *Physical Review D* **87** no. 5, (Mar, 2013). <http://dx.doi.org/10.1103/PhysRevD.87.052016>.
- [159] ALICE Collaboration, K. Aamodt *et al.*, “Femtoscopia of pp collisions at  $\sqrt{s} = 0.9$  and 7 TeV at the LHC with two-pion Bose-Einstein correlations,” *Phys. Rev. D* **84** (Dec, 2011) 112004. <https://link.aps.org/doi/10.1103/PhysRevD.84.112004>.
- [160] ALICE Collaboration, J. Adam *et al.*, “Two-pion femtoscopia in p-Pb collisions at  $\sqrt{s_{NN}} = 5.02$  TeV,” *Phys. Rev. C* **91** (Mar, 2015) 034906. <https://link.aps.org/doi/10.1103/PhysRevC.91.034906>.
- [161] ALICE Collaboration, S. Acharya *et al.*, “Scattering studies with low-energy kaon-proton femtoscopia in proton-proton collisions at the LHC,” *Phys. Rev. Lett.* **124** no. 9, (2020) 092301, arXiv:1905.13470 [nucl-ex].
- [162] The ALICE Collaboration, “Multiplicity dependence of jet-like two-particle correlation structures in p–Pb collisions at  $\sqrt{s_{NN}} = 5.02$  TeV,” *Physics Letters B* **741** (2015) 38 – 50. <http://www.sciencedirect.com/science/article/pii/S0370269314008302>.
- [163] The ALICE Collaboration, “Transverse sphericity of primary charged particles in minimum bias proton–proton collisions at  $\sqrt{s} = 0.9, 2.76$  and 7 TeV,” *The European Physical Journal C* **72** no. 9, (Sep, 2012) 2124. <https://doi.org/10.1140/epjc/s10052-012-2124-9>.
- [164] ALICE Collaboration, S. Acharya *et al.*, “Search for a common baryon source in high-multiplicity pp collisions at the LHC,” *Phys. Lett. B* **811** (2020) 135849, arXiv:2004.08018 [nucl-ex].
- [165] ALICE Collaboration, S. Acharya *et al.*, “Production of light-flavor hadrons in pp collisions at  $\sqrt{s} = 7$  and  $\sqrt{s} = 13$  TeV,” *Eur. Phys. J. C* **81** no. 3, (2021) 256, arXiv:2005.11120 [nucl-ex].
- [166] A. G. Knospe *et al.*, “Measurement of phi Mesons at Mid-Rapidity in Minimum-Bias pp Collisions at 13 TeV,”. <https://alice-notes.web.cern.ch/node/466>.
- [167] G. D’Agostini, “A Multidimensional unfolding method based on Bayes’ theorem,” *Nucl. Instrum. Meth. A* **362** (1995) 487–498.
- [168] T. Adye, “Unfolding algorithms and tests using roounfold,” 2011.
- [169] “Rounfold.” <https://gitlab.cern.ch/RooUnfold/RooUnfold>.

- [170] O. Arnold, “Two-particle baryon femtoscopy studies in proton-proton reactions at  $\sqrt{s_{NN}} = 7$  TeV measured with the ALICE experiment at the Large Hadron Collider,” <https://alice-notes.web.cern.ch/node/552>.
- [171] **ALICE Collaboration**, J. Adam *et al.*, “Insight into particle production mechanisms via angular correlations of identified particles in pp collisions at  $\sqrt{s} = 7$  TeV,” *Eur. Phys. J. C* **77** no. 8, (2017) 569, arXiv:1612.08975 [nucl-ex]. [Erratum: *Eur.Phys.J.C* **79**, 998 (2019)].
- [172] F. Becattini, P. Castorina, A. Milov, and H. Satz, “Predictions of hadron abundances in pp collisions at the LHC,” *J. Phys. G* **38** (2011) 025002, arXiv:0912.2855 [hep-ph].
- [173] T. Pierog, I. Karpenko, J. Katzy, E. Yatsenko, and K. Werner, “EPOS LHC: Test of collective hadronization with data measured at the CERN Large Hadron Collider,” *Phys. Rev. C* **92** no. 3, (2015) 034906, arXiv:1306.0121 [hep-ph].
- [174] H. Polinder, J. Haidenbauer, and U.-G. Meißner, “Hyperon-nucleon interactions—a chiral effective field theory approach,” *Nuclear Physics A* **779** (2006) 244–266. <https://www.sciencedirect.com/science/article/pii/S0375947406006312>.
- [175] J. Haidenbauer, S. Petschauer, N. Kaiser, U.-G. Meißner, A. Nogga, and W. Weise, “Hyperon-nucleon interaction at next-to-leading order in chiral effective field theory,” *Nuclear Physics A* **915** (2013) 24–58. <https://www.sciencedirect.com/science/article/pii/S0375947413006167>.
- [176] F. Becattini, P. Castorina, A. Milov, and H. Satz, “Predictions of hadron abundances in pp collisions at the LHC,” *Journal of Physics G: Nuclear and Particle Physics* **38** no. 2, (Jan, 2011) 025002. <http://dx.doi.org/10.1088/0954-3899/38/2/025002>.
- [177] A. Collaboration, “Experimental evidence for an attractive p- $\phi$  interaction,” 2021. <https://arxiv.org/abs/2105.05578>. Accepted by PRL.
- [178] T. Sugiura, Y. Ikeda, and N. Ishii, “Charmonium-nucleon interactions from  $2 + 1$  flavor lattice QCD,” *PoS LATTICE2018* (2019) 093.
- [179] I. I. Strakovsky, L. Pentchev, and A. Titov, “Comparative analysis of  $\omega p$ ,  $\phi p$ , and  $J/\psi p$  scattering lengths from A2, CLAS, and GlueX threshold measurements,” *Phys. Rev. C* **101** (2020) 045201.
- [180] Y. Koike and A. Hayashigaki, “QCD Sum Rules for  $\rho$ ,  $\omega$ ,  $\phi$  Meson-Nucleon Scattering Lengths and the Mass Shifts in Nuclear Medium,” *Progr. Theo. Phys.* **98** (1997) 631.
- [181] **LEPS Collaboration** Collaboration, T. e. a. Mibe, “Near-threshold diffractive  $\phi$ -meson photoproduction from the proton,” *Phys. Rev. Lett.* **95** (Oct, 2005) 182001. <https://link.aps.org/doi/10.1103/PhysRevLett.95.182001>.
- [182] W. C. Chang *et al.*, “Forward coherent phi-meson photoproduction from deuterons near threshold,” *Phys. Lett.* **B658** (2008) 209.
- [183] F. Klingl, N. Kaiser, and W. Weise, “Current correlation functions, QCD sum rules and vector mesons in baryonic matter,” *Nucl. Phys. A* **624** (1997) 527–563, arXiv:hep-ph/9704398.

- [184] S. Acharya, D. Adamová, S. Adhya, A. Adler, J. Adolfsson, M. Aggarwal, G. Aglieri Rinella, M. Agnello, N. Agrawal, Z. Ahammed, and et al., “Study of the  $\lambda$ - $\lambda$  interaction with femtoscopy correlations in pp and p-Pb collisions at the LHC,” *Physics Letters B* **797** (Oct, 2019) 134822. <http://dx.doi.org/10.1016/j.physletb.2019.134822>.
- [185] F. James, “MINUIT Function Minimization and Error Analysis: Reference Manual Version 94.1,”.
- [186] R. D. Grande, L. Šerkšnytė, L. Fabbietti, V. M. Sarti, and D. Mihaylov, “A method to remove lower order contributions in multi-particle femtoscopic correlation functions,” 2021.
- [187] R. Kubo, “Generalized cumulant expansion method,” *Journal of the Physical Society of Japan* **17** no. 7, (1962) 1100–1120, <https://doi.org/10.1143/JPSJ.17.1100>.  
<https://doi.org/10.1143/JPSJ.17.1100>.